Asymmetrical zinc(II) phthalocyanines conjugated to nanomaterials for degradation of organic pollutants and inactivation of *Staphylococcus aureus bacteria*

Thesis submitted for the degree of

Doctor of Philosophy

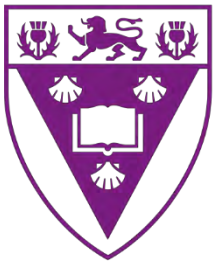

RHODES UNIVERSITY

Where leaders learn

Sithi Mgidlana

January 2023

Dedication

To my parents: Christopher Mziwenkosi Mgidlana and Vivienne Nolungile Mgidlana.

Acknowledgements

Distinguished Prof. Tebello Nyokong: My incredible supervisor for your valuable guidance, encouragement, and constructive suggestions which made possible the successful completion of this work. My education has expanded in several ways, thanks to you.

Dr Jonathan Britton: My co-supervisor, I would like to show gratitude to you for supporting my work throughout the programme.

Prof John Mack: Great appreciation for assistance with the laser, which significantly influenced the outcome of this thesis.

Drs: Śen, Openda, and Managa: Thank you all for your assistance and for always being there whenever I needed you.

S22 lab members: I value how engaging and motivating the institute for nanotechnology innovation is.

Funding:

- National Research Foundation (NRF) through DSI/NRF South African Research Chairs Initiative for Professor of Medicinal Chemistry and Nanotechnology.
- HWSETA postgraduate scholarship.
- NRF postgraduate scholarship.

Abstract

This thesis reports on the syntheses and characterization of asymmetrical phthalocyanines (Pcs) with different ring substituents (tert-butyl, ester, diimide, trimethoxy, acetophenone, heptanoylphenoxy, perfluorophenoxy, dimethoxy, propanoic acid, acetic acid, carboxylic acid, aminophenoxy, acrylic acid). Several nanoparticles including metal tungstate, capped with glutathione and 1-mercaptohexanol are prepared and characterized using analytical techniques. The synthesized Pcs are covalently linked to various nanoparticles (NPs) through ester and amide bonds to form Pc-NP conjugates, in order to improve their catalytic properties. The Pcs and their conjugates are characterized using different analytical techniques. The photophysics and photochemistry of the MPcs and conjugates are studied. The conjugates exhibited high triplet quantum yields (Φ_T). The complexes and the conjugates with nanomaterials are evaluated for singlet oxygen-generating ability. Conjugates generate higher singlet oxygen in comparison to Pc complexes alone.

The photocatalytic activity of the conjugates of ZnPc complexes with $NiWO_4$, Ag_2WO_4, Bi_2WO_6, $CoWO_4$, and Ag-Fe_3O_4-based nanoparticles is evaluated based on photodegradation of methylene blue, tetracycline, and dibenzothiophene. The photocatalytic efficiencies of the synthesized phthalocyanine complexes increased in the presence of nanoparticles. This work also reports on the photodynamic antimicrobial chemotherapy activity of these materials against *Staphylococcus aureus (S. aureus)* bacteria in DMSO. The results indicated that silver-based nanoconjugates exhibit high antimicrobial activity with high log reductions compared to $NiWO_4$, $CoWO_4$, and Ag-Fe_3O_4-based materials. The *z*-scan technique is employed to experimentally test the nonlinear optical response of complexes and nanoconjugates in solution. The nonlinear absorption coefficient, third-order optical susceptibility and optical limiting threshold of the materials are obtained from the Z-scan aperture data. The nonlinear absorption parameters improved in the presence of semiconductor quantum dots, with **1**-ethanoic-CdTe/ZnSeS/ZnO giving the best results due to the presence of electron-donating substituents.

Table of content

Table of contents

Table of contents

Table of contents

List of symbols

A – absorbance

F – area under fluorescence curve

N_A – Avogadro constant

w_o – beam waist

r – center-to-center distance

ΔA_T – change in absorbance in the triplet state

β_{eff} – effective nonlinear absorption coefficient

L_{eff} – effective path length

E_{ff} – efficiency of energy transfer

σ_{ex} – excited state absorption cross section

S_1 – first excited singlet state

T_1 – first excited triplet state

τ_F – fluorescence lifetime

Φ_F – fluorescence quantum yield

υ – frequency of light

S_o – ground singlet state

I_o – input irradiance

τ_{isc} – intersystem crossing period

τ – lifetime

I_{lim} – limiting threshold intensity

α – linear absorbance

k - magnitude of absorption cross-sections ratio

β – nonlinear absorption coefficient

S_n – nth excited singlet state

T_n – nth excited triplet state

List of symbols

I_{oo} – on-focus peak input irradiance

I_{out} – output intensity

ϵ_o – permittivity of free space

h – Planck's constant

z_o – Rayleigh length

n – refractive index

z – sample position

Φ_Δ – singlet oxygen quantum yield

$X^{(3)}$ – third-order susceptibility

τ_T – triplet lifetime

Φ_T – triplet quantum yield

λ – wavelength

List of abbreviations

Abs – absorbance

ADMA – anthracene-9,10-bis-methylmalonate

AOP – advanced oxidation process

CFU – colony forming unit

DBU – 1,8-diazabicyclo-[5.4.0]-undec-7-ene

DCC – dicyclohexylcarbodiimide

DLS – dynamic light scattering

DMF – dimethyl formamide

DMSO – dimethyl sulfoxide

DMSO-d_6 – deuterated dimethylsulfoxide

DPBF – diphenylisobenzofuran

EDX – energy dispersive X-ray

ESA – excited state absorption

FRET – Förster resonance energy transfer

FCA – free-carrier absorption

FTIR – Fourier transform infra-red

F – fluorescence

HOMO – highest occupied molecular orbital

^{1}H-NMR – proton nuclear magnetic resonance

ISC – intersystem crossing

LUMO – lowest unoccupied molecular orbital

MS – mass spectroscopy

MB – methylene blue

MALDI – matrix-assisted laser desorption ionization

MPcs – metallophthalocyanines

NIR – near infra-red

Nd-YAG – neodymium-doped yttrium aluminium garnet

NLA – nonlinear absorption

NLO – nonlinear optics

NLR – nonlinear refraction

NLS – nonlinear scattering

List of abbreviations

NP – nanoparticle

OL – optical limiting

PACT – photodynamic antimicrobial chemotherapy

PDT – photodynamic therapy

PL – photoluminescence

Pcs – phthalocyanines

QDs – quantum dots

RSA – reverse saturable absorption

S. aureus – staphylococcus aureus

TCSPC – time correlated single photon counting

THF – tetrahydrofuran

TOF – time-of-flight

TEM – transmission electron microscopy

UV-vis – ultraviolet-visible

VR – vibrational relaxation

XRD – x-ray diffraction

Preamble

Globally there is an increasing scarcity of clean water which is mainly due to the presence of a large amount of various organic pollutants and bacteria. To solve these global burdens, this work presents photocatalytic degradation of pollutants, desulfurization of compounds, and photodynamic antimicrobial chemotherapy (PACT) for the removal of bacteria in water (*Staphylococcus aureus* in this case).

To do so, this work presents a combination of novel metallophthalocyanine (MPcs), and nanoparticles with photophysicochemical properties suitable for various applications such as photocatalysis and PACT. As a side application, please note that this work also presents nonlinear optics (NLO) of the selected conjugates.

Chapter 1

This chapter provides a brief overview of the literature relating to organic pollutants, nanomaterials, asymmetrical metallophthalocyanines, combinations of the latter two, and their applications in photocatalysis, photodynamic antimicrobial chemotherapy (PACT), and nonlinear optics (NLO).

1.1 Background on organic pollutants and bacteria addressed in this thesis.

Organic pollutants are toxic molecules that can be found in diverse environments and can cause various diseases in humans and animals when exceeding acceptable limits [1]. These contaminants include industrial products such as petroleum hydrocarbons and dyes, as well as antibiotic residues [1-3]. Dibenzothiophenes (DBT), methylene blue (MB), and tetracycline (TC) are the targeted organic pollutants in this work.

DBT (structure in **Figure 1.1**) and their derivatives account for the high amount of sulfur in fuel. The use of fuel containing sulfur results in the emission of sulfur oxide compounds (SO_x) upon combustion [4-6]. These gases negatively impact the atmosphere and cause health concerns [1]. Hence, it is essential for petroleum industries to comply with recent environmental regulations that focus on reaching low sulfur content in fuels [3,7].

MB is largely produced in the printing and dye industries and is widely used as a chemical indicator [8,9]. MB has high chromaticity, high organic matter content, and low biodegradability. MB negatively affects health and in the environment [10-12].

On the other hand, the extensive use of antibiotics in humans and animals has led to important environmental pollution [13]. Tetracycline (TC, structure in **Figure 1.1**) is one of the most widely used antibiotics in aquaculture and veterinary medicines [14,15]. The concern is that the effect of antibiotic

residues like TC in the environment lead to the development of multi-drug resistant bacteria [**16**].

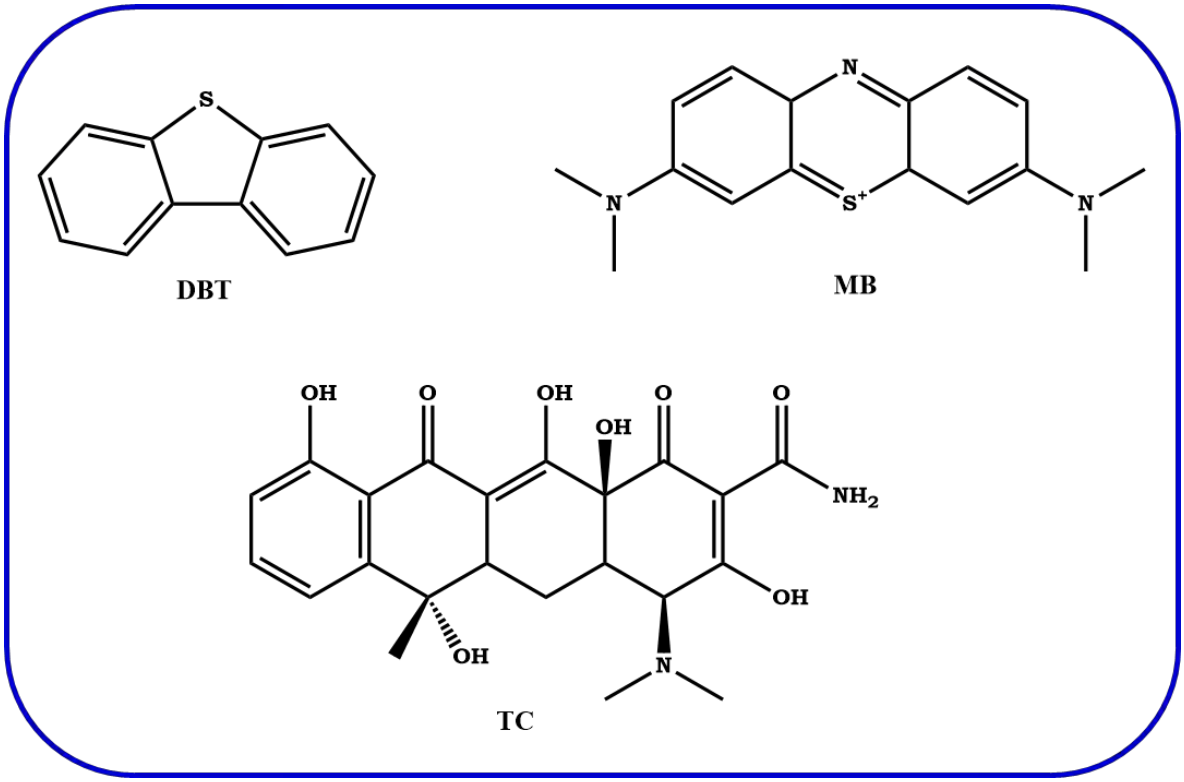

Figure 1.1: *Organic Pollutants studied in this thesis.*

It is hard to degrade TC in living organisms and it can even be converted to more toxic substances. Antibiotics have been detected in soil, waste, and drinking water [**17,18**]. Photocatalysis will be used as an advanced oxidation process to degrade MB, TC and desulfurize DBT using phthalocyanines as photocatalysts.

Bacteria, commonly the Gram (+) strain *S. aureus*, constitute on their own another form of biological water contaminant. Generally, the greatest microbial risks come from the ingestion of water that is contaminated with microorganisms. Photodynamic antimicrobial chemotherapy (PACT) has been reported as the efficient alternative to eradicate the bacteria via the

photosensitization process **[19]**. Hence, photocatalysis and PACT are used in the present work for water purification purposes.

1.2 Metallophthalocyanine (MPcs)

Metallophthalocyanines (MPcs) (**Figure 1.2A**) are a family of highly stable and versatile macrocycles containing 18 π-electron conjugated systems [**20**].

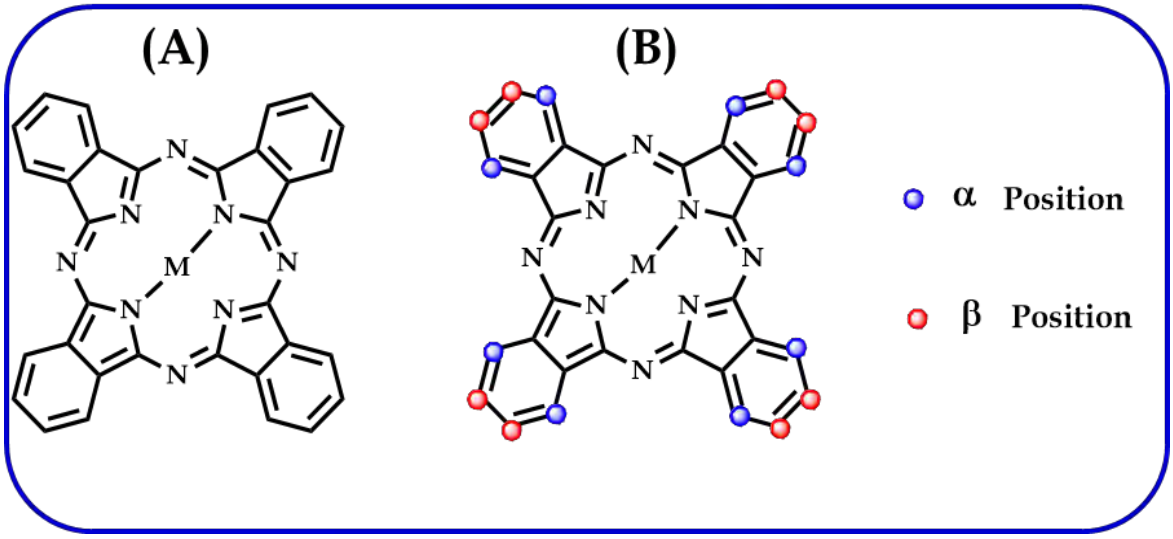

Figure 1.2: *(**A**) The structure of metallophthalocyanine (**B**) a and β positions on the metallophthalocyanine.*

The existence of a single, strong, asymmetric Q-band and broad B-band in the near-infrared, and ultraviolet regions, respectively, characterize the electronic absorption spectra of the MPcs (**Figure 1.3**) [**21-23**]. **Figure 1.3** (**inset**) indicates that the transition from the ground state of the highest occupied molecular orbital (HOMO), a_{1u}, to the doubly degenerate e_g of the lowest unoccupied molecular orbital (LUMO), causes the appearance of the Q band. The π-π* transitions from a_{2u} and b_{2u} of the HOMO to the e_g of the LUMO are what cause the B band (B_1 and B_2 combined) to be produced.

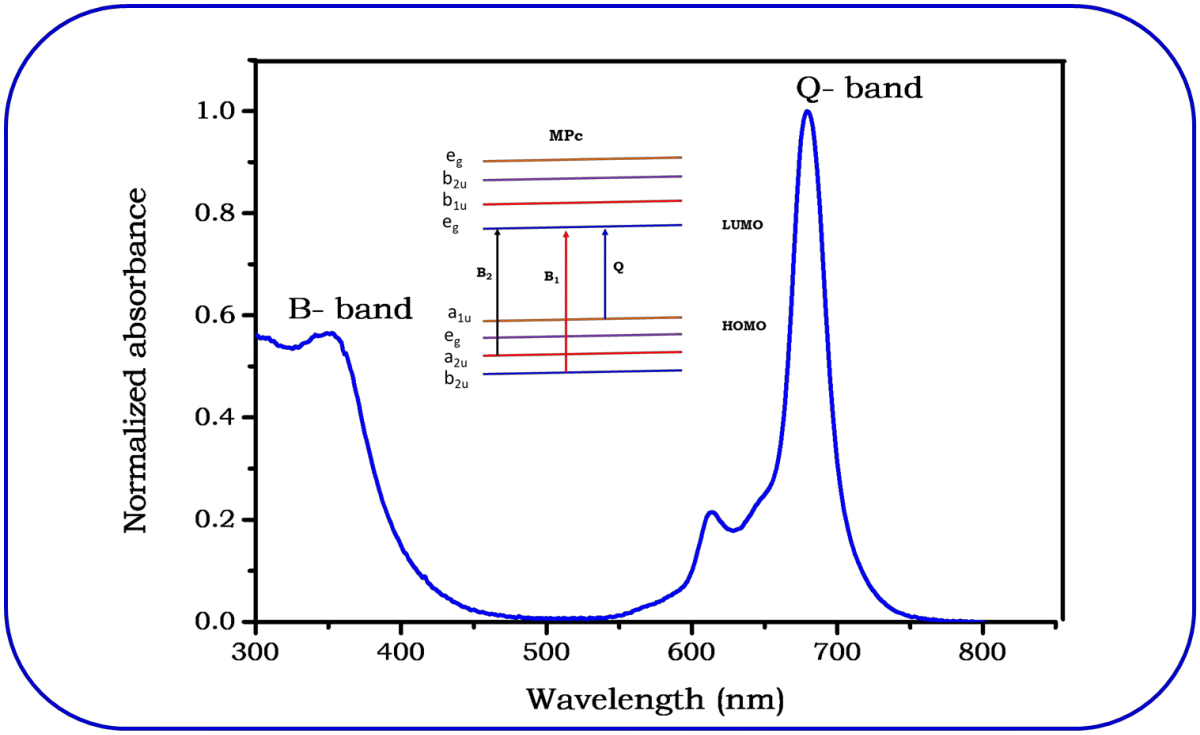

Figure 1.3: *Typical electronic absorption spectrum of a metallophthalocyanine.*

Due to the ease of synthetic modification, π-electron conjugated systems and absorption bands ranging from UV to IR region, MPcs have been employed in organic electronic devices such as sensors [**24**], light-emitting diodes [**25**], memory devices [**26**], solar cells [**27**], nonlinear optics [**28**], and photocatalysis [**29**]. However, there are still some drawbacks that limit their further development, such as aggregation, which affects their photochemical and photophysical properties. Bulkier substituents on the α or β positions (**Figure 1.2B**) are known to reduce aggregation [**30**]. Hence, this work reports on the syntheses of asymmetrical substituted MPcs containing bulky substituents.

1.2.1 Synthesis of MPcs

Design and synthesis of asymmetrical MPcs (**Scheme 1.1**) have recently been a center of focus amongst phthalocyanine researchers. A_3B MPcs are the focus of the present work.

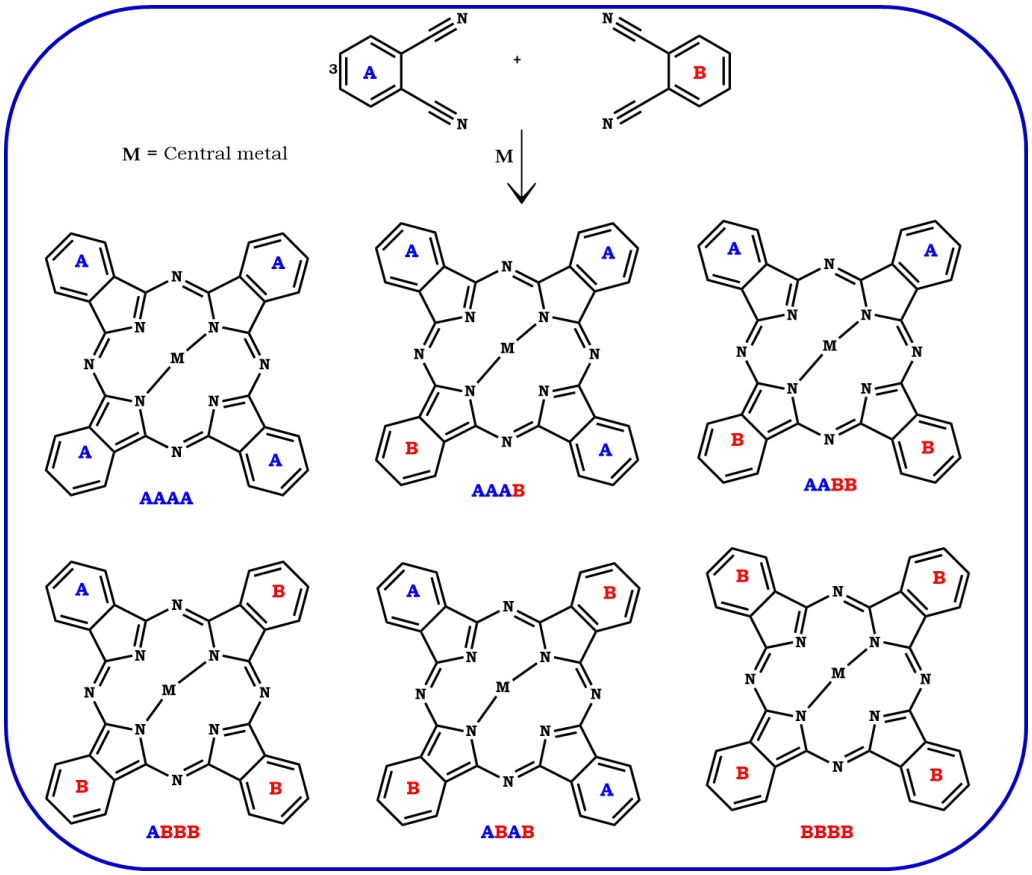

Scheme. 1.1: *Synthetic methods of asymmetrical MPcs using the statistical condensation of phthalonitriles **A** and **B**.*

Asymmetric A_3B MPcs can be obtained by using different methods such as the subphthalocyanine ring expansion route [**31**], statistical-mixed condensation route [**32-34**], and polymeric–support-based route [**35**]. However, the most utilized protocol for A_3B MPcs is the statistical mixed condensation, which uses two non-identical phthalonitriles in the presence

or absence of a metal salt, **Scheme 1.1**. A mixture of six different products is obtained and chromatography is usually used to isolate the target molecule.

1.2.2 MPcs used in this thesis

In this work, using zinc as a central metal, novel asymmetrical ZnPcs (A_3B type) along with their nanoconjugates with nanoparticles are synthesized and employed as photocatalysts for phototransformation of organic pollutants, photoinactivation of bacteria, and in NLO. All the complexes are designed such that they have amino (NH_2) or carboxylic acid (COOH) moieties thereby allowing covalent bonds with the functional groups of the NPs (**Table 1.1**). The Pc complexes are presented as **1-8** with their non-dominant substituents following the complex number throughout the thesis. The moieties are presented as follows: ethanoic acid (ethanoic), propionic acid (propionic), carboxy (COOH), amino (NH_2), acrylic acid (acrylic), and acetic acid (acetic). The rationale for the use of the complexes will be discussed below.

Table 1.1: Metallophthalocyanine complexes employed in this thesis.

Complex	NPs	Application
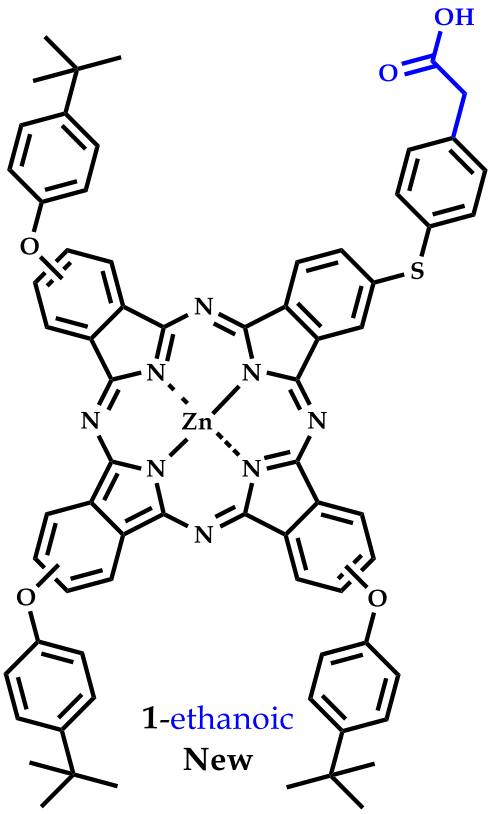 1-ethanoic = Mono 4-(2-thio phenyl) ethanoic acid) tris(4-tert-butylphenoxy) Zn(II) phthalocyanine	CdTe/ZnSe/ZnO QDs Glutathione (GSH) capped	NLO

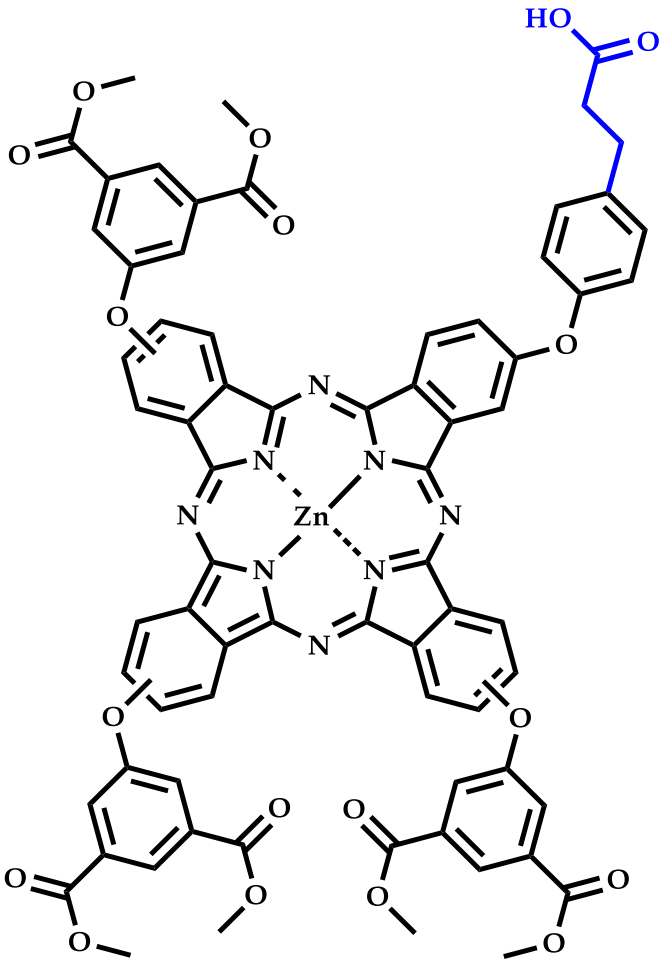 **2-propionic** **New** **2-propionic** = Mono 4 (phenoxy)propionic acid) tris[(dimethyl-5-phenoxy)isophthalate] Zn(II)phthalocyanine	CdTe/ZnSe/ZnO QDs $CoWO_4$ Glutathione (GSH) capped	NLO and TC

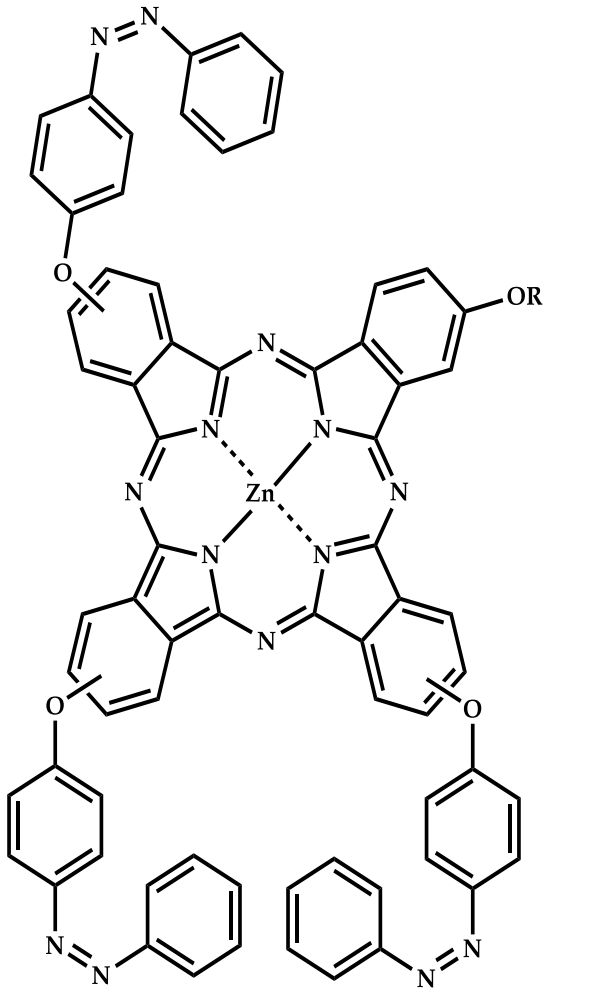

R =

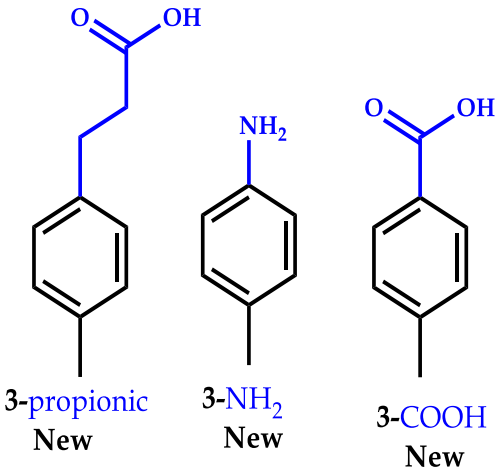

3-propionic
New

3-NH_2
New

3-COOH
New

3-propionic = Mono (4-propanoic acid phenoxy) tris (phenylazo phenoxy) Zn(II) phthalocyanine

3-NH_2 = Mono (4-amino phenoxy) tris (phenylazo phenoxy) Zn(II)phthalocyanine

3-COOH = Mono (4-carboxy phenoxy) tris (phenylazo phenoxy) Zn(II)phthalocyanine

$Ag\text{-}Fe_3O_4$

1-mercatohexanol (mph) capped (for **3**-COOH, **3**-propionic)

1-mercaptopropionic acid (mpa) capped (for **3**-NH_2)

DBT

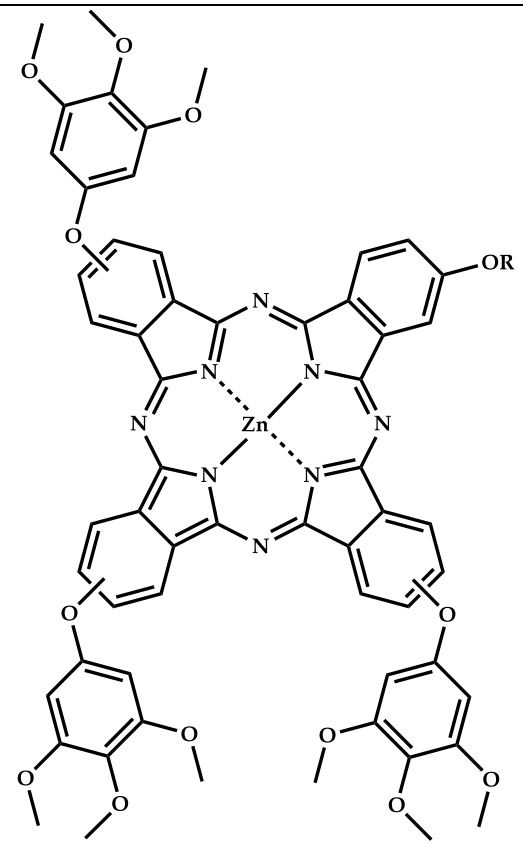 **4**-COOH **New** **4**-propionic **New** **4**-acetic **New** **4**-COOH = Mono 4(carboxyphenoxy) tris(4-(3,4,5-trimethoxyphenoxy) Zn(II) phthalocyanine **4**-propionic = Mono 4-phenoxy)-propionic acid) tris(4-(3,4,5-trimethoxyphenoxy) Zn(II)phthalocyanine **4**-acetic = Mono 4-(oxy)phenoxy) acetic acid) tris(4-(3,4,5-trimethoxyphenoxy) Zn(II)phthalocyanine	$NiWO_4$ & Bi_2WO_6 Glutathione (GSH) capped. **4**-COOH also linked to $CoWO_4$	DBT and PACT

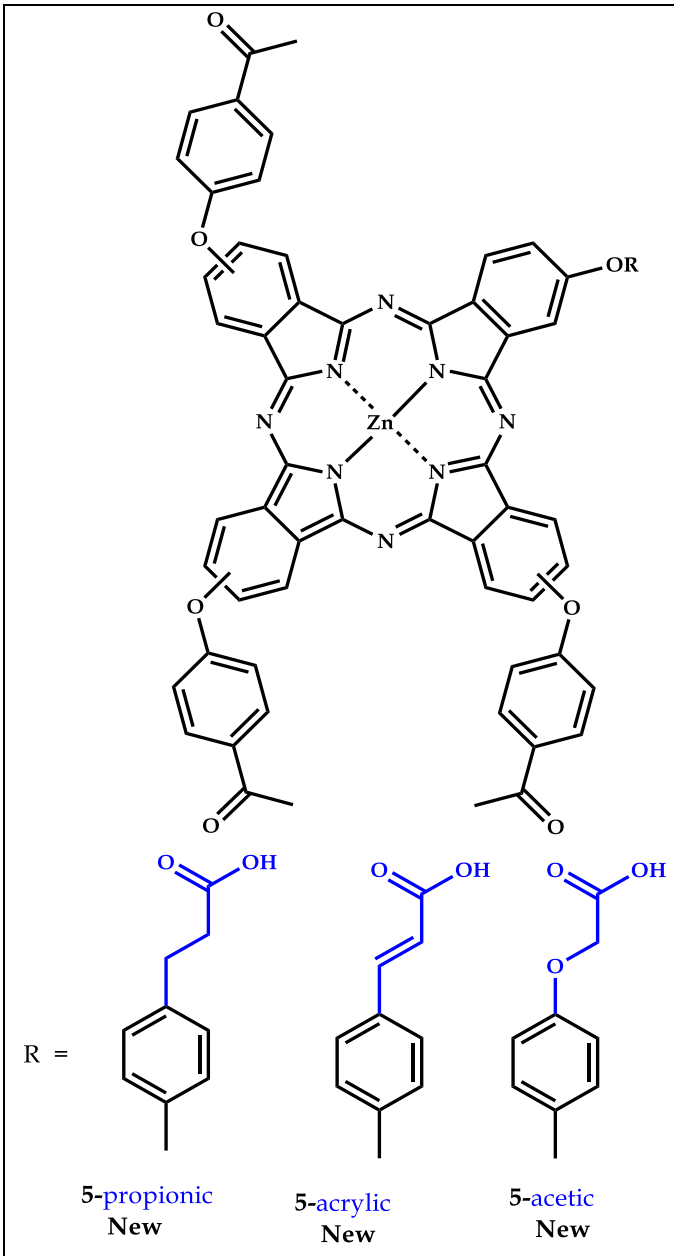 **5**-propionic = Mono (4-propanoic acid phenoxy) tris (4-acetophenoxy) Zn(II)phthalocyanine **5**-acrylic = Mono (4-acrylic acid phenoxy) tris (4-acetophenoxy) Zn(II)phthalocyanine **5**-acetic = Mono (3-(4-oxy)phenoxy)acetic acid) tris (4-acetlyphenoxy) Zn(II)phthalocyanine	$CoWO_4$ Glutathione (GSH) capped. **5**-acetic also linked to $NiWO_4$, Ag_2WO_4, Ag-Fe_3O_4, $CoWO_4$	MB and PACT DBT and TC

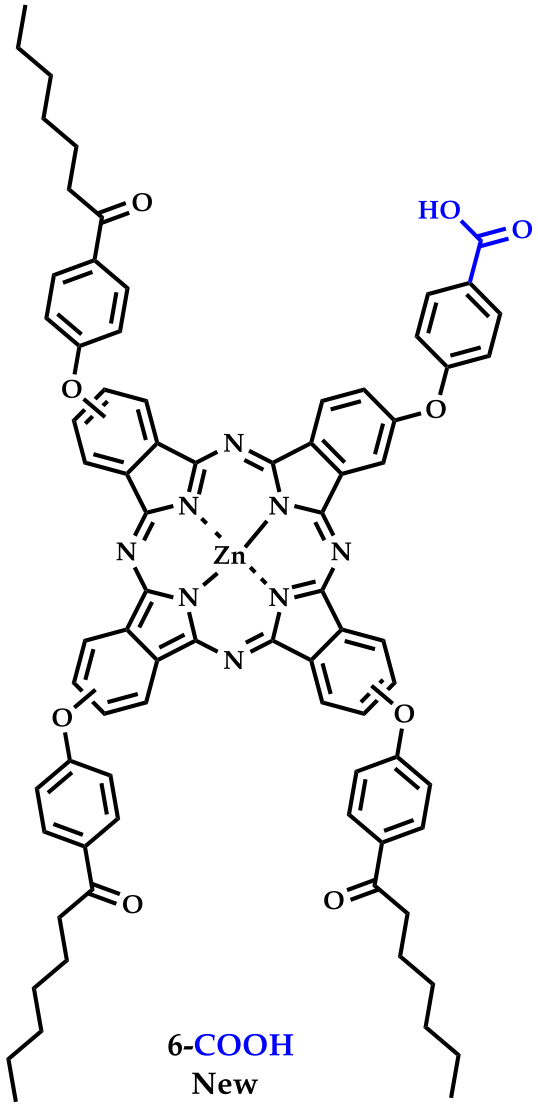 **6-COOH** **New** **6**-COOH = Mono (4-carboxy phenoxy) tris(4-heptanoylphenoxy) Zn(II)phthalocyanine	$CoWO_4$ Glutathione (GSH) capped	TC

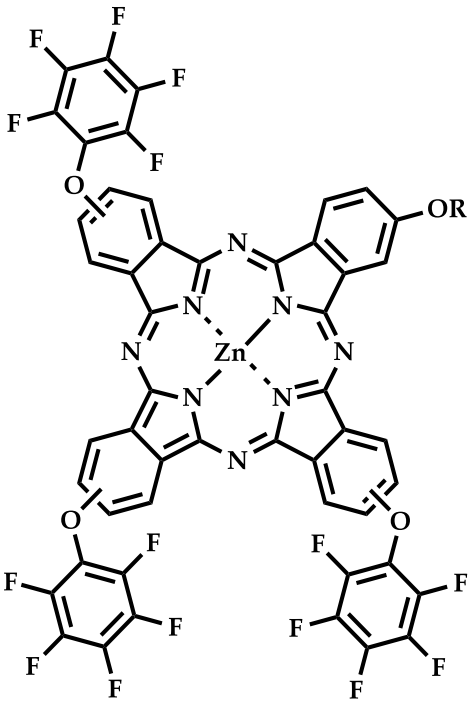 R = 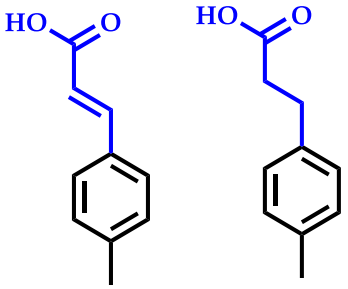 **7-acrylic New** **7-propionic New** 7-acrylic = Mono (4-acrylic acid phenoxy) tris(4-perfluorophenoxy) Zn(II)phthalocyanine 7-propionic = Mono (4-propanoic acid phenoxy) tris(4-perfluorophenoxy) Zn(II)phthalocyanine	$CoWO_4$ Glutathione (GSH) capped	TC

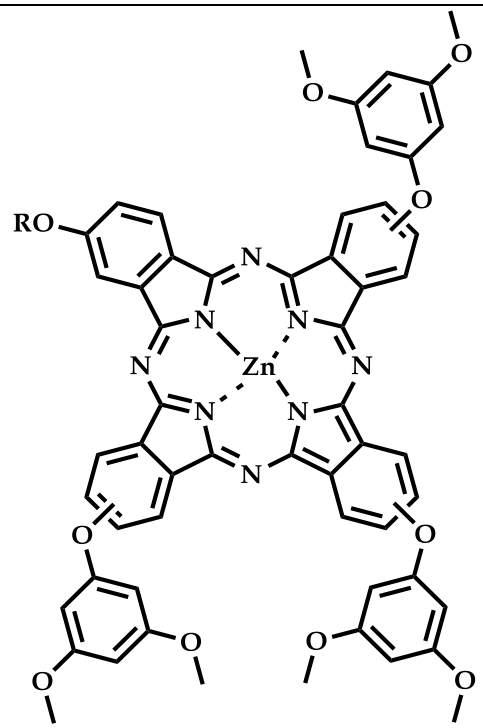 R = 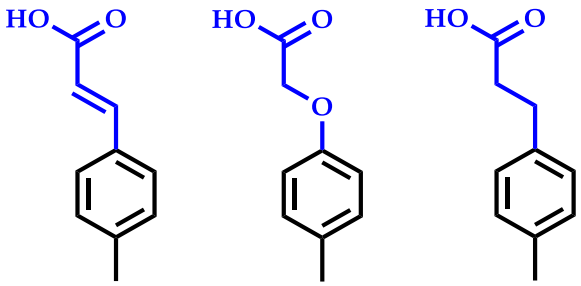 **8**-acrylic **New** **8**-acetic **New** **8**-propionic **New** **8**-propionic = Mono (4-propanoic acid phenoxy) tris (4- 4-(3,5-dimethoxyphenoxy) Zn(II)phthalocyanine **8**-acetic = Mono (3-(4-oxy)phenoxy)acetic acid) tris (4-(3,5-dimethoxyphenoxy) Zn(II)phthalocyanine **8**-acrylic = Mono (4-acrylic acid phenoxy) tris (4-(3,5-dimethoxyphenoxy) Zn(II)phthalocyanine	Ag_2WO_4 Glutathione (GSH) capped	TC and PACT

1.2.3 Photophysicochemical properties

The processes that take place when MPcs absorb light are frequently illustrated using a Jablonski diagram, **Figure 1.4** [**36-40**].

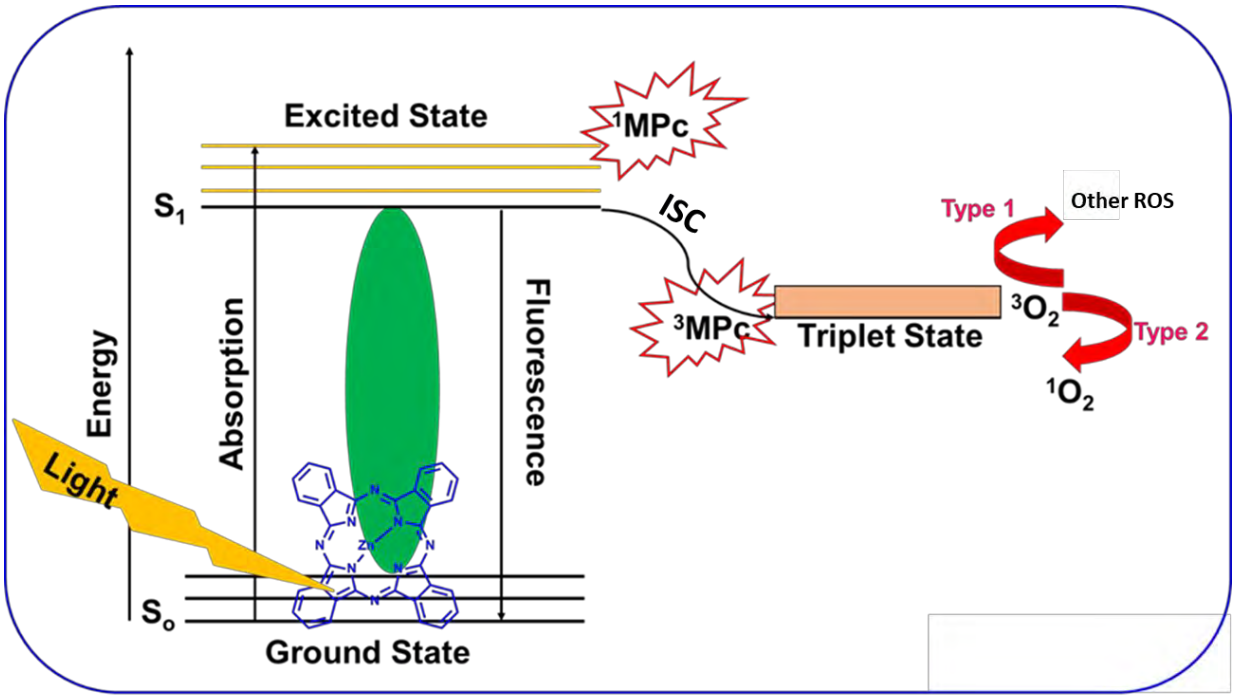

Figure 1.4: *Basic Jablonski diagram. The transitions between ground state (S_0) and electronically excited states.*

The processes are as follows: the MPc absorbs a photon from the ground state (S_o) to the excited singlet excited state (S_1). The molecule can either fluoresce and then return to the ground state (S_o) or it can undergo intersystem crossing (ISC) to occupy the triplet excited states where MPc will transfer energy to ground state molecular oxygen ($^3O_2$) thereby generating various reactive oxygen species (ROS) including singlet oxygen ($^1O_2$) which are important for photocatalysis and PACT [**41,42**]. Photophysicochemical parameters, such as Förster resonance energy transfer, fluorescence, triplet, singlet oxygen

quantum yields, and fluorescence and triplet lifetimes may be determined as shown in the following sections.

1.2.3.1 Fluorescence Quantum yields (Φ_F) and lifetimes (τ_F)

For MPc complexes, fluorescence quantum yield (Φ_F) is mostly determined by the comparative method, equation 1.1 [43].

$$\Phi_F = \Phi_F^{std} \frac{F\ A_{std}\ n^2}{F_{std} A\ n_{std}^2} \qquad 1.1$$

where A and A_{std} are the absorbances of the sample and standard at the excitation, and F and F_{std} are the areas under the fluorescence emission curves of the sample and the reference, respectively. Whereas n_{std} and n are the refractive indexes of the solvents used for the reference and the sample, respectively. The unsubstituted ZnPc in dimethyl sulfoxide (DMSO) is used as a standard with Φ_F = 0.20 [44], and where semiconductor quantum dots (QDs) absorb, quinine sulfate is used as a standard with Φ_F^{std}=0.52 [45]. On the other hand, fluorescence lifetimes presented in this thesis were determined using time-correlated single photon counting (TCSPC) as reported in literature [46].

1.2.3.2 Förster resonance energy transfer (FRET)

A photo-excited fluorescent donor molecule, such as quantum dots (QDs) (donors), transmits energy to an acceptor molecule (MPcs) by dipole-dipole coupling in a process known as Förster resonance energy transfer (FRET). Equation 1.2 is used to determine FRET efficiencies [47-49].

$$Eff = 1 - \frac{\tau_{F(Donor)}^{conjugate}}{\tau_{F(Donor)}} \qquad 1.2$$

where $\tau_{F(Donor)}$ is fluorescence lifetime of the donor (QDs alone), $\tau_{F(Donor)}^{conjugate}$ is the fluorescence lifetime of the QDs in the conjugates. Förster resonance energy transfer efficiencies between MPcs (acceptors) and QDs (donors) were evaluated in this work.

1.2.3.3 Triplet Quantum yields (Φ_T) and lifetimes (τ_T)

The triplet quantum yields are determined using a comparative method and the Equations 1.3-1.5 [**50**,**51**].

$$\Phi_T = \Phi_T^{std} \frac{\Delta A_T \, \varepsilon_T^{std}}{\Delta A_T^{std} \varepsilon_T} \qquad 1.3$$

$$\varepsilon_T = \varepsilon_S \frac{\Delta A_T}{\Delta A_s} \qquad 1.4$$

$$\varepsilon_T^{std} = \frac{\Delta A_T^{std}}{\Delta A_S^{std}} \varepsilon_S^{std} \qquad 1.5$$

where Φ_T^{std}, ΔA_T^{std}, ε_T^{std} and ε_s^{std}, ΔA_S^{std} are triplet quantum yield of standard (Φ_T =0.65 in DMSO ZnPc) [**50**,**51**], changes in the triplet state absorption and molar extinction coefficients of the ZnPc standard and change in absorbance of the ground state of the standard, respectively. Where ΔA_s, ΔA_T, ε_S, and ε_T are the changes in the singlet state absorption of the samples, changes in the triplet state absorption of the samples, ground state molar extinction coefficient, and triplet state molar extinction coefficient, respectively.

Triplet lifetimes of species (average amount of time spent in the triplet state) are determined by fitting exponential data of the triplet decay curves using origin Pro. 8.0 program.

1.2.3.4 Singlet oxygen quantum yields (Φ_Δ)

Singlet oxygen quantum yield (Φ_Δ) values are determined using comparative methods and singlet oxygen quenchers. The Φ_Δ values are calculated using Equation 1.6 [**52**,**53**].

$$\Phi_\Delta = \Phi_\Delta^{std} \frac{R\, I_{Abs}^{std}}{R^{std} I_{Abs}} \qquad 1.6$$

where Φ_Δ^{std}, R and R^{std} are the singlet oxygen quantum yield of the standard, the rates of photobleaching of the singlet oxygen quencher in the presence of the sample and the standard, respectively. Where I_T^{std} and I_{Abs} are the intensities (standard and a sample, respectively). In this work, ZnPc is used as a standard in DMSO with $\Phi_{\Delta(Std)}$ = 0.67 [**53**], with 1,3-diphenylisobenzofuran (DPBF) as a singlet oxygen quencher. 9,10-Anthracenediyl-bis(methylene)dimalonic acid (ADMA) is used as a singlet oxygen quencher in water using $AlPc_{mix}$ (mixture of sulfonated Pc derivatives) as standard with Φ_Δ=0.42 [**51**].

1.2.4 Metallophthalocyanine nanomaterial conjugates

MPcs and nanoparticles (NPs) that have been employed in literature for the photodegradation of the selected organic dyes and in PACT are presented in **Table 1.2** [**54-85**]. The employed MPcs are predominantly mixed with NPs. There are no MPcs used with metal tungstate. Some of the MPcs previously

reported featured paramagnetic central metals like cobalt, copper, nickel, and iron, which are have weak photosensitizing properties. In this thesis, metal tungstate nanoparticles are used for the first time and three organic pollutants MB, TC, DBT as well as PACT were investigated.

Table 1.2: Metallophthalocyanine complexes employed in photocatalysis of dyes, TC, DBT and in PACT.

MPc	NPs	Application	Refs
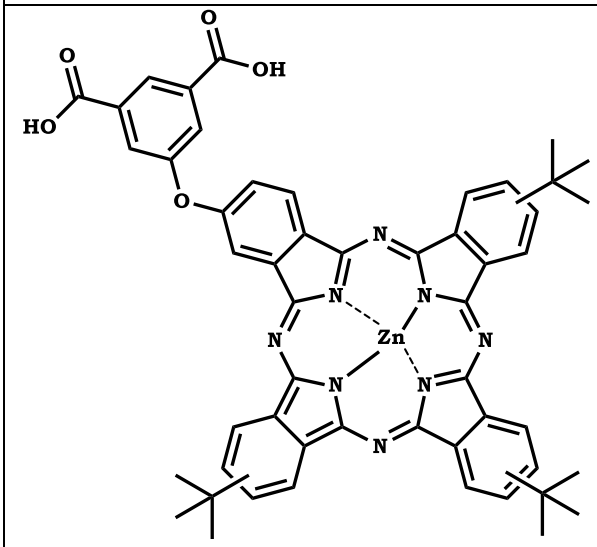	CoF_3O_4 (Amide) nanofibers	Methyl Orange and Orange G	[54]
	Ag-Fe_3O_4 (Amide) nanofibers	PACT	[55]
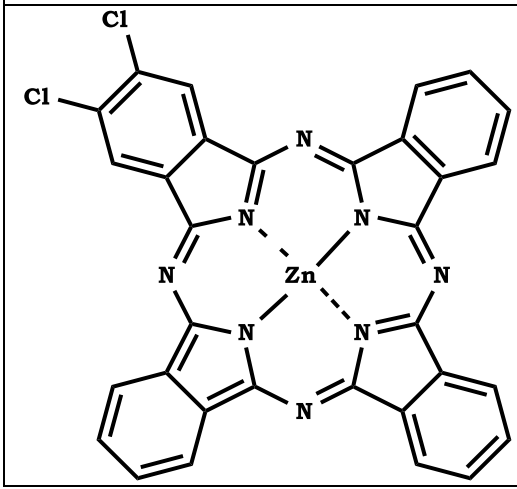	TiO_2 (Assembled)	Rhodamine	[56]

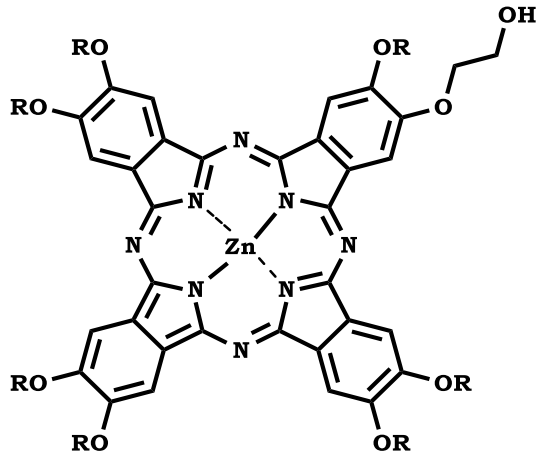 **R = poly(N-isopropylacrylamide)**	None	Rhodamine	[**57**]

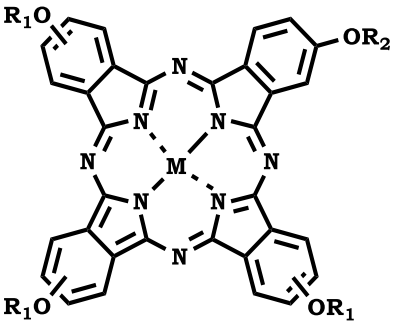 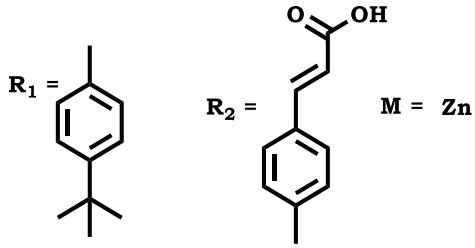	Ag	PACT	[58]
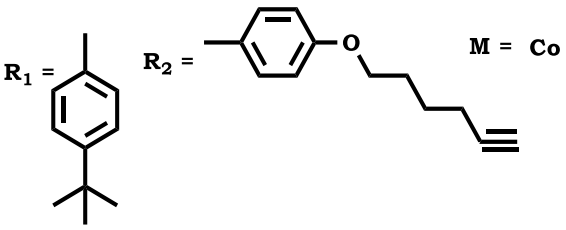	None	MB	[59]
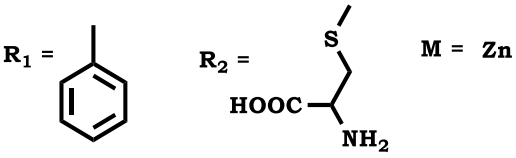	Electrospun fibers	PACT	[60]
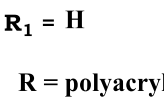 R = polyacrylamide	Ti-MOF (metal-organic framework)	MB	[61]
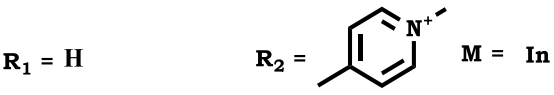	Electrospun fibers	PACT, Bisphenol, 4-chlorophenol	[62, 63]
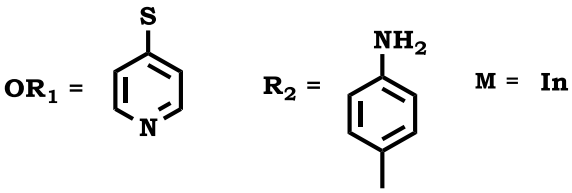	Fe_3O_4	PACT	[64]

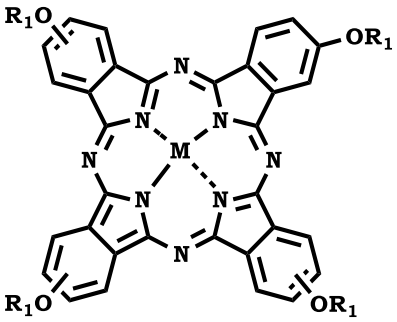 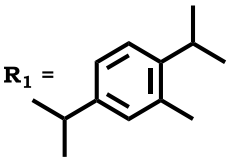 M = Cu	TiO_2	MB	[65]
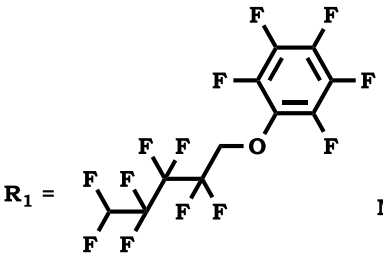 M = Co	TiO_2 nanofibers	MB	[66]
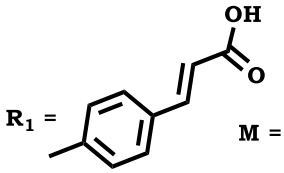 M = Co, Zn, Cu, Ti	TiO_2 (mixture)	MB	[67]
R_1 = COOH M = Co, Zn	Fe_3O_4 (Adsorption, hydrogen bond) & TiO_2	MB MB	[68] [69]
R_1 = SO_3^- M = Fe	None	MB	[70]
R_1 = NH_2 M = Fe	TiO_2 (Covalent)	DBT	[71]

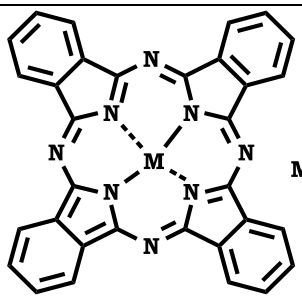 M = central metal M = Co, Ni, Mn, Zn, Fe	Graphene (π-π stacking)	DBT	[72]
	$La_{0.8}Ce_{0.2}NiO_3$ (mixture)	DBT	[73]
	Carbon fiber	DBT	[74]
M = Fe	Fe_3O_4	MB	[75]
	TiO_2 (mixture)	Real fuel	[76]
	Polystyrene fiber.	TC	[77]
M = Zn	TiO_2–SiO_2 (covalent)	TC	[78]
	g-C_3N_4 (π-πstacking)	Thiophene	[79]
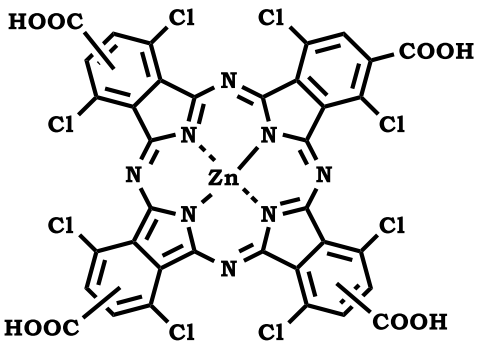	CeO_2/Bi_2MoO_6 nanofibers	TC	[80]
	ZnO (mixture)	MB	[81]

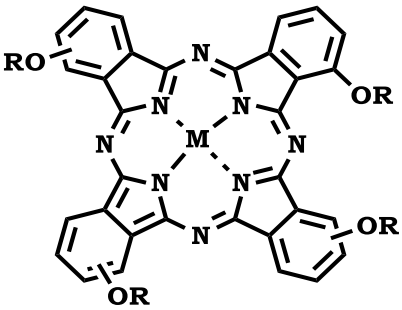 R = 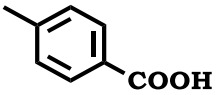 M = Zn R = 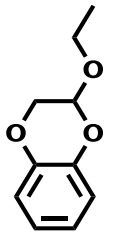 M = Zn, Co, Ni, Cu	g-C_3N_4 (π-π stacking) TiO_2	MB TC & MB	[82] [83]
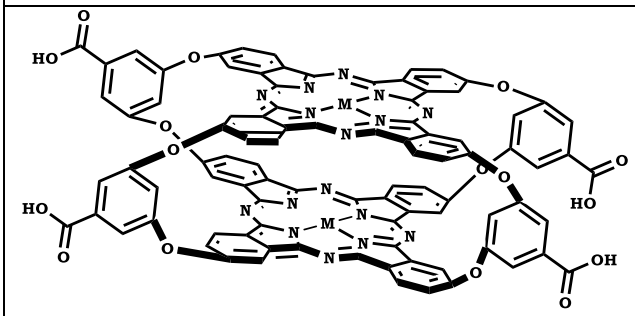	Carbon nanotubes (π-π stacking)	DBT	[84]
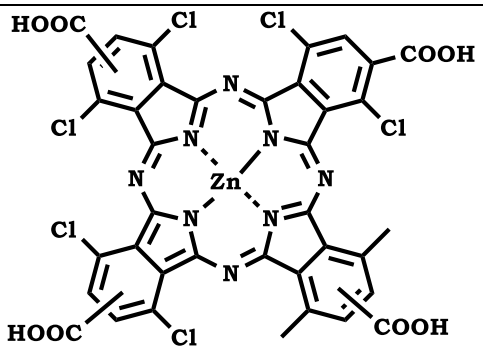	None	DBT	[85]

1.3 Nanoparticles

Nanoparticles (NPs) are a broad class of materials that comprise of particulate compounds with a size of less than 100 nm in diameter [**86-88**]. Depending on their shape, size, physical, and chemical properties, NPs are classified into a variety of groups. Some of the most well-known classes of NPs include carbon-based NPs (such as single-walled nanotubes (SWNTs), carbon nanotubes (CNTs)), metal NPs (Ag, Au), metal oxide (TiO_2, MWO_x), semiconductor NPs (CdTe CdSe) and bimetallic NPs (PtFe, $PtFe_3$, CuCo). NPs offer several benefits, including the capacity to deliver medications to particular places in the body, the ability to boost water solubility of other materials, and the ability to allow the addition of various functional groups to their surfaces.

When linked or immobilized with other molecules, their large surface area-to-volume ratio combined with flexible surface chemistry gives them a good scaffold for the development of dyad nano-platforms. In this study, the following NPs are considered: metal tungstate (MWO_x, M= Ag, Bi, Co, Ni), dimerized silver-iron oxide (Ag-Fe_3O_4), and core/shell/shell semiconductor quantum dots (QDs) CdTe/ZnSe/ZnO), **Figure 1.5**. Metal tungstate and dimerized silver-iron oxide are used to enhance photocatalyst behaviour of MPcs while CdTe/ZnSe/ZnO are employed to enhance nonlinear optical response of MPcs.

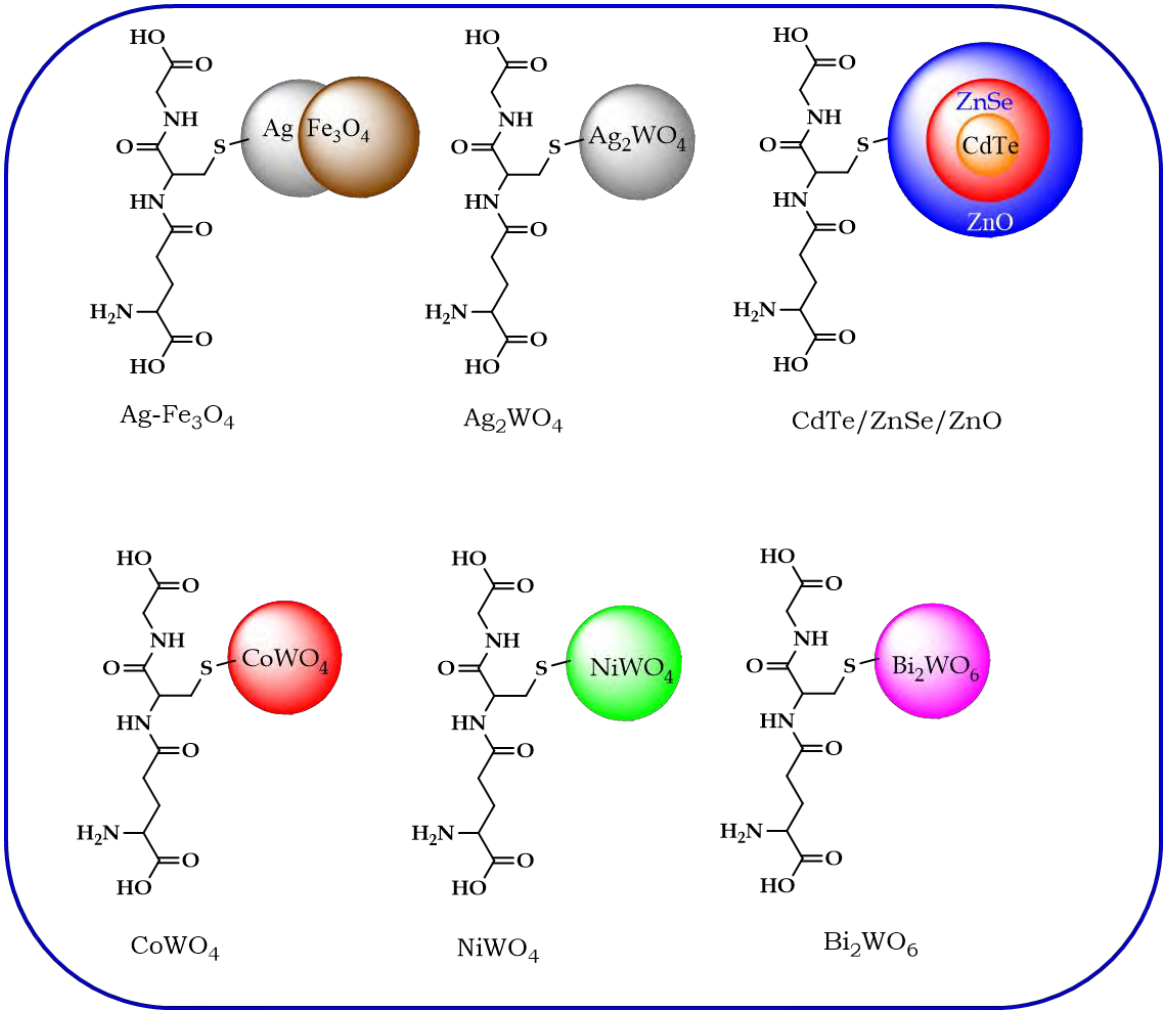

Figure 1.5: *Nanoparticles employed in this thesis.*

1.3.1 Metal tungstate nanoparticles (MWO_x)

Metal oxide nanoparticles have received an increasing amount of attention, owing to their chemical stability, low cost, nontoxicity, and high photocatalytic activity. Unfortunately, the limitation of visible light absorption and the fast recombination rate of electron–hole pairs still restrict the application of some metal oxide NPs in the field of photocatalysis [**89,90**]. MWO_x is employed in this work to enhance MPc properties.

Metal tungstate NPs (MWO_x) are an example of bimetallic oxide NPs. Due to their unique characteristics, such as low cost, environmental friendliness,

and excellent stability under acidic and oxidative circumstances, MWO_x NPs are rapidly being explored for energy conversion and environmental remediation applications. Metal tungstate NPs have found applications in a wide range of areas including: in photodegradation [**91-94**], as antimicrobial agents [**95**], in ion batteries [**96**], in fuel cells [**97**], in electrocatalysis [**98**,**99**] and in desulfurization [**100**,**101**]. In contrast to other metal oxides, metal tungstate (MWO_x) nanoparticles exhibit high photostability and have an appropriate narrow energy band gap which makes them good photocatalysts for the degradation of organic pollutants [**100**]. In addition, MWO_x exhibit magnetic properties which allow for recovery after use. Hence, Ag-Fe_3O_4, Bi_2WO_6, $NiWO_4$, Ag_2WO_4, $CoWO_4$ will be extensively explored in this thesis with MPcs.

1.3.2 Dimerized silver-iron oxide nanoparticles (Ag-Fe_3O_4)

Importantly, magnetic Fe_3O_4 systems can be functionalized with numerous functional groups for carrying noble metals and are used to improve the intersystem crossing of the MPcs due to the heavy atom effect [**54**].

1.3.3 Semiconductor quantum dots (QDs)

QDs are photostable, high fluorescent nanocrystals with sizes ranging from 2-20 nm in diameter [**102**] and have been reported for various applications [**103-106**]. Depending on the application, QDs can be synthesized as core, core/shell, or core/shell/shell [**107**]. The QDs of interest in this thesis are core/shell/shell with CdTe quantum dots used as the core (**Figure 1.5**). CdTe quantum dots can exhibit high nonlinear absorption coefficient [**105**], as a result, they are chosen here to enhance the nonlinear optics (NLO) of MPcs.

1.4 Rationale

There are limited reports for asymmetrical MPcs containing diamagnetic central metal ions used in combination with NPs for the phototransformation of MB (**Table 1.2**). Hence, this thesis reports on the photodegradation of MB using asymmetrical complexes **5**-propionic, **5-**acrylic and **5**-acetic (**Table 1.1**) in combination with metal tungstate NPs for the first time. In terms of TC or DBT, the phototransformation of these analytes using asymmetric MPcs and MPc-NPs is the focus of this study as there are no studies in literature. It is known that asymmetric in MPc improves photocatalytic behaviour [**54**].

The effect of dominant and non-dominant substituents on the MPcs for phototransformation of pollutants, PACT and NLO will be investigated. The following trends will be evaluated:

(A) Photodegradation of TC

I. Effect of non-dominant substituents on complexes **7** and **8** will be compared.

II. Complexes **7** and **8** will be compared to assess the effect of dominant substituents.

III. The effect of introducing a long chain in complex **6** will be investigated.

(B) Phototransformation of DBT

Effect non-dominant and dominant substituents will be compared using complexes **3** and **4**.

(C) Photodegradation of MB

The effect of non-dominant substituents on complexes **5**.

(D) PACT

Evaluation of the effects of substituent on complexes **4**, **5** and **8**.

(E) DBT versus PACT activity

Efficiency of complex **4** in the degradation of DBT and PACT activity towards photoinactivation of *S. aureus*.

(F) Nonlinear optics

Effect of QDs on NLO response of complexes ***1*** and ***2***.

(G) *Photodegradation of* MB versus PACT

Photocatalytic activity towards MB of complexes **5** will be compared to their PACT activity.

(H) Effect of NPs

Various nanoparticles will be conjugated to **5**-acetic for photodegradation of DBT, TC, MB and PACT.

1.5 Details on the application of MPcs and conjugates

The applicability of MPcs in photosensitized processes is due to their ability to absorb light and subsequently generate ROS (including singlet oxygen), as seen in **Figure 1.4**. Based on their photocatalytic activities, efficiency as nonlinear absorbers, and antimicrobial agents, MPcs are reported in this work as photocatalysts for treating contaminated water and for nonlinear optics.

1.5.1 Photodegradation of organic water pollutants

Over the past few decades, green technologies and approaches have gathered steam as a means of minimizing the number of dangerous compounds

released into the environment, therefore lessening the problem of environmental pollution [**108**,**109**].

Various approaches have been employed for the removal of pollutants **[110-114]**. Advanced oxidation processes (AOPs) have been proposed as an efficient method for the degradation of organic pollutants in water **[115]**. Compared to conventional methods such as membrane separation **[116]**, biodegradation **[117]**, and physical adsorption **[118]**, AOP has been proposed as a cleaner and safer alternative for degradation of recalcitrant organic dyes **[115]**. AOPs involve the use of reactive oxygen species (ROS), which may oxidize a wide range of organic molecules in water **[119]**. Photocatalysis is classified as AOP **[115]**. Due to the recovery and reusability of photocatalysts, this work focuses on heterogeneous photocatalysis for TC, MB and DBT.

1.5.2 Photodynamic antimicrobial chemotherapy (PACT)

PACT has become a promising therapeutic option against bacteria **[55]**. PACT uses photosensitizers (PSs) and light irradiation to induce microbial cell death **[120]**. Upon exposure to light of appropriate wavelength, the PS can transfer energy to surrounding oxygen molecules and produce cytotoxic ROS, including singlet oxygen, which efficiently eliminate highly proliferating cells by irreversible damage to their organelle **[121–123]**. PACT offers various advantages over antibiotics such as minimal possibility of developing resistance, since in PACT, multiple and alternative sites in the bacteria cell are targeted **[124-126]**.

1.5.3 Phthalocyanines as nonlinear optical materials.

There has been great interest in the development of nonlinear optical (NLO) materials and the focus has been on the synthesis of novel organic molecules that are photochemically stable [**127**]. These molecules exhibit strong nonlinear absorption and fast response time [**128**]. Various organic materials have been found to fulfill these requirements [**127-129**]. Among them, phthalocyanines (Pcs) are known as efficient materials for NLO due to their reverse saturable absorption (RSA) behaviour [**127**]. Recent reports have been focusing on the production of asymmetrical MPcs due to their improved triplet quantum yields and NLO properties [**128,129**].

Phthalocyanines and semiconductor quantum dots show NLO behaviour with strong nonlinear optical absorption and the focus of this thesis is on the covalent linkage of phthalocyanines to QDs (Pc-QDs) for NLO application [**130**]. Pcs have been covalently conjugated to quantum dots for applications in fluorescence sensing [**130**] and for photophysical studies [**131**]. The combination of MPcs with QDs for NLO is known [**132-135**]. There are limited reports on the investigation of NLO properties of asymmetrical MPc covalently linked to core/shell/shell QDs [**128**]. Hence, the evaluation of the NLO response of novel asymmetrical Pcs when conjugated to core/shell/shell QDs is studied in this thesis. Some of the reported NLO studies of these combined systems have been performed in mixture [**135**], however in this work the focus is on NLO properties of phthalocyanines when covalently linked to QDs.

Photophysical properties and NLO properties of **1**-ethanoic and **2**-propionic and their conjugates with core/shell/shell QDs are investigated and

compared in this work. The determination of NLO parameters using the Z-scan technique will be described in **Chapter 7** of this thesis.

1.6 Aims of the study

The thesis describes the syntheses of composite nanocatalysts for the removal of organic water pollutants and bacteria. The nonlinear optical response of the nanoconjugates is studied as well.

The precise objectives of the thesis are as follows:

1. Syntheses and characterisation of asymmetrical zinc(II)phthalocyanine complexes **1-8**.
2. Evaluation of photophysical and photochemical properties of synthesized asymmetrical zinc(II)phthalocyanine complexes **1-8**
3. Syntheses of various NPs (metal: cobalt, bismuth, nickel, and silver) and characterization.
4. Conjugation of MPc to NPs.
5. PACT.
6. Photocatalysis.
7. NLO

Chapter 2

This chapter provides information on the materials, equipment, and experimental techniques used in the synthesis as well as on the characterization and application of the synthesized metallophthalocyanine, nanomaterials, and their nanoconjugates.

2.1 Materials

Zinc(II) acetate dihydrate $Zn(OAc)_2$, nickel(II)acetate tetrahydrate $Ni(OAc)_2$, cobalt acetate tetrahydrate $Co(OAc)_2$, bismuth oxide (Bi_2O_3), silver acetate dihydrate (AgOAc), methylene blue (MB), tetracycline (TC), 2,2,6,6-tetramethylpiperidine (TEMP), 5,5-dimethyl-1-pyrroline N-oxide (DMPO), 1,3-diphenylisobenzofuran (DPBF), dibenzothiophene (DBT), iron(III) acetylacetonate, 1,2-dodecanediol, 6-mercaptohexanol (mph), unsubstituted Zn(II) phthalocyanine (ZnPc), thioglycolic acid (TGA), 1,8-diazabicyclo[5.4.0]undec-7-5ene (DBU), sodium hydroxide dihydrate, $Na_2WO_4.2H_2O$, glutathione (GSH), and N′,-dicyclohexylcarbodiimide (DCC), 4-nitrophthalonitrile, potassium carbonate (K_2CO_3) , 2-(4-mercaptophenyl) acetic acid, 3,4,5-trimethoxyphenol, 1-(4-hydroxyphenyl)heptan-1-one, 2,3,4,5,6-pentafluorophenol, anthracene-9,10-diyl-bis-methylmalonate (ADMA), silica gel were obtained from Sigma-Aldrich and SAAR Chem-Trade Pvt. Ltd. Mueller Hinton broth and Nutrient agar and bacteriological BBL Mueller Hinton broth were purchased from Merck, *S. aureus* (ATCC 25923) was obtained from Davies Diagnostics, Phosphate buffer saline (PBS, pH 7.4) was prepared using weighed amounts of sodium phosphate (Na_2HPO_4) and sodium phosphate monobasic (NaH_2PO_4). The syntheses of the phthalonitriles (**Figure 3.1**): 4-(4-(*tert*-butyl)phenoxy)phthalonitrile (***a***) [**136**], dimethyl-5-(phenoxy)-isophthalate (***b***) [**137**], 3(4-phenoxy)-propanoic acid) phthalonitrile (***c***) [**138**], 4-phenylazo phenoxy phthalonitrile (***d***) [**139**], 4-aminophenoxy phthalonitrile (***e***) [**140**], carboxyphenoxyphthalonitrile (***f***) [**141**], 3–(4–oxy)phenoxy)acetic acid phthalonitrile (***g***) [**142**], 4-(4-

acetylphenoxy)phthalonitrile (***h***) [**143**], 3(4-phenoxy) acrylic acid phthalonitrile (***i***) [**144**], 4-(3,5-dimethoxyphenoxy) phthalonitrile (***j***) [**145**] have been reported. Glutathione (GSH) capped CdTe/ZnSe/ZnO SQDs and mercapto propionic acid (mpa) capped Ag-Fe_3O_4 were also synthesized as reported in the literature [**146**,**147**].

2.2 Solvents

Dimethyl formamide (DMF), absolute ethanol, deuterated dimethyl sulphoxide (DMSO-d_6), n-octane and cyclohexane, tetrahydrofuran (THF), acetone, 1-pentanol, 1-hexanol, dimethyl sulfoxide (DMSO), and methanol (MeOH), were used as purchased from Sigma-Aldrich. The Ultrapure type I and type II Millipore water were obtained from the Elga PURELAB chorus 2 (RO/DI) system.

2.3 Equipment

1. The ground state electronic absorption spectra were obtained at room temperature, on a Shimadzu UV-2550 spectrophotometer with a 1 cm pathlength cuvette in solution. A Perkin-Elmer Lambda 950 UV-visible spectrophotometer was used to record solid state spectra
2. A Bruker® ALPHA FT-IR spectrometer with a universal attenuated total reflectance (ATR) sample attachment was used to collect FT-IR spectra.
3. The elemental compositions (CHN) of complexes were obtained on the elemental analyzer Vario EL III.

4. Data for mass spectra were collected using a Bruker Auto FLEX III Smart beam TOF/TOF mass spectrometer in positive ion mode with α-cyano-4-hydroxycinnamic acid as a matrix.
5. Proton nuclear magnetic resonance spectra were recorded on a Bruker AMX 600 MHz NMR spectrometer using tetramethylsilane (TMS) as an internal reference.
6. Fluorescence excitation and emission spectra of Zn(II) phthalocyanine were obtained using a 360 – 1100 nm filter on a Varian Eclipse® spectrofluorometer, with absorbance at the excitation wavelength set to 0.05 to reduce inner filter effects [**148**].
7. Fluorescence lifetimes were determined with a Time-Correlated Single Photon Counting (TCSPC) system (FluoTime 300, Picoquant GmbH) and a diode laser (LDH-P-670, Picoquant® GmbH, 20 MHz repetition rate, 44 ps pulse width) [**148**].
8. The triplet state quantum yields and lifetimes of the samples were obtained by laser flash photolysis sys consisting of an LP980 spectrometer with a PMT-LP detector and an ICCD camera (Andor DH320T-25F03). The signal from the PMT detector was recorded on a Tektronix TDS3012C digital storage oscilloscope, **Figure 2.1**. The solution was deaerated with argon for 30 min before experiments. Triplet lifetimes of species (a measure of the length of time spent in the excited triplet state) are determined by fitting exponential data of the triplet decay curves using origin Pro. 8.0 program.

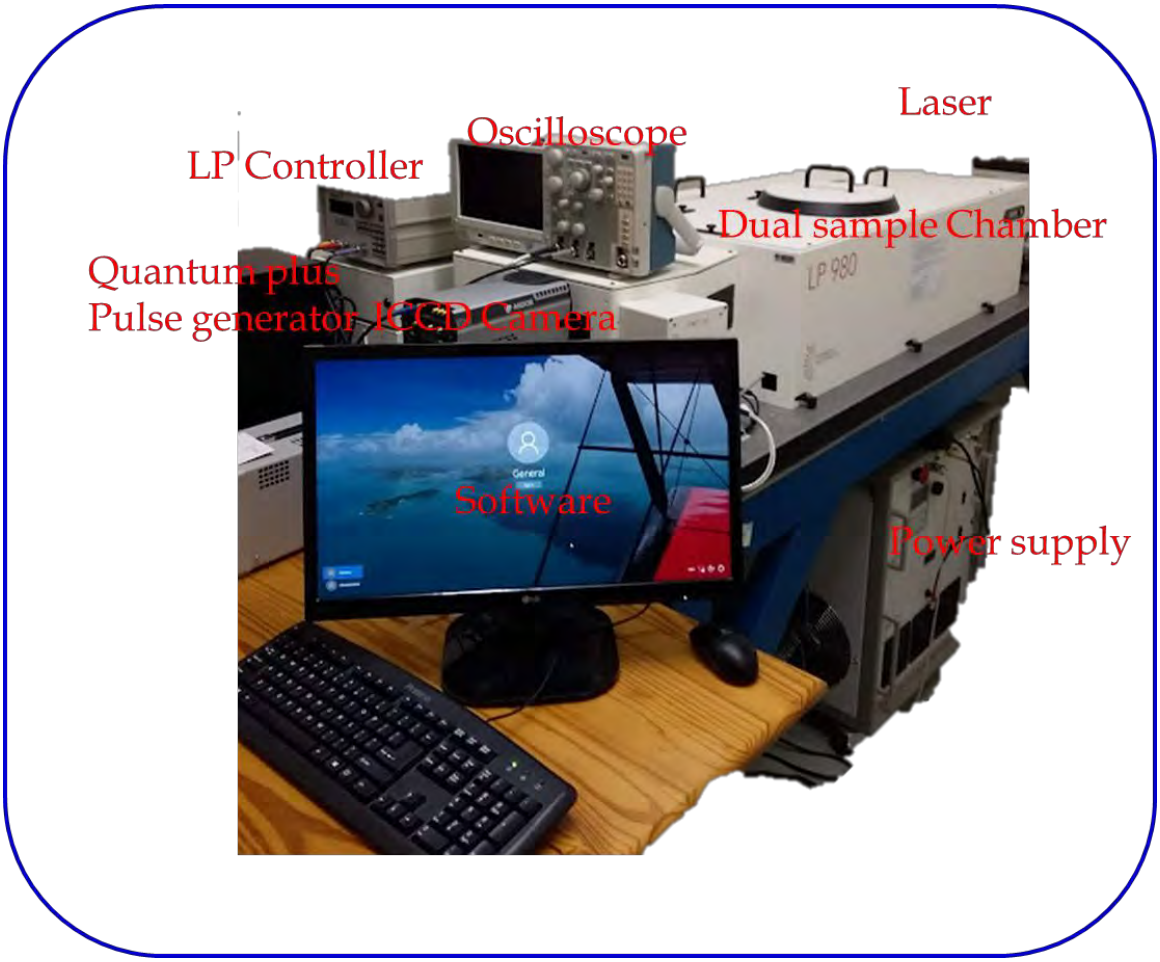

***Figure 2.1**: Laser flash photolysis system.*

9. Singlet oxygen quantum yields studies were done using a tunable laser system consisting of an Nd:YAG laser (355 nm, 135 Mj/4–6 ns) pumping an optical parametric oscillator (OPO, 30 Mj/3–5 ns) with a wavelength range of 420–2300 nm (NT-342B, Ekspla) at excitation wavelength = 680 nm.
10. For the photocatalytic investigations, the Modulight® Medical Laser system (ML) 7710-670- RHO was employed.

11. Dynamic light scattering (DLS) experiments were carried out on a Malvern Zetasizer nano series, Nano-ZS90.
12. A ZEISS LIBRA® Transmission electron microscopy (TEM) was used to obtain TEM images of the NPs and conjugates.
13. The elemental compositions of the nanomaterials and their nanoconjugates with MPcs were qualitatively determined using an energy-dispersive X-ray spectrometer (EDX, INCA PENTA FET coupled with VAGA TESCAM operated at 20 Kv).
14. X-ray powder diffraction (XRD) patterns were measured on a Bruker D8 Discover equipped with a Lynx Eye detector (proportional counter), using Cu Kα radiation (λ = 1.5405 A°, nickel filter) as described before in the literature [**149**].
15. Atomic force microscopy (AFM) measurements were performed in tapping mode using an MFP-3D Origin donated by Asylum Research (Oxford instruments company, USA).
16. MPcs/NPs/conjugates were characterized using differential thermal analysis (DSC) (DSC 2500-TA Instruments) in nitrogen flow and at a heating rate of 20 °C min-1 up to 400°C.
17. Thermogravimetric analysis (TGA) was performed using a Perkin Elmer TGA 800 thermogravimetric 39 analyser at a heating rate of 20 °C min^{-1} in a high-purity nitrogen and air environment.
18. The electron paramagnetic resonance (EPR) spectroscopy measurements were carried out using the Bruker EMX Plus EPR spectrometer. The spin Hamiltonian parameters were obtained by the simulation of the spectra. The static field (2500 G), center field

(3500 G), modulation amplitude (100 G), sweep time (20.97 ms), time constant (10.24 ms), conversion time (5.12 ms), resolution (2048 pts), power (2.00 mW) and modulation frequency (100 kHz) were used as the experimental parameters at 298 K with 10 scans.

19. Optical nonlinear responses of the Pc complexes and their conjugates with SQDs were studied using a Z-scan set–up as described in the literature using a frequency-doubled Nd:YAG laser (Quanta-Ray, 1.5 J/10 ns fwhm pulse duration) as the excitation source [**150**]. A standard quartz cuvette with a lid (0.2 cm), purchased from Purshee, was used for the experiments performed in solution.

2.4 Syntheses

2.4.1 Syntheses of phthalonitriles (k-n), Scheme 3.1

2.4.1.1 Synthesis of thiophenylphthalonitrile (k)

Phthalonitrile ***k*** was synthesized as follows: into a 100 mL round bottom flask containing DMF (70 mL), 4-nitrophthalonitrile (2.00 g, 11.56 mmol), and 2-(4-mercaptophenyl) acetic acid (1.94 g, 11.53 mmol) were added. The mixture was allowed to stir at room temperature under nitrogen flow. After 2 h of stirring, dry potassium carbonate (5.0 g, 36.18 mmol) was added to the flask, and the mixture was allowed to stir for a further 46 h. The resulting product was precipitated out by pouring the mixture into the protonated (using 6 drops of concentrated HCl) ice-water mixture. The formed precipitate was collected by filtration under a high-pressure vacuum and dried.

Yield: 82% (3.2 g). FT-IR (UATR-TWO™) ν_{max}/cm^{-1}: 3195 (OH stretch), 2340 (CN) 1630(C=O), 1463(C=C), 1085(Ar-O-Ar). ^{1}H-NMR (600 MHz, DMSO- d_6): 8.81 (*d*, J= 9Hz, 1H, H-Ar), 8.44 (*d*, J = 3Hz, 1H, H-Ar), 8.05 (*dd*, J = 9Hz; 3Hz, 1H, H-Ar), 7.89 (*d*, J = 9Hz, 2H, H-Ar), 7.77 (*d*, J = 9Hz, 2H, H-Ar), 5.44 (*s*, 2H, CH_2), 4.34 (*s*, 1H, OH broad).

2.4.1.2 Synthesis of 4-(3,4,5-trimethoxyphenoxy)phthalonitrile (l)

Phthalonitrile ***l*** was synthesized as follows: a mixture of 3,4,5-trimethoxyphenol (2.13 g, 11.6 mmol) and 4-nitrophthalonitrile (2 g, 11.6 mmol), and K_2CO_3 (5 g, 36.18 mmol) was added to DMF (75 mL) under N_2 flow at room temperature. After 48 h under constant magnetic stirring, the

solution was allowed to precipitate in ice, then isolated under reduced pressure, and purified with hot methanol. Yield: 2.69 g, (65%), IR [max /cm^{-1}] 2800 (C-H), 2330 (CN) 1493 (C=C), 1216 (Ar-O-Ar). ^{1}H-NMR (600 MHz in DMSO – d_6): 6.9 (*s*, 2H, Ar), 6.8 (*s*, 1H, Ar), 6.6 (*s*, 1H, Ar), 6.5 (*s*, 1H, Ar), 3.6–3.9 (*m*, 9H, CH_3).

2.4.1.3 Synthesis of 4-(4-heptanoylphenoxy) phthalonitrile (m)

Phthalonitrile ***m*** was obtained by reacting 4-nitrophthalonitrile (0.415 g, 2.42 mmol) with 1-(4-hydroxyphenyl)heptan-1-one (0.501 g, 2.42 mmol), K_2CO_3 (0.668 g, 4.84 mmol) in DMF (60 mL) under nitrogen atmosphere with stirring for 24 h at 60 °C. The product was isolated in ice-water, filtered under reduced pressure, and allowed to dry in the fume hood. Thereafter, the resultant solid was washed with hot methanol, and purified with ethanol, and dried to obtain compound ***m***.

Yield: 0.805 g (88%) IR (ATR), ν/cm^{-1}: 3039-3088 (Ar-H), 2935-2848 (Aliph. C-H), 2230(CN), 1478 (C=C), 1212(Ar-O-Ar). ^{1}H-NMR (DMSO-d_6), (δ:ppm): 8.13 (*d*, J = 8.1Hz, 2H), 7.88 (*d*, J = 7.9Hz, 2H), 7.51 (*s*, 1H), 7.38 (*d*, J = 7.4Hz, 2H), 3.24 (*s*, 2H), 3.12 (*t*, 2H), 2.88 (*s*, 1H), 2.75 (m, 1H), 1.63 (*m*, 2H), 1.25 (*s*, 2H), 0.88 (t, 3H).

2.4.1.4 Synthesis of 4-(perfluorophenoxy) phthalonitrile (n)

Phthalonitrile ***n*** was synthesized as follows: in 70 mL of dry DMF, a mixture of 4-nitrophthalonitrile (1.12 g, 6.5 mmol), 2,3,4,5,6-pentafluorophenol (1.19

g, 0.650 mmol), and K_2CO_3 (1.50 g, 10.85 mmol) was stirred under nitrogen atmosphere for 48 h. The product was precipitated in ice-water after which it was filtered off under reduced pressure and washed in hot methanol.

Yield: 1.81 g (78%) IR (ATR), ν/cm^{-1}: 3037-3098 (Ar-H), 2235 (CN), 1478 (C=C), 1212 (Ar-O-Ar). ^{1}H-NMR (DMSO-d$_6$), (δ:ppm): 8.13 (*d*, J = 8.1Hz, 1H), 7.88(*d*, J = 7.8Hz, 1H), 7.63 (*t*, J = 7.7Hz, 1H).

2.4.2 Syntheses of MPc complexes

2.4.2.1 Synthesis of complex 1-ethanoic, **Scheme 3.2**

Complex **1**-ethanoic was synthesized as follows: phthalonitrile ***k*** (0.50 g, 1.69 mmol), ***a*** (1.41g, 5.10 mmol), and zinc acetate dihydrate (0.40, 1.82 mmol) were dissolved in 3 mL of 1-hexanol and 1 mL of DBU. The solution was heated to 160 ˚C under constant magnetic stirring and under nitrogen gas flow. After 6 h, the crude product was precipitated out with the addition of methanol and subsequently collected by centrifugation. The product was washed 3 times in the centrifuge with methanol and ethanol. The crude product was allowed to dry in the fume hood and washed in hot methanol. The purification and isolation of the A_3B target were performed by using silica packed column with gradient eluents of tetrahydrofuran and methanol (5:1).

Yield: 34% (0.79 g). UV-vis (DMSO): λ_{max} (nm) (log ε) 687(5.15), 616(4.07), 358(4.54). FT-IR (UATR-TWO™) ν_{max}/cm^{-1}: 3033 (OH, stretch), 2965(C-H stretch), 1718(C=O), 1388 (C=C), 1226(Ar-O-Ar). ^{1}H-NMR (DMSO-d$_6$) δ(ppm): 9.33 (*s*, 1H-OH), 9.07-9.12 (*m*, J=Hz, 4H-Ar), 8.70-8.88 (*m*, J=8.75, 6H-Ar),

8.56-8.63 (*m*, J= 8.61, 6H-Ar), 8.26-8.34 (*m*, J = 8.31 Hz, 12H, Ar), 3.50-4.25 (*m*, 27H, CH_3), 3.25 (s, 2H, CH_2). MS (MALDI-TOF): calcd: 1186.35, found: 1186.48 m/z $[M]^+$ experimental. Elemental Anal. Calcd. $C_{70}H58N_8O_5SZn$: C, 70.73; H, 4.92; N, 9.43; S, 2.70 found C, 70.55; H, 5.20; N, 9.77, S, 2.47.

2.4.2.2 Synthesis of complex 2-propionic, Scheme 3.3

Synthesis of compound **2**-propionic was the same as **1**-ethanoic but using a mixture of phthalonitrile ***b*** (0.862 g, 2.57 mmol) and phthalonitrile ***c*** (0.25 g, 0.856 mmol) to 160 ˚C under constant magnetic stirring in 1-hexanol. Its purification was carried out using the same purification method for **1**-ethanoic.

Yield: 36% (0.54g). UV-vis (DMSO): λ_{max} (nm) (log ε) 677 (5.12), 607(4.04), 345 (4.49). FT-IR (UATR-TWO™) ν_{max}/cm^{-1}: 3249 (OH stretch), 2923(C-H stretch), 1591(C=O stretch), 1719(C=O stretch), 1384 (C=C), 1227(Ar-O-Ar). ^{1}H-NMR (DMSO-d_6) δ (ppm): 10.25 (s, 1H, OH), 9.50-9.25 (*m*, 12H-Ar), 9.07-9.10 (*m*, 4H, Ar), 6.0-6.22 (*m*, 9H, Ar), 5.28 (s, 18H, CH_3), 5.25 (s, 2H, CH_2), 5.21(s, 2H, CH_2). MS (MALDI-TOF): Calcd: 1364.24, found: 1364.38 m/z $[M]^+$. Elemental Anal. Calcd. $C_{71}H_{48}N_8O_{18}Zn$: C, 62.40; H, 3.54; N, 8.20, found C, 62.39; H, 3.73; N, 7.79.

2.4.2.3 Syntheses of complexes 3-propionic, 3-NH_2 and 3-COOH, ***Scheme 3.4***

Synthesis of 3-COOH

Phthalonitrile ***d*** (1.84 g, 5.68 mmol) was mixed with phthalonitrile ***f*** (0.5 g, 1.89 mmol, for **3**-COOH) in 3.00 mL of 1-pentanol and 0.2 mL of DBU in the presence of zinc acetate dihydrate (0.44 g, 2.40 mmol). The mixture was allowed to stir at 140 °C under nitrogen flow for 6 h. Afterwards, the crude product was precipitated with methanol, centrifuged, and allowed to dry in fume-hood. The product was purified using a silica gel packed column and eluting with tetrahydrofuran and later with cyclohexane solvent system.

Yield = 27% (0.751 g) UV–Vis in DMSO λ_{max}/nm (log ε) 680 (5.38), 613 (4.12), 343 (4.1). IR [ν_{max}/cm^{-1}] 3062(OH), 1715(C=O), N=N (1477), 1227 (Ar-O-Ar). ^{1}H-NMR (600 MHz in DMSO-d_6), δ (ppm): 11.52 (*s*, 1H), 8.00–8.25 (*m*, 16H), 7.25 (*m*, J = 7.58 Hz, 12H), 6.75–6.8 (*m*, 15H). MALDI-TOF-MS: m/z $[M+H]^+$ Calcd. 1300.29, found = 1300.99. Anal. Calc. $C_{75}H_{44}N_{14}O_6Zn$: C, 69.15; H, 3.40; N 15.05, found C, 69.33; H, 3.38; N, 15.04.

Synthesis of 3-NH_2

The synthesis of complex **3**-NH_2 was as described for **3**-COOH except that phthalonitrile ***e*** (0.5 g, 2.13 mmol) and phthalonitrile ***d*** (2.07 g, 6.4 mmol) was used. Reaction conditions and purification were as described for **3**-COOH. Yield = 21% (0.632 g). UV–Vis in DMSO λ_{max}/nm (log ε) 680 (4.6), 613 (4.06), 349 (4.07). IR [ν_{max}/cm^{-1}] 3335(NH2), 1591 (C=C), N=N (1478), 1224 (Ar-O-

Ar). ^{1}H-NMR (600 MHz in DMSO-d_6), δ (ppm): 8.8–9.0 (*m*, 16H) 8.4–8.5 (*m*, 12H), 7.5–8.4 (m, 15H), 6.6 (*d*, 2H). MALDI-TOF-MS: m/z $[M+2H]^+$ Calcd 1271.31, found = 1273.06. Anal. Calcd. $C_{74}H_{45}N_{15}O_4Zn$: C, 68.81; H, 3.67; N, 16.27 found C, 68.81; H, 3.63; N, 16.30.

***Synthesis of 3**-propionic*

The synthesis of complex **3**-propionic was as described for **3**-COOH except that phthalonitrile ***c*** (0.5 g, 1.71 mmol) and phthalonitrile ***d*** (1.66 g, 5.14 mmol) was used. Reaction conditions and purification were as described for **3**-COOH.

Yield = 35%. (0.910 g). UV–Vis in DMSO λ_{max}/nm (log ε) 680 (4.97), 613 (4.08) 343 (4.15). IR [ν_{max}/cm^{-1}] 3057(OH), 1720(C=O), N=N (1477), 1230 (Ar-O-Ar). ^{1}H-NMR (600 MHz in DMSO-d_6) δ (ppm): 10.20 (*s*, 1H), 9.8 (*d*, J = 9.69 Hz, 2H), 9.6 (*d*, J = 9.80 Hz, 2H) 9.0–9.3 (*m*, 12H), 8.7–8.9 (*m*, 12H), 7.5–8.6 (*m*, 15H), 4.2 (*d*, 4H). MALDI-TOF-MS: m/z Calcd 1330.32, found $[M+2H]^+$ = 1332.26. Anal. Calcd $C_{77}H_{48}N_{14}O_6Zn$, C, 68.19; H, 3.64; N, 14.54, found C, 68.18; H, 3.65; N, 14.52.

2.4.2.4 Syntheses of complexes **4**-*COOH*, **4**-*propionic*, *and* **4**- *acetic*, ***Scheme 3.5***

***Synthesis of* 4**-COOH)

A mixture of phthalonitrile ***l*** (0.881 g, 2.84 mmol), phthalonitrile ***f*** (0.25 g, 0.947 mmol), $Zn(OAc)_2$ (0.44 g, 2.01 mmol), and 0.2 mL of DBU in 1-hexanol (5 mL) was stirred at 160 °C for 6 h. After cooling the product to 25 °C, methanol was added to precipitate out the solid. The crude product was purified by column chromatography packed with silica gel using a (THF/methanol 5:1) solvent system to give complex **4**-COOH.

Yield: 29% (0.46 g). UV–vis in DMSO λ_{max}/nm (log ε): 683 (5.37), 613 (3.71), 356 (4.09). IR [ν_{max} /cm^{-1}] 3231(OH), 2850–2918 m (C-H), 1597 ν(C=C), 1760 ν(C=O), 1220 ν(Ar-O-Ar). ^{1}H NMR (600 MHz in DMSO-d_6). δ(ppm): 11.7 (*s*, 1H) 7.7–7.9 (*m*, 6H, Ar), 7.3–7.4 (*d*, J = 7.64 Hz, 2H, Ar), 7.3 (*s*, 2H, Ar), 6.8–6.9 (*m*, 3H, Ar), 6.6–6.8 (*m*, 4H, Ar), 6.5–6.6 (*m*, 5H, Ar), 3.5–4.0 (*m*, 27H, CH_3). MALDI-TOF-MS: m/z $[M]^+$ Calcd. 1258.5, found = 1259.2 Anal. Calc. $C_{66}H_{50}N_8O_{15}Zn$: C, 62.89; H, 4.00; N, 8.89, found C, 62.86; H, 4.11; N, 9.11.

***Synthesis of* 4**-propionic

The procedure described for **4**-COOH was followed for the synthesis of complex **4**-propionic except that phthalonitrile ***c*** (0.25 g, 0.855 mmol) was used instead of phthalonitrile ***f*** with a reduced amount of phthalonitrile ***l*** (0.796 g, 2.57 mmol).

Yield: 31% (0.46 g). UV–vis. λ_{max}/nm (log ε): 683(5.44), 614 (3.79), 357 (4.06) UV–vis., IR [ν_{max} /cm^{-1}] 2990(OH), 2800–2923 (C-H), 1460 (C=C), 1718 (C=O), 1216 (Ar-O-Ar). ^{1}H-NMR (600 MHz in DMSO-d$_6$). 8.60 (*s*, 1H), 7.7–7.9(*m*, 4H, Ar), 7.2–7.4(*m*, 2H, Ar), 6.7–6.9 (*m*, 4H, Ar) 6.5–6.7 (m, 12H, Ar), 3.9 (*s*, 2H, CH_2), 3.8 (*s*, 2H, CH_2), 3.7 (*m*, 27H, CH_3). MALDI-TOF-MS: m/z $[M]^+$ Calcd. 1286.5, found = 1288.3 Anal. Calc. $C_{68}H_{54}N_8O_{15}Zn$: C, 62.51; H, 4.32; N, 8.08, found C, 62.37; H, 4.34; N, 7.98.

***Synthesis of* 4**-acetic

4-acetic was prepared as described for **4**-COOH, except, phthalonitrile ***g*** (0.25 g, 0.849 mmol) was used in place of ***f*** with a decreased quantity of phthalonitrile ***l*** (0.791 g, 2.55 mmol). Other reaction conditions and purification techniques were the same as before.

Yield: 0.41 g (28%), UV–vis. (DMSO), λ_{max}/nm (log ε): 683 (5.49), 613 (3.83), 353 (4.49). IR [ν_{max} /cm^{-1}] 3226 ν(OH), 2851–2920 ν(C-H), 1417 ν(C=C), 1722 ν(C=O) (1722), 1219 ν(Ar-O-Ar). ^{1}H-NMR (600 MHz in DMSO – d$_6$). δ(ppm): 8.8 (*s*, 1H), 7.6–8.2 (*m*, 6H, Ar), 7.2–7.4 (*m*, 4H, Ar), 6.5–7.1 (*m*, 12H, Ar), 4.2 (s, 2H, CH_2), 3.8 (*m*, 19H, CH_3), 3.7 (*m*, 8H, CH_3). MALDI-TOF-MS: m/z $[M]^+$ Calcd. 1288.28, found = 1288.45 Anal. Calc. $C_{67}H_{52}N_8O_{16}Zn$: C, 61.50.; H, 4.16; N, 8.86, found C, 61.40; H, 4.14; N, 8.88.

*2.4.2.5 Syntheses of complexes **5**-propionic, **5**-acrylic, and **5**-acetic, **Scheme 3.6***

***Synthesis of 5**-propionic*

Under an inert argon atmosphere, phthalonitrile ***c*** (0.25 g, 0.855 mmol), and phthalonitrile ***h*** (0.673 g, 2.57 mmol) were dissolved in 1-hexanol (5 mL). Then, DBU (0.5 mL) and zinc(II) acetate (0.44 g, 6.77 mmol) were added to this solution. The reaction mixture was refluxed to 160 °C with stirring for 6 h. The product was precipitated with methanol, purified with ethanol, and dried in a vacuum. Finally, the obtained crude product was washed in hot methanol and the AB_3 target product was isolated using a silica gel-packed column, eluting with tetrahydrofuran/methanol (5:1). The obtained blue product was soluble in DMSO and hot methanol.

Yield: 33% (0.452 g). UV–vis in DMSO, λ_{max}/nm (log ε): 678 (5.12), 611(3.8), 356(4.49). IR [ν_{max}/cm^{-1}]; 3267(OH), 2964 ν(C-H), 1652 ν(C=O), 1587 ν(C=O), (1230 (Ar-O-Ar). ^{1}H-NMR (600 MHz in DMSO–d_6). δ(ppm): δ (ppm) = 8.25 (*s*, 2H, Ar) 8.21 (*s*, 6H, Ar); 8.11 (*d*, J = 8 Hz, 4H, Ar); 7.93 (*s*, 2H, Ar); 7.85 (*s*, 2H, Ar); 7.56 (*s*, 2H, Ar); 7.45 (*d*, J = 7.4 Hz, 2H, Ar); 7.35 (*m*, 2H, Ar); 7.20 (*m*, 6H, Ar); 5.75 (*s*, 1H, OH bond); 2.91 (*s*, 6H, CH_3); 2.82 (*s*, 3H, CH_3); 2.71 (*s*, 2H, CH_2); 2.60 (*s*, 2H, CH_2). MALDI-TOF-MS: m/z $[M]^+$ Calcd., found = 1140.48. Elemental Analysis: $C_{65}H_{42}N_8O_9Zn$ Expected C, 68.22; H, 3.70; N, 9.79, experimental C, 68.23; H, 3.47; N, 9.88.

Synthesis of 5-acrylic

Complex **5**-acrylic was synthesized by following a similar procedure used for the synthesis of **5**-propionic. Except for that phthalonitrile ***i*** (0.745 g, 2.565 mmol) was used instead of phthalonitrile ***c***. Amounts and purification method were the same as described for **5**-propionic.

Yield: 37% (0.511 g). UV–vis. (DMSO), λ_{max}/nm (log ε): (DMSO) 678 (5.08), 611(2.29), 356(4.55).IR [ν_{max} /cm^{-1}]; 3268(OH), 2925 ν(C–H), 1672 ν(C=O), 1588 ν(C=O), 1231 (Ar-O-Ar). ^{1}H NMR (600 MHz in DMSO – d_6). δ (ppm): 8.90 (*s*, 1H, OH bond); 8.15(*m*, 4H, Ar); 8.05(*d*, J = 8.2, 4H, Ar); 7.95(*s*, 4H, Ar); 7.90 (*d*, J = 8.1, 4H, Ar); 7.5(*m*, 6H, Ar), 7.35(*d*, J =8.7, 2H, Ar); 7.25(*m*, 4H, Ar), 2.73–2.90 (*d*, 9H, CH_3); 2.63(d, 2H, CH). MALDI-TOF-MS: m/z $[M]^+$ Calcd. 1142.24 Found = 1142.47. Elemental Analysis: $C_{65}H_{40}N_8O_9Zn$ C, 68.34; H, 3.53; N, 9.81 and found C, 68.35; H, 3.10; N, 9.95.

Synthesis of 5-acetic

Complex **5**-acetic was synthesized by following a similar procedure used for the synthesis of **5**-propionic. The only difference is that phthalonitrile ***g*** (0.25 g, 0.849 mmol) was used instead of phthalonitrile ***c***. The purification procedure and quantity were identical to those for **5**-propionic.

Yield: 0.532 g (39%) UV–vis. (DMSO), λ_{max}/nm (log ε): 680 (5.17), 614 (2.29), 353 (4.55) IR [ν_{max} /cm^{-1}]: 3293(OH), 2924 ν(C–H), 1669 ν(C=O), 1585 ν(C=O), 1227 (Ar-O-Ar). ^{1}H NMR (600 MHz, DMSO-d_6): δ (ppm) = 8.08 (*d*, J = 8 Hz, 2H, Ar); 7.95 (*s*, 4H, Ar); 7.88 (*d*, J = 7.8 Hz, 2H, Ar); 7.45 (*d*, J = 7.4 Hz, 2H,

Ar); 7.36 (*d*, J = 7.3 Hz, 2H, Ar); 7.22 (*dd*, J = 7.2 Hz, 4H, Ar); 6.88 (*s*, 6H, Ar); 6.63 (*s*, 6H, Ar); 2.90 (*s*, 9H, CH_3) ; 2.70 (*s*, 1H, OH bond); 2.60 (*d*, 2H, CH_2) ppm. MALDI-TOF-MS: m/z $[M]^+$ Calcd. 1144.26, found = 1144.33. Elemental Analysis: $C_{64}H_{40}N_8O_{10}Zn$: C, 67.05; H, 3.52; N, 9.77 and found C, 67.34; H, 3.38; N, 9.44.

2.4.2.6 Synthesis of (6-COOH), Scheme 3.7

In 1-pentanol (5 mL) and DBU (0.2 mL), zinc acetate (Zn(OAc)2 (0.0960 g, 0.526 mmol), phthalonitrile m (0.175 g, 0.526 mmol), phthalonitrile f (0.092 g, 0.350 mmol) were mixed, and the mixture was heated under reflux for 8 h. The product was allowed to cool to room temperature, precipitated in with methanol/water mixture, and purified using silica packed column chromatography, and eluting with tetrahydrofuran/methanol to obtain pure complex **6**-COOH.

Yield: 29% (0.105.3). UV–vis. (DMSO) λ_{max}/nm (log ε): 688 (5.34), 618 (3.48), 351 (4.60). IR (ATR), ν/cm^{-1}: 3241 (OH), 3067 (Ar-H), 29242859 (Aliph. C-H), 1667-1584 (C=O), 1473 (C=C), 1232 (Ar-O-Ar). ^{1}H-NMR (DMSO-d_6), δ (ppm): 8.23-7.96 (*m*, 12H, Ar-HPc), 7.82 (*d*, J = 6.6 Hz, 4H, Ar-H), 7.65 (*d*, J = 6.0 Hz, 4H, Ar-H), 7.35 (*d*, J = 7.0 Hz, 4H, Ar-H), 7.11 (*d*, J = 6.8 Hz, 4H, Ar-H), 4.22(1H, *s*, OH), 2.93 (*t*, 6H, CH_2), 1.53 (*m*, 6H, CH_2), 1.31(*m*, 18H, CH_2,), 0.83 (*t*, 9H, CH_3). MALDI-TOF-MS m/z calc. 1324.44; found: $[M]^+$. 1324.42 Elemental Analysis, Anal. Calc. for $C_{78}H_{68}N_8O_9Zn$ C, 70.61; H, 5.17; N,8.45, Found: C,70.26; H, 4.78; N, 8.11.

2.4.2.7 Syntheses of complexes **7**-*acrylic and* **7**-*propionic,* ***Scheme 3.8***

Synthesis of* 7-*acrylic

Reaction conditions for the synthesis of complex **7**-acrylic were kept the same as described in for complex **6**-COOH, except that phthalonitrile ***n*** (0.150 g, 0.483 mmol) and phthalonitrile ***i*** (0.093 g, 0.322 mmol) were used instead of phthalonitrile ***f*** and ***m***. Quantities and the method of purification were as described for **6**-COOH.

Yield: 31% (0.105.1 g). UV–vis. (DMSO) λ_{max}/nm (log ε): 675 (5.04), 612 (4.09), 349 (4.89). IR (ATR), ν/cm^{-1}: 3233 (OH), 2955 (Ar-H), 2882 (Aliph. C-H), 1711 (C=O), 1499(C=C), 1218 (Ar-O-Ar). ^{1}H-NMR (DMSO-d_6), (δ: ppm): 10.76 (s, 1H, OH), 8.67 (d, J=8.1 Hz, 2H, Ar-HPc), 8.14 (*d*, J= 8.8Hz, 2H, Ar-HPc), 7.90 (*d*, J=8.2 Hz, 4H, Ar-HPc), 6.86 (*m*, 1H, Ar-H), 6.75 (*d*, J=16.2 Hz, 2H, *Trans*-H), 6.56 (*d*, J=2.2Hz, 2H, Ar-HPc), 5.91 (*m*, 1H, Ar-H), 5.76 (*d*, J=11.1Hz, 4H, Ar-H). MALDI-TOF-MS m/z calc. 1284.05; found: 1284.09. Elemental Analysis, Anal. Calc. for Calc. for $C_{59}H_{19}F_{15}N_8O_6Zn$: C,55.10; H,1.49; N,8.71 Found: C,54.93; H,1.41; N,9.15.

Synthesis of* 7-*propionic

The synthesis of complex **7**-propionic was achieved similarly to **6**-COOH. However, phthalonitrile ***n*** (0.150 g, 0.483 mmol) and ***c*** (94 mg, 0.322 mmol) were used instead of phthalonitrile ***f*** and ***m***. Amounts and the purification technique were as stated for **6**-COOH.

Yield: 88.4 mg (26%). UV–vis. (DMSO), λ_{max}/nm (log ε): 675 (5.02), 612 (3.76, 349 (4.55). IR (ATR), ν/cm^{-1}: 3240.41 (OH), 2929 (Ar-H), 2873 (Aliph. C-H), 1723 (C=O), 1605 (C=C), 1215 (Ar-O-Ar). ^{1}H-NMR (DMSO-d_6), (δ:ppm): 11.71 *(s*, 1H, OH), 7.87 (*d*, J=8.0, 2H, Ar-H), 6.74 (*d*, J = 8.9Hz, 4H, Ar-HPc), 6.57 (*d*, J=8.0, 2H, Ar-H), 5.90 (s, 4H, Ar-HPc), 5.76(*d*, J=8.4 Hz, 4H, Ar-HPc), 2.86 (*t*, 2H, CH_2), 2.64 (*t*, 2H, CH_2). MALDI-TOF-MS m/z calc. 1286.06; found: 1286.66 $[M+H]^+$. Elemental Analysis, Anal. Calc. for $C_{59}H_{20}F_{15}N_8O_6Zn$; C, 55.01; H, 1.64; N, 8.70 Found: C, 55.17; H, 1.43;N, 9.14.

*2.4.2.8 Syntheses of complexes **8**-propionic, **8**-acetic and **8**-acrylic, **Scheme 3.9***

***Synthesis of 8**-propionic*

Phthalonitrile ***j*** (1.09 g, 3.88 mmol), phthalonitrile ***c*** (0.375 g, 1.28 mmol), and DBU (0.2 mL) were mixed in 1-pentanol (5.00 ml) in the presence of anhydrous zinc acetate (0.45 g, 2.03 mmol). The mixture was stirred and allowed to reflux for 6 h. Thereafter, the product was precipitated with methanol followed by washing with ethanol using a centrifuge. The desired AB_3 molecule was isolated on a silica-packed column, eluting with THF/MeOH (5:1). The obtained green product was soluble in DMSO and hot methanol.

Yield (0.54 g) 28%. UV–vis. (DMSO) λ_{max} (log ε) nm: 680 (5.21), 615 (2.88), 350 (4.18). IR (ATR), ν/cm^{-1}: 3225 (OH), 3067 (Ar-H), 2936-2836 (C-H, CH_3), 1712 (C=O), 1431 (C=C), 1220 (Ar-O-Ar). ^{1}H-NMR (DMSO-d_6), (δ: ppm): 11.30 (*s*, 1H; OH), 7.81 (*d*, J=8.2Hz, 4H; Ar-H, Pc ring), 7.36 (*dd*, J=8.2 Hz, 2.3Hz, 4H;

Ar-H, Pc ring), 7.23 (*d*, J=2.3 Hz, 4H; Ar-H, Pc ring), 6.87 (*d*, J=6.8 Hz, 2H; carboxyl ring), 6.58 (*d*, J=6.8 Hz, 2H; carboxyl ring), 6.43 (*t*, J=2.3Hz, 3H, OCH_3 ring), 6.33 (*d*, J=2.3 Hz, 6H; CH_3 ring), 3.74 (*s*, 18H; CH_3), 1.35 (*t*, 2H, -CH_2), 1.17 (*t*, 2H, -CH_2). MALDI-TOF-MS m/z calc. 1196.27; found: 1196.92 $[M]^+$. Elemental Analysis, Anal. Calc. For $C_{65}H_{48}N_8O_{12}Zn$(II): Expected: C, 65.94; H, 4.04; N, 9.35, found C, 64.95; H, 3.05; N, 9.34.

Synthesis of* 8-*acrylic

A similar procedure was used for the synthesis of **8**-propionic except that phthalonitrile ***i*** (0.375 g, 1.28 mmol) instead of phthalonitrile ***c*** was employed. The amounts of all the other reagents were the same as well as the purification method.

Yield (0.56 g) 29%. UV–vis. (DMSO) λ_{max} (log ε) nm: 680 (4.96), 614 (3.11), 349 (4.55). IR (ATR), ν/cm^{-1} : 3161 (OH), 3026 (Ar-H), 2932-2835 (C-H, CH_3), 1766 (C=O), 1464 (C=C), 1265 (Ar-O-Ar). ^{1}H-NMR (DMSO-d_6), (δ:): 11.36 (*s*, 1H; OH), 7.87 (*d*, J=8.2 Hz, 4H; Ar-H, Pc ring), 7.43 (*dd*, J = 8.2 Hz, 2.3Hz, 4H; Ar-H Pc ring), 7.41 (*d*, J= 16.2 Hz, 1H, CH *Trans*), 7.29 (*d*, J= 2.3 Hz, 4H; Ar-H, Pc ring), 6.69 (*d*, J=6.9 Hz, 2H; carboxyl ring), 6.57 (d, J=6.9 Hz, 2H; carboxyl ring), 6.49 (*t*, J= 2.3 Hz, 3H, CH_3 ring), 6.39 (*d*, J= 2.3 Hz, 6H; CH_3 ring), 6.35 (*d*, J= 16.2 Hz, 1H, -CH *Trans*), 3.80 (*s*, 18H; CH_3). MALDI-TOF MS m/z calc. 1194.25; found: 1194.29 $[M]^+$. Elemental Analysis, Anal. Calc. For $C_{65}H_{46}N_8O_{12}Zn$(II): Expected: C, 65.25; H, 3.88; N, 9.37, found C, 65.26; H, 3.87; N, 9.38.

Synthesis of *8*-*acetic*

A similar procedure was used for the synthesis of **8**-propionic except that phthalonitrile ***g*** (0.375 g, 1.27 mmol) instead of phthalonitrile ***c*** was employed. The amounts of all other reagents and the purification method were the same as before.

Yield 33%, (0.63 g). UV–vis. (DMSO), λ_{max} (log ε) nm : 685 (5.15), 619 (3.31), 352 (3.96). IR (ATR), ν/cm^{-1}: 3226 (OH), 3067 (Ar-H), 2944-2836 (C-H, CH_3), 1717(C=O), 1428 (C=C), 1219(Ar-O-Ar). ^{1}H-NMR (DMSO-d_6), (δ:ppm): 11.30 (*s*, 1H; OH), 7.81 (*d*, J= 8.2 Hz, 4H; Ar-H, Pc ring), 7.35 (*dd*, J= 8.2 Hz, 2.3Hz, 4H; Ar-H, Pc ring), 7.22 (*d*, J= 2.3 Hz, 4H; Ar-H, Pc ring), 6.57 (*d*, J= 6.8 Hz, 2H; carboxyl ring), 6.42 (*d*, J= 6.8 Hz, 2H; carboxyl ring), 6.32 (*d*, J= 2.3 Hz, 6H; CH_3 ring), 6.28 (*d*, J= 2.3 Hz, 3H, CH_3 ring), 3.81 (*d*, 2H, CH_2), 3.73 (*s*, 18H; CH_3). MALDI-TOF-MS m/z calc. 1198.25; found: 1198.29 $[M]^+$. Elemental Analysis, Anal. Calc. for $C_{64}H_{46}N_8O_{13}Zn$(II): Expected: C, 64.03; H, 3.86; N, 9.33, found C, 64.05; H, 3.83; N, 9.34.

2.4.3 Syntheses of nanoparticles

2.4.3.1 Syntheses of metal tungstate nanoparticles

Cobalt tungstate nanoparticles ($CoWO_4$), Scheme 3.10

A mixture containing cobalt acetate tetrahydrate (0.8 g, 3.21 mmol), thioglycolic acid (TGA, 0.5 mL, 0.0125 M), and Millipore water (100 mL) was heated to 100˚C under magnetic stirring. Thereafter, NaOH (40 mL, 1M) solution was added to increase the pH to 11 pH. After 40 min of stirring, $Na_2WO_4 \cdot 2H_2O$ (0.64 g, 1.94 mmol) was added and the mixture was allowed to reflux further for 50 min. UV–visible spectra were monitored in 10 min intervals until well-resolved bands were obtained. A solution of GSH (50 mL, 0.0250 M) was added while stirring for 30 min to achieve the ligand exchange between GSH and TGA. The product was precipitated out using a centrifuge with ethyl alcohol and purified with acetone. The same procedure used for $CoWO_4$ was followed for the synthesis of $NiWO_4$/Ag_2WO_4/Bi_2WO_6 with the exception that different reagent quantities were utilized to create each nanoparticle. **Table 2.1** shows the amounts of the reagents used for the rest of the NPs.

Table 2.1: Amounts of reagents used for the synthesis of $NiWO_4$/Ag_2WO_4/Bi_2WO_6. The amount of GSH was maintained at (50 mL, 0.025 M).

NP	TGA	NaOH	Na_2WO_4	Water (mL)	Metal salt
$NiWO_4$	0.62 mL 0.0125 M	70 mL 1 M	0.64 g 1.94 mmol	200 mL	$Ni(OAc)_2$ 1.2 g 4.82 mmol
Ag_2WO_4	0.40 mL 0.0125 M	30 mL 1 M	0.64 g 1.94 mmol	70 mL	AgOAc 0.78g 3.84 mmol
Bi_2WO_6	0.62 mL 0.0125 M	70 mL 1 M	0.64 g 1.94 mmol	200 mL	Bi_2O_3 1.8 g 3.86 mmol

2.4.3.2 Syntheses of dimerized silver-magnetic nanoparticles (Ag-Fe_3O_4), Scheme 3.11

Magnetic nanoparticles were synthesized as reported in the literature with modification [**147**] for Ag-Fe_3O_4 as follows: iron(III) acetylacetonate (0.05 g, 0.142 mmol), silver acetate (0.05 g, 0.30 mmol), and 1,2-dodecanediol (0.1 g, 0.495 mmol) were added to 20 mL of dimethylformamide in a around bottom flask under magnetic stirring and heated at 100 °C. Then 6-mercaptohexanol 97% (1 mL) was injected after 5 min of heating, the reaction was left to proceed for 2 h. Ag-Fe_3O_4 was precipitated in methanol and purified with ethanol.

2.4.4 Syntheses of nanoconjugates, Scheme 3.12

For covalent linkage, the Pc complexes (except for **3**-NH_2) were weighed into a separate round bottom flask containing of DMF and DCC. The reactions were left undisturbed for 48 h under argon flow, after which NPs were added to the mixtures which were allowed to stir for a further 72 h. The same procedure was used for complex **3**-NH_2, with the exception that Ag-Fe_3O_4 was activated first under the same conditions and with the same amount of DCC before the Pc complex was added. **Table 2.2** lists the reagents used to synthesize nanoconjugates using the same method.

Table 2.2: Amounts of all reagents to form conjugates at 48 h reaction time and room temperature.

Pc	Amount of Pc	NPs	Amount of NP	DCC amounts	DMF vol
1-ethanoic	28 mg, 0.0236 mmol	QDs	40 mg	18 mg, 0.0872 mmol	2 mL
2-propionic	28 mg, 0.0205 mmol 30 mg, 0.0263 mmol	QDs $CoWO_4$	0.040 g 0.050 g	18 mg, 0.0872 mmol 35 mg, 0.169 mmol	3 mL 2 mL
3-propionic	0.051 g, 0.0383 mmol	Ag-Fe_3O_4	0.102 g	0.038 g, 0.184 mmol	4 mL
3-NH2	0.051 g, 0.0401 mmol	Ag-Fe_3O_4	0.102 g	0.038 g, 0.184 mmol	4 mL
3-COOH	0.051 g, 0.0392 mmol	Ag-Fe_3O_4	0.102 g	0.038 g, 0.184 mmol	4 mL
4-propionic	0.015g, 0.0116 mmol	$NiWO_4$ Bi_2WO_6	0.025 g	0.013 g, 0.063 mmol	3 mL
4-acetic	0.015g, 0.0116 mmol	$NiWO_4$ Bi_2WO_6	0.025 g	0.013 g, 0.063 mmol	3 mL
4-COOH	0.015g, 0.0119 mmol 0.030 g,	$NiWO_4$ Bi_2WO_6 $CoWO_4$	0.025 g 0.050 g	0.013 g, 0.063 mmol 35 mg, 0.169 mmol	3 mL 2 mL
5-propionic	30 mg, 0.0262 mmol	$CoWO_4$	50 mg	35 mg, 0.169 mmol	2 mL
5-acetic	0.015g, 0.0131 mmol 30 mg, 0.0262 mmol 0.051 g, 0.0446 mmol 0.028 g, 0.0245 mmol	$NiWO_4$ $CoWO_4$ Ag-Fe_3O_4 Ag_2WO_4	0.025 g 50 mg 0.102 g 0.050 g	0.013 g, 0.063 mmol 35 mg, 0.169 mmol 0.038 g, 0.184 mmol 35 mg, 0.169 mmol	3 mL 2 mL 3 mL 2 mL

5-acrylic	30 mg, 0.0261 mmol	$CoWO_4$	50 mg	35 mg, 0.169 mmol	2 mL
6-COOH	30 mg, 0.0226 mmol	$CoWO_4$	50 mg	35 mg, 0.169 mmol	2 mL
7-propionic	30 mg, 0.0234mmol	$CoWO_4$	50 mg	35 mg, 0.169 mmol	2 mL
7-acrylic	30 mg, 0.0233 mmol	$CoWO_4$	50 mg	35 mg, 0.169 mmol	2 mL
8-propionic	0.028 g, 00234 mmol	Ag_2WO_4	50 mg	35 mg, 0.169 mmol	2 mL
8-acetic	0.028 g, 00234 mmol	Ag_2WO_4	50 mg	35 mg, 0.169 mmol	2 mL
8-acrylic	0.028 g, 00234 mmol	Ag_2WO_4	50 mg	35 mg, 0.169 mmol	2 mL

2.5 Photodegradation studies.

Modulight® Medical Laser system (ML) 7710-670, with cylindrical output channels, a focusing beam, an integrated calibration module, hand-tuning pedal, fiber sensors (subminiature version A) connectors, and safety interlocks were used to photocatalyze TC, DBT and MB. The system consists of a small magnetic stirrer and a sample holder. The light source, with a 670 nm excitation wavelength, carrying 80 mW/cm^2 irradiance power in energy doses between 0.9 and 3.6 kJ cm^{-2} was directed to the sample with spectral readings being recorded after using a UV-visible spectrophotometer.

The photocatalytic activities of the as-prepared samples (Pc complexes and their nanoconjugates) were evaluated by the photodegradation of organic pollutants in an aqueous (n-octane for DBT) solution. The stock solution of organic pollutants was prepared and then diluted to give the working concentrations. For photocatalytic studies, 5 mg of the as-prepared photocatalyst samples were placed (suspended) in a cuvette containing 2 mL

of each of the working concentrations of organic pollutants in solution. The suspension was then stirred in the dark at 30 min intervals for 12 h to reach adsorption equilibrium before being exposed to visible light. The attainment of equilibrium was confirmed by the of lack change in the spectra of organic pollutants with irradiation time.

2.6 Photodynamic inactivation of bacteria

One bacterial strain was used as a model; *Staphylococcus aureus* as a Gram-positive bacterium. Stock culture of *S. aureus* was grown aerobically in 6 mL of nutrient broth and incubated at 37 °C on a rotary shaker (~200 rpm) to obtain bacteria culture. The incubation was maintained until the optical density of the culture recorded at 620 nm was determined to be between 0.6 and 0.8. The resulting bacterial solution was centrifuged to remove the broth, and bacterial cells were washed three times with PBS. The bacterial culture was then diluted to 1/1000 (10^9 colony-forming unit (CFU)/mL) in PBS to make a working stock suspension.

PACT studies on *S. aureus* were performed using a reported procedure with slight modifications [**151**]. In the present work, in all cases, 5% DMSO in PBS was used as a medium. In order to determine the optimal concentration, of the photosensitizers, different concentrations of 0.1 to 40 μg/mL (data not shown) were tested and the optimum concentration was found to be at 0.5 μg/mL, the concentration that inhibits 100% of bacteria at a given irradiation time. The bacterial solutions containing 0.5 μg/mL of each sample were incubated in a shaking incubator for 30 min in the dark at 37°C. Afterwards, 2.5 mL of the bacterial solution was subjected to a light at a constant

irradiance of 0.5 W cm^{-2}, resulting in energy doses ranging from 0.9 kJ cm^{-2} to 3.6 kJ cm^{-2} corresponding to time periods ranging from 15 min to 60 min at 670 nm excitation wavelength. The other 2.5 mL suspension was also immediately kept in the dark for the same time. At the end of each irradiation or in the dark, 100 µL of each sample were aseptically inoculated on agar plates and then statically incubated for 24 h at 37°C in the dark.

The number of colonies was then counted on each plate after 18 h of incubation at 37°C. Also, the control treatments were performed without photosensitizer both with irradiation and in the dark in order to determine the effect of light and solvents. The data for CFU/mL were converted to the logarithmic form. Three independent (n = 3) experiments were performed and the obtained data were compared using a 3-way factorial ANOVA. The data are presented as mean ± standard deviation (SD) of log10 CFU values. A p-value of 0.05 was considered statistically significant.

Publications

The following **Chapters 3-7** discuss findings that have been published or accepted in peer-reviewed publications. The articles are listed below.

1. **Sithi Mgidlana**, Yolande Ikala Openda, Tebello Nyokong, Asymmetrical zinc phthalocyanine conjugated to various nanomaterials for applications in phototransformation of organic pollutants and photoinactivation of bacteria. Journal of Molecular Structure 1277 (2023) 134850.
2. **Sithi Mgidlana**, Pinar Sen, Tebello Nyokong, Dual Action of Asymmetrical Zinc(II) phthalocyanines conjugated to Silver tungstate nanoparticles towards photodegradation of Tetracycline and inactivation of *Staphylococcus Aureus* bacteria. Journal of Photochemistry and Photobiology A: Chemistry 437 (2022) 114444.
3. **Sithi Mgidlana**, Pinar Sen, Tebello Nyokong, Photodegradation of tetracycline by asymmetrical zinc (II) phthalocyanines conjugated to cobalt tungstate nanoparticles. Journal of Molecular Structure 1261 (2022) 132938.
4. **Sithi Mgidlana**, Muthumuni Managa, Tebello Nyokong, Asymmetrical zinc(II) phthalocyanines conjugated to metal tungstate nanoparticles for photoinactivation of Staphylococcus aureus. Journal of Coordination Chemistry 75 (2022) 1097-1111.
5. **Sithi Mgidlana**, Tebello Nyokong, Asymmetrical zinc (II) phthalocyanines cobalt tungstate nanomaterial conjugates for

photodegradation of methylene blue. Journal of Photochemistry and Photobiology A: Chemistry 418 (2021) 113421.

6. **Sithi Mgidlana**, Nnamdi Nwahara, Tebello Nyokong, Photocatalytic desulfurization of dibenzothiophene using methoxy substituted asymmetrical zinc (II) phthalocyanines conjugated to metal tungstate nanomaterials. Polyhedron 197 (2021) 115053.
7. **Sithi Mgidlana**, Tebello Nyokong, Photocatalytic desulfurization of dibenzothiophene using asymmetrical zinc (II) phthalocyanines conjugated to silver-magnetic nanoparticles. Inorganica Chimica Acta 514 (2020) 119970.
8. **Sithi Mgidlana**, Pinar Sen, Tebello Nyokong, Direct nonlinear optical absorption measurements of asymmetrical zinc (II) phthalocyanine when covalently linked to semiconductor quantum dots. Journal of Molecular Structure 1220 (2020) 128729.

Extra publications

9. Sixolile Centane, **Sithi Mgidlana**, Yolande Ikala Openda, Tebello Nyokong, Electrochemical detection of human epidermal growth factor receptor 2 using an aptamer on cobalt phthalocyanines–Cerium oxide nanoparticle conjugate. Bioelectrochemistry 146 (2022) 108146.
10. Pinar Sen, Rodah Soy, **Sithi Mgidlana**, John Mack, Tebello Nyokong, Light-driven antimicrobial therapy of palladium porphyrins and their chitosan immobilization derivatives and their photophysical-chemical properties. Dyes and Pigments 203 (2022) 110313.

11. Yolande Ikala Openda, **Sithi Mgidlana**, Tebello Nyokong, In vitro photoinactivation of S. aureus and photocatalytic degradation of tetracycline by novel phthalocyanine-graphene quantum dots nano-assemblies. Journal of Luminescence 246 (2022) 118863.
12. Nobuhle Ndebele, **Sithi Mgidlana**, Tebello Nyokong, Electrochemical Detection of Nitrite Using an Asymmetrically Substituted Cobalt Phthalocyanine Conjugated to Metal Tungstate Nanoparticles. Electroanalysis 34 (2022) 1348.
13. Nobuhle Ndebele, **Sithi Mgidlana**, Tebello Nyokong, Electrocatalytic Activity of Cobalt Phthalocyanines Revisited: Effect of the Number of Oxygen Atoms and Conjugation to Carbon Nanomaterials. Electrocatalysis 12 (2021) 499.
14. L. Collen Makola, **Sithi Mgidlana**, Tebello Nyokong, Amphiphilic axially modified cationic indium-porphyrins linked to hydrophilic magnetic nanoparticles for photodynamic antimicrobial chemotherapy against gram-negative strain; *Escherichia coli*. Dyes and Pigments 192 (2021) 109262.
15. Muthumuni Managa, **Sithi Mgidlana**, Samson Khene, Tebello Nyokong Optical limiting properties of indium 5, 10, 15, 20-tetrakis (4-aminophenyl) porphyrin covalently linked to semiconductor quantum dots. Inorganica Chimica Acta 511 (2020) 119838.

Chapter 3

Herein, this chapter provides information on the syntheses, characterization of MPcs, NPs, and their corresponding conjugates. The techniques employed include MALDI-TOF MS, ^{1}H-NMR, FT-IR, UV-vis spectrophotometry, CHN elemental analysis, TEM, XRD, EDX, DLS, TGA, and DSC.

In the following subsections, the synthesis and characterization of all Pc complexes employed in this thesis will be discussed.

3.1 Syntheses

3.1.1 Phthalonitriles

The syntheses and characterization of phthalonitriles ***a***-***j*** have been reported in literature and are listed in **Figure 3.1** [**136-145**]. On the other hand, this thesis is the first to report on the synthesis and characterization of the phthalonitriles ***k***-***n***. Briefly, in the presence of K_2CO_3, 4-nitrophthalonitrile is reacted with 2-(4-mercaptophenyl) ethanoic acid, 3,4,5- trimethoxyphenol or 1-(4-hydroxyphenyl)heptan-1-one, 2,3,4,5,6-pentafluorophenol in DMF to give ***k***, ***l***, ***m***, and ***n***, respectively (**Schemes 3.1A-D**). The phthalonitriles were characterized by FT-IR and ^{1}H-NMR and gave satisfactory results shown in section 2.4.

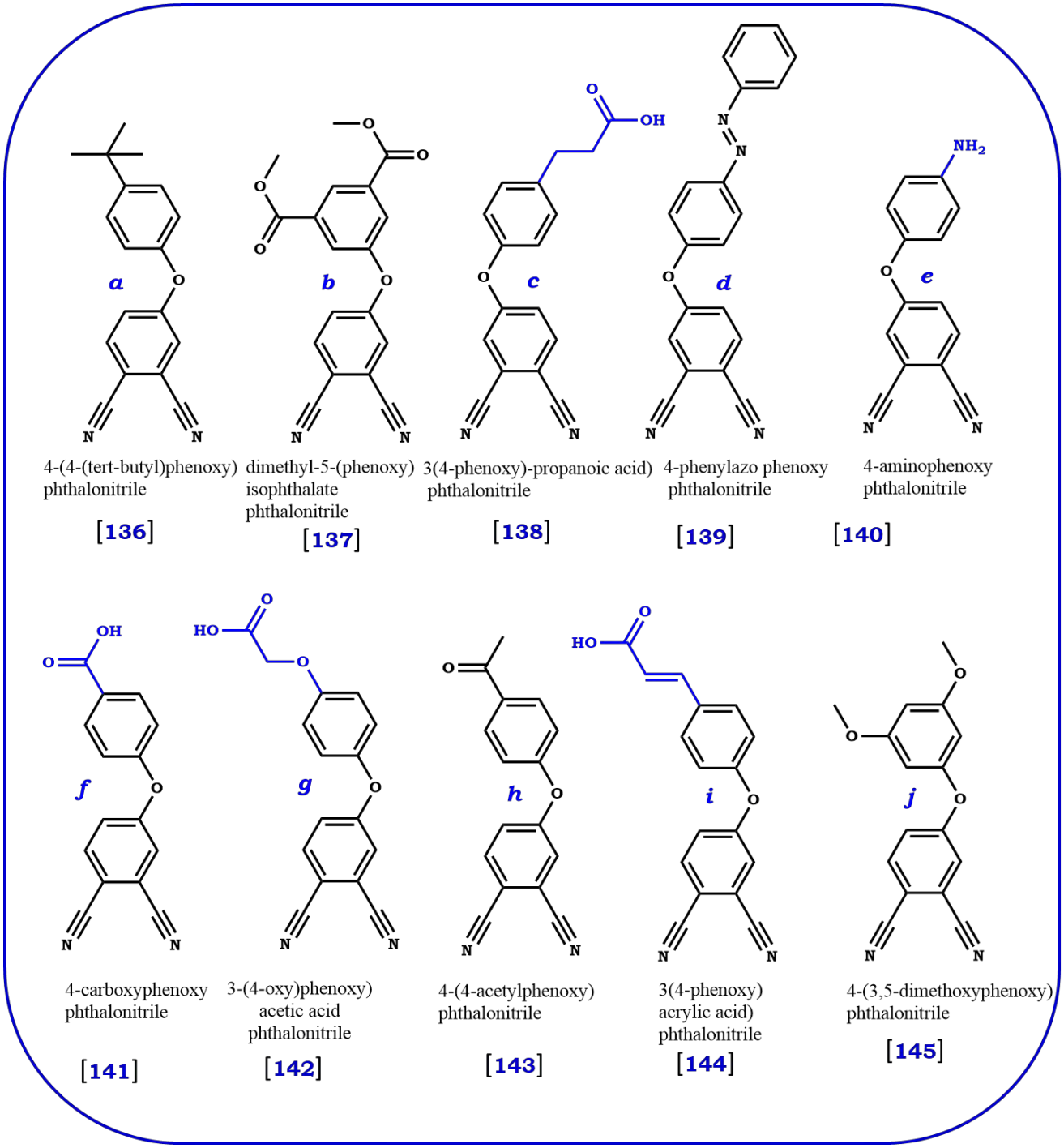

Figure 3.1: *Reported phthalonitrile precursors employed in this work for the syntheses of MPcs.*

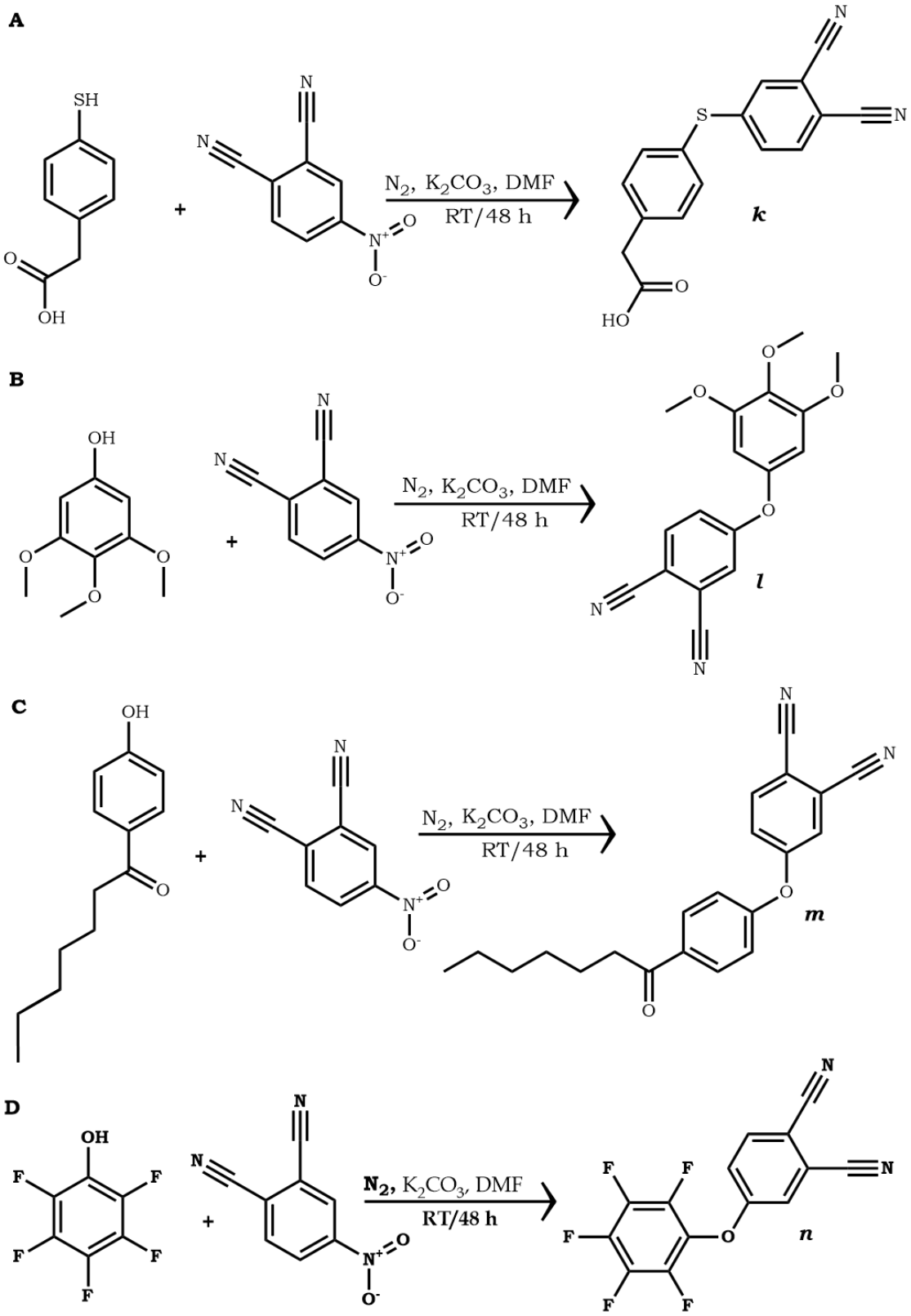

***Scheme 3.1**: Syntheses of phthalonitrile **k-n**.*

3.1.2 Syntheses of Pc complexes

A complete list of Pcs employed in this work is provided in **Figure 3.2** and in **Table 1.1**. The targeted AB_3 complexes are synthesized by statistical cross-condensation of two different phthalonitriles in a 1:3 ratio in 1-pentanol or 1-hexanol in the presence of zinc acetate catalyzed by DBU. The COOH and NH_2 ligands are chosen for the linking to the nanoparticles. MPcs contain one linking group allowing for a more defined conjugation. Complex **1**-ethanoic is prepared from cross-condensation of ***a*** and ***k*** while **2**-propionic is synthesized from ***b*** and ***c*** (**Schemes 3.2** and **3.3**). A dominant phthalonitrile ***d*** reacted through statistical cross-condensation with non-dominant phthalonitriles ***c***, ***f***, and ***e*** yielding **3**-propionic, **3**-COOH, and **3**-NH_2, respectively (**Scheme 3.4**). Similarly, **Scheme 3.5** shows that cross condensation of phthalonitriles ***l*** reacted with ***f***, ***c***, and ***g*** to give results **4**-COOH, **4**-propionic, and **4**-acetic complexes, respectively. Phthalonitriles ***c***, ***i***, and ***g*** reacted with phthalonitrile ***h*** producing acetophenone based Pc complexes, **5**-propionic, **5**-acrylic, and **5**-acetic complexes, respectively (**Scheme 3.6**). Complex **6**-COOH in **Scheme 3.7** result from reaction of phthalonitriles ***m*** and ***f***. Fluorinated Pc complexes, **7**-propionic and **7**-acrylic complexes are formed when the phthalonitriles ***c*** and ***i***, respectively react with phthalonitrile ***n*** (**Scheme 3.8**). Finally, as indicated in **Scheme 3.9**, the complexes **8**-propionic, **8**-acetic, and **8**-acrylic are formed when phthalonitrile ***j*** reacts by statistical cross condensation with phthalonitrile ***c***, ***g***, and ***i***, respectively. The desired AB_3 products were isolated and purified by applying column chromatography using silica gel and

THF/methanol (5:1) as the eluent. All the ZnPcs contain a COOH except for **3**-NH_2 for linking to NPs.

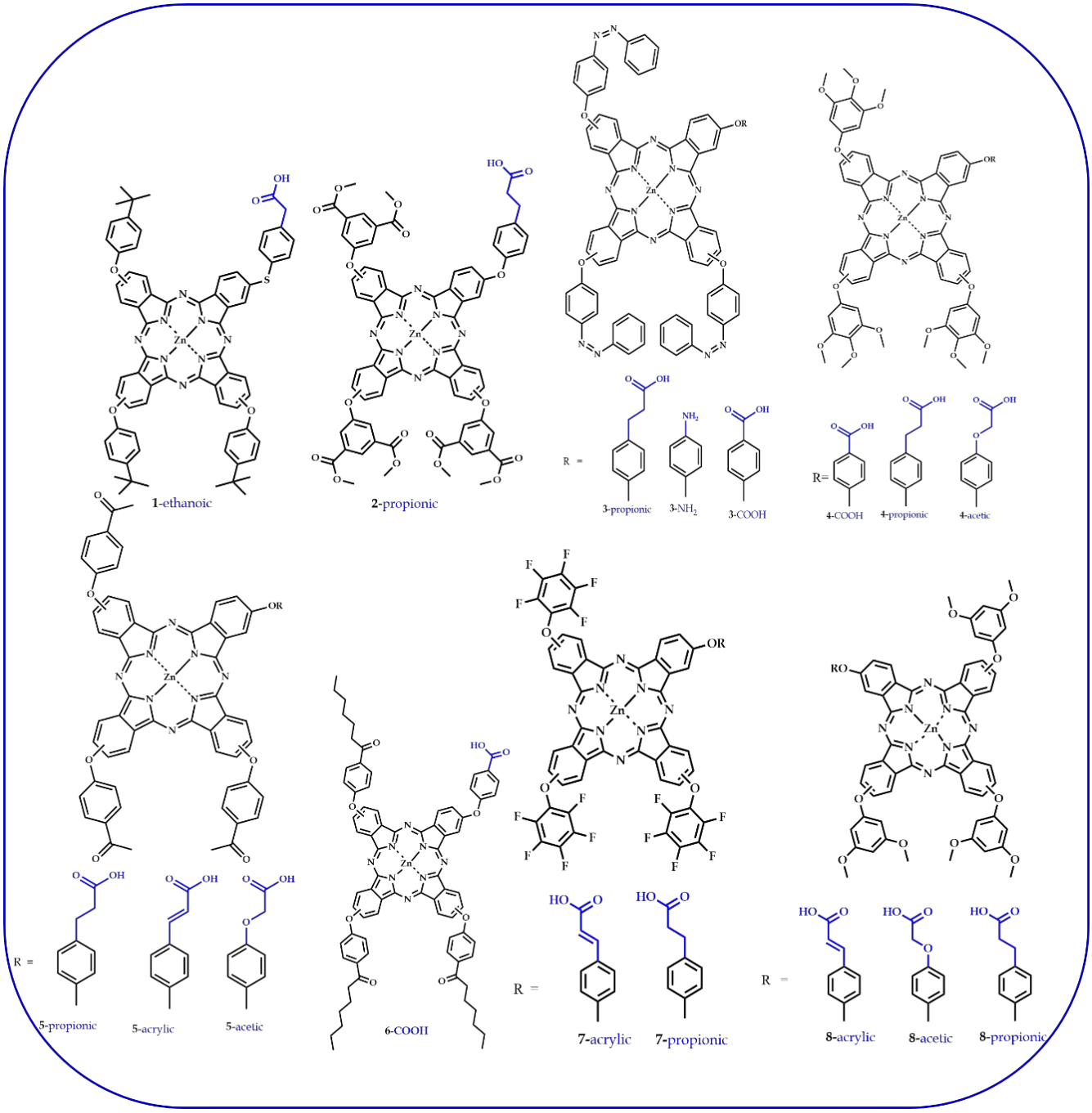

***Figure 3.2**: MPc complexes employed in this thesis.*

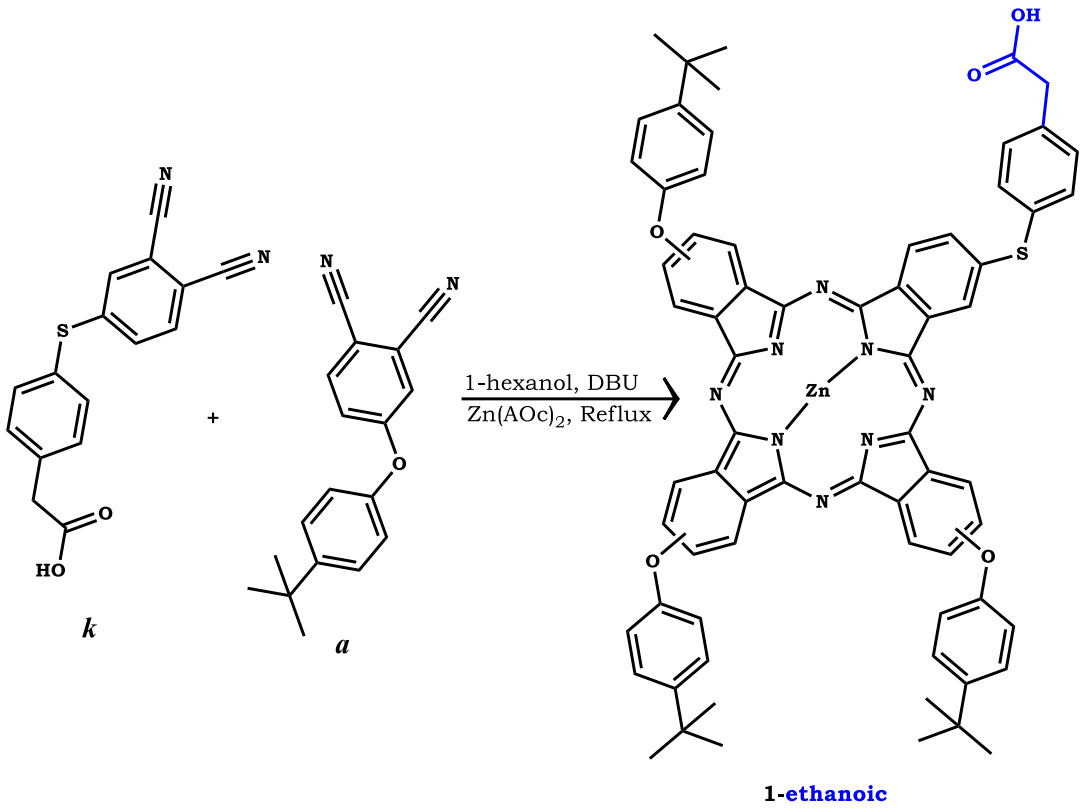

***Scheme 3.2**: Synthesis of **1**-ethanoic complex.*

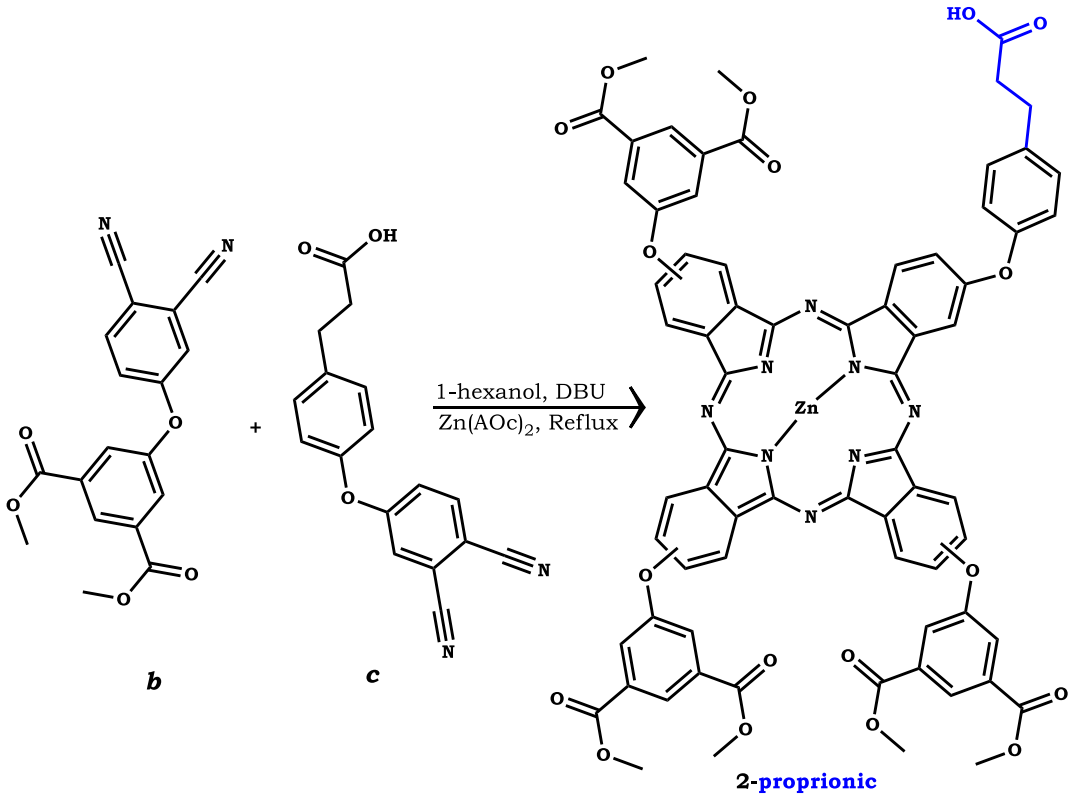

***Scheme 3.3**: Synthesis of **2**-propionic complex.*

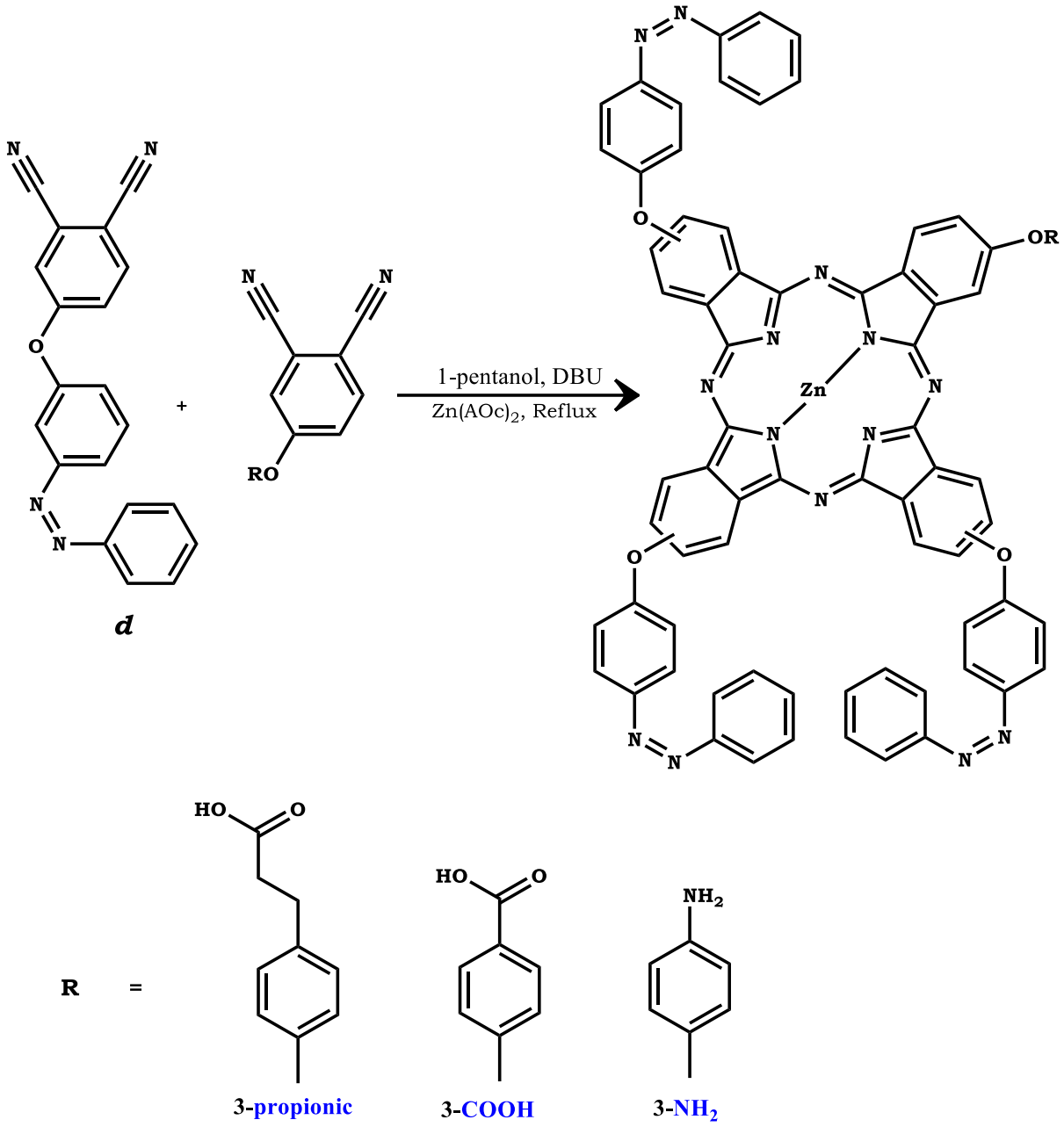

***Scheme 3.4**: Syntheses of **3**-COOH, **3**-NH_2, and **3**-propionic complexes.*

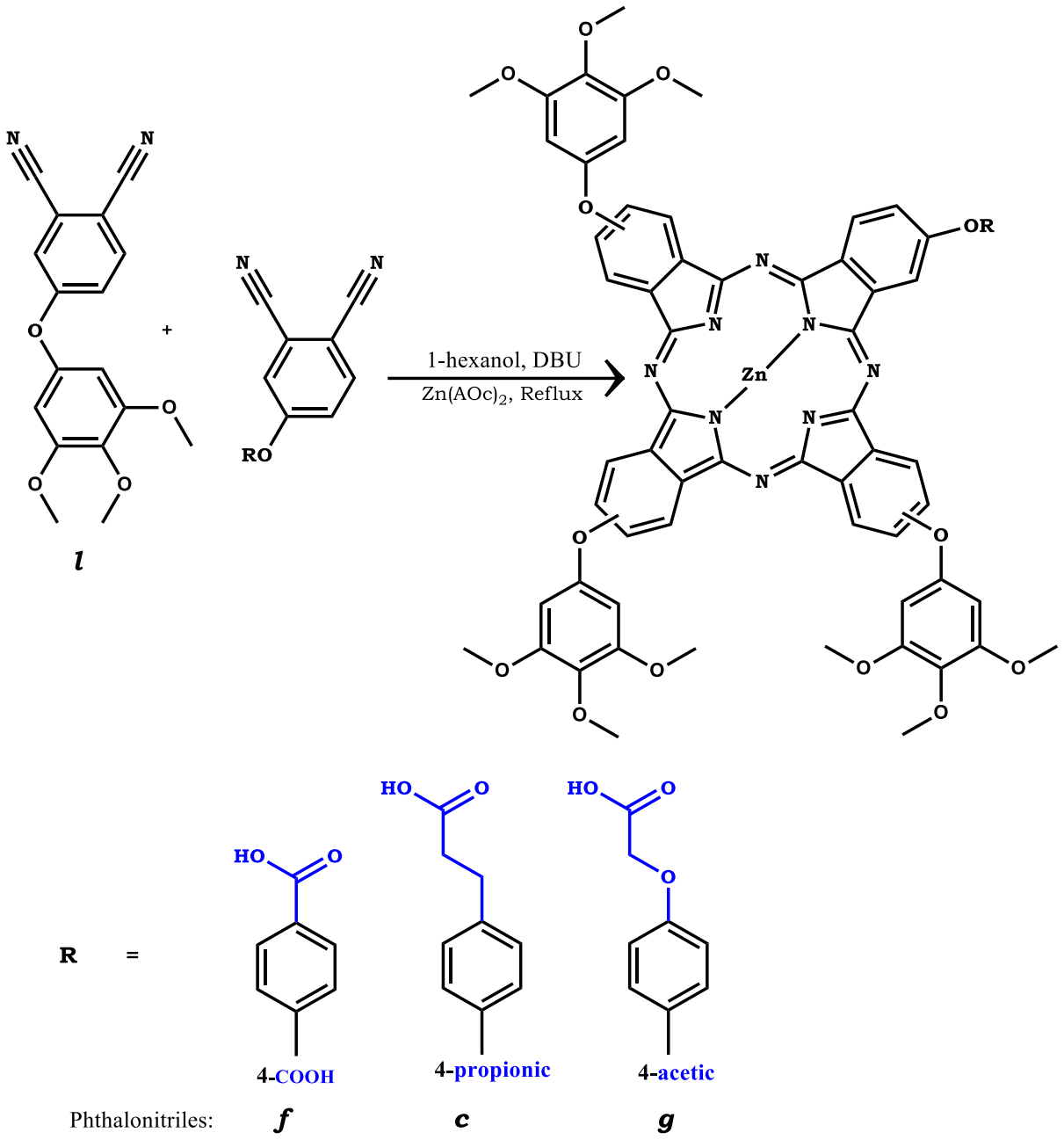

***Scheme 3.5**: Syntheses of **4**-COOH, **4**-propionic, and **4**-acetic complexes.*

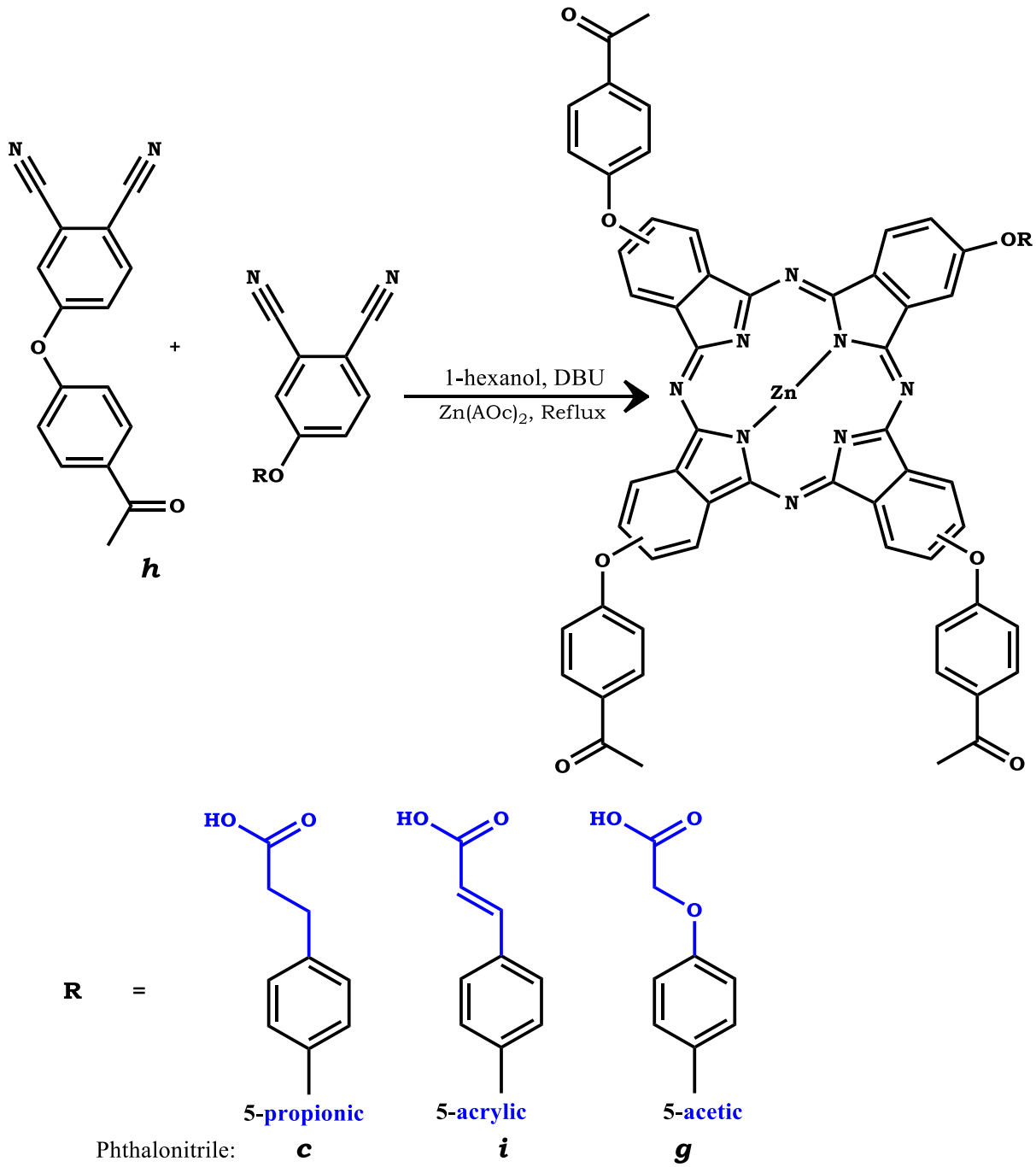

***Scheme 3.6**: Syntheses of **5**-propionic, **5**-acrylic, and **5**-acetic complexes.*

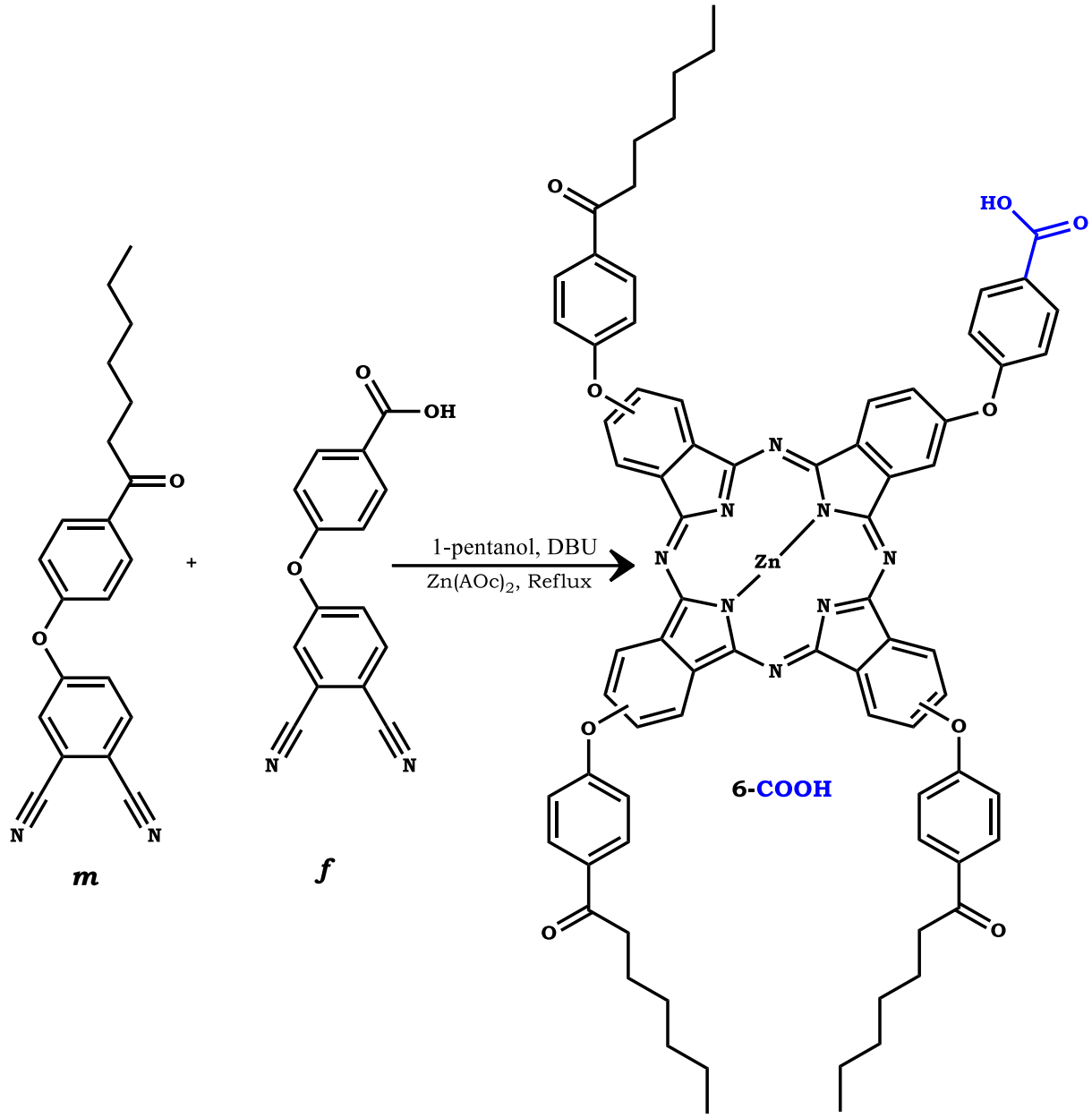

***Scheme 3.7**: Synthesis of **6**-COOH complex*

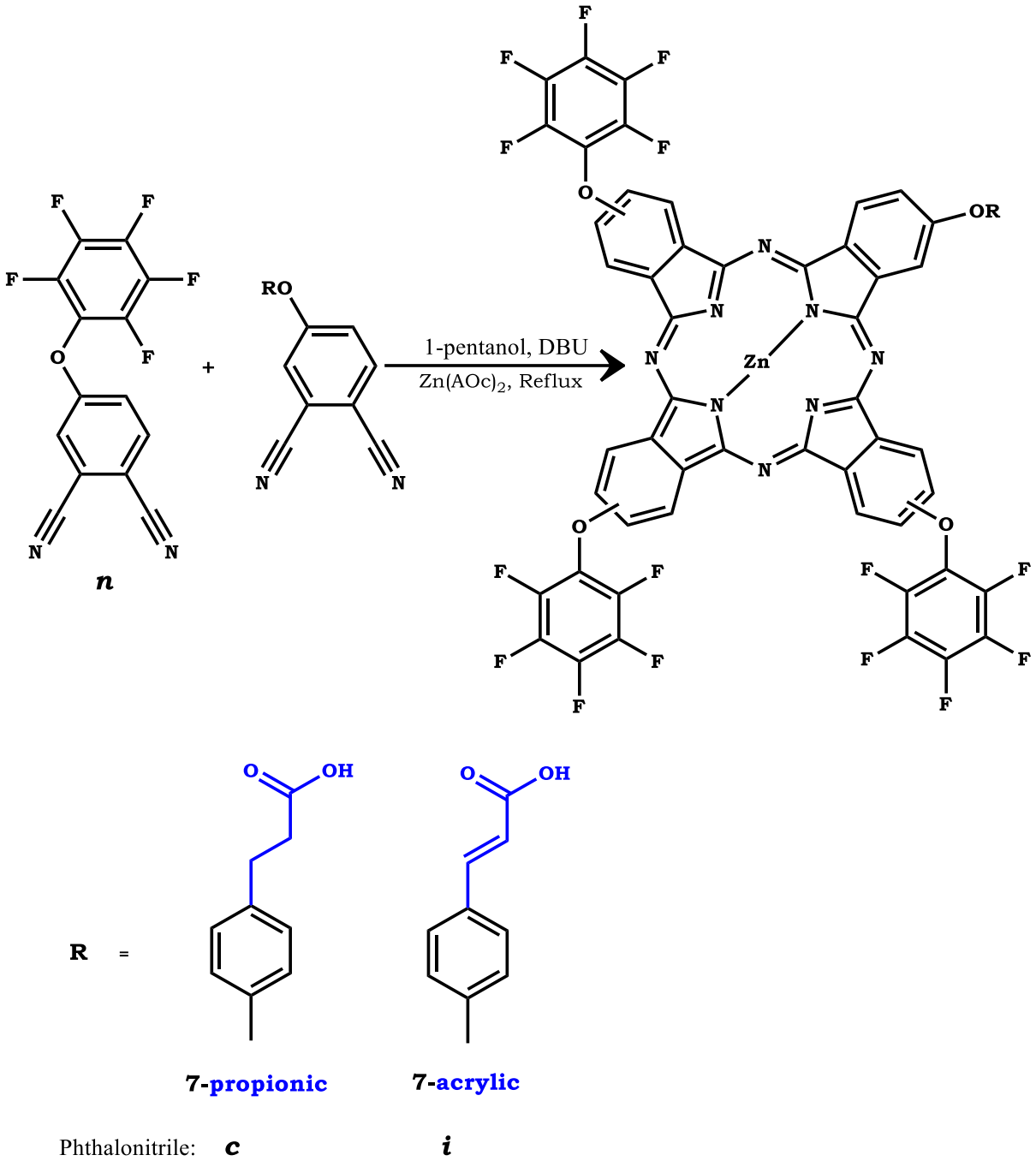

***Scheme 3.8**: Syntheses of **7**-acrylic and **7**-propionic complexes.*

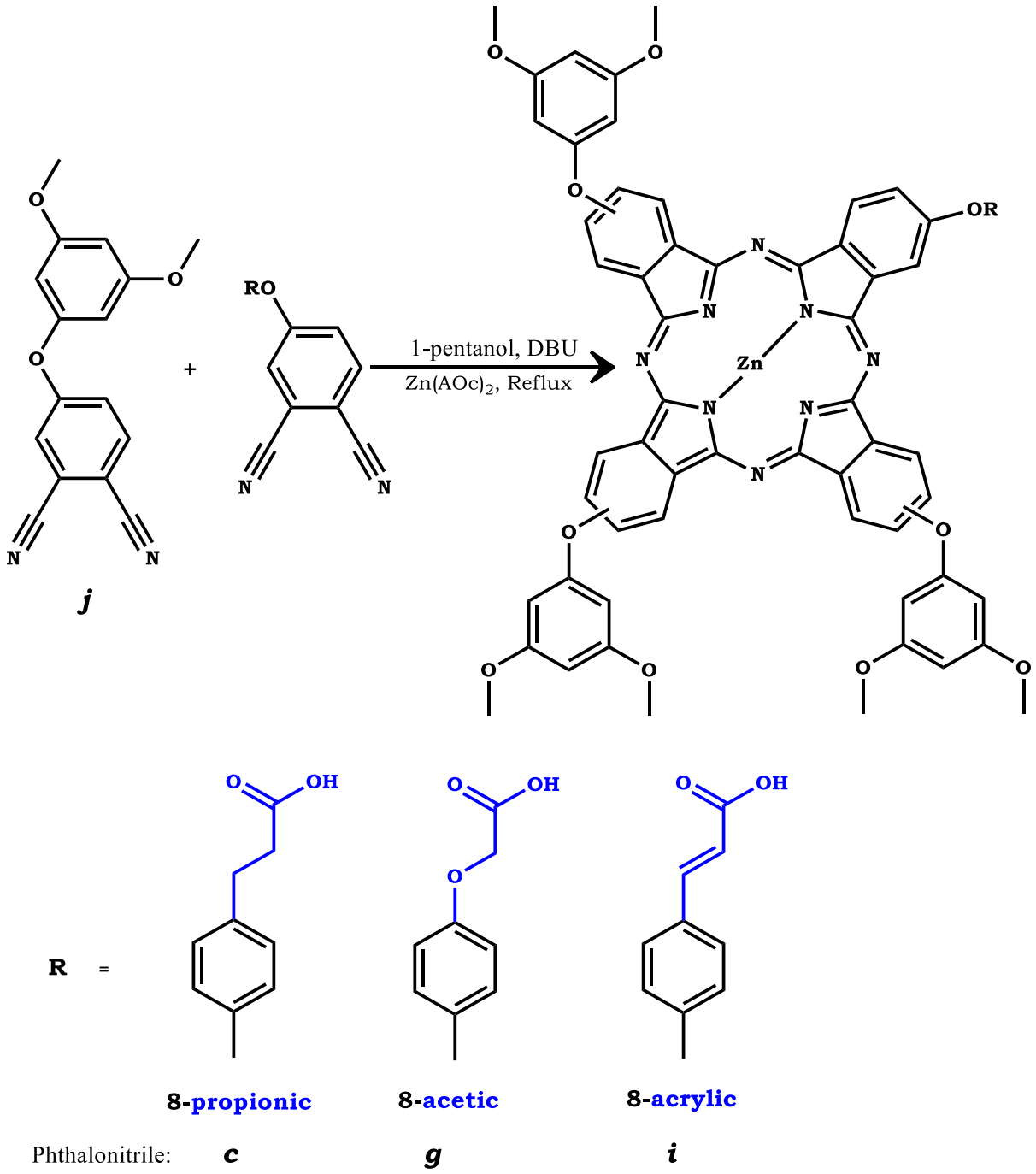

***Scheme 3.9**: Syntheses of **8**-propionic, **8**-acetic and **8**-acrylic complexe*

3.1.3 Syntheses of nanoparticles (NPs)

Hydrothermal methods under mild conditions are employed for the syntheses of $CoWO_4$, Ag_2WO_4, $NiWO_4$, and Bi_2WO_6 nanoparticles, **Scheme 3.10**, $CoWO_4$ used as an example. To produce narrow particle size distribution, the temperature was kept at lower levels and refluxing for a shorter time period. In the first step using sodium tungstate, metal salt, and TGA in the presence of sodium hydroxide at 100˚C, TGA capped nanoparticles were obtained. The second step involves ligand exchange between GSH and TGA. GSH capping agent was used to stabilize nanoparticles, improve solubility and allow for linking to phthalocyanine complexes. Silver magnetic (Ag-Fe_3O_4) nanoparticles are synthesized in two steps by reacting iron (III) acetylacetonate, silver acetate dihydrates and 1,2-dodecanediol, followed by the addition of 6-mercaptohexanol (mph) or GSH producing mph capped and GSH-capped Ag-Fe_3O_4 NPs (**Scheme 3.11**).

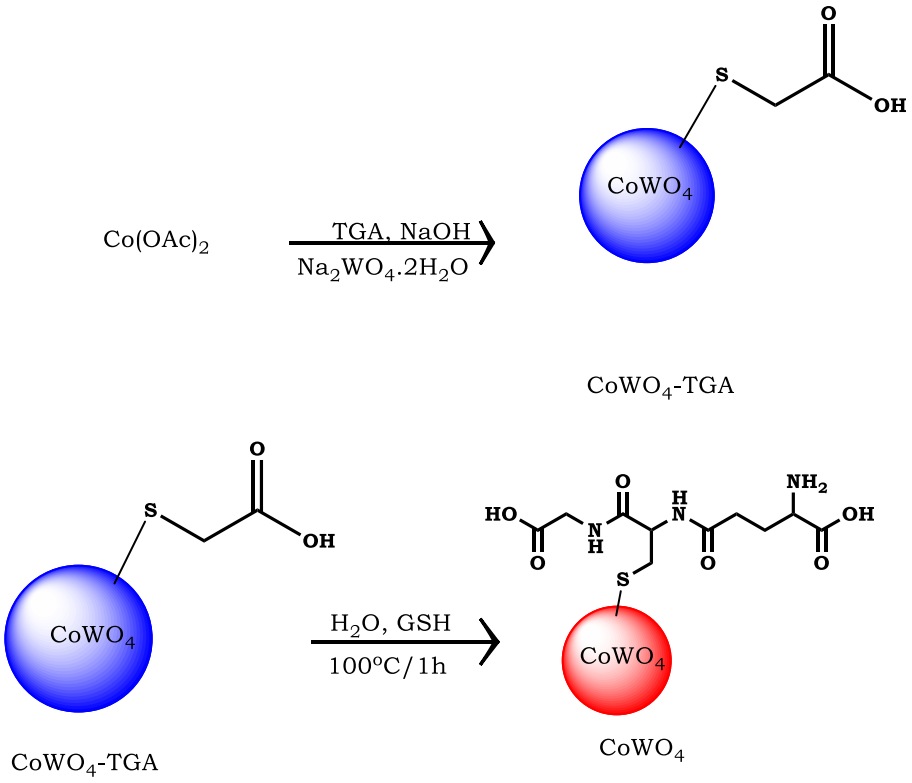

***Scheme 3.10**: Syntheses of NPs ($CoWO_4$ used as an example).*

HO〰 = mercaptohexanol (mph)

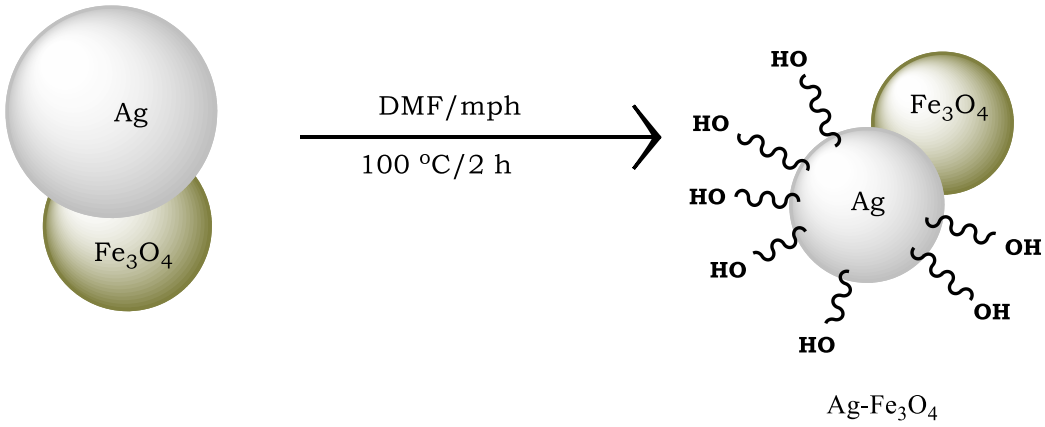

***Scheme 3.11**: Synthetic route to mph capped Ag-Fe_3O_4 nanoparticles.*

3.1.4 Sytheses of nanoconjugates

Scheme 3.12 shows a synthetic scheme for amide bond formation (using **4**-COOH and $NiWO_4$ as examples). All metal tungstate NPs were GSH-capped and were linked to MPcs via amide bonds. Following a similar synthetic method, GSH semiconductor quantum dots were conjugated to complexes **1**-ethanoic and **2**-propionic. Complexes **3**-COOH, **3**-propionic and **5**-acetic were linked to mercaptohexanol (mph) capped Ag-Fe_3O_4 NPs, forming ester bond, **Scheme 3.13** (using **3**-COOH as an example) due to low yields when using GSH-capped Ag-Fe_3O_4. Complex **3**-NH_2 was linked to 1-mercaptopropionic acid (mpa) capped Ag-Fe_3O_4 NPs through amide bonds between the amine of the former and activated carboxylic acid of the latter, **Scheme 3.14**. This is due to the difficulty in forming covalent bonds when an -NH_2 (amino) of the Pc complex and an OH (alcohol) of mph capped Ag-Fe_3O_4.

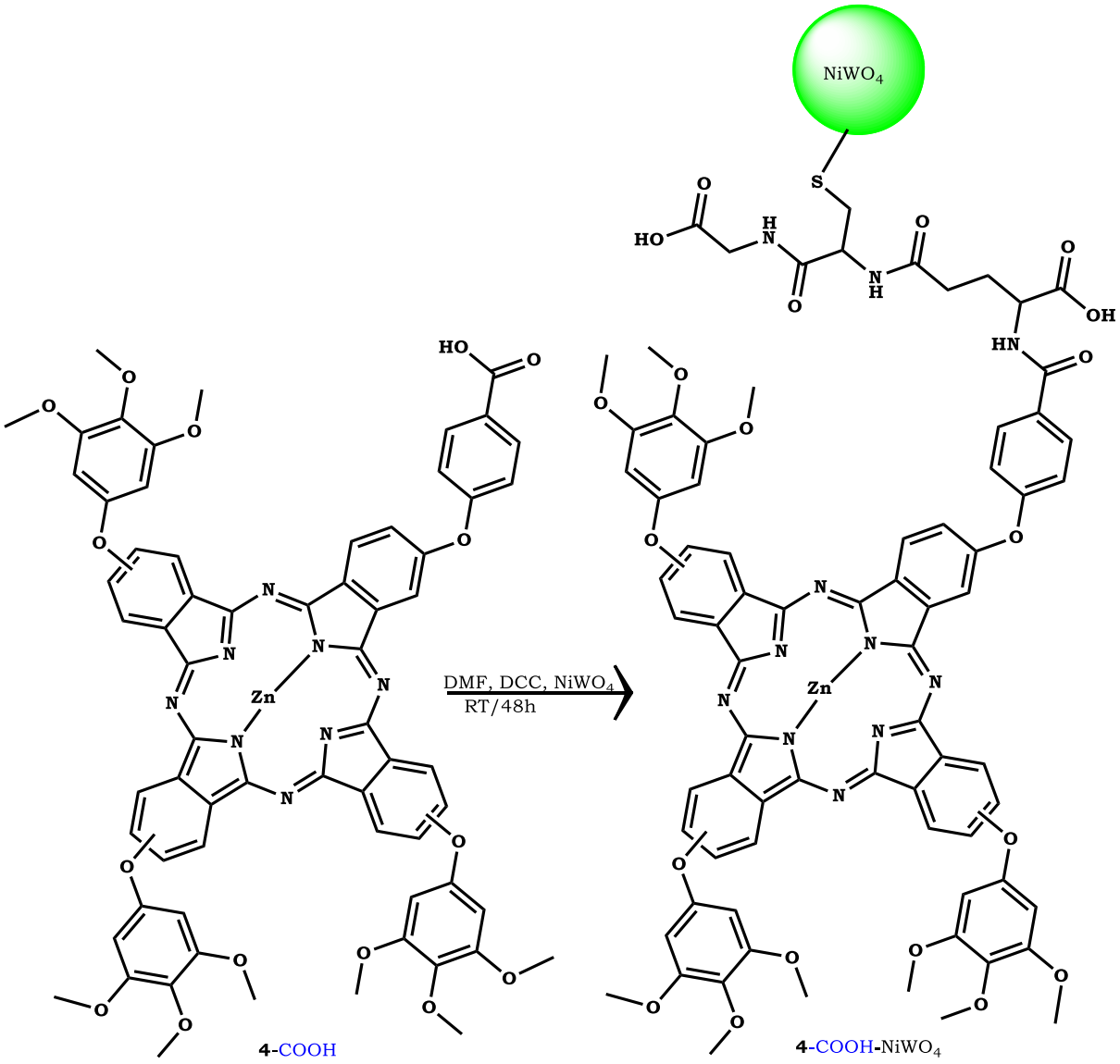

***Scheme 3.12**: Principle scheme for covalent coupling of the complexes to GSH capped NPs via amide bonds (using **4**-COOH and $NiWO_4$ as examples).*

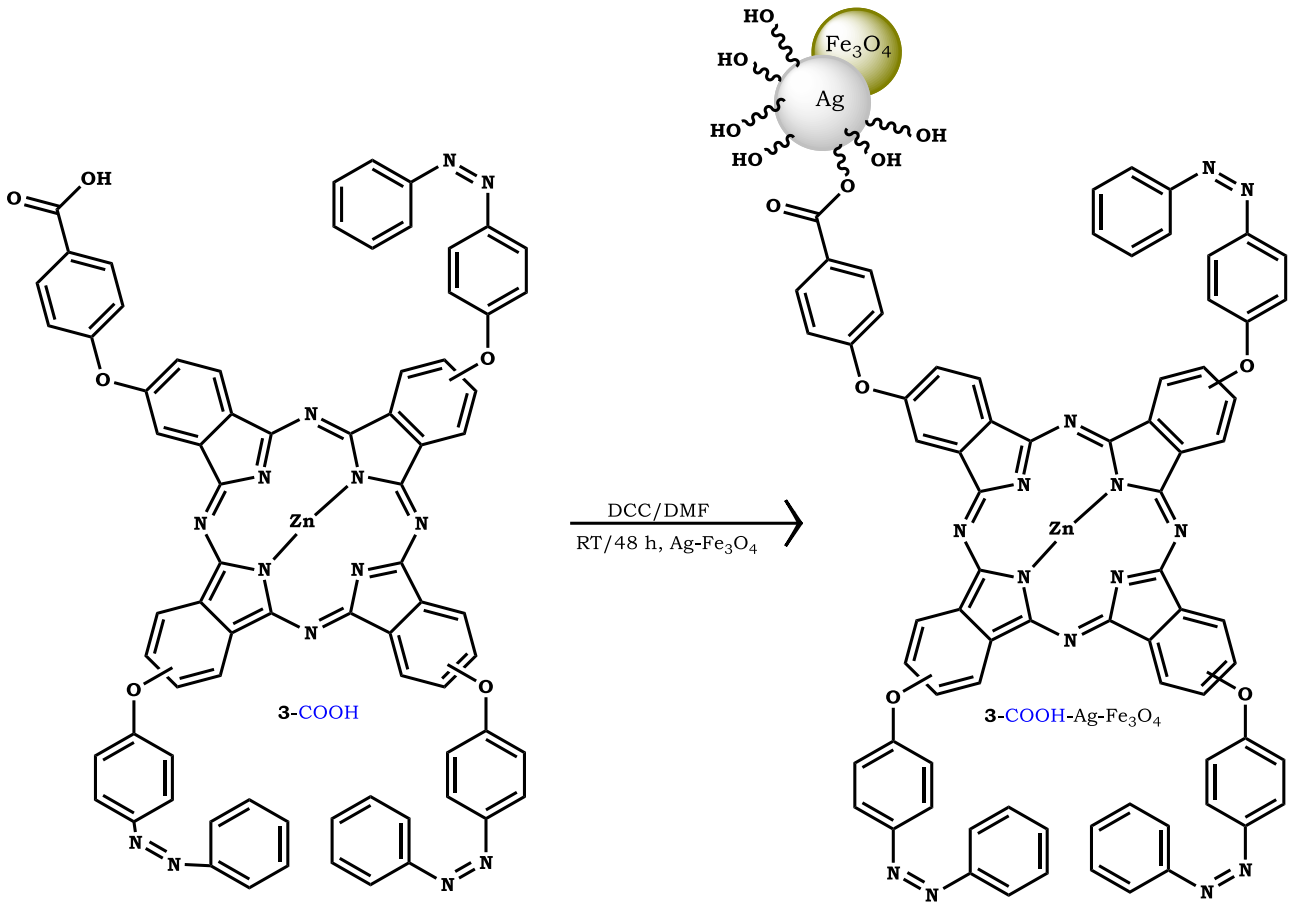

Scheme 3.13: *Principle scheme for covalent linking complexes to mph capped NPs via ester bonds (using* ***3****-COOH and Ag-Fe3O4 as examples).*

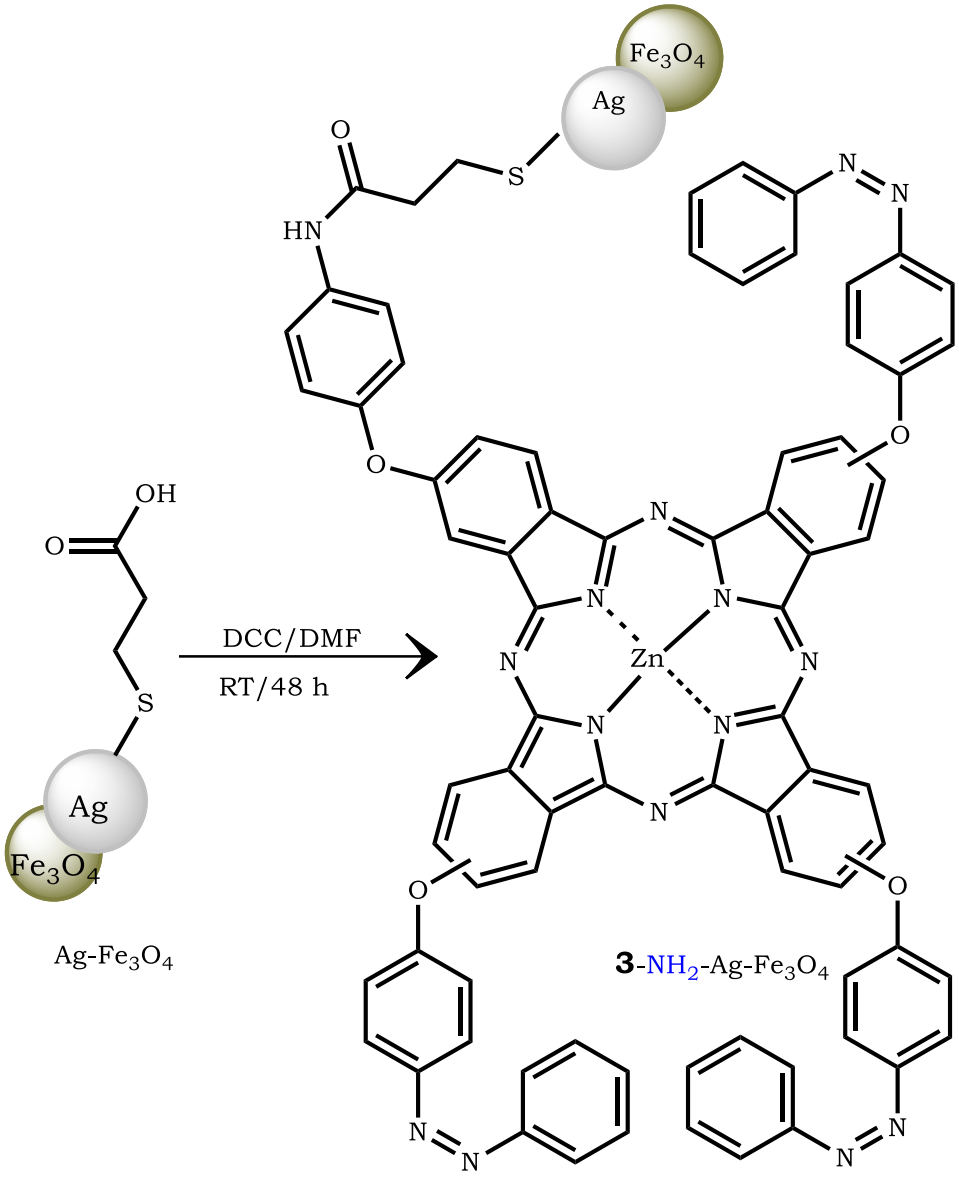

Scheme 3.14: *Conjugation of complex* ***3****-NH_2 to Ag-Fe_3O_4.*

3.2 Characterization of MPc, NPs and conjugates

UV-vis, FT-IR, elemental analysis, and ^{1}H-NMR spectroscopic techniques are used to characterize the MPc complexes. The obtained results confirm the successful formation of predicted structures. The ^{1}H NMR spectra of all the complexes are recorded in DMSO d_6 and gave the expected number of protons (**Figures A1-A8,** using **1**-ethanoic, **2**-propionic, **3**-NH_2, **4**-acetic, **5**-acetic, **6**-COOH, **7**-propionic**,** and **8**-acrylic as examples). The nanoconjugates are characterized using UV-vis, FT-IR, XRD, TEM, EDX, EDS, AFM, DLS, DSC and TGA.

3.2.1 UV-visible Spectra

UV–vis spectroscopy is one of the most reliable methods for the characterization of MPcs. The UV–vis spectra of the Pc complexes were recorded in DMSO (**Figure 3.3**). The Q-bands are observed between 675 and 687 nm, the Q-band maxima are recorded in **Table 3.1**. These results are typical for non-aggregated MPcs. Complex **7**-propionic showed some minimal aggregation with broadening near 630 nm, typical of H-aggregates [**152**]. All MPcs showed a single sharp symmetrical Q-band and a broad B-band, typical of metallated Pcs [**153**]. The broad intense B-band of the complexes **3**-NH_2, **3**-propionic, and **3**-COOH is attributed to the electron-rich –N=N- group. Complexes **1**-ethanoic and **6**-COOH exhibit red-shifted Q-band maxima at 687 nm and 688 nm, respectively. This is typical of alkylyn-containing Pcs [**154**,**155**]. Alkylyn chains are known to red shift the Q band in phthalocyanines [**155**].

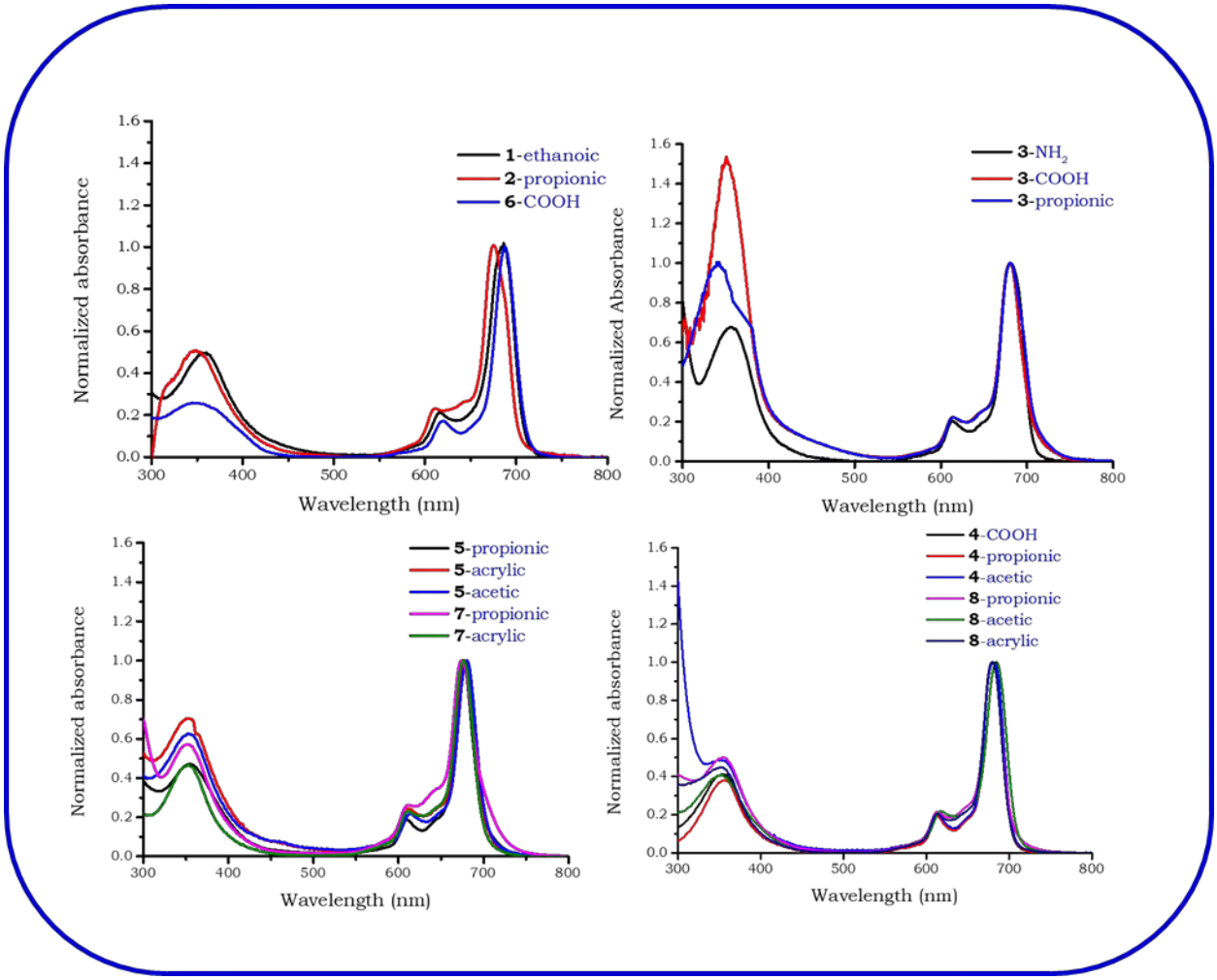

***Figure 3.3**: Normalized UV-visible spectra for Q bands of the Pc complexes synthesized in this research work in DMSO.*

Table 3.1: Q-bands (solvent = DMSO) of the Pc complexes and their respective conjugates employed in this work. Energy band gaps, and sizes of the NPs and the conjugates.

Complex	Q-band λ_{max} (nm)	Loading (µm/mg)	E_g (eV)	XRD Sizes (nm)	DLS size (nm)
1-ethanoic	687	---	---	---	---
1-ethanoic-CdTe/ZnSe/ZnO	687	7	2.5	7.3	8.9
2-propionic	677	---	---	---	---
2-propionic-CdTe/ZnSe/ZnO	677	9	2.6	9.7	11.1
2-propionic-$CoWO_4$	677	6	1.87	12.3	15.4
3-propionic	680	---	---	---	---
3-propionic-Ag-Fe_3O_4	680	9	2.13	50.3	78.1
3-COOH	680	---	---	---	---
3-COOH-Ag-Fe_3O_4	680	8	2.12	43.4	91.3
3-NH_2	680	---	---	---	---
3-NH_2-Ag-Fe_3O_4	680	8	2.34	40.5	70.3
4-COOH	683	---	---	---	---
4-COOH-$NiWO_4$	683	13	3.15	28.6	33.2
4-COOH-$CoWO_4$	683	23	1.77	14.3	16.7
4-COOH-Bi_2WO_6	683	18	3.12	54.5	79.3
4-propionic	683	---	---	---	---
4-propionic-$NiWO_4$	683	9	3.13	26.9	32.2
4-propionic-Bi_2WO_6	683	38	3.12	38.7	78.9
4-acetic	684	---	---	---	---
4-acetic-$NiWO_4$	684	17	3.11	24.8	28.6
4-acetic-Bi_2WO_6	684	42	3.12	38.5	50.9
5-propionic	678	---	---	---	---
5-propionic-$CoWO_4$	679	26	1.5	22.5	24.4
5-acrylic	678	---	---	---	---
5-acrylic-$CoWO_4$	680	24	1.61	20.3	21.0

5-acetic	680	---	---	---	---
5-acetic-$CoWO_4$	683	20	1.55	19.8	24.3
5-acetic-Ag-Fe_3O_4	680	5	2.34	44.7	72.4
5-acetic-Ag_2WO_4	680	7	2.22	18.2	20.2
5-acetic-$NiWO_4$	680	23	3.12	23.6	26.5
6-COOH	688	---	---	---	---
6-COOH-$CoWO_4$	688	9	1.67	18.5	21.3
7-propionic	675	---	---		---
7-propionic-$CoWO_4$	675	11	1.78	18.8	20.7
7-acrylic	675	---	---	---	---
7-acrylic-$CoWO_4$	675	12	1.72	22.7	25.8
8-propionic	680	---	---	---	---
8-propionic-Ag_2WO_4	680	13	1.58	35.5	68.2
8-acetic	685	---	---	---	---
8-acetic-Ag_2WO_4	685	9	1.57	26.1	50.2
8-acrylic	680	---	---	---	---
8-acrylic-Ag_2WO_4	680	15	1.57	35.8	68.3
$CoWO_4$	487/587	---	2.30	9.7	11.7
Ag_2WO_4	429	---	2.47	18.3	18.2
Ag-Fe_3O_4	418	---	2.53	24.4	68.4
$NiWO_4$	480	---	3.25	20.2	22.9
Bi_2WO_4	480	---	3.51	38.9	44.2
CdTe/ZnSe/ZnO	480	---	2.83	4.7	5.3

Figure 3.4: shows the absorption spectra of $CoWO_4$ nanoparticles with two typical absorption peaks at 487 nm and 587 nm in 2% DMSO [**156**]. The absorption spectrum of the Ag_2WO_4 NPs extends from UV to the visible region,

Figure 3.4. The UV–vis absorption spectrum of Ag_2WO_4 NPs showed the maximum absorption at 429 nm which can be attributed to the surface plasmon resonance (SPR) band from silver. **Figure 3.4** shows the SPR band of the Ag in the Ag-Fe_3O_4 NPs observed at 418 nm in 2% DMSO. Broad electronic absorption bands are observed at 480 nm for $NiWO_4$ and Bi_2WO_6, **Figure 3.4**, Bi_2WO_6 used as an example. The studied nanoparticles and nanoconjugates are typical for their counterparts in the literature, although some redshift is observed [**157**].

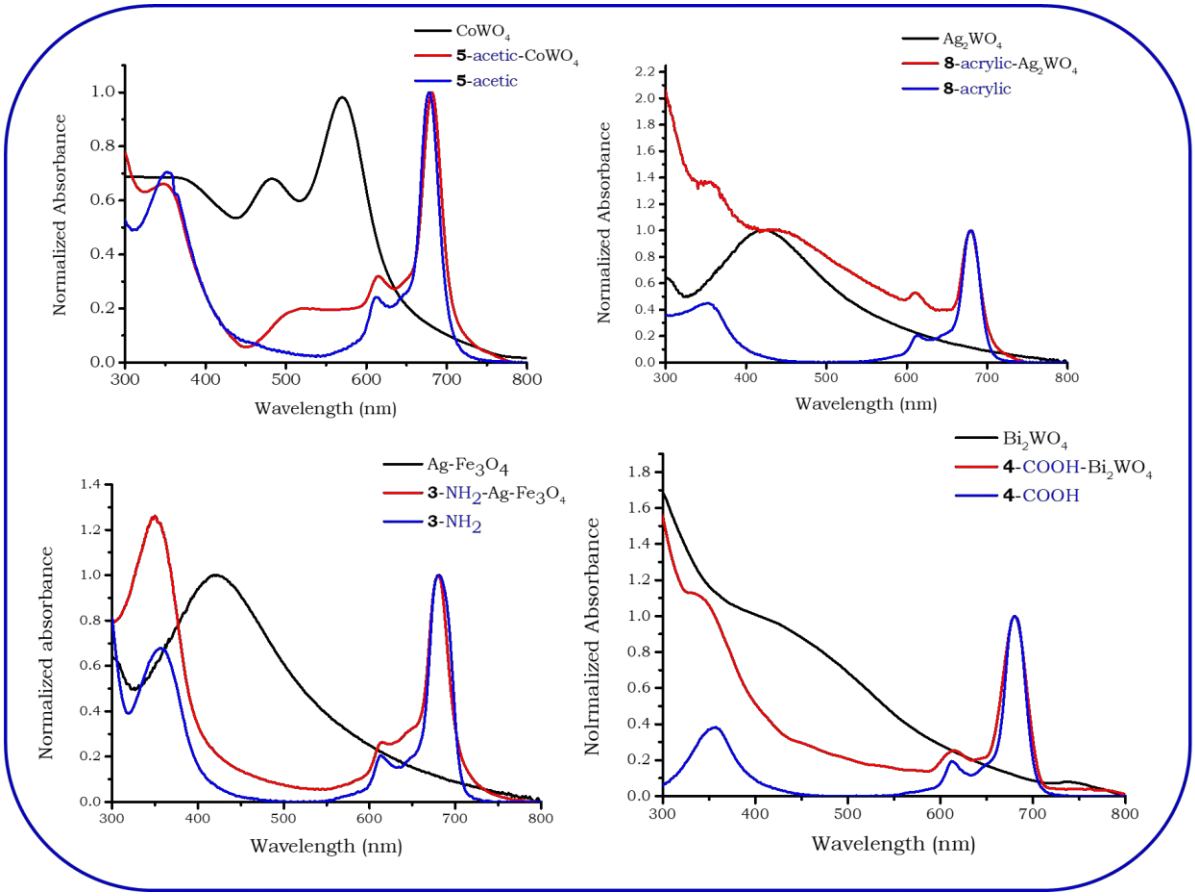

***Figure 3.4**: Normalized UV-visible spectra of nanoparticles, and nanoconjugates in DMSO.*

There are no significant shifts in the Q-band of Pc complexes following conjugation, except the broadening observed in the conjugate due to the

presence of NPs (**Figure 3.4, Table 3.1**). Also, the observed enhancement in absorbance of the Q-band near 630 nm indicates aggregation in the conjugates. Additionally, there is a noticeable increase in intensity in the B-band region for the conjugates compared to Pc complexes alone due to absorption by the nanoparticles.

The loading of complexes onto nanoparticles was assessed using UV-vis spectra, as described in the literature [**158**] as follows: Pc and conjugates of the same mass are separately weighed and dissolved in equal amounts of solvent. Their Q-band absorbance intensities of MPcs in the conjugate are then compared to those of the Pcs alone. As seen in **Table 3.1**, there are loading variations between conjugates. The loading is generally high for Bi_2WO_6 with the highest, DLS/XRD sizes (to be discussed below)

Since the NPs employed in this work are a crystalline semiconductors, the Tauc Equation 3.1 was used to determine their band gap [**159**].

$$(\alpha h\nu)^{1/n} = k(h\nu - E_g) \qquad \text{---------- 3.1}$$

where E_g, h, α, ν, and k, are the band gap, Planck's constant, the absorption coefficient, the photon's frequency, and a proportionality constant, respectively. The value of n in the exponent shows the nature of the electronic transition and the value of n in the exponent is n = 1/2 for direct allowed transitions [**160**]. Since there are fewer phonons at low temperatures and fewer photons are present, it is less likely that a photons can be simultaneously absorbed to produce an indirect transition [**160**]. The optical band gap of the material was obtained using the linear region extrapolated to

the x-axis intercept [**159**]. The estimated band gap for NPs, and conjugates is presented in **Figure 3.5**, **Table 3.1** (using $CoWO_4$ and **5**-propionic-$CoWO_4$ as examples). The energy band gaps for the NPs decreased in the nanoconjugates. It has been reported that a narrower energy band gap < 3.0 eV results in the absorption of light in the visible part of the spectrum which is good for photocatalysis as it enables the excitation of a notable number of electrons into the conduction band [**161**]. The results obtained are in line with reports found in literature [**161-166**].

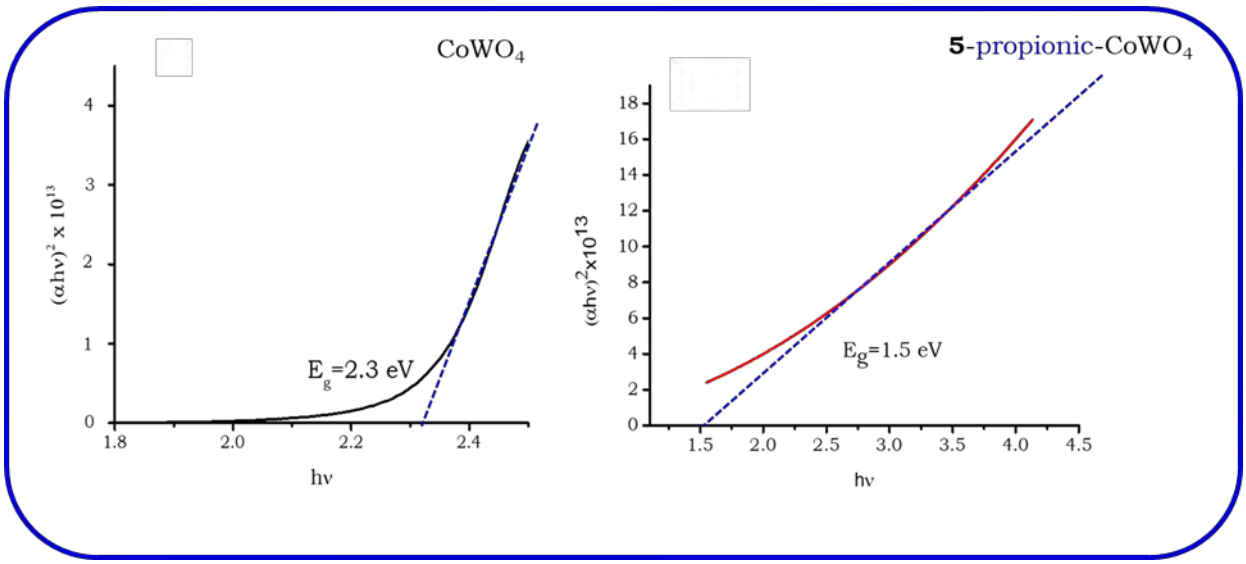

***Figure 3.5**: Direct energy band gaps determination from the analysis of the absorption spectra of NPs and conjugates (using $CoWO_4$ and **5**-propionic-$CoWO_4$ as examples).*

3.2.2 FT-IR spectra

All Pc complexes show the presence of Ar-O-Ar in the range 1224-1230 cm^{-1}. In the FT-IR of the phthalonitriles, the characteristic nitrile peaks were observed at 2230 cm^{-1} for ***m*** as an example (**Figure 3.6A**). The absence of the

nitrile peak from phthalonitriles in the MPcs spectrum confirmed successful formation of the Pc complexes (**Figure 3.6A**, using **6**-COOH as an example).

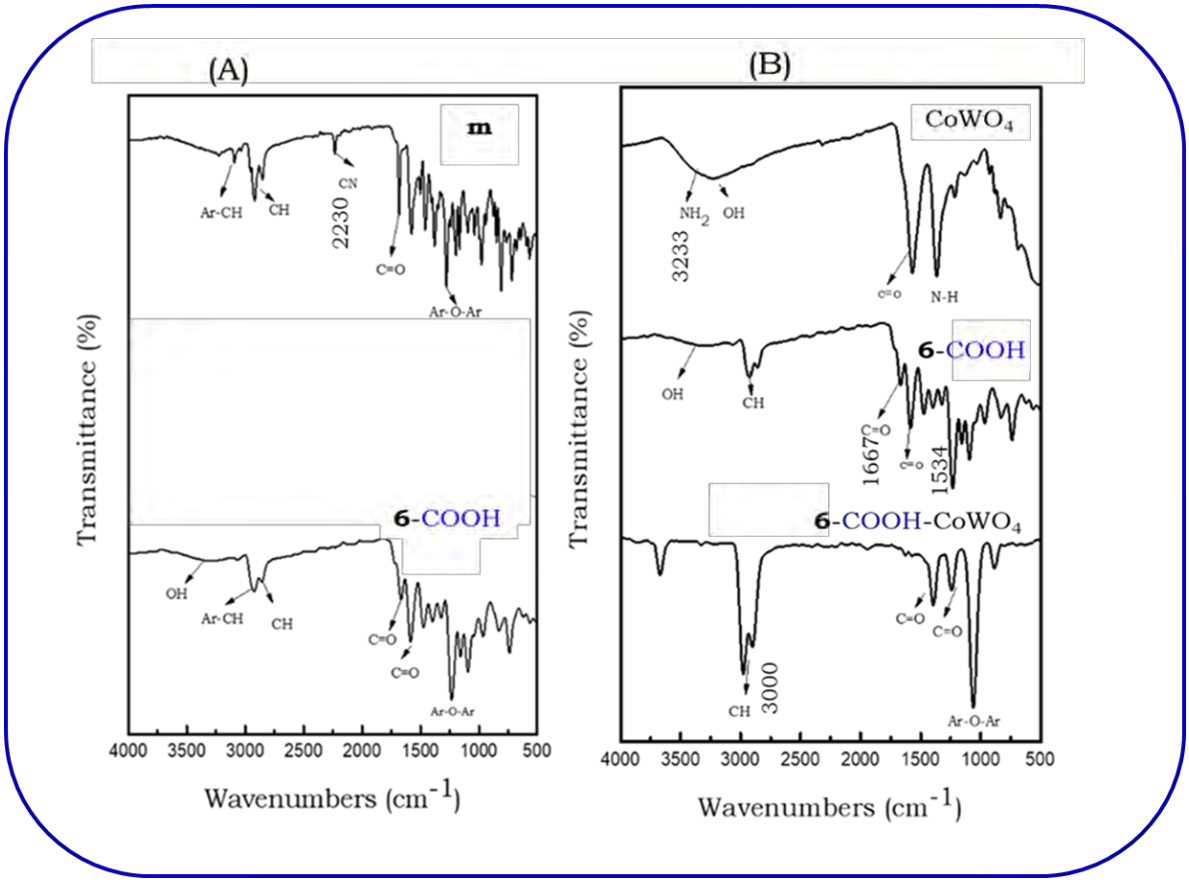

***Figure 3.6**: FT-IR spectra of (A) phthalonitrile **m**, **6**-COOH, (B) $CoWO_4$, **6**-COOH, and **6**-COOH–$CoWO_4$.*

The carbonyl stretch for Pc complexes appears between 1567 and 1723 cm^{-1} with complex **6**-COOH spectrum showing two ν (C=O) vibrational bands at 1667 cm^{-1} and 1534 cm^{-1} attributed to the ketone and the carboxylic acid functional groups, respectively (**Figure 3.6**). An intense (CH) stretch at 3000 cm^{-1} is observed for **6**-COOH-$CoWO_4$ conjugate due to overlap of the alkyl groups from GSH of $CoWO_4$ NPs and **6**-COOH, (**Figure 3.6B**. The spectra of the $CoWO_4$ and Pc complexes alone are compared to confirm the covalent linkage involved in the formation of the conjugates. The NH_2 band at 3233

cm^{-1} in the $CoWO_4$ spectrum is reduced in the conjugates, confirming the amide bond formation between NPs and Pc complexes (**6**-COOH -$CoWO_4$). Except for **3**-propionic-Ag-Fe_3O_4, **3**-COOH-Ag-Fe_3O_4, and **5**-acetic-Ag-Fe_3O_4 with ester bonds, similar results were obtained for the rest of the conjugates. The functional groups, broad OH band of **3**-propionic and **3**-COOH appeared at 3062 cm^{-1} and 3057 cm^{-1}, respectively (**Figure 3.7**, using **3**-propionic as an example).

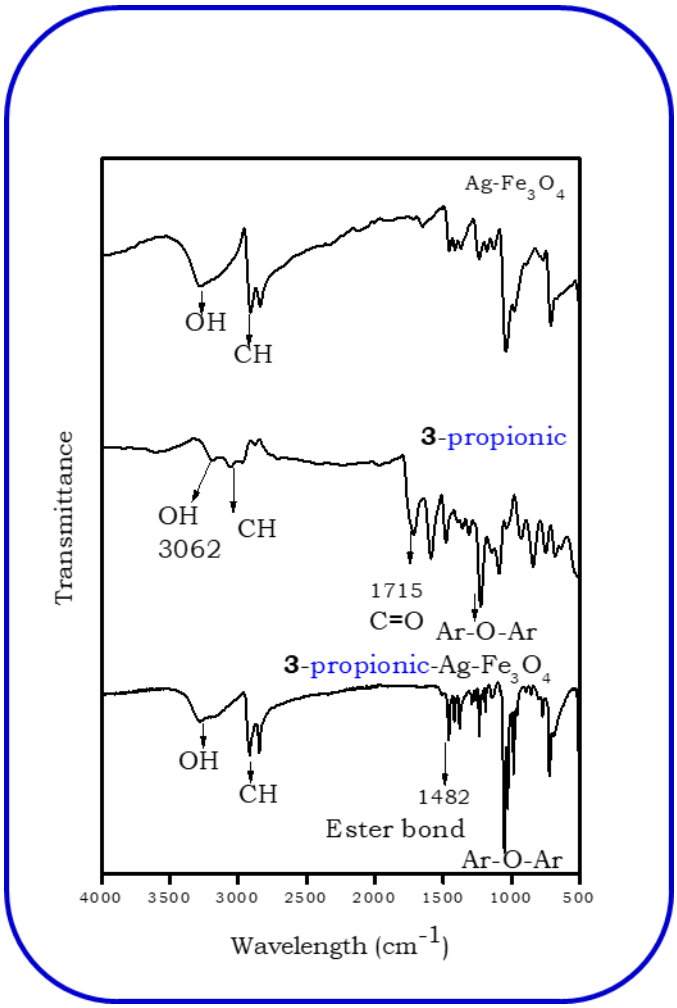

Figure 3.7: *FT-IR showing covalent linkage of Pcs to NPs via ester bond.*

The carbonyl (C=O) of the carboxylic acid of **3**-propionic appeared at 1715 cm^{-1} and shifted to 1482 cm^{-1} for **3**-propionic. Also following the conjugation of complex **3**-propionic-Ag-Fe_3O_4 to Ag-Fe_3O_4, the OH group of Ag-Fe_3O_4 was reduced in intensity, confirming successful covalent linkage via ester bond at 1482 cm^{-1}.

3.2.3 X-ray Diffraction (XRD) Patterns

XRD studies are conducted to investigate the crystallinity of the nanoparticles and nanoconjugate, **Figure 3.8**.

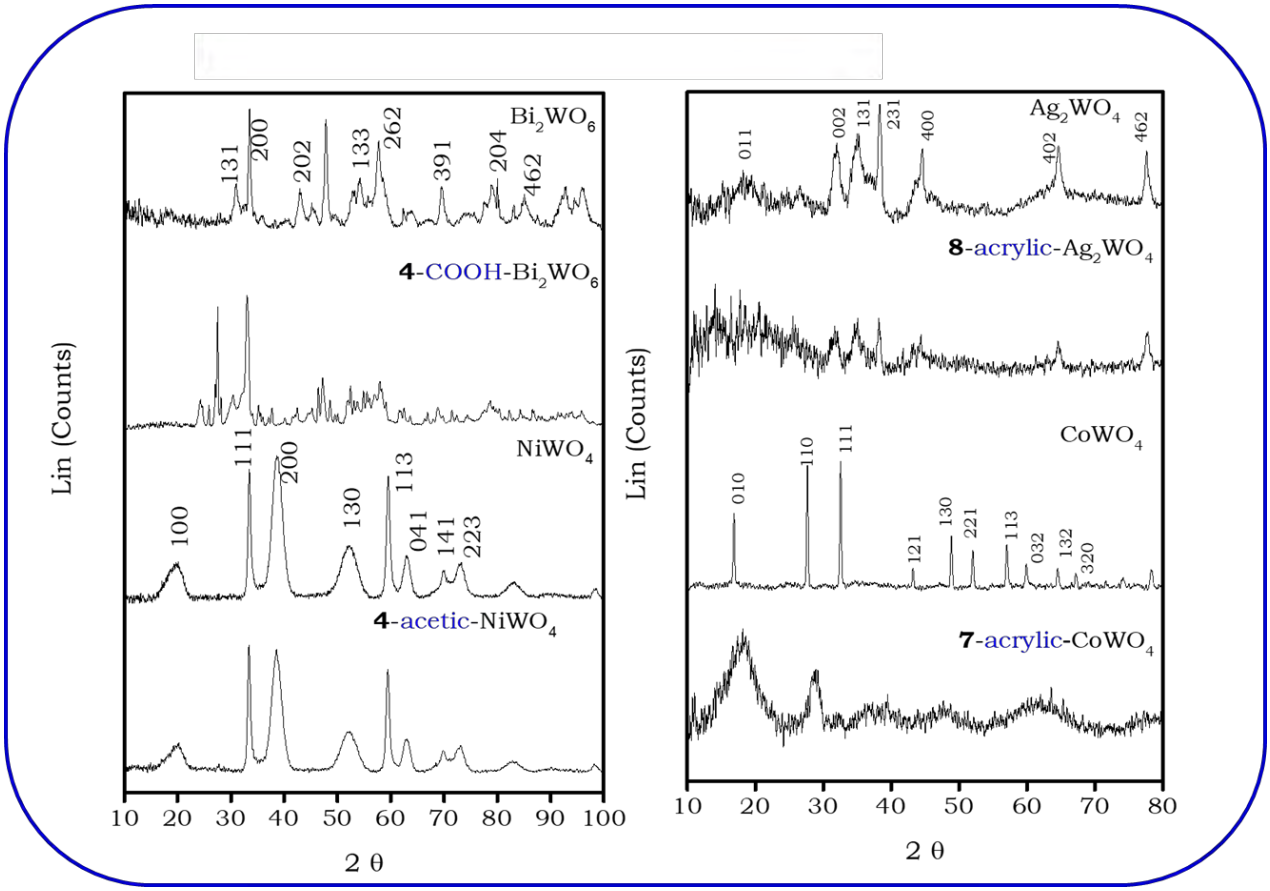

***Figure 3.8**: XRD diffraction patterns for the nanoparticles and the conjugates.*

Diffraction peaks of Bi_2WO_6 showed orthorhombic crystalline phase in agreement with (JCPDS card number: 79-2381) [**166**], with major peaks at 2θ = 28.9°, 33.5°, 42.9°, 54.2°, 57.5°, 69.9°, 79.4°, and 87.4° corresponding to crystal planes 131, 200, 202, 133, 262, 391, 204, and 462, respectively, **Figure 3.8**. On the other hand, diffraction peaks for $NiWO_4$ perfectly indexed to the hexagonal structure of nickel observed at 19.2 °, 30.9°, 39.1°, 52.3°, 62.3°, 68.9°, 72.3°, and 79.3° in accordance to 100, 111, 200, 130, 113, 041, 141 and 223 (JCPDS no. 15-0755) planes [**167**], respectively, **Figure 3.8**. The peaks of $NiWO_4$ and Bi_2WO_6 can be found in the XRD patterns of conjugates, **Figure 3.8** (using **4**-COOH- Bi_2WO_6 and **4**-acetic-$NiWO_4$ as examples).

The $CoWO_4$ NPs exhibit peaks that are assigned in accordance to the monoclinic wolframite structure JCPDS card 00-015-0867 for $CoWO_4$. XRD demonstrated peaks at 2θ = 16°, 28°, 33°, 43°, 48°, 52°, 57°, 60°, 64°, 67° corresponding to indices at 010, 110, 111, 121, 130, 221, 113, 032, 132, and 320, respectively. The nanoparticles are pure since no additional peaks were recorded and the peaks are narrow which confirmed the crystalline nature of NPs. A noticeable broadening of the spectrum was observed in the conjugates due to the interaction between Pc and the NPs. Ag_2WO_4 demonstrated peaks indexed as an orthorhombic structure phase at 011, 002, 131, 231, 400, 402, and 462 at 2θ = 18˚, 28˚, 32˚, 35˚, 38˚, 45˚, 65˚, respectively. This outcome corresponds to the card number (JCPDS No 00-034-0061). The Ag_2WO_4 diffraction peaks were mainly sharp and well-defined, showing a high degree of purity, structural order, and crystallinity. Due to the presence of the Pc complex which has low crystallinity in the nanoconjugates, a broad peak

emerged between 10 and 20˚. Pcs are known to show broad XRD peaks due to their amorphous nature [**168**], as shown in **Figure 3.8**. There are no shifts in any of the Ag_2WO_4 characteristic peaks following conjugation to the Pcs, indicating that the addition of Pc complexes did not affect the crystal phase of Ag_2WO_4 as shown in **Figure 3.8**.

The Debye-Scherrer equation was used to calculate crystallite diameter

Debye-Scherrer equation (Equation 1) [**169**].

$$d = \frac{k\lambda}{\beta Cos\theta} \qquad 3.2$$

where λ is the wavelength of the X-ray source (1.5405 Å), k is an empirical constant equal to 0.9, β is the full width at half maximum of the diffraction peak and θ is the angular position.

Particle sizes of nanocatalysts were calculated to be 20.2 nm for $NiWO_4$, 38.9 nm for Bi_2WO_6, 18.3 nm for Ag_2WO_4, 24.4 nm for Ag-Fe_3O_4, and 9.7 nm for $CoWO_4$, **Table 3.1**. The obtained sizes for the nanoconjugates increased and are recorded in **Table 3.1**. The increase is attributed to the aggregation of Pcs onto the NPs [**152**]. Ag-Fe_3O_4 and Bi_2WO_6 and their conjugates gave the largest sizes.

3.2.4 Energy-dispersive X-ray (EDX) spectroscopy

The energy-dispersive X-ray spectroscopy (EDX) analysis was performed to determine the elemental composition of all prepared NPs and nanoconjugates. **Figure 3.9** presents EDX spectra of the nanoparticles and the conjugates (using Ag_2WO_4, $CoWO_4$, **8**-acrylic-Ag_2WO_4, and **2**-propionic-$CoWO_4$ as examples). The EDX analysis confirmed the successful composition of Ag_2WO_4 nanoparticles with expected elements. The spectrum for GSH-capped Ag_2WO_4 nanoparticle alone shows the presence of carbon, sulfur, oxygen, nitrogen, silver, and tungsten. Sulfur, carbon, oxygen, nitrogen, cobalt, and tungsten are observed in the case of $CoWO_4$. This is a good argument to confirm the pure NPs ($CoWO_4$ and Ag_2WO_4 are used as examples). In the case of the conjugates, the zinc atom observed on the spectra, confirms the presence of the Pcs in the conjugates. These findings indicate that Pc complexes are present in nanocomposites and confirmed the purity of the nanoconjugates.

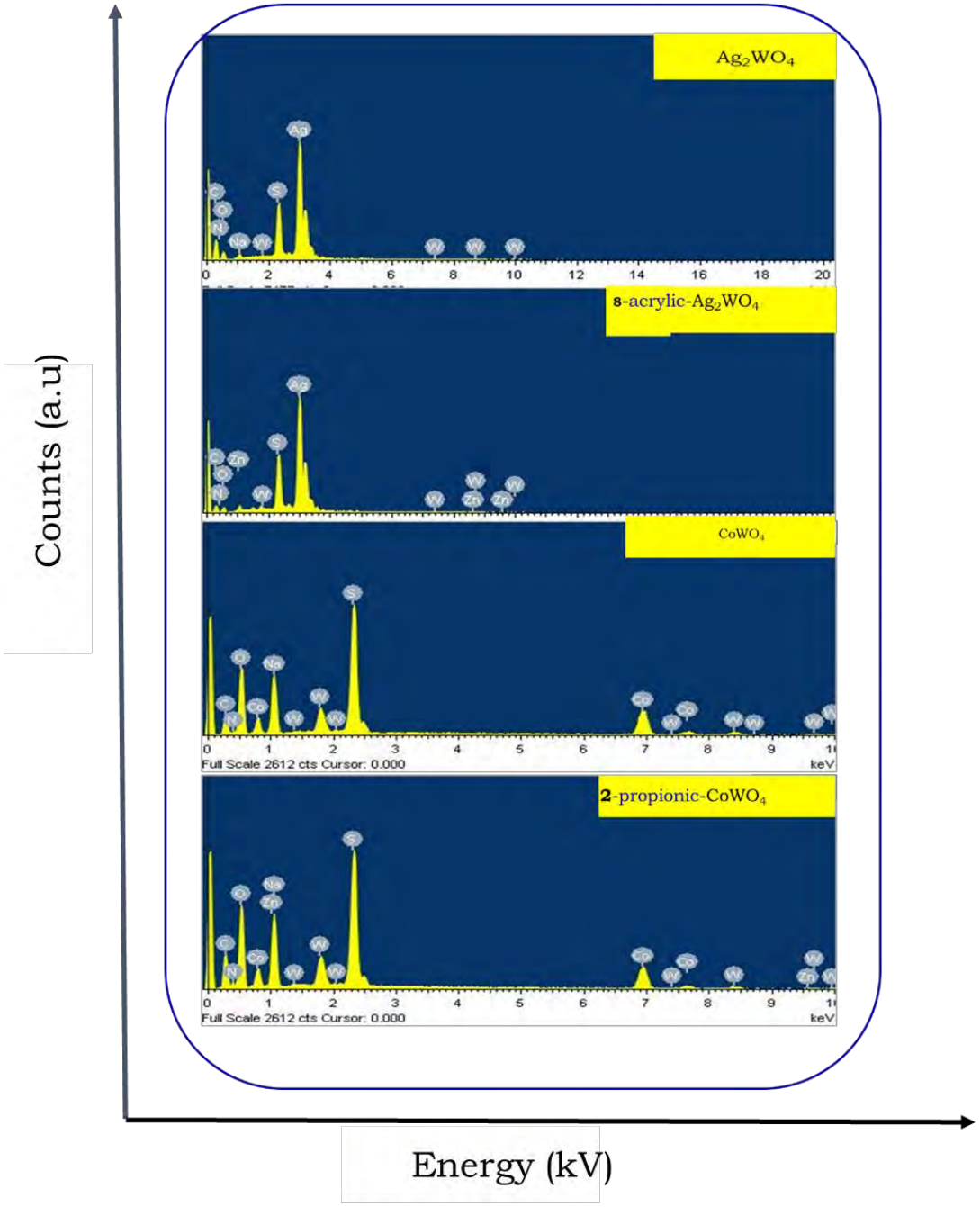

***Figure 3.9**: EDX for the nanoparticles and the nanoconjugates ($CoWO_4$, Ag_2WO_4, **2**-propionic, and **8**-acrylic used examples).*

3.2.5 Atomic Force Microscopy (AFM)

The successful syntheses of nanoparticles and nanoconjugates were confirmed using atomic force microscopy (AFM). AFM is a sensitive surface technique that can reveal differences in surface topology. AFM imaging of the nanoparticles alone shows aggregates of particles with an average section height of 60 nm and surface roughness of 32.2 nm (**Figure 3.10A (i and ii)** $NiWO_4$ used as an example). On the modification of the nanoparticles with the phthalocyanine (**4**-COOH-$NiWO_4$ used as an example), a clear increase in the section height to about 30 nm can be seen (**Figure 3.10B** (**i and ii**)). The surface roughness of the latter (**4**-COOH-$NiWO_4$) was calculated to be 20.4 nm. The decrease in the surface roughness is indicative of a modified surface which presents a more uniform surface. The changes in the cross-sectional height, as well as the surface roughness of NPs, imply the possibly successful conjugation and hence the formation of the respective conjugates.

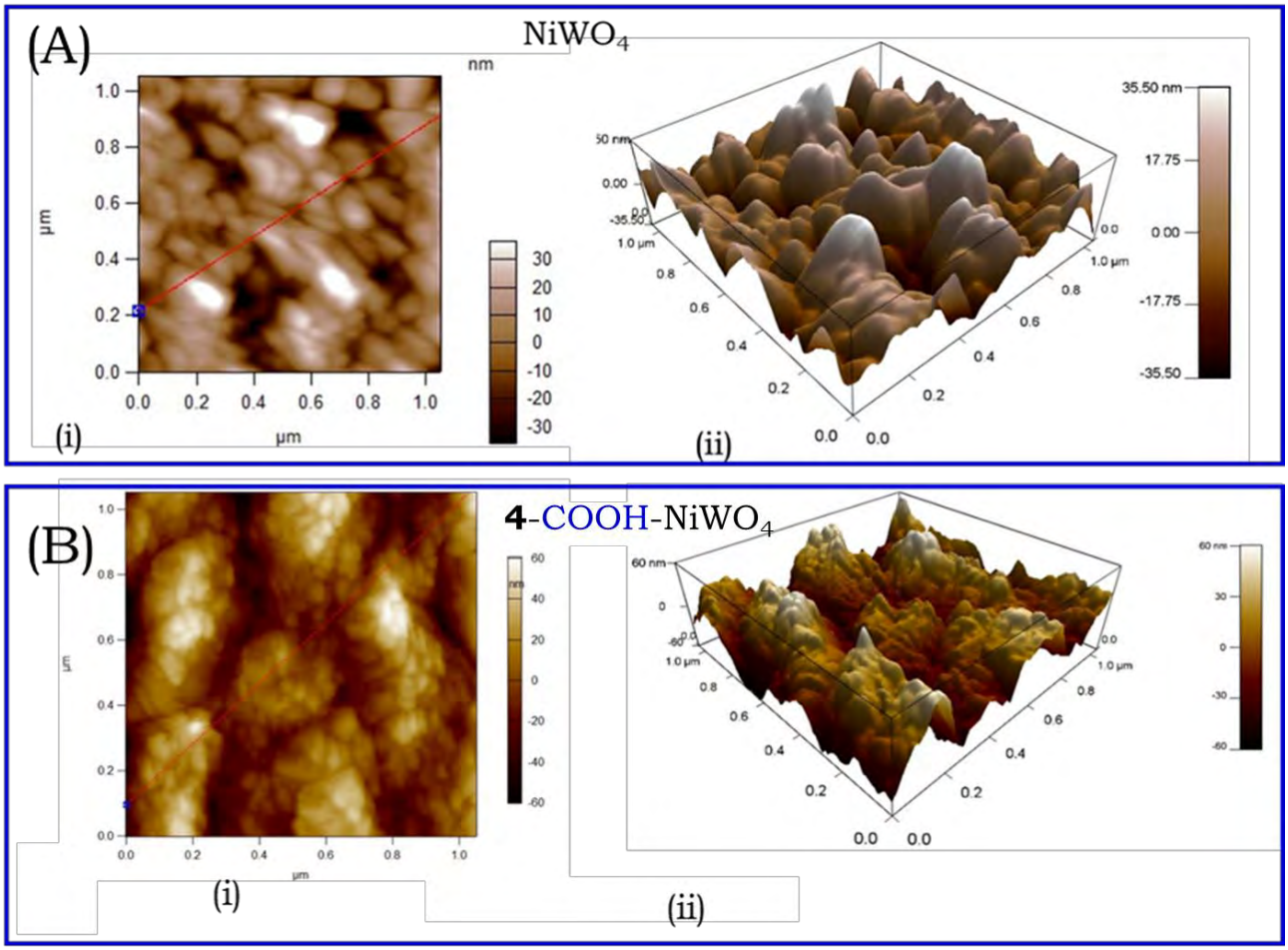

***Figuire 3.10**: AFM images AFM images (A) $NiWO_4$ and (B) **4**-COOH-$NiWO_4$. (i) 2D surface topology and (ii) 3D surface topology.*

3.2.6 Transmission Electron Microscopy (TEM)

Transmission electron microscopy (TEM) was used for morphological analysis of the conjugates and nanoparticles. The distribution of the NPs in the absence and presence of the Pc complexes was estimated using TEM imaging. TEM images indicated that metal tungstate nanoparticles consist of irregular sphere-like particles, shown in **Figure 3.11** (using Ag_2WO_4 and **8**-acetic-Ag-Fe_3O_4 as examples).

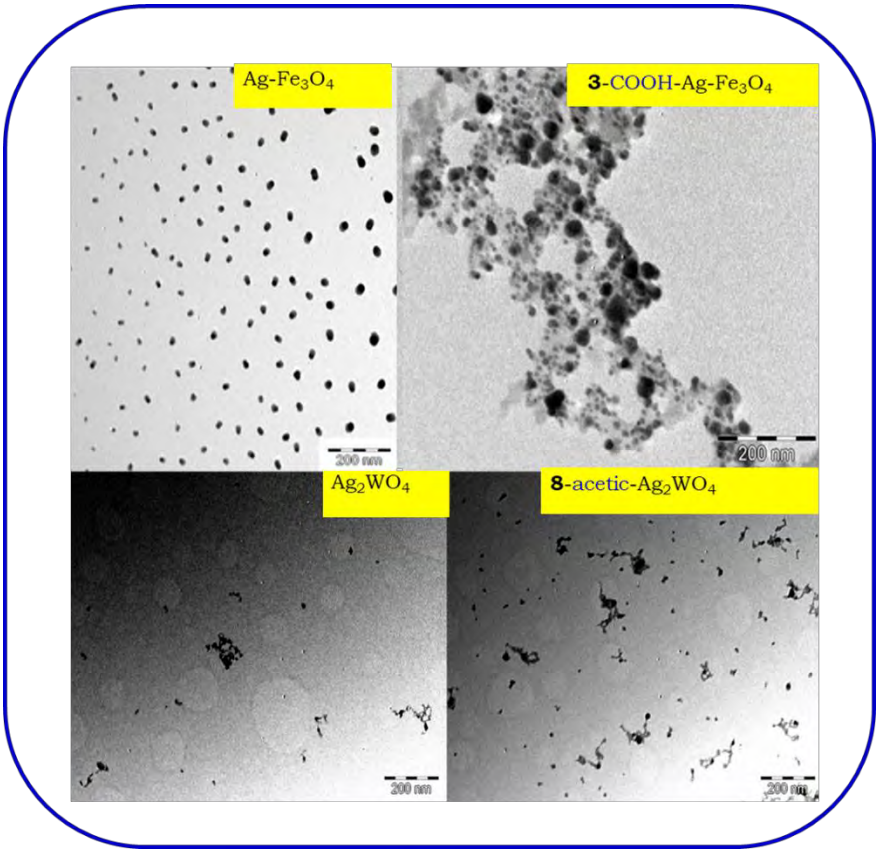

***Figure 3.11**: TEM images for the nanoparticles and the conjugates.*

The particle size increased for nanoconjugates **Figure 3.11**. The agglomerated image of the nanoconjugates suggests that Ag_2WO_4 and Pc complexes have been successfully combined. TEM images for Ag-Fe_3O_4 nanoparticles showed fairly spherical morphology and monodispersed particles. On linking Ag-Fe_3O_4 to Pc complexes, a significant increase in the sizes of NPs is observed, **Figure 3.11**. The increase in sizes of NPs in the presence of phthalocyanine is known and result from the aggregation of Pcs on the adjacent NPs [**152**].

3.2.7 Dynamic Light Scattering (DLS)

DLS was conducted to study the sizes of the conjugates and the nanoparticles in the solution. The DLS plots are shown in **Figure 3.12** (using Ag-Fe_3O_4, **3**-COOH-Ag-Fe_3O_4, $CoWO_4$, and **7**-acrylic-$CoWO_4$ as examples) and the hydrodynamic sizes obtained are listed in **Table 3.1**. The sizes increased in the conjugates. The conjugates exhibited a proclivity for rapid aggregation with sizes ranging between 8.9 to 91.3 nm. The increase is due to aggregation which is caused by π-π interactions of Pcs on the surface of NPs [**152**].

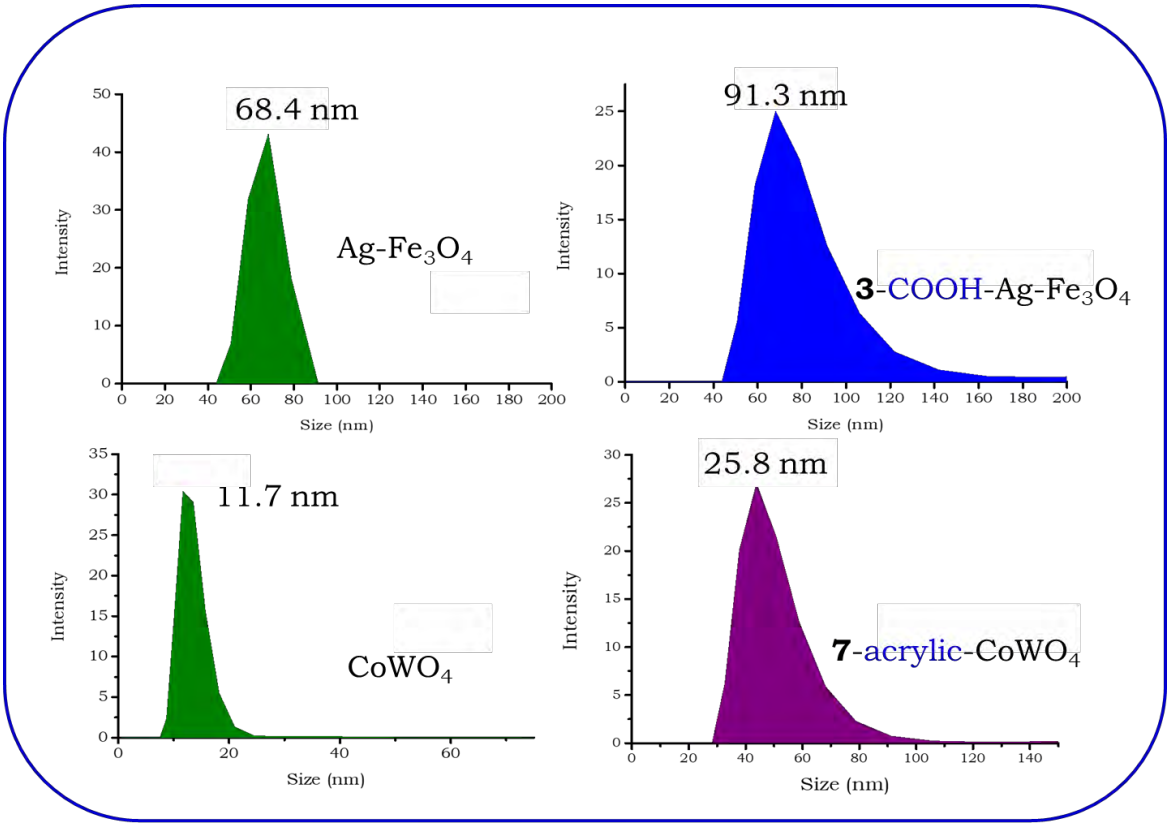

***Figure 3.12**: DLS of for the nanoparticles and the conjugates (using Ag-Fe_3O_4, **3**-COOH-Ag-Fe_3O_4, $CoWO_4$ and **7**-acrylic-$CoWO_4$ as examples).*

3.2.8 Thermal analysis

Figure 3.13 shows the TGA (thermogravimetric analysis) and DSC (differential scanning calorimetry) thermograms of nanoparticles (using $NiWO_4$ and **4**-propionic-$NiWO_4$, Bi_2WO_6 and **4**-acetic-Bi_2WO_6 as examples). The first step in TGA indicates that NPs lose weight at less than 200°C due to dehydration, **Figure 3.13A** [**170**]. In the second step, TGA reveals a sharp decrease in the mass of NPs at 200 to 260°C due to the decomposition of end groups in the GSH capping the NPs. It has been reported before that small molecules are lost around this temperature [**170**]. The nanoconjugates maintained the thermal properties of NPs from 50 to 550°C. However, there is a decrease in the mass of the conjugates at 550 to 600°C, followed by a sharp decrease from 900 to 100°C. The $NiWO_4$ gave no evidence of weight loss from 600 to 1000°C. The sharp exothermic peak at 270°C in DSC (**Figure 3.13B**) corresponds to the melting points of the bismuth [**171**]. The second exothermic peak is attributed to the combustion of the organic material, in comparison with the literature [**172**]. In the case of Bi_2WO_6, rapid volatilization of gases trapped in the material can cause observed sharp peaks. Sharp peaks may also indicate instrumental interference [**173**].

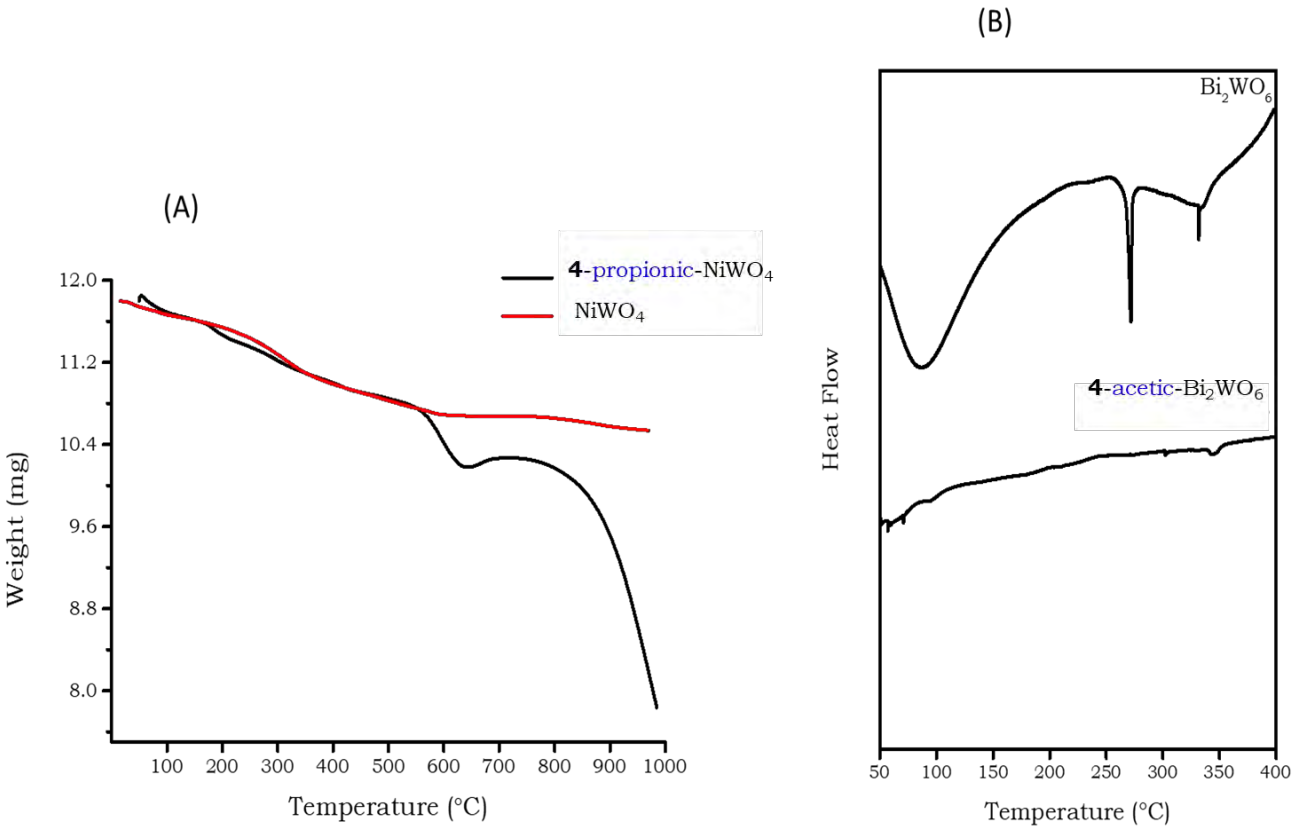

***Figure 3.11**: (A) TGA thermograms and (B) DSC for the nanoparticles and the conjugates, using $NiWO_4$ and **4**-propionic-$NiWO_4$ (A), Bi_2WO_6 and **4**-acetic-Bi_2WO_6 (B) as examples.*

3.3 Conclusion

Seventeen new asymmetric phthalocyanine complexes containing zinc(II) as the metal ion in the center and different types of substituents in the ring were designed and synthesized. Data and spectra obtained using versatile characterization techniques confirm the structures of successfully synthesized proposed phthalocyanine complexes. In addition, data and spectra obtained using characterization techniques also confirm that zinc(II) phthalocyanines are covalently bound to functionalized nanoparticles.

Chapter 4

This chapter covers the photochemical and photophysical properties of phthalocyanines and their conjugates with various NPs.

Photophysichochemical properties of MPcs, NPs, and conjugates

The photophysical and photochemical properties of the synthesized Pc complexes **1**-**8** are discussed here. Comparisons are made concerning the presence of various substituents and their interactions with NPs in the conjugates. The predominant aim of this work is to enhance intersystem crossing to the triplet state, hence improving the production of singlet oxygen. It is expected that the intersystem crossing to the triplet state will be increased due to higher molecular dipole moments arising from the lack of symmetry of the selected molecules [**174**]. In addition, the complexes are linked to nanoparticles containing heavy atoms. The spin-orbit interaction arising from the heavy atom effect in the conjugates will deactivate the fluorescence behaviour of the complexes, resulting in a high singlet oxygen quantum yield [**175**].

4.1 Fluorescence quantum yields (Φ_F) and lifetimes (τ_F)

Table 4.1 list the photophysicochemical parameters of all complexes and conjugates. The Φ_F are calculated using Equation 1.1 using ZnPc standard as discussed in **Chapter 1**. **Figure 4.1A** shows fluorescence spectra, the excitation spectra are the same as absorption spectra and both are mirror images of the emission spectra, showing that the molecule emitting is the same as the one absorbing. The $\mathbf{\Phi_F}$ values range between 0.07 and 0.20 for the Pc complexes alone. The fluorinated complexes, **7**-acrylic and **7**-propionic exhibit a lower $\mathbf{\Phi_F}$ value of 0.07. Electron-withdrawing groups such as fluorine are known to reduce fluorescence [**176**]. The Pc complexes with halogens generally exhibit high intersystem crossing (ISC) resulting in small

fluorescence quantum yields [177]. The Φ_F values decreased in the presence of NPs as expected, due to the heavy atom effect of the nanoparticles. The fluorescence lifetimes (τ_F) for the complexes and conjugates were determined using time-correlated single photon counting (TCSPC) as illustrated in **Figure 4.1B** (using **1**-ethanoic-CdTe/ZnSe/ZnO as an example). The τ_F is found to range from 1.8 to 3.2 ns for Pcs alone. The τ_F values should be high, where Φ_F values are high, in **Table 4.1**. The lifetimes are shorter in the conjugates due to higher intersystem crossing which diminishes the fluorescence lifetime, corresponding to the decrease in fluorescence quantum yields.

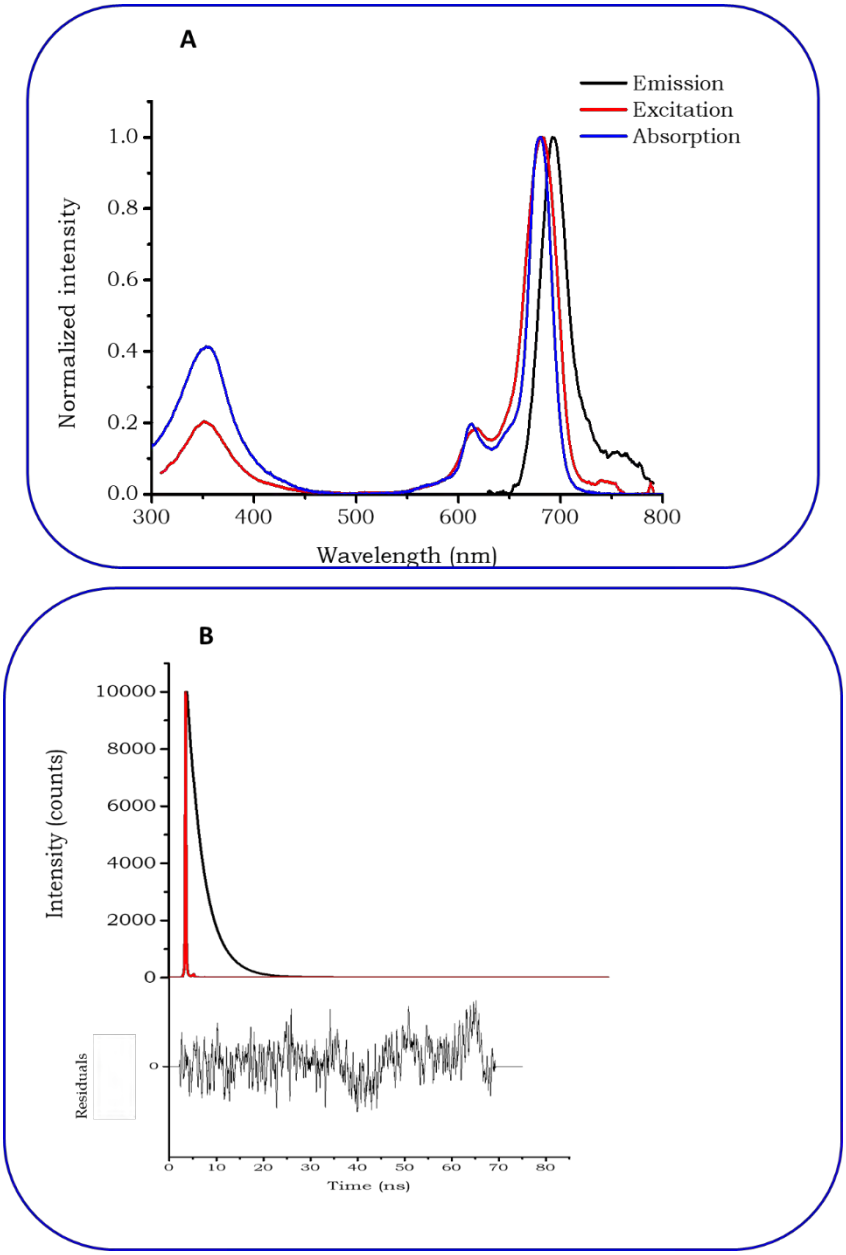

***Figure 4.1**: (A) Absorption, excitation and emission spectra of complexes in DMSO (using **3**-COOH as an example). (B) Fluorescence decay curve for complex in DMSO (using **1**-ethanoic-CdTe/ZnSe/ZnO as an example).*

Table 4.1: Photophysicochemical parameters of **1-8** and their conjugates with NPs in DMSO. 'a' values in brackets are when exciting where QDs absorb. 'b' values in brackets are in water for selected molecules.

Complexes	Φ_F[a]	τ_F (ns)[a]	Φ_T	τ_T (µs)	Φ_Δ[b]	**FRET *eff***
1-ethanoic	0.15	2.7	0.51	184	--	--
1-ethanoic-CdTe/ZnSe/ZnO	0.09 (>0.01)	2.3 (0.73)	0.57	187	--	74.5
2-propionic	0.19	2.9	0.46	208	0.31 (0.14)	--
2-propionic-CdTe/ZnSe/ZnO	0.11 (0.03)	2.4 (>0.01)	0.59	244	--	99.9
2-propionic-$CoWO_4$	0.19	2.90	0.46	208	0.61 (0.29)	--
3-propionic	0.10	1.8	0.64	150	0.44	--
3-propionic-Ag-Fe_3O_4	0.05	2.9	0.81	233	0.48	--
3-COOH	0.10	2.7	0.62	171	0.43	--
3-COOH-Ag-Fe_3O_4	0.06	2.9	0.75	316	0.48	--
3-NH_2	0.18	2.8	0.65	171	0.38	--
3-NH_2-Ag-Fe_3O_4	0.14	3.1	0.74	206	0.42	--
4-COOH	0.14	2.9	0.78	244	0.59	--
4-COOH-$NiWO_4$	0.04	2.8	0.81	274	0.63	--
4-COOH-$CoWO_4$	0.03	2.7	0.79	255	0.68	--
4-COOH-Bi_2WO_6	0.03	2.7	0.83	288	0.64	--
4-propionic	0.14	3.0	0.74	267	0.61	--
4-propionic-$NiWO_4$	0.08	2.4	0.78	278	0.65	--
4-propionic-Bi_2WO_6	0.03	2.4	0.78	292	0.65	--
4-acetic	0.16	3.2	0.68	234	0.54	--
4-acetic-$NiWO_4$	0.12	2.9	0.74	278	0.59	--

4-acetic-Bi_2WO_6	0.12	2.7	0.73	278	0.60	--
5-propionic	0.17	2.9	0.76	128	0.75 (0.22)	--
5-propionic-$CoWO_4$	0.03	2.2	0.79	237	0.77 (0.31)	--
5-acrylic	0.16	2.8	0.74	227	0.72 (0.19)	--
5-acrylic-$CoWO_4$	0.04	2.5	0.80	347	0.75 (0.28)	--
5-acetic	0.14	2.7	0.79	285	0.69 (0.16)	--
5-acetic-$CoWO_4$	0.04	2.2	0.83	293	0.75 (0.29)	--
5-acetic-Ag-Fe_3O_4	0.08	2.5	0.84	295	0.75 (0.32)	--
5-acetic-Ag_2WO_4	0.09	2.3	0.87	234	0.74 (0.33)	--
5-acetic-$NiWO_4$	0.10	2.4	0.84	237	0.73 (0.27)	--
6-COOH	0.17	3.2	0.71	228	0.52 (0.21)	--
6-COOH-$CoWO_4$	0.13	2.9	0.79	253	0.63 (0.42)	--
7-acrylic	0.07	3.0	0.57	166	0.41 (0.22)	--
7-acrylic-$CoWO_4$	0.07	2.6	0.79	195	0.45 (0.26)	--
7-propionic	0.07	2.8	0.47	208	0.41	--

					(0.21)	
7-propionic-$CoWO_4$	0.07	2.6	0.71	210	0.46 (0.28)	--
8-propionic	0.16	2.9	0.64	224	0.50 (0.21)	--
8-propionic-Ag_2WO_4	0.12	2.0	0.68	266	0.57 (0.34)	--
8-acrylic	0.20	2.9	0.66	224	0.53 (0.21)	--
8-acrylic-Ag_2WO_4	0.11	2.2	0.74	227	0.59 (0.31)	--
8-acetic	0.17	3.0	0.76	183	0.55 (0.26)	--
8-acetic-Ag_2WO_4	0.14	2.1	0.86	236	0.58 (0.33)	
CdTe/ZnSe/ZnO	(0.24)	(2.9)	--	--	--	--

4.2 Förster resonance energy transfer (FRET)

The energy transfer typically occurs when the emission intensity of QDs decreases while the fluorescence emission of MPcs is induced. This stimulated emission can be attributed to a nonradioactive energy transfer from the donor (quantum dots) to the acceptor (MPcs). **Figure 4.2** illustrates the mechanism of FRET. The mechanism involves energy transfer from QDs (donor) to an MPc (acceptor) through long-range dipole-dipole interactions. Due to FRET and other processes that could deactivate the excited states of QDs, there are decreases in both τ_F and Φ_F values when exciting the region where QDs absorb, **Table 4.1**.

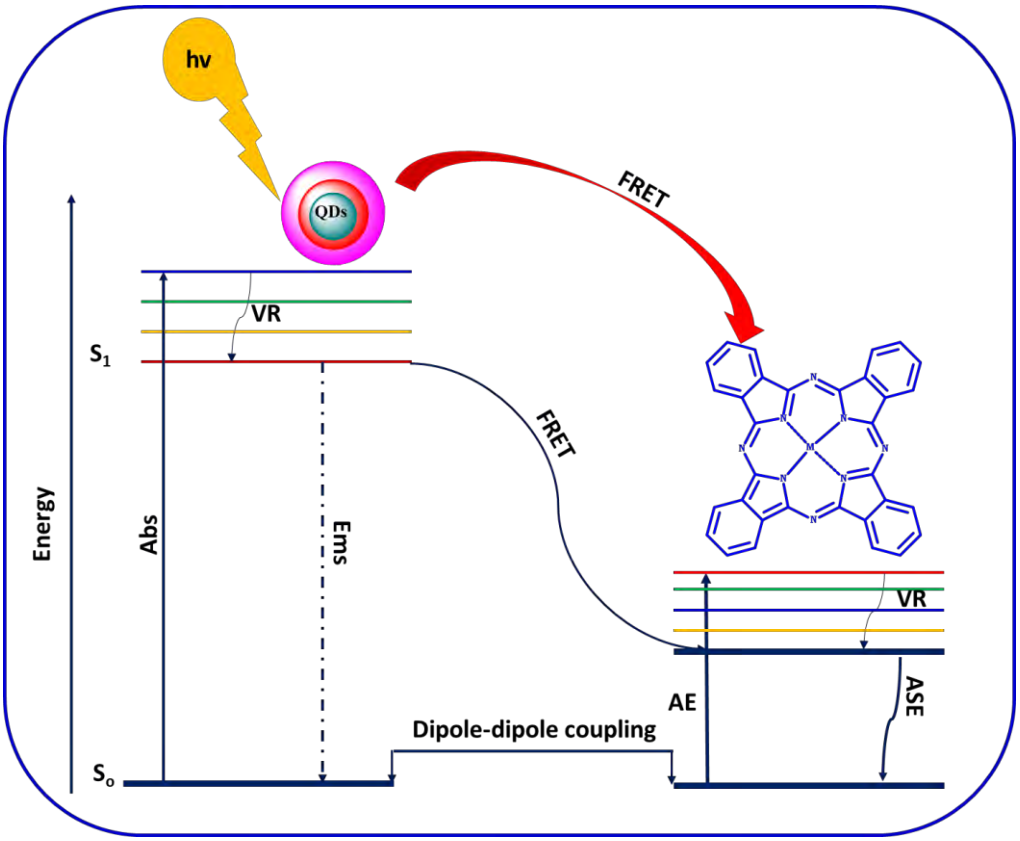

***Figure 4.2**: FRET diagram showing energy transfer from QDs to MPc. **Abs** = absorption, **Ems** = emission, **AE** = non-radioactive acceptor excitation, **ASE** = acceptor stimulated emission, **S_o** = singlet ground state, **S_1** = singlet excited states, **VR** = vibrational relaxation.*

A decrease in the fluorescence emission of QDs and stimulated emission of the MPcs is observed when exciting the conjugates where QDs absorb, **Figure 4.3A**. FRET depends on the spectral overlap between the absorption spectra of the MPcs and the emission spectrum of the QDs (**Figure. 4.3B**).

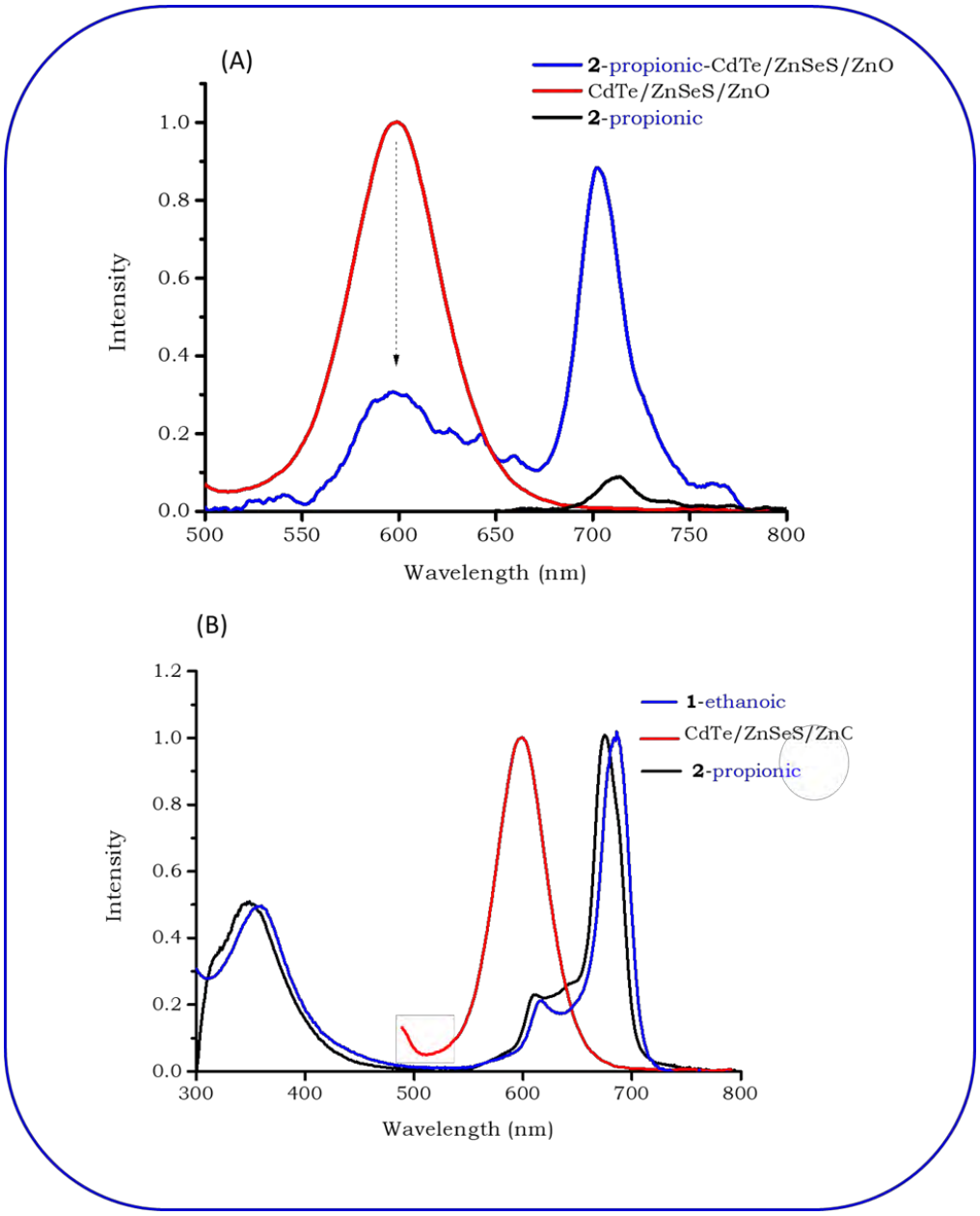

Figure. 4.3 *(A) Emission spectrum of QDs alone, of complex* ***2****-propionic and* ***2****-propionic-CdTe/ZnSe/ZnO (B) Emission spectrum of QDs alone, absorption spectra of complexes* ***2****-propionic and* ***1****-ethanoic. excitating wavelength = 430 nm (where QDs absorb) in DMSO.*

Using Equation 1.2 (detailed in **Chapter 1**), FRET efficiency (E*ff*) values are determined and listed in **Table 4.1**. The E*ff* value is higher for **2**-propionic compared to **1**-ethanoic due to a more blue-shifted Q band for the former, which overlaps better with the emission spectrum of QDs in **Figure 4.3B**.

4.3 Triplet quantum yields (Φ_F) and lifetimes (τ_F)

The transient absorption and triplet decay curves of complexes (using **8**-acetic as an example) are shown in **Figure 4.4A**. The spectra were measured in a degassed DMSO solution. The Pc complexes showed triplet–triplet absorption around 500 nm, **Figure 4.4A**. The triplet decay curves are shown in **Figure 4.4B** (using **8**-acetic and **8**-acetic-Ag_2WO_4 as examples) and the triplet quantum yield ($\mathbf{\Phi_T}$) values are listed in **Table 4.1**. Due to triplet-triplet recombination, the triplet decay curve followed second-order kinetics, which is typical of MPc complexes at high concentrations [**178**].

Complexes **7** had the lowest $\mathbf{\Phi_T}$ values even though halogenation should increase ISC and decrease fluorescence. Complex **2**-propionic with a large number of oxygen groups, also shows a low $\mathbf{\Phi_T}$ value. When comparing the non-dominant substituent for each Pc, acetic acid gives the higher $\mathbf{\Phi_T}$ for complexes **8** and **5** than acrylic. This is probably due to extra π-electrons from the latter which may cause more aggregation. In comparing complexes **3** with propionic, and NH_2, there is no difference in $\mathbf{\Phi_T}$ values. The triplet quantum yield increased in the nanoconjugates due to the heavy atom effect of NPs. With **4**-COOH, higher $\mathbf{\Phi_T}$ values are obtained for $NiWO_4$ and Bi_2WO_6 conjugates. For complex **5**-acetic with all NPs (except for QDs and Bi_2WO_6),

the Φ_T value is higher for **5**-acetic-Ag_2WO_4. As it is in the case for MPc complexes, increasing triplet quantum yields should result in shorter triplet lifetimes [**179**]. However, it is not the case for nanoconjugates. The triplet lifetimes (τ_F) lengthened, most likely due to the protection of the MPc by the NPs.

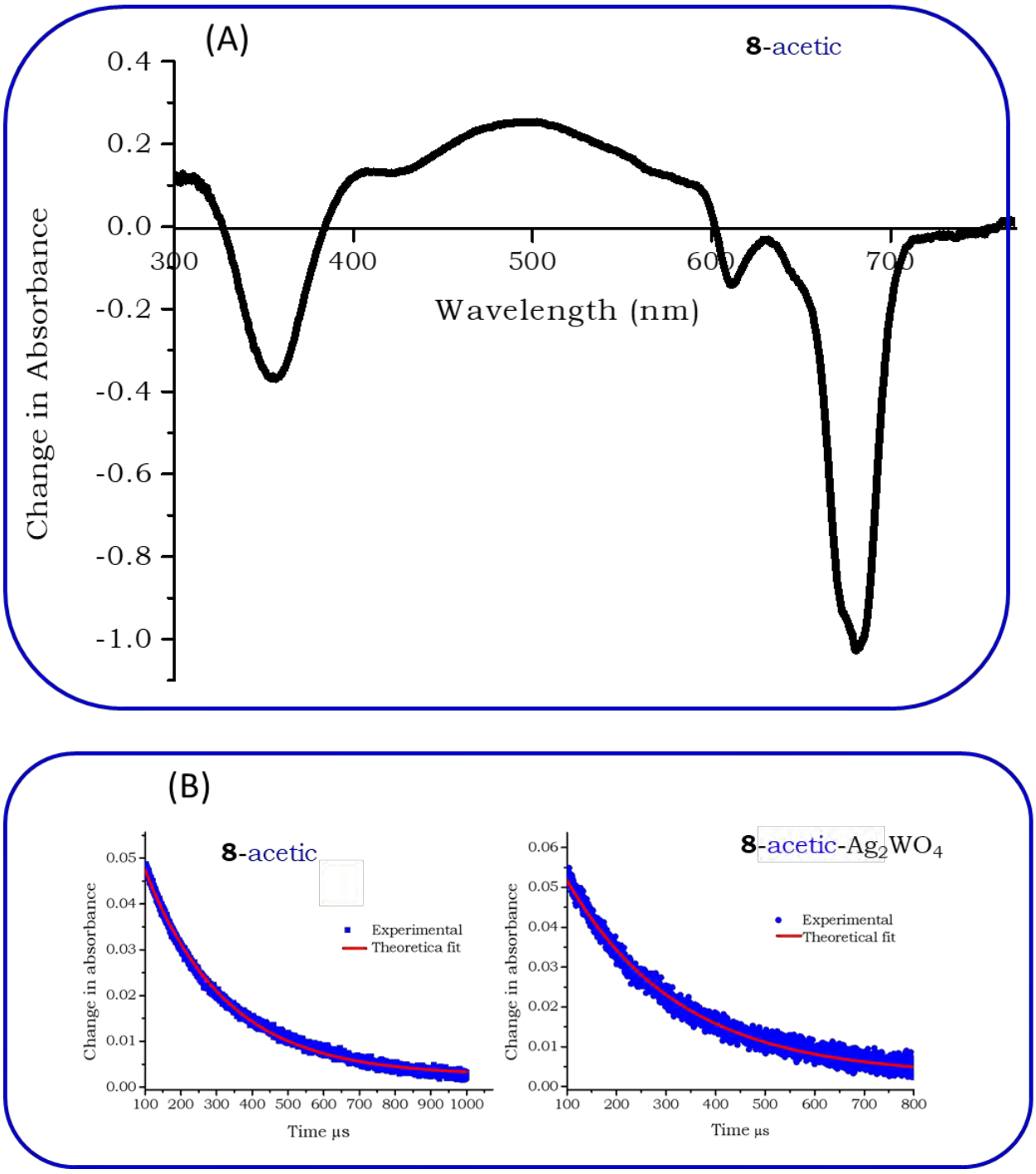

Figure 4.4 *(A) Transient and triplet decay curve of complexes, using complex* ***8****-acetic, as an example. (B) Triplet absorption decay curve for Pc complexes and conjugates (****8****-acetic and* ***8****-acetic-Ag_2WO_4 used as examples) in DMSO with the fitting curve.*

4.4 Singlet oxygen quantum yield.

The singlet oxygen generating ability of Pcs and the nanocomposites is evaluated by monitoring varying absorbance of DPBF at 417 nm intensity. The chemical approach based on the chemical quenching of DPBF in DMSO was used to determine the singlet oxygen quantum yields in the presence of Pc complexes and conjugates. No significant change in the Q-band absorption speak in the course of the DPBF degradation showing that the Pcs and their conjugates are stable following irradiation to generate singlet oxygen, **Figure 4.5** (using **3**-NH_2 and **3**-NH_2-Ag-Fe_3O_4 as examples). The Φ_Δ values of Pc complexes and the conjugates are given in **Table 4.1**. Complexes **5** gave the largest Φ_Δ values in DMSO, corresponding to Φ_T values while complexes **7** show the least. Due to the heavy atom effect of NPs, the observed Φ_Δ values for conjugates are relatively higher than that of Pc complexes alone. The degradation of ADMA of Pc complexes and conjugates is presented in **Figure 4.6** (Using **5**-acrylic and **5**-acrylic-$CoWO_4$ as examples). The absorption peaks for Pc complexes and conjugates are not noticed because Pcs are not water-soluble. When compared to investigations in DMSO, the singlet oxygen quantum yields of Pc complexes and conjugates in water are lower (**Table 4.1**). This is to be expected because water quenches singlet oxygen [**44**].

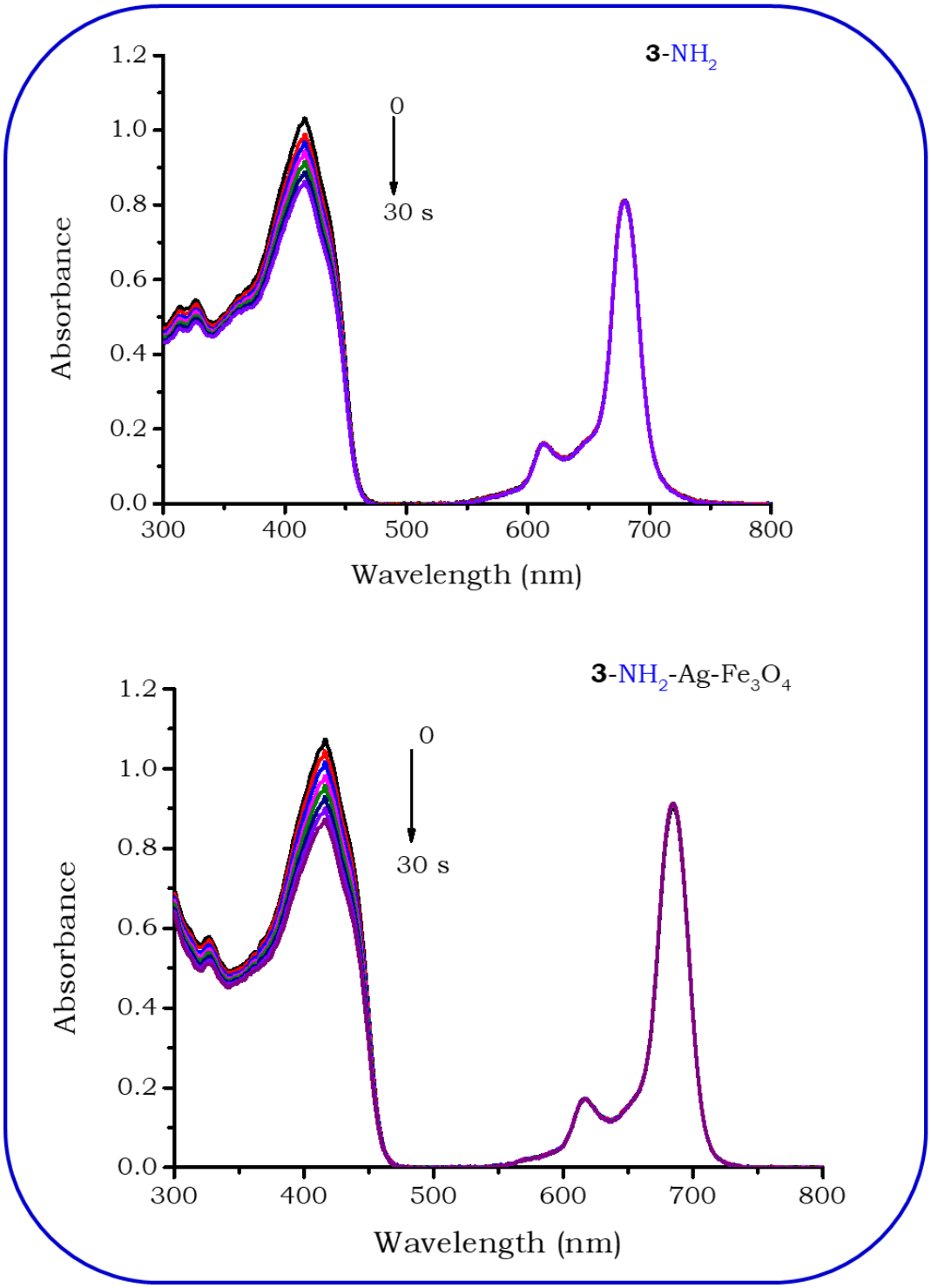

***Figure 4.5**: Degradation of DPBF in the presence of Pc complexes and conjugates (using **3**-NH_2 and **3**-NH_2-Ag-Fe_3O_4 as examples) in DMSO.*

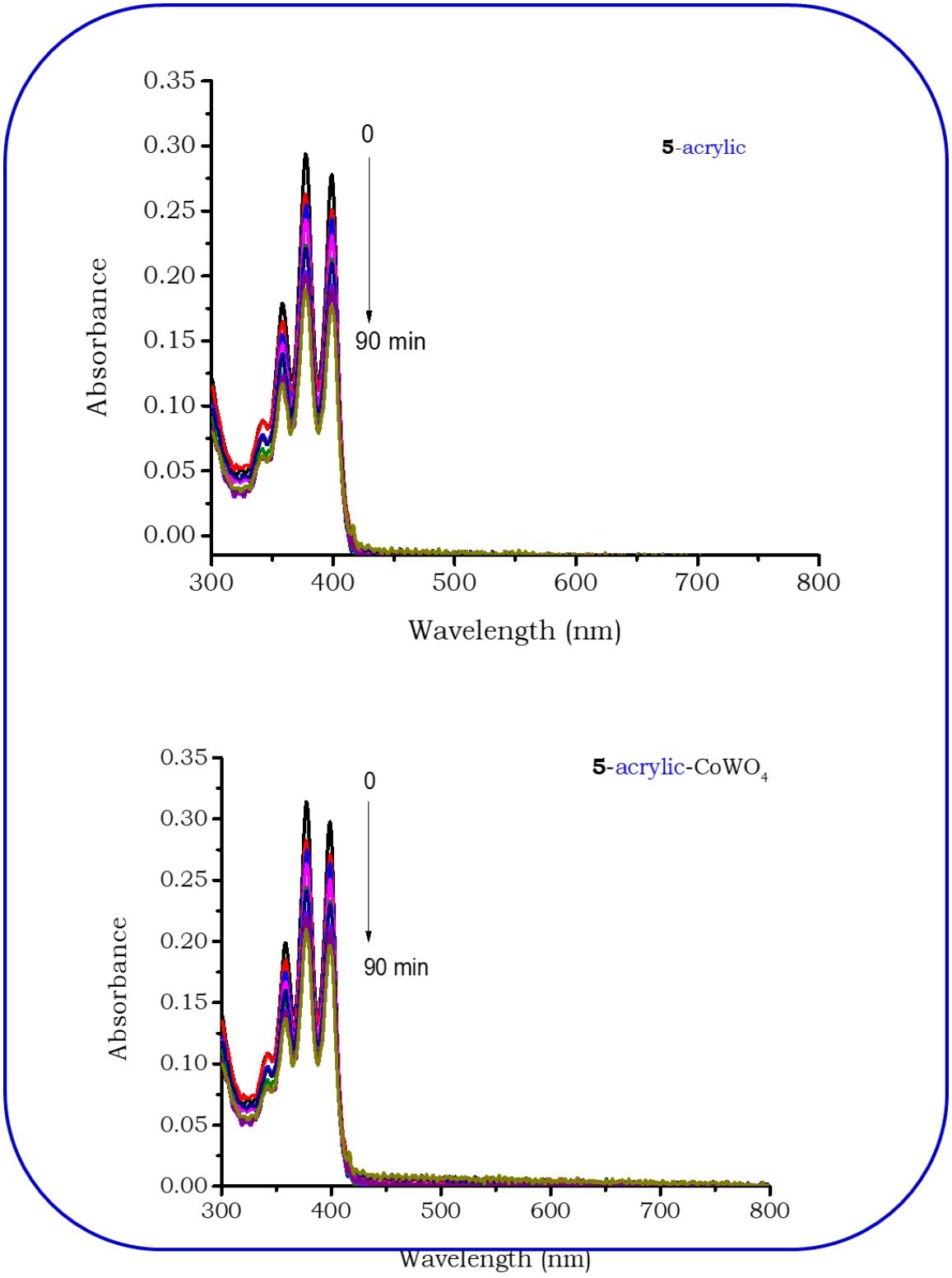

***Figure 4.6**: UV–vis spectrum showing the photodegradation of ADMA (in water) in the presence of the Pc complexes and conjugates (using **5**-acrylic and **5**-acrylic-$CoWO_4$ as examples*).

4.5 Final remarks

The photophysical and photochemical behaviour of Pcs and nanoconjugates were investigated. The nanoconjugates generated a higher triplet quantum yields and singlet oxygen quantum yields than the ZnPcs. An increase in triplet quantum yields with corresponding decrease in fluorescence quantum yields of conjugates compared to Pc complexes was observed.

Chapter 5

Details on the application of Pc complexes, NPs, and their corresponding conjugates as antibacterial agents are given in this chapter.

Photodynamic antimicrobial chemotherapy (PACT) studies of *S. aureus*.

In this thesis, the complexes substituted asymmetrically to the phthalocyanine ring (**4**-propionic, **4**-acetic, **4**-COOH, **5**-acetic, **5**-acrylic, **5**-propionic, **8**-acetic, **8**-acrylic and **8**-propionic) and their corresponding conjugates are employed for photoinactivation of *S. aureus* a Gram-positive bacterium in 2% DMSO (in PBS). The findings are quantified using log reductions (**Table 5.1**) from the PACT activity of the selected Pc complexes and conjugates (**Figure 5.1**, **Table 5.1**). Log reductions are calculated according to the reported literature to determine the level of inactive microorganisms [**180**].

5.1 PACT Activity of MPc complexes

Dark toxicity studies are done to verify that the micro-organism inactivation is due solely to the introduction of light. The Pc complexes and nanoconjugates showed no significant dark toxicity even at high concentrations (**Figure 5.2A**). Considering complexes **5**, containing acetophenone groups, there are considerable similarities in antimicrobial activity of **5**-acrylic, and **5**-propionic while **5**-acetic showed a larger PACT activity with a log reduction of 2.59, 3.18, and 3.52 (**Table 1**). Complexes **5** show antibacterial activity properties that could be due to the presence of the acetophenone substituents as they have been reported to show antibacterial activity [**181**]. For **5**-acetic, the high log value can be attributed to an acetic acid substituent, which has known antimicrobial properties [**182**] in addition to the high singlet-oxygen generating ability.

Table 5.1: Log reduction values in 2% DMSO after 60 min irradiation at 670 nm.

Complex	Log reduction	Seleted loading (µg/mg)	Φ_Δ
4-propionic	2.59	---	0.61
4-propionic-$NiWO_4$	3.77	9	0.65
4-propionic-Bi_2WO_6	3.25	13	0.65
4-acetic	3.12	---	0.54
4-acetic-$NiWO_4$	3.95	17	0.59
4-acetic-Bi_2WO_6	4.55	42	0.60
4-COOH	2.88	--	0.59
4-COOH-$NiWO_4$	3.97	13	0.63
4-COOH-Bi_2WO_6	3.85	18	0.64
4-COOH-$CoWO_4$	3.65	23	0.68
5-acetic	3.52	--	0.69
5-acetic-Ag-FeO_4	7.28	5	0.75
5-acetic-Ag_2WO_4	7.33	7	0.74
5-acetic-$CoWO_4$	6.85	20	0.75
5-acetic-$NiWO_4$	6.86	23	0.73
5-acrylic	2.59	--	0.72
5-acrylic-$CoWO_4$	7.11	24	0.75
5-propionic	3.18	---	0.75
5-propionic-$CoWO_4$	7.14	26	0.77
8-acetic	3.11	--	0.55
8-acetic-Ag_2WO_4	6.97	9	0.58
8-acrylic	3.01	--	0.53
8-acrylic-Ag_2WO_4	6.87	15	0.59
8-propionic	3.02	--	0.50
8-propionic-Ag_2WO_4	6.90	13	0.57
Ag_2WO_4	2.21	--	--
Ag-FeO_4	2.05	--	--

Bi_2WO_6	1.97	--	--
$CoWO_4$	1.95	--	--
$NiWO_4$	1.96	--	--

Log reduction values obtained for complexes **4** are less than compared to **3** due to the presence of 9 methoxy groups on the peripheral positions of the Pc. Methoxy groups are known to reduce antimicrobial activity, hence will reduce the PACT activity of the Pcs [**183**]. For the non-dominant substituents (propionic, acetic, acrylic) for complexes **8**, the acetic outperforms the acrylic and propionic acid groups. Additionally, the Pc complexes **8** alone did not show acceptable log reduction values. The log reduction values of: 3.01, 3.02, and 3.11 are recorded for **8**-propionic, **8**-acrylic, and **8**-acetic, respectively.

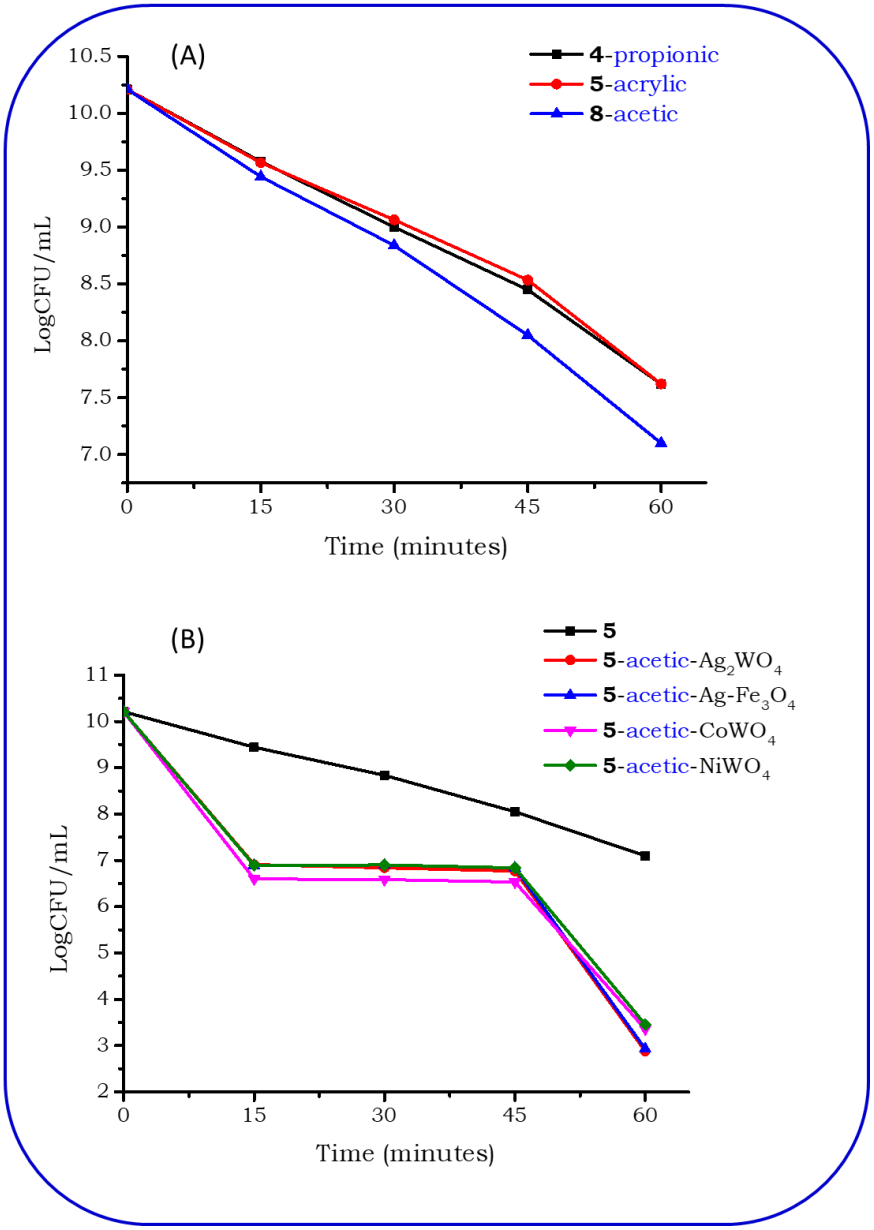

***Figure 5.1**: (A) Logarithmic reduction of S. aureus in presence of MPcs (using **4**-propionic, **5**-acrylic and **8**-acetic), (B) conjugates (**5**-acetic-Ag_2WO_4, **5**-acetic-Ag-Fe_3O_4, **5**-acetic-$CoWO_4$, **5**-acetic-$NiWO_4$ used as examples) with light, treated with 0.5 µM concentrations of the photosensitizers.*

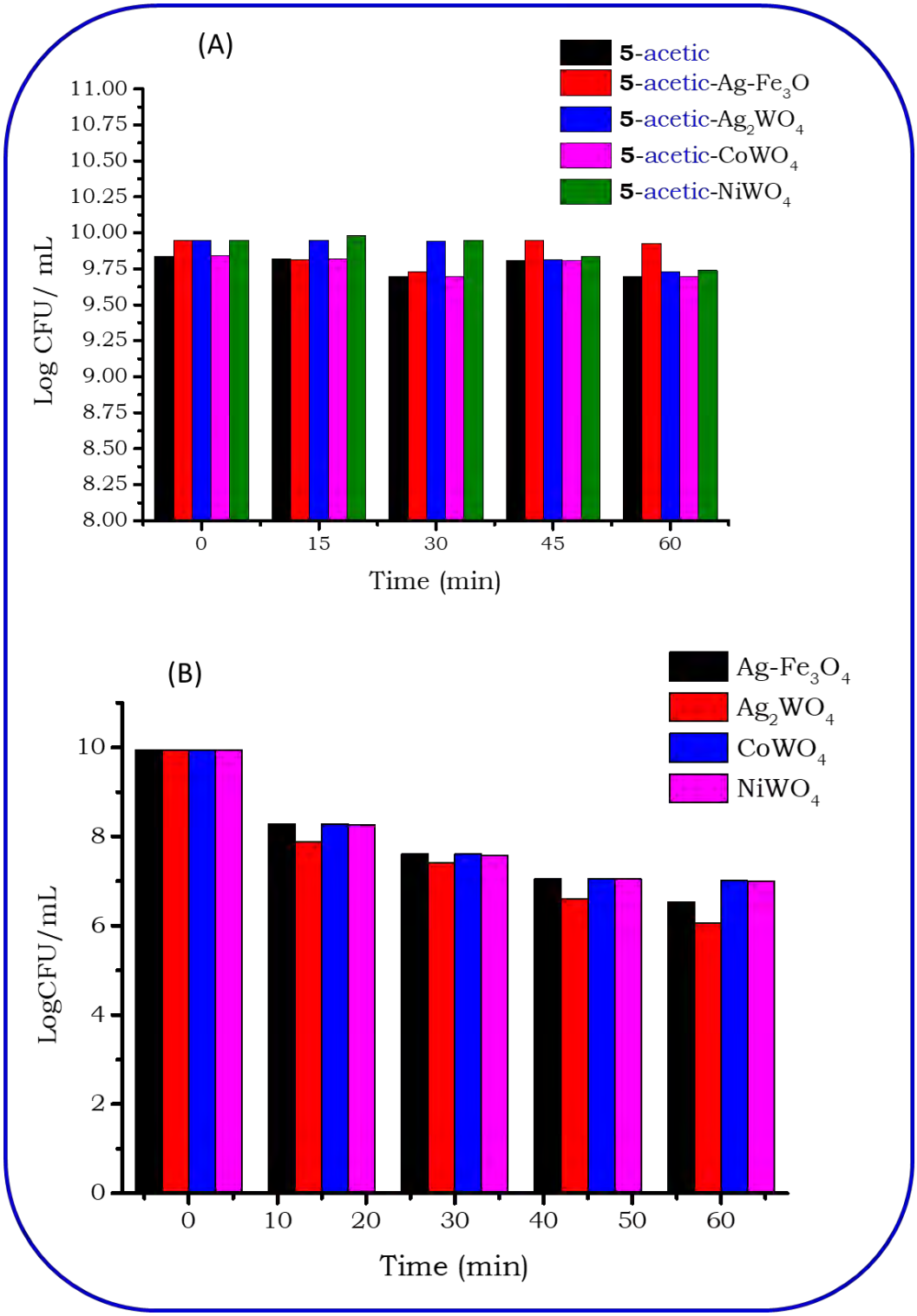

***Figure 5.2**: (A) Dark toxicity of complexes and conjugates (using **5**-acetic, **5**-acetic-Ag_2WO_4, **5**-acetic-$CoWO_4$, **5**-acetic-$NiWO_4$, and **5**-acetic-Ag-Fe_3O_4 as examples). (B) PACT activity for NPs alone.*

5.2 PACT Activity of nanoconjugates

Nanoparticles alone show activity with log reduction values between 2.21 and 1.95 (**Table 5.1**, **Figure 5.2B**). Ag_2WO_4 and Ag-FeO_4 display high log reduction values compared to other NPs (Bi_2WO_6, $CoWO_4$, $NiWO_4$).

Nanoparticles increase the log reduction values of the Pc, consistent with the increase in singlet oxygen quantum yield (**Table 5.1**). Also, metal tungstate-based nanoparticles show antibacterial activity [**95**], which could enhance the PACT activity of the Pcs. Conjugates of complexes **5** show relatively high log reductions (6.85-7.33), **Table 5.1**, corresponding to high Φ_Δ values.

For nanoconjugates of complexes **4**, **4**-COOH-Bi_2WO_6, **4**-COOH-$NiWO_4$, and **4**-COOH-$CoWO_4$, the highest log reduction is obtained for **4**-COOH-$NiWO_4$ with the lowest loading, possibly due to lower aggregation for the latter. **4**-COOH-$CoWO_4$ with the largest loading of the three gave the least log reduction, **Table 5.1**. **4**-COOH-$CoWO_4$ had the largest singlet oxygen quantum yield of the three conjugates with different nanoparticles, but gave the lowest log reduction. This also applies to **4**-propionic-$NiWO_4$ and **4**-propionic-Bi_2WO_6, where the former has a lower loading and a higher log reduction, yet they have the same singlet oxygen quantum yield. However, this does not apply to conjugates of **4**-acetic, both with similar singlet oxygen quantum yield, but **4**-acetic-Bi_2WO_6, with a larger loading, has a larger log reduction. Thus, it is not only the singlet oxygen quantum yield that affects PACT activity.

Upon conjugation of the Pcs **8** or **5**-acetic to the Ag_2WO_4 nanoparticles, the photodynamic activity increased. It is known that Ag ions and Ag-based

compounds have strong antimicrobial effects in terms of causing more cell membrane damage resulting in more cellular uptake [**184**] and showing a high degree of activity for killing microorganisms. This was supported by the log reductions of 6.90 for **8**-propionic-Ag_2WO_4, 6.97 for **8**-acetic-Ag_2WO_4, 6.87 for **8**-acrylic-Ag_2WO_4, and 7.33 **5**-acetic-Ag_2WO_4, 7.28 for **5**-acetic-Ag-Fe_3O_4 (**Table 5.1**).

5.3 Closing remarks

During in *vitro* photodynamic antibacterial activities towards *S. aureus*, the high activities were observed with nanoconjugates. Pc complexes conjugated to silver tungstate and silver-iron oxide NPs gave the highest activities. This can be attributed to known antimicrobial effects of silver.

Chapter 6

This chapter provides details on the photodegradation efficiencies of both MPcs and nanoconjugates.

Catalytic reactions are carried out at room temperature. For ease of comparison the Φ_Δ values provided in **Table 4.1** are presented in **Tabe 6.1**, since photoactivity is related to singlet oxygen quantum yields. The photocatalytic studies of Pc complexes and conjugates are investigated and the aim is to design heterogeneous photocatalysts. The photocatalytic activities of selected MPc complexes and their nanoconjugates are evaluated for the photodegradation of TC, MB, and DBT under visible irradiation. In the absence of nanoconjugates, the absorption spectra of the organic pollutants remained constant with increasing irradiation time, demonstrating that TC, MB, and DBT photolysis is minimal in the absence of a photocatalyst. Before visible light exposure, synthesized Pcs and composites are allowed to interact with the pollutants in the dark overnight in order to achieve adsorption equilibrium.

6.1 Photodegradation of tetracycline (TC)

The photodegradation studies are performed at pH 6 as reported [**185**] (complexes **2, 5, 6, 7, 8** and their conjugates are used as examples). The stock solution of TC of 1×10^{-3} is prepared and then diluted to give the working concentrations of 1.45×10^{-5}, 2.70×10^{-5}, 3.80×10^{-5}, 4.44×10^{-5}, and 6.63×10^{-5} M. The MPc complexes **2**, **5**-acetic, **6**, **7**, **8**, and their conjugates are assessed under the same conditions to compare their photocatalytic activity as prepared photocatalysts. Complexes **2**, **6**, and **7** are studied with conjugates with $CoWO_4$, complexes **8** with Ag_2WO_4, and **5**-acetic with $NiWO_4$, Ag_2WO_4, $CoWO_4$, Ag-Fe_3O_4 (**Tables 6.2A** and **A1**). **Figure 6.1** depicts the time-dependent absorption spectra of TC in the presence of photocatalysts under visible-light irradiation (using **7**-acrylic-$CoWO_4$ as an example).

Table 6.1: Photochemical properties (Φ_Δ in DMSO) and loading for selected Pc complexes and conjugates.

Complex	Seleted loading (µg/mg)	Φ_Δ
2-propionic	---	0.31
2-propionic-$CoWO_4$	6	0.61
3-propionic	---	0.44
3-propionic-Ag-Fe_3O_4	9	0.48
3-COOH	---	0.43
3-COOH-Ag-Fe_3O_4	8	0.48
3-NH_2	---	0.38
3-NH_2-Ag-Fe_3O_4	8	0.42
4-COOH	---	0.59
4-COOH-$NiWO_4$	13	0.63
4-COOH-$CoWO_4$	23	0.68
4-COOH-Bi_2WO_6	18	0.64
4-propionic	---	0.61
4-propionic-$NiWO_4$	9	0.65
4-propionic-Bi_2WO_6	38	0.65
4-acetic	13	0.54
4-acetic-$NiWO_4$	18	0.59
4-acetic-Bi_2WO_6	23	0.60
5-propionic	--	0.75
5-propionic-$CoWO_4$	26	0.77
5-acrylic	7	0.72
5-acrylic-$CoWO_4$	20	0.75
5-acetic	---	0.69
5-acetic-$CoWO_4$	20	0.75

5-acetic-Ag-Fe_3O_4	5	0.75
5-acetic-Ag_2WO_4	7	0.74
5-acetic-$NiWO_4$	23	0.73
6-COOH	---	0.52
6-COOH-$CoWO_4$	9	0.63
7-acrylic	---	0.41
7-acrylic-$CoWO_4$	12	0.45
7-propionic	---	0.41
7-propionic-$CoWO_4$	11	0.46
8-propionic	--	0.50
8-propionic-Ag_2WO_4	13	0.57
8-acrylic	---	0.53
8-acrylic-Ag_2WO_4	9	0.59
8-acetic	--	0.55
8-acetic-Ag_2WO_4	13	0.58

Due to high solubility in water, catalytic studies on the nanoparticles alone are not performed. TC exhibited two main absorption bands at 257 and 357 nm in an aqueous solution, **Figure 6.1**, similar to literature reports [**186**].

These two bands are attributed to carbonyls and enolic groups, respectively [**187**]. As irradiation time increases, the absorption peak at 357 nm of decreases, showing that photocatalysts effectively photodegrade the TC pollutant in aqueous media. The decrease in intensity of the 357 nm absorption peak suggests that enolic groups have been effectively reduced, and that tetracycline has been mineralized and intermediates are formed [**188**,**189**]. The peak increase at 257 nm is due to formation of intermediates.

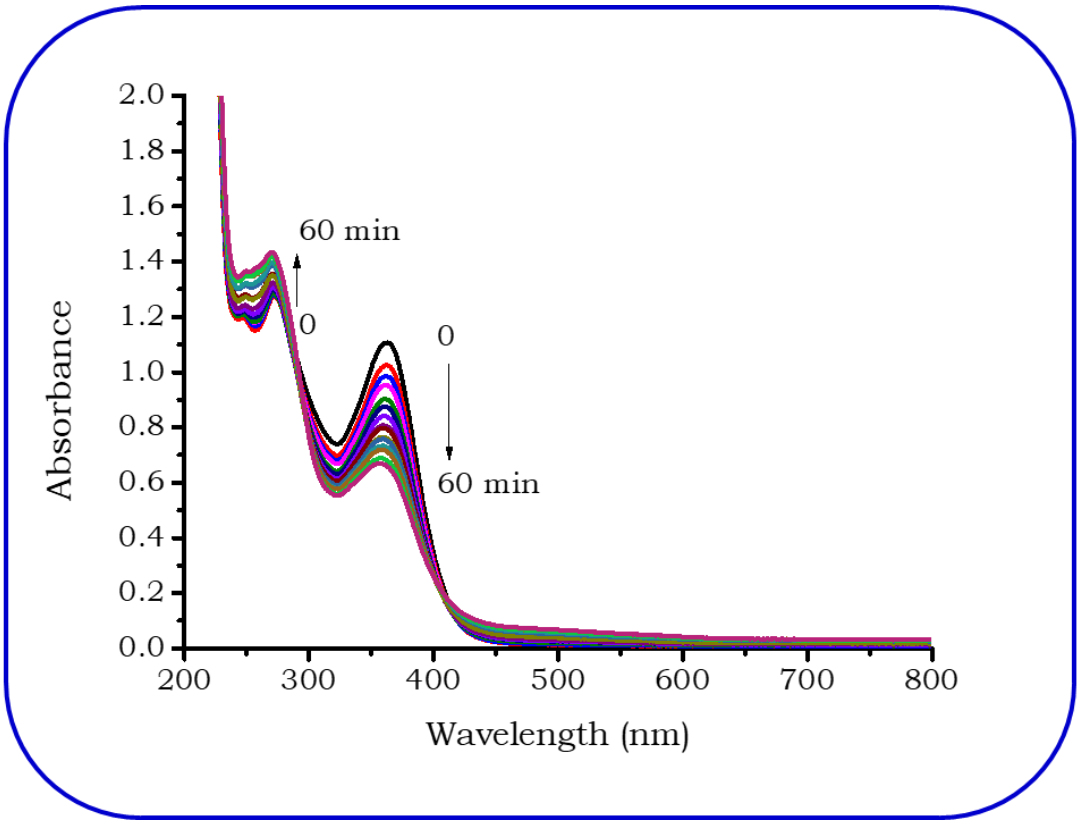

***Figure 6.1**: UV-vis spectral changes of TC in aqueous solution (**7**-acrylic-$CoWO_4$ used as an example) at 6.63× 10^{-5} M.*

Degradation of TC followed the pseudo-first-order model, **Figure 6.2** (using complex **8**-acrylic as an example). The observed kinetic rate constants (k_{obs}) are determined by plotting ln (C_o/C) vs irradiation time and are listed in **Tables 6.2A**, **6.2B**, and **A1** in the appendix. Initial rates and k_{obs} decreased with increase in organic pollutant concentration, while the half-lives increased for all the photocatalysts, **Table 6.2**. Thus the photocatalytic activity of the catalysts increased with decrease concentration of organic pollutant. This means that the photocatalytic activity of the photocatalysts decreases as the amount of antibiotic in water increases.

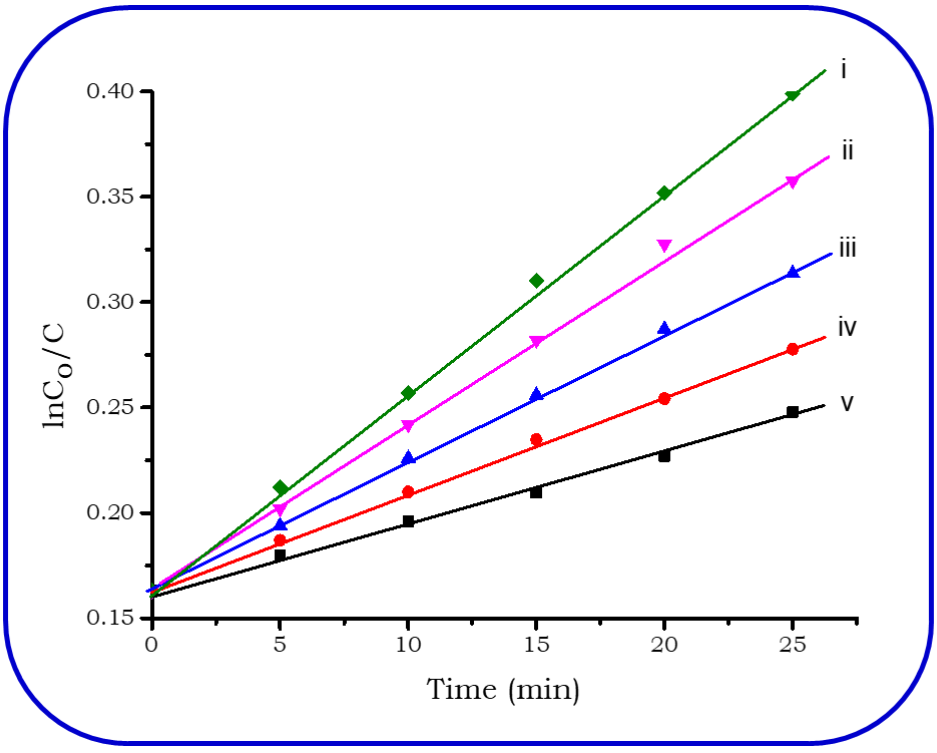

***Figure 6.2**: Pseudo first order kinetics plot for the degradation of organic polutantants at various concetarations (i-v) in the presence of Pc/conjugate (**8**-acrylic used as an example), i* = 1.45× 10^{-5}, ii= 2.70× 10^{-5}, iii= 3.80× 10^{-5}, iv= 4.44× 10^{-5}, and v= 6.63× 10^{-5} M.

Pc complexes **7**-acrylic and **7**-propionic show the least catalytic activity in **Table 6.2** due to low Φ_Δ values. Among complexes **8**, the highest activity is observed for **8**-acetic (containing acetic acid substituents) could be due to the fact that acetic acid derivatives have photocatalytic activity [**190**]. **5**-acetic with different NPs, Ag_2WO_4 gave the highest k_{obs} except for **5**-acetic-$CoWO_4$ at a concentration of 1.45 M, **Table A1**. When compared to Pc complexes alone, the nanoconjugates have larger initial rates and k_{obs}, and shorter half-lives, **Table 6.2A, 6.2B, A1**. These results indicate that the MPc-NPs combination significantly enhances the photocatalytic activity under visible-light irradiation.

Table 6.2A: Initial rates, rate constants (k_{obs}) and half-lives ($\tau_{1/2}$) of various initial concentrations for the Pc and conjugates (the latter in square brackets) in water. Curly brackets are for reusability studies of conjugates; NPs= Ag_2WO_4.

	k_{obs} ($\times 10^{-3}$ min^{-1})			Initial rates ($\times 10^{-8}$ mol $L^{-1}min^{-1}$)			$\tau_{1/2}$($\times 10^{2}$min)		
[TC]($\times 10^{-5}$ M)	**8**-propionic	**8**-acrylic	**8**-acetic	**8**-propionic	**8**-acrylic	**8**-acetic	**8**-propionic	**8**-acrylic	**8**-acetic
1.45	3.19 [4.47] {4.55}	4.24 [6.45] {6.38}	5.91 [8.93] {8.87}	4.63 [6.48] {6.59}	6.15 [9.36] {9.25}	8.57 [12.90] {12.86}	2.17 [1.55] {1.52}	1.63 [1.07] {1.08}	1.17 [0.77] {0.78}
2.70	1.64 [2.29]	2.19 [3.33]	3.06 [4.62]	4.43 [6.20]	5.91 [9.00]	8.25 [12.50]	4.23 [3.01]	3.17 [2.08]	2.27 [1.50]
3.80	1.11 [1.55]	1.01 [1.54]	2.07 [3.12]	4.22 [5.91]	3.82 [5.84]	7.87 [11.90]	6.24 [4.46]	6.86 [4.51]	3.35 [2.22]
4.44	0.71 [0.94]	0.82 [1.25]	1.04 [1.57]	3.15 [4.41]	3.64 [5.54]	4.62 [6.89]	9.76 [6.97]	8.45 [5.55]	6.66 [4.41]
6.63	0.41 [0.58]	0.54 [0.82]	0.65 [0.97]	2.73 [3.82]	3.58 [5.45]	4.24 [6.41]	16.8 [12.03]	12.8 [8.43]	10.8 [7.17]

Table 6.2B: Initial rates, rate constants (k_{obs}) and half-lives ($\tau_{1/2}$) of various initial concentrations for the Pc complexes and conjugates (the latter in square brackets) in water. Curly brackets are for reusability studies of conjugates. NPs= $CoWO_4$.

	k_{obs} ($\times 10^{-3}$ min^{-1})				Initial rates ($\times 10^{-8}$ mol $L^{-1}min^{-1}$)				$\tau_{1/2}$($\times 10^{2}$min)			
[TC]($\times 10^{-5}$M)	**6**-COOH	**2**-propionic	**7**-acrylic	**7**-propionic	**6**-COOH	**2**-propionic	**7**-acrylic	**7**-propionic	**6**-COOH	**2**-propionic	**7**-acrylic	**7**-propionic
1.45	2.86 [3.54] {3.38}	2.88 [3.58] {3.24}	1.45 [1.62] {1.52}	1.73 [1.94] {1.82}	4.15 [5.13] {4.91}	4.13 [5.12] {4.6}	2.10 [2.35] {2.20}	2.51 [2.81] {2.62}	2.42 [1.96] {2.05}	2.41 [1.9] {2.13}	4.78 [4.27] {4.56}	4.01 3.57 3.80
2.70	1.41 [1.87] {1.60}	1.10 [1.36]	0.74 [0.83] {0.79}	0.81 [0.88] {0.79}	0.38 [5.05] {4.47}	3.13 [3.89]	2.02 [2.24] {2.13}	2.19 [2.30] {2.11}	4.92 3.71] 4.18}	6.30 [5.09]	9.27 8.34 8.78	8.51 7.84 8.06
3.80	0.68 [0.82] {0.68}	0.80 [1.01]	0.23 [0.39] {0.38}	0.29 [0.44] {0.40}	2.61 [3.12] {2.61}	2.57 [3.19]	0.89 [1.46] {1.51}	1.12 [1.68] {1.55}	10.01 [8.44] {10.10}	7.87 6.86	29.49 [17.50] {18.18}	23.55 [15.61] {17.06}
4.44	0.331 [0.37] {0.27}	0.36 [0.45]	0.11 [0.14] {0.11}	0.11 [0.19] {0.15}	1.47 [1.68] {1.23}	2.09 [2.59]	0.48 [0.69] {0.47}	0.51 [0.87] {0.69}	20.94 [18.28] {25.05}	19.25 [15.40]	64.24 [48.10] {66.54}	60.2 [35.58] {44.71}
6.63	0.15 [0.17] {0.10}	0.20 [0.25]	0.04 [0.11] {0.08}	0.05 [0.12] {0.08}	0.10 [1.14] {0.67}	1.30 [1.61]	0.31 [0.74] {0.57}	0.37 [0.76] {0.58}	43.92 40.32 {68.68}	 34.65 [27.72]	146.5 [61.88] {78.59}	123.54 [60.89] [80.62]

6.2 Photodegradation of methylene blue (MB)

Only complexes **5** and their conjugates with $CoWO_4$, and **5**-acetic with $NiWO_4$, Ag_2WO_4, and Ag-Fe_3O_4 are employed for the degradation of MB. Five concentrations of MB solutions are prepared and a UV-visible spectrophotometer is used to record the photodegradation of MB at 5 min intervals. **Figure 6.3** shows spectral changes observed during the photodegradation of methylene blue under visible irradiation. The UV-visible spectrum of MB shows three distinctive bands at 240, 287, and 664 nm [**191**], and the solution appears in bright blue. The most important band is at 664 nm which is due to the azo dye content [**192**]. The peaks below 300 nm are due to the benzene rings [**191**,**193**]. The photocatalysts (Pcs and conjugates) are not soluble in water, hence the Q-band absorption (which would overlap with MB absorption) is not expected in **Figure 6.3**.

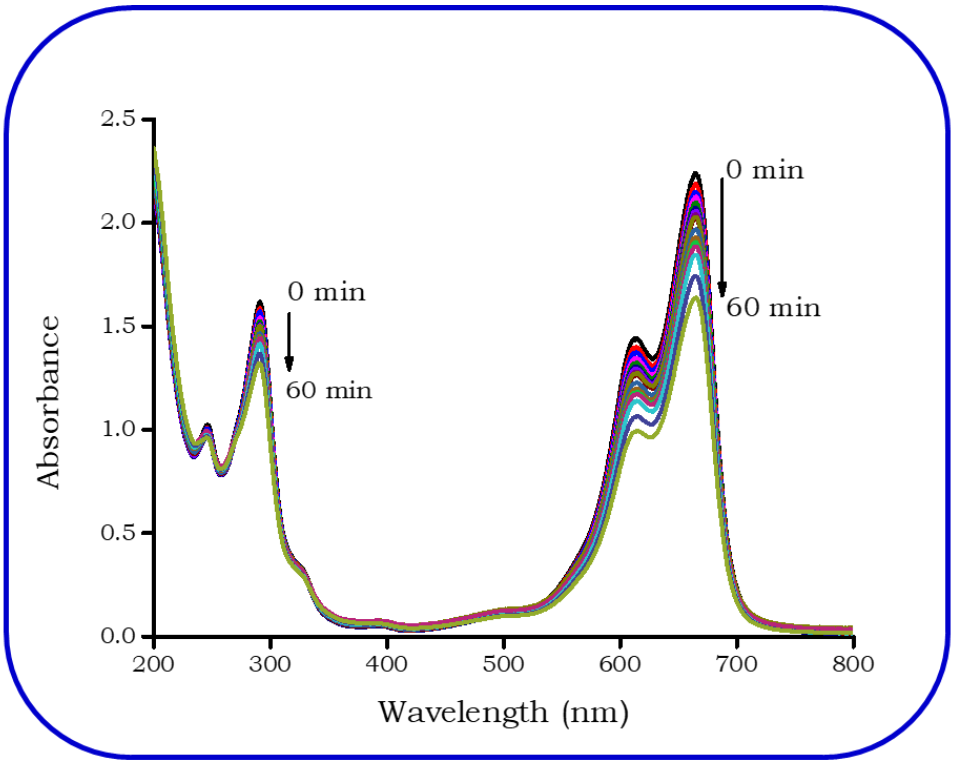

***Figure 6.3**: UV–vis spectra showing degradation of MB in water (using **5**-acrylic-$CoWO_4$ as a catalyst).*

There are no changes in the UV-visible absorption spectrum of MB when the irradiation is conducted in the absence of the photocatalysts (Pc complexes and nanoconjugates). Also, no degradation was observed in the dark. However, when the studies were carried out in the presence of photocatalysts and visible light there is an observable degradation of MB with the peak at 664 nm decreasing. The bright-blue MB became colorless, indicating degradation of MB as reported before [**194**]. The results confirm that the employed catalysts are photocatalytically active under visible radiation. The spectral changes of MB when illuminated with light are in accordance with observation in literature [**195**]. The decrease at 287 nm suggests that the benzene is degraded.

The obtained k_{obs} and initial rates increased with the decrease in the concentration of MB, **Tables 6.3**, and **A2** in the appendix. Complex **5**-acetic (Φ_{Δ}= 0.69) possesses better photocatalytic activity than **5**-acrylic (Φ_{Δ}= 0.72) and **5**-propionic (Φ_{Δ}= 0.75) even though it generates less singlet oxygen quantum yield in water, **Table 6.1**. The high activity of **5**-acetic (containing acetic acid substituents) could be because that acetic acid derivatives have photocatalytic activity as stated above [**190**]. In addition, the varying extends of aggregation of the Pc complexes can be affected by the presence of MB in the solution. MB has π electrons and complex **5**-acrylic has an extra π electron compared to complex **5**-acetic, meaning complex **5**-acrylic might be more affected by the presence of MB. Aggregates are photo-inactive.

Linking of Pc complexes to $CoWO_4$ proved to be a beneficial alternative method for improving the photocatalytic activity of phthalocyanines. Rate constants

and initial rates for Pc-$CoWO_4$ increased in comparison with Pcs alone. **5**-propionic and **5**-acetic conjugates showed fast initial rates and high rate constants with shorter half-lives ($\tau_{1/2}$), compared to **5**-acrylic. When comparing the effect of NPs, it is generally found that the presence of NPs containing silver results in the highest rate constants, **Table A2**. The presence of silver in NPs is known to enhance photocatalytic activity towards the degradation of MB [**196**].

Table 6.3:Initial rates, rate constants (k_{obs}), and half-lives ($\tau_{1/2}$) of various initial concentrations for the Pc **5** and conjugates with $CoWO_4$ (The latter in square in brackets) in water. Curly brackets are for reusability studies of conjugates.

	k_{obs} ($\times 10^{-3}$ min^{-1})			Initial rates ($\times 10^{-7}$ mol $L^{-1}min^{-1}$)			$\tau_{1/2}$($\times 10^{2}$min)		
[MB] ($\times 10^{-5}$ M)	**5**- propionic	**5**-acrylic	**5**-acetic	**5**- propionic	**5**-acrylic	**5**-acetic	**5**-propionic	**5**-acrylic	**5**-acetic
2.63	6.63 [8.28] {8.04}	5.17 [6.33] {6.21}	6.76 [8.73] {8.56}	0.44 [2.18] {2.11}	0.31 [1.66] {1.63}	1.74 [2.29] {2.25}	1.05 [0.84] {0.86}	1.34 [1.10] {1.12}	1.03 [0.79] {0.81}
3.32	4.39 [6.36]	3.98 [4.86]	4.74 [6.83]	0.37 [2.11]	0.29 [1.50]	1.45 [2.26]	1.58 [1.09]	1.74 [1.43]	1.46 [1.01]
4.23	3.39 [4.14]	2.45 [3.55]	3.65 [4.85]	3.13 [1.75]	0.27 [1.48]	1.43 [2.05]	2.04 [1.67]	2.83 [1.95]	1.90 [1.43]
5.51	2.49 [3.12]	1.78 [2.56]	2.52 [3.65]	0.23 [1.71]	0.21 [1.41]	1.37 [2.01]	2.78 [2.21]	3.89 [2.71]	2.75 [1.90]
5.68	1.39 [1.73]	1.03 [1.63]	1.71 [2.65]	0.17 [0.98]	0.13 [0.92]	0.78 [1.50]	4.99 [4.01]	6.75 [4.25]	4.05 [2.62]

6.3 Phototransformation of dibenzothiophene (DBT)

Complexes **4**, and **3** and their conjugates as well as **5**-acetic with Ag-Fe_3O_4, $NiWO_4$, Ag_2WO_4 $CoWO_4$ are employed for desulfurization. The spectra of dibenzothiophene in **Figure 6.4** is similar to that reported in literature [**173**]. The maximum absorption at 325 nm is due to the presence of benzene rings in the structure. Benzene rings are known to have absorption bands around this region [**191,197**]. Only small spectral changes were observed in this region, **Figure 6.4**, suggesting that benzene rings remain intact during photooxidation as reported in the literature [**197**]. The absorption peak at 254 nm, due to thiol, decreased in intensity with increasing irradiation time.

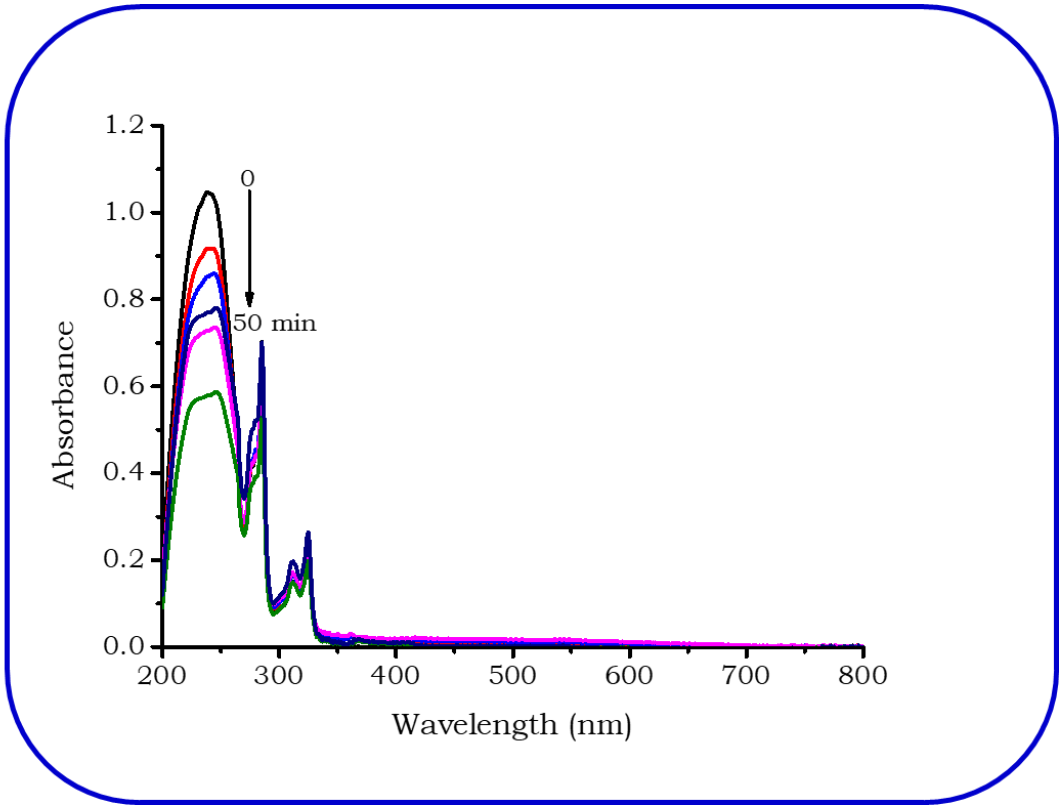

***Figure 6.4**: UV–vis spectra showing degradation of organic pollutants (using DBT as an example) in n-octane when **3**-COOH-Ag-F_3O_4 is used as a catalyst.*

The changes at 254 nm are due to the degradation of sulfur, i.e desulfurization. The degradation of DBT spectrum is in accordance with observations in literature [**173**]. A decrease in k_{obs} and initial rates with an increase in concentration of DBT is observed for all the photocatalysts, **Tables 6.4A**, **B**, and **A3**. Comparing complexes with carboxylic moiety (**3**-COOH and **3**-propionic) alone, results show that complex **3**-propionic performs better than **3**-COOH as photocatalyst even though they have the same singlet oxygen quantum yields (in DMSO).

Respective conjugates showed greater photocatalytic activity with faster initial rates and higher rate constants for desulfurization of DBT compared to Pcs alone. Half-lives decreased in the presence of nanoparticles with **3**-propionic-Ag-Fe_3O_4 having the least $\tau_{1/2}$ values (**Table 6.4A**) corresponding to their highest k_{obs} values. The lower the $\tau_{1/2}$ value the better the catalyst.

Complex **4**-acetic and its conjugates gave higher k_{obs} values compared to **4**-COOH and **4**-propionic and their conjugates, **Table 6.4B**. Bi_2WO_6 conjugates showed greater catalytic activity than $NiWO_4$ conjugates for all the photocatalysts even at higher concentrations of DBT (**Table 6.4B**). The Φ_Δ values are about the same for **5**-acetic conjugates but Ag-Fe_3O_4 shows greater catalytic activity than metal tungstate NPs, **Table A3**.

Table 6.4A: Initial rates, rate constants (k_{obs}), and half-lives ($\tau_{1/2}$) of various initial concentrations for the Pc complexes and conjugates (The latter in square brackets) in *n*-octane. Curly brackets are for reusability of conjugates studies for concentration 1.43 M. NPs = Ag-Fe_3O_4.

	k_{obs} ($\times 10^{-4}$ min^{-1})			Initial rates ($\times 10^{-9}$ mol $L^{-1}min^{-1}$)			$\tau_{1/2}$($\times 10^{4}$min)		
[DBT] ($\times 10^{-5}$ M)	**3**-COOH	**3**-NH_2	**3**-propionic	**3**-COOH	**3**-NH_2	**3**-propionic	**3**-COOH	**3**-NH_2	**3**-propionic
1.43	6.70 [6.83] {6.04}	7.03 [7.17] {6.40}	8.91 [9.68] {8.49}	9.58 [9.77] {9.77)	10.01 [10.3] {10.2}	12.8 [14.6] {13.8}	1.03 [0.10] {0.11}	0.98 [0.09] {0.10}	0.78 [0.07] {0.08}
2.85	4.10 [4.14]	5.73 [5.84]	7.72 [7.87]	6.81 [6.68]	9.51 [9.82]	12.7 [13.1]	1.69 [0.16]	1.21 [0.11]	0.89 [0.09]
3.16	3.12 [3.15]	4.48 [4.56]	6.47 [5.58]	6.71 [6.77]	9.63 [9.07]	13.9 [11.4]	2.22 [0.22]	1.55 [0.15]	1.07 [0.13]
5.71	1.92 [1.93]	2.15 [2.19]	5.32 [5.33]	6.37 [6.43]	7.14 [7.28]	17.7 [11.8]	3.61 [0.35]	3.22 [0.31]	1.30 [0.19]
6.41	1.33 [1.34]	1.35 [1.37]	2.89 [2.14]	5.77 [5.82]	5.86 [5.97]	12.5 [9.28]	5.21 [0.52]	5.13 [0.50]	2.40 [0.32]

Table 6.4B: Initial rates, rate constants (k_{obs}), and half-lives ($\tau_{1/2}$) for the Pc and conjugates (The latter in round for $NiWO_4$ and square brackets for Bi_2WO_6) in *n*-octane. Curly brackets are for reused catalyst conjugates for concentration 2.85 M (using **4**-COOH-$NiWO_4$ as an example).

	k_{obs} ($\times 10^{-4}$ min^{-1})			Initial rates ($\times 10^{-9}$ mol $L^{-1}min^{-1}$)			$\tau_{1/2}$($\times 10^{2}$min)		
[DBT]($\times 10^{-5}$ M)	**4**-acetic	**4**-COOH	**4**-propionic	**4**-acetic	**4**-COOH	**4**-propionic	**4**-acetic	**4**-COOH	**4**-propionic
1.43	3.80 (5.98) [6.15]	1.52 (5.66) [5.79]	1.46 (2.98) [3.10]	5.44 (8.54) [8.81]	2.18 (8.10) [8.28]	2.10 (4.26) [4.44]	0.18 (0.12) [0.11]	0.45 (0.12) [0.11]	0.47 (0.23) [0.22]
2.85	0.91 (3.12) [3.15]	0.75 (2.76) {2.13} [2.82]	0.72 (1.43) [1.50]	2.62 (8.91) [8.99]	2.14 (7.88) {6.07} [8.04]	2.04 (4.10) [4.28]	0.75 (0.22) [0.21]	0.92 (0.25) {0.32} [0.24]	0.96 (0.48) {} [0.46]
3.16	0.81 (2.62) [2.71]	0.66 (2.51) [2.54]	0.62 (1.25) 1.29	2.56 (8.31) [8.66]	2.10 (7.72) [7.96]	1.96 (3.96) [4.10]	0.85 (0.26) [0.25]	1.04 (0.27) [0.28]	1.11 (0.55) [0.53]
5.71	0.32 (1.26) [1.28]	0.30 (1.18) [1.28]	0.27 (0.90) [1.06]	1.88 7.21) [730]	1.72 (6.78) [7.32]	1.54 (5.16) [6.10]	2.10 (0.54) [0.53]	2.30 (0.58) [0.54]	2.56 (0.76) [0.64]
6.41	0.17 (0.66) [0.94]	0.24 (0.64) [0.89]	0.11 (0.38) [0.48]	1.12 (4.26) [6.06]	1.55 (4.16) [5.72]	0.68 (2.46) [3.12]	3.97 (1.04) [0.73]	2.86 (1.06) [0.77]	6.53 (1.81) [1.42]

6.4 Langmuir–Hinshelwood model

The Langmuir–Hinshelwood model [**198**], which is given in Equation 6.1, has been successfully used to explore solid-liquid reactions in heterogeneous photocatalytic degradation reactions.

$$\frac{1}{r_0} = \frac{1}{kK_A}\frac{1}{C_0} + \frac{1}{k} \quad \text{-----} \quad 6.1$$

where r_o represents the initial photocatalytic degradation rate (mol $L^{-1}min^{-1}$), while C_o is the initial concentration of the organic pollutant, k is the apparent reaction rate constant (mol $L^{-1}min^{-1}$), and K_A is the adsorption coefficient. **Figure 6.5** shows the plot of $1/r_o$ versus $1/C_o$ (using **8**-acrylic and **8**-acrylic-Ag_2WO_4 as examples), which was used to determine the values of k and K_A, listed in **Table 6.5**.

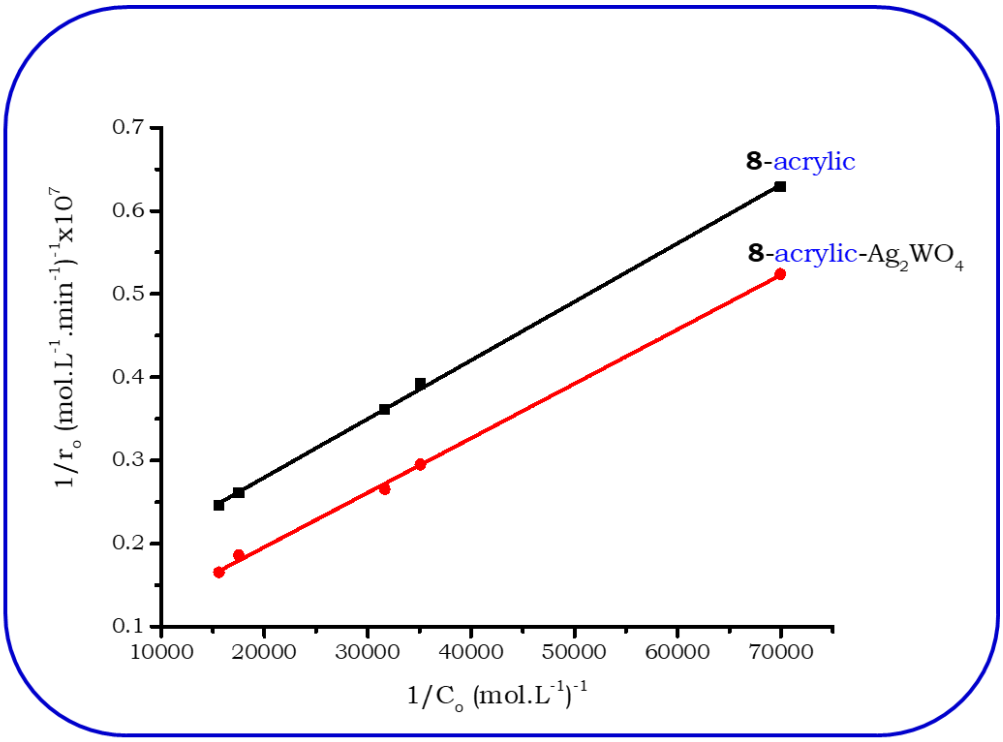

***Figure 6.5**: Plots of the reciprocal of initial reaction rate versus the reciprocal of the initial concentration for the photodegradation of DBT using **8**-acrylic and **8**-acrylic-Ag_2WO_4 as examples.*

The plots are linear, with y-intercept values larger than zero, suggesting that the Langmuir–Hinshelwood kinetics model is followed when an organic pollutant is degraded by Pc complexes and their conjugates under visible light. K_A values obtained for the nanoconjugates are higher than for Pcs alone, **Table 6.5**. Complex **5**-acetic for the degradation of MB gave the highest K_A compared to **5**-acrylic and **5**-propionic. MB and DBT give higher values when comparing K_A values for the degradation of three organic contaminants using **5**-acetic-$CoWO_4$ conjugates. Bi_2WO_6 generally exhibits higher K_A values than $NiWO_4$ in complexes **4** conjugated with both NPs for degradation DBT. This indicates that as the photocatalytic activity progresses, the adsorption of organic pollutants onto the conjugates also increases.

Table 6.5: Langmuir–Hinshelwood parameters for selected photocatalysts for the phototransformation of TC, MB, and DBT.

Photocatalyst	K_A ($mol^{-1}L$) 10^4	k($mol.L^{-1}min^{-1}$)10^{-8}	Pollutant
4-COOH **4**-COOH-$NiWO_4$ **4**-COOH-Bi_2WO_6	2.9 4.3 4.5	1.7 3.5 3.8	DBT
4-propionic **4**-propionic-$NiWO_4$ **4**-propionic-Bi_2WO_6	3.7 4.1 4.3	1.4 3.2 3.7	DBT
4-acetic **4**-acetic-$NiWO_4$ **4**-acetic-Bi_2WO_6	3.8 4.6 4.7	1.5 2.1 2.5	DBT
5-propionic **5**-propionic-$CoWO_4$	5.2 7.5	3.3 4.4	MB
5-acrylic **5**-acrylic-$CoWO_4$	4.7 5.4	2.2 3.8	MB
5-acetic **5**-acetic-$CoWO_4$ **5**-acetic-$CoWO_4$ **5**-acetic-$CoWO_4$	5.4 6.6 7.6 7.7	3.5 4.4 4.8 4.8	MB TC MB DBT
6-COOH **6**-COOH-$CoWO_4$	2.2 5.2	1.8 2.2	TC
7-acrylic **7**-acrylic-$CoWO_4$	1.6 2.3	1.1 1.3	TC
7-propionic	1.8 3.3	1.4 1.7	TC
8-propionic **8**-propionic-Ag_2WO_4	3.6 4.1	2.3 3.8	TC
8-acrylic **8**-acrylic-Ag_2WO_4	3.2 3.5	2.1 3.4	TC
8-acetic **8**-acetic-Ag_2WO_4	4.2 4.7	2.5 3.8	TC

6.5 Reusability studies

Considering industrial costs and practical applications, the recyclability of photocatalysts is fundamental in catalysis. Following filtration and magnetic separation, reusability studies of these complexes were performed. There is only a small decrease in k_{obs} and in initial rates following reuse, hence showing that the photocatalysts could be recovered (**Tables 6.2-6.4**). **Figure A9** in the appendix shows a slight decrease in the Q band intensity following the use of the catalyst but the Q band is still observed, thus the re-used photocatalysts may still be employed further.

6.6 The trends of the Pc complexes towards applications in this thesis

$NiWO_4$ and Bi_2WO_6 NPs are coupled to complexes **4** and are investigated for PACT and degrading DBT. The PACT and photodegradation of MB of complexes **5** and their conjugates with $CoWO_4$ are also evaluated.

In **Table 6.6**, **4**-acetic-Bi_2WO_6 exhibits the highest log reduction and K_{obs} degradation of DBT when compared to all complex **4** conjugates. The photodegradation of DBT and PACT activity are intimately correlated, as demonstrated by complex **4** and their conjugates. For the degradation of MB vs. PACT, low log reduction value and high photodegradation of MB are observed when **5**-acetic-$CoWO_4$ used as a catalyst. This could be due to the photocatalytic activity of acetic acid [**190**] not for PACT. **5**-acetic is linked to various nanoparticles (Ag-Fe_3O_4, Ag_2WO_4, $NiWO_4$, $CoWO_4$). The nanoconjugates are used to investigate the effect of NPs on the complex for photodegradation of MB/TC/DBT and PACT (**Table A1-A3**). The silver-based NPs give better PACT activity. Comparing different conjugates, k_{obs} values for

DBT phototransformation are larger for **5**-acetic-$CoWO_4$ and **5**-acetic-Ag-Fe_3O_4, this is not always the case for TC. In the case of MB, **5**-acetic-Ag-Fe_3O_4 shows the highest rate constants.

Table 6.6: PACT and photocatalytic activity of selectected catalysts.

Catalyst	PACT (log reduction)	DBT (k_{obs}) min^{-1} at 1.43×10^{-5} M
4-acetic-$NiWO_4$	3.95	5.98
4- acetic-Bi_2WO_6	4.55	6.15
4- COOH- $NiWO_4$	3.97	5.66
4- COOH-Bi_2WO_6	3.85	5.79
4-propionic-$NiWO_4$	3.77	2.98
4-propionic- Bi_2WO_6	3.25	3.10
Catalyst	PACT(log reduction)	MB(k_{obs}) min^{-1} at 2.63×10^{-5} M
5-acetic-$CoWO_4$	6.85	8.73
5-acrylic-$CoWO_4$	7.11	6.33
5-propionic-$CoWO_4$	7.14	8.28

6.7 Mechanism

To identify the generated reactive oxygen species under visible light irradiation, electron paramagnetic resonance (EPR) was employed. Possible photogenerated ROS include H_2O_2, $^1O_2$, $^{\bullet}OH$, as well as generated electron-holes. No ESR signals were observed in the dark. To investigate the involvement of $^{\bullet}OH$ radicals in photocatalytic reactions, DMPO was used. **Figure 6.6** presents no EPR spin trap signals for $^{\bullet}OH$, implying that these radicals were not involved in the photodegradation of organic pollutants and killing of bacteria in 2% DMSO dispersion.

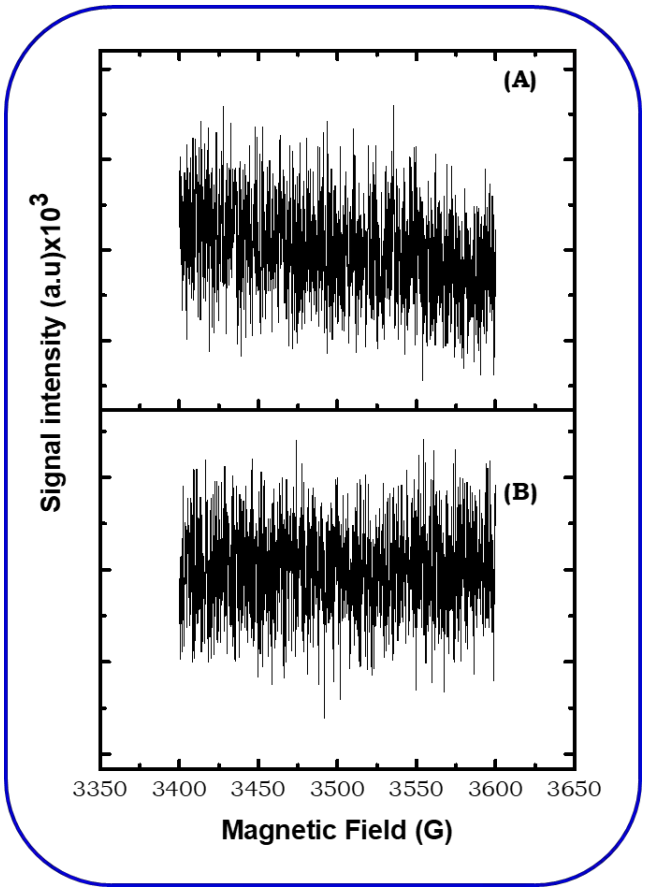

Figure 6.6: *EPR spectra showing DMPO results using Pc complexes and conjugates excited at (A) 670 nm and (B) 420 nm where the NPs absorb.*

Whereas, under similar conditions, when MPcs were excited at 670 nm in the presence of TEMP a three-peaked signal will appear between 3400 G - 3550 G as an indication of singlet oxygen generation by MPcs. The EPR signal intensified in MPc-NPs, showing that NPs enhanced the photoactivity of the MPc, **Figure 6.7**.

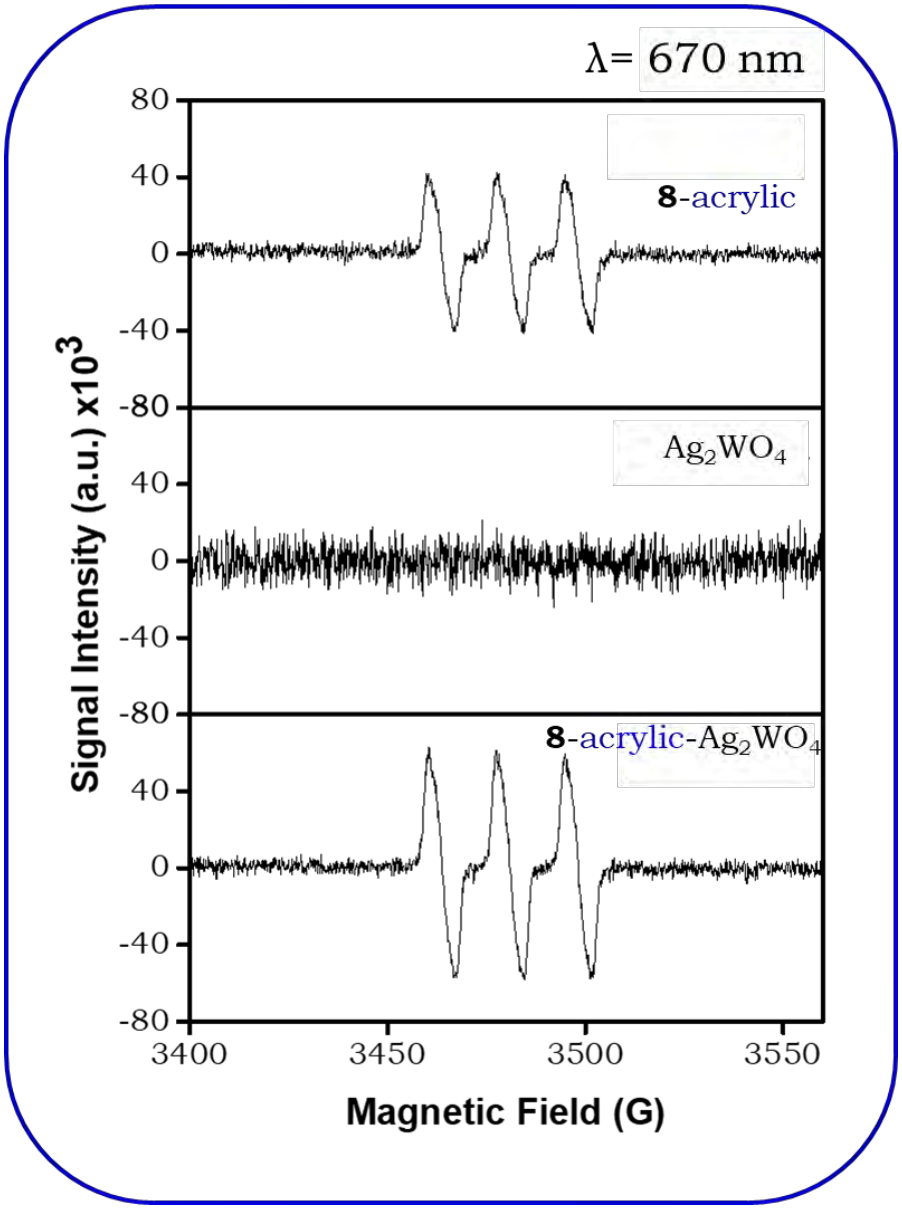

***Figure 6.7**: EPR showing singlet oxygen generated by MPcs and nanoconjugates in the presence of TEMP.*

The proposed mechanism is shown in **Scheme 6.1**. When the Pc alone or in conjugation with NPs is irradiated (step 1), it gets excited to a singlet excited state ^{1}Pc (step 2), as shown in **Scheme 6.1**. In the presence of the nanoparticles, intersystem crossing (ISC) (step 3), of the Pc to the triplet state (step 4) is enhanced which improves singlet oxygen generation and hence favors the degradation of organic pollutants or PACT against *S. aureus* (step 5). This work confirms that •OH radicals are not involved but $^1O_2$ is involved.

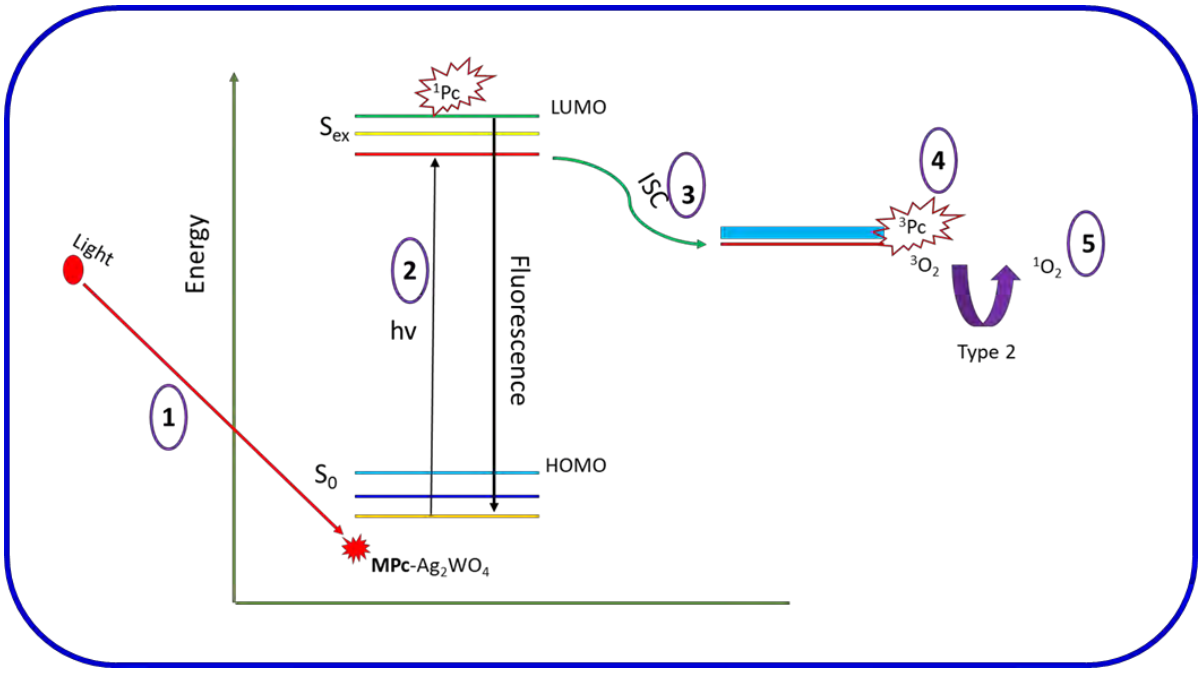

***Scheme 6.1**: Mechanism for the formation of ROS used for photodegradation of organic pollutants in the presence of Pc complex and conjugates (using TC as an example).*

6.5 Closing remarks

The conjugates produce high yields of singlet oxygen and photocatalytic activity. The employed photocatalysts followed first-order kinetics demonstrating high rate constants. The obtained results show that as-prepared asymmetrical zinc(II) phthalocyanines conjugated to NPs have a high potential to be used as suitable photocatalysts for the treatment of wastewaters. The enhanced photocatalytic activity of the conjugates is due to their higher singlet oxygen quantum yields.

Chapter 7

This chapter details on the use of Pcs, NPs and their respective conjugates as nonlinear optical absorbers. A side application using complexes **1**-ethanoic, **2**-propionic, and their conjugates with QDs.

7.1 Nonlinear optical (NLO) parameters

NLO studies are carried out as a side applicacation using using complexes **1**-ethanoic, **2**-propionic and their conjugates with QDs. The open Z-scan open aperture with 7 ns excitation pulses at 532 nm wavelength was used to obtain the nonlinear optical parameters. The experimental data were analyzed using the literature method [**199**], Equations (7.1 and 7.2).

$$T_{(Z)} = \frac{1}{1 + \beta_{eff} L_{eff} (I_{00}/(1 + (z/z_0)^2))} \qquad (7.1)$$

$$l_{eff} = \frac{1 - e^{-\alpha l}}{\alpha} \qquad (7.2)$$

where I_{oo} is the intensity of the light on focus, $T_{(Z)}$ is the normalized transmittance of the sample, z_o is the Rayleigh length, β_{eff} is the two-photon nonlinear absorption coefficient, z is the sample position with respect to input intensity, l_{eff} is the effective length for two-photon absorption, l is the path length of the sample and α is the linear absorption. The imaginary component of the third-order optical susceptibility

($I_m[\chi^{(3)}]$ in (esu) is directly proportional to β_{eff} via Equation 7.3 [**200**,**201**]

$$I_m[\chi^{(3)}] = \frac{n^2 \varepsilon_0 c \lambda \beta_{eff}}{2\pi} \qquad (7.3)$$

where λ is the wavelength of the laser light, ε_o is the permittivity of free space, c and n, are the speed of light in vacuum and the linear refractive index, respectively.

The ground state absorption cross-section (δ_o) is obtained from absorption spectroscopy using Equation 7.4

$$\delta_0 = {}^{\alpha}/_{N_0} \qquad (7.4)$$

where α is the linear absorption and N_o is the number of molecules per cm^3.

The magnitude of absorption cross-sections ratio (k) for the Pcs alone and conjugates is obtained from the ratios (δ_{ex}/δ_o) (where δ_{ex} = excited-state absorption cross-section), δ_{ex} is obtained by fitting experimental data set from Z-scan into excited-state absorption, Eq. 7.5 and 7.6 [**202,203**]

$$\frac{T}{T_{linear}} = \frac{\ln(1+q)}{q} \qquad (7.5)$$

$$q = \frac{\alpha}{2h\nu}\delta_{ex}I_oL_{eff} \qquad (7.6)$$

where T, T_{linear}, h, ν, I_o, are the nonlinear transmittance, linear transmittance, Planck's constant, frequency of the laser, and the total fluence on-axis, respectively. The final parameter is the limiting threshold (I_{lim}), describing the values of input fluence at which the transmittance is reduced by 50% of the linear transmittance value [**204**].

7.2 NLO response of complexes **1**-ethanoic and **2**-propionic

The NLO responses of complexes **1**-ethanoic and **2**-propionic are investigated in DMSO at 1.5 absorbances at the Q-band. Complexes **1**-ethanoic and **2**-propionic exhibits reverse saturable absorption (RSA). RSA observed in the **Figure 7.1** is typical of phthalocyanines [**205,206**]. The Z-scan curves of both complexes showed that complex **1**-ethanoic (Φ_T = 0.51) reduced transmittances better than **2**-propionic (Φ_T = 0.46) which is in agreement with the higher triplet quantum yield for the former.

There are no changes in the electronic absorption spectra of complexes or conjugates following Z-scan readings. Third-order nonlinear susceptibility ($I_mX^{(3)}$]), and nonlinear absorption coefficient (β_{eff}) are obtained using Equation **7.1-7.3**. Complex **1**-ethanoic has larger β_{eff} and ($I_mX^{(3)}$]) values of 59.5 cm/GW and 1.39×10^{-8} esu, respectively (**Table 7.1**), compared to complex **2**-propionic alone, in line with triplet state quantum yields. A material can be a good optical limiter if it has high β_{eff} and ($I_mX^{(3)}$]) values. The mechanism for the nonlinear optical behaviour of semiconductor quantum dots is reported to be based on the free carrier absorption (FCA) [**133**], which contributes to the NLO behaviour of the Pcs. Conjugation of complexes (**1**-ethanoic and **2**-propionic) to CdTe/ZnSeS/ZnO yield a further dip in the Z-scan profiles of the conjugates, **Figure 7.1**. β_{eff} values of 74.1 cm/GW and 51.0 cm/GW were obtained for **1**-ethanoic-CdTe/ZnSeS/ZnO and **2**-propionic-CdTe/ZnSeS/ZnO, respectively, the values are much higher than the Pc complexes alone.

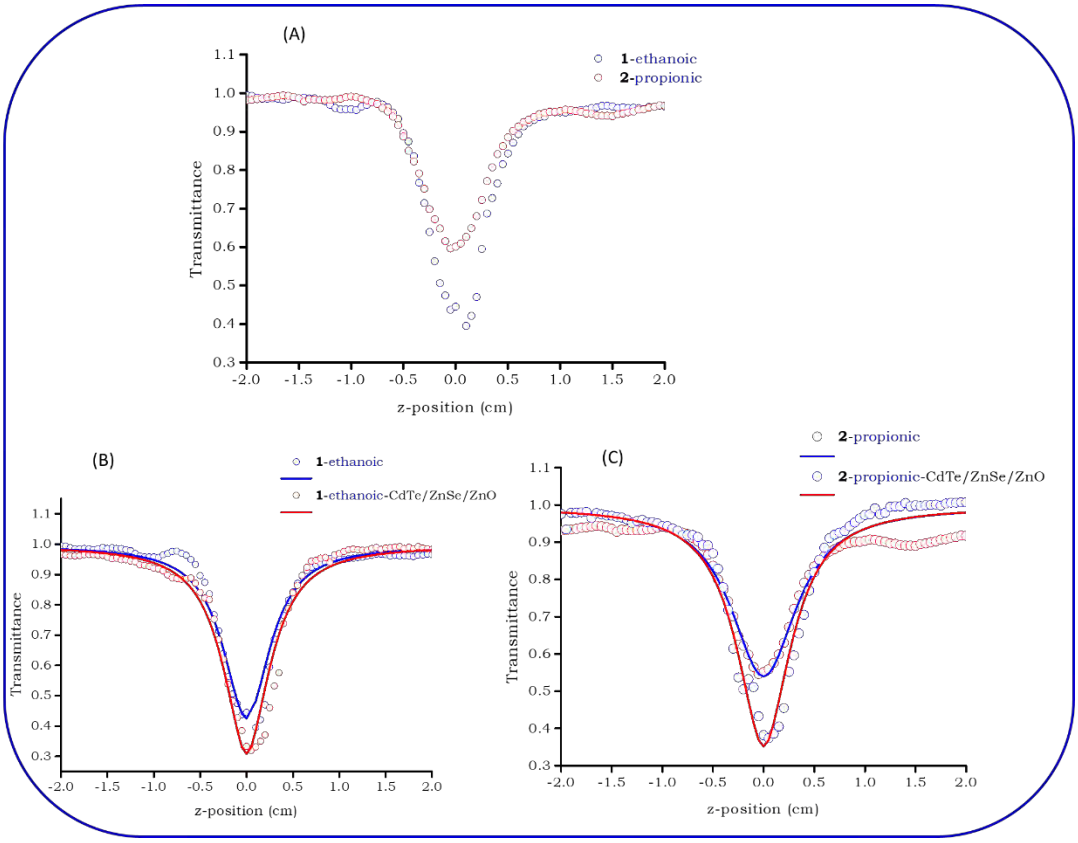

***Figure 7.1**: (A) Open aperture Z-scan signature for complexes **1** and **2**, (B) **1** and its conjugate with CdTe/ZnSeS/ZnO, (C) **2** and its conjugate with CdTe/ZnSeS/ZnO.*

One more important term in optical limiting is limiting threshold (I_{lim}), describing the values of input fluence at which the transmittance is reduced by 50% of the linear transmittance value. As illustrated in **Figure 7.2** transmittance decreases slowly for the Pc and conjugates with an increase in incident fluence. I_{lim} is much lower for the conjugates, **Table 7.1**, showing that the Pc-QDs combination offers a great advantage. Higher δ_{ex} values for the conjugates confirmed great absorption cross-sections in the excited state which favour strong NLO response as indicated by high k values listed in **Table 7.1**.

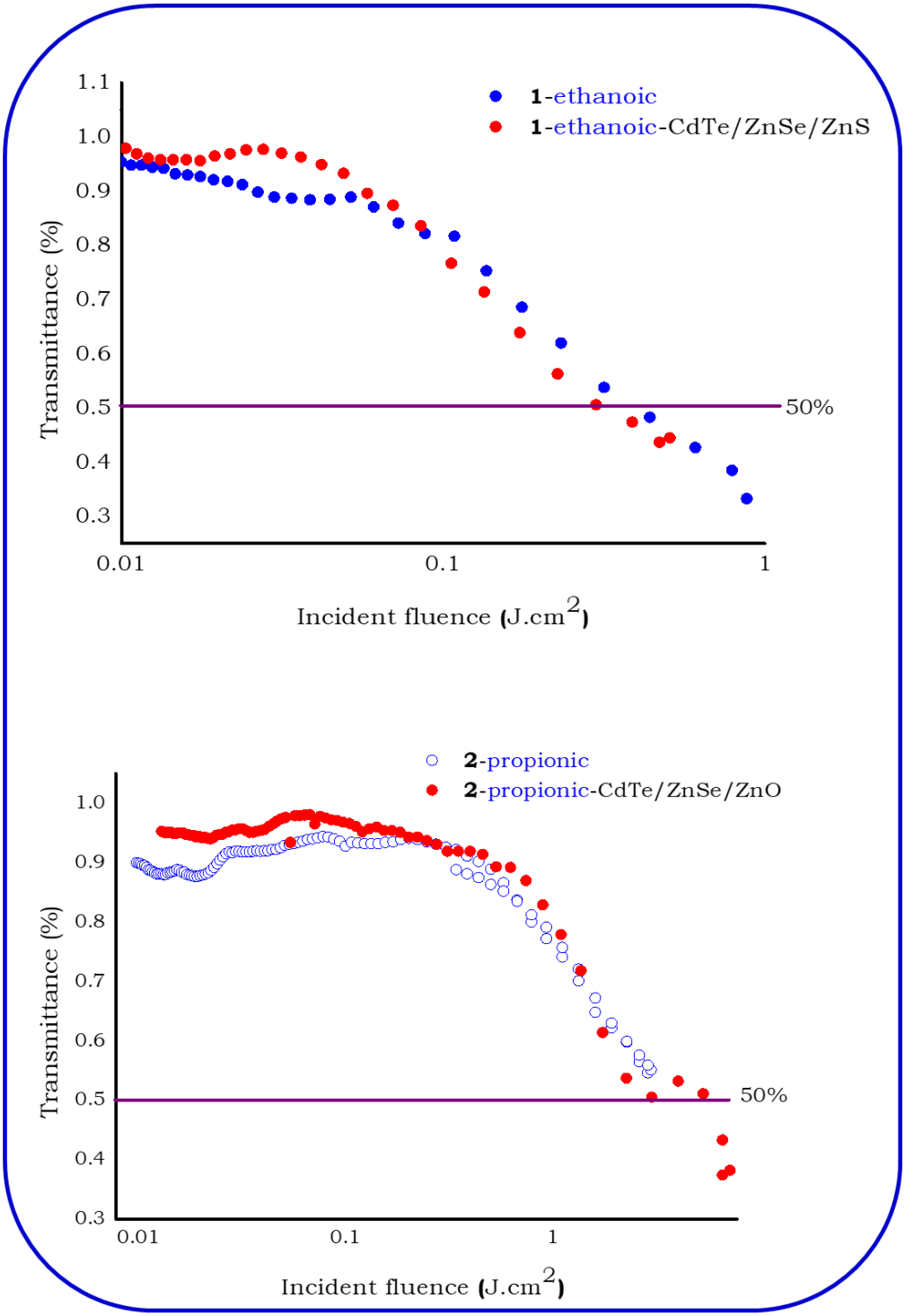

***Figure 7.2**: Transmittance versus incident fluence for complexes **1**-ethanoic and **2**-propionic and their nanoconjugates with CdTe/ZnSeS/ZnO.*

Table 7.1*:* NLO studies of complexes and conjugates in DMSO.

Complex	I_{lim}	$\kappa(\sigma_{ex}/\sigma_1)$	β_{eff}***(cm/GW)***	$L_m[\chi^3]$ ***(esu)***
1-ethanoic	0.49	6.61	59.5	1.39×10^{-8}
1-ethanoic-CdTe/ZnSeS/ZnO	0.29	8.10	74.1	1.73×10^{-8}
2-propionic	1.45	3.81	3.00	6.99×10^{-9}
2-propionic CdTe/ZnSeS/ZnO	1.20	4.16	51.0	1.19×10^{-8}

7.3 Closing remarks

The Z-scan technique was employed to experimentally test the nonlinear optical response of complexes and nanoconjugates in solution at the laser excitation wavelength of 532 nm with a 7 ns pulse. The bonlinear absorption coefficient, third-order optical susceptibility and optical limiting threshold of the materials were obtained from the Z-scan data. The nonlinear absorption parameters improved in the presence of CdTe/ZnSe/ZnO, with **1**, and **1**-CdTe/ZnSe/ZnO, giving the best results due to the presence of electron-donating substituents.

Chapter 8

This chapter discusses the conclusion and future prospects of this work.

8. Conclusion

In this thesis, new asymmetric phthalocyanines containg was a zinc(II) metal and substituted with different groups on the ring were designed and their synthesis methods were described. Their structures were characterized using different spectroscopic techniques such as MALDI-TOF MS, ^{1}H-NMR, FTIR, UV-vis, elemental analysis. According to the determined photophysical properties of asymmetric phthalocyanines, it has been reported that asymmetric substitution resulted in higher triplet quantum yields due to the increased dipole moment, thus higher singlet oxygen quantum yields.

Efficient yield-rich singlet oxygen quantum yields of asymmetric PCs were obtained by covalently linking phthalocyanines to nanoparticles via ester or amide bonds.

It has been found that the PACT activities and photocatalytic activities of the studied asymmetric zinc(II) Pc complexes increase in the conjugates corresponding to high singlet oxygen quantum yield values.

The effect of Ag-Fe_3O_4 on the Pc complexes towards degradation of MB/DBT indicated fast degradation rate with higher rate constants. EPR trapping agents revealed that the predominant reactive species was singlet oxygen quantum yield while •OH showed no influence on the photocatalytic reaction.

Metallophthalocyanines showed reverse saturable absorption behaviour. Complex **1**-ethanoic exhibit higher third-order nonlinear susceptibility, nonlinear absorption coefficient, and lower limiting threshold (I_{lim}), hence better optical limiting behaviour. The combination of Pc complexes and

quantum dots show great promise as optical limiter. The nonlinear absorption parameters improved in the presence of CdTe/ZnSe/ZnO QDs.

Future prospects

It could be of high interest to explore photodegradation of organic pollutants in water and photoinactivation of *S. aureus* concurrently using a comparable approach and under the same conditions.

1. M.S. El-Shahawi, A. Hamza, A.S. Bashammakh, W.T. Al-Saggaf, An overview on the accumulation, distribution, transformations, toxicity and analytical methods for the monitoring of persistent organic pollutants. Talanta 80 (2010) 1587.
2. F. Konečný, Z. Boháček, P.Müller, M. Kovářová, I. Sedláčková, Contamination of soils and groundwater by petroleum hydrocarbons and volatile organic compounds – Case study: ELSLAV BRNO. Bull. Geosci. 78 (2003) 225.
3. S. Vedachalam, N. Baquerizo, A.K. Dalai, Review on impacts of low sulfur regulations on marine fuels and compliance option. Fuel 310 (2022) 122243.
4. M. Te, C. Fairbridge, Z. Ring, Oxidation reactivities of dibenzothiophenes in polyoxometalate/H_2O_2 and formic acid/H_2O_2 systems. Appl. Catal. A: General 219 (2001) 267.
5. M.T. Timko, J.A Wang, J. Burgess, P. Kracke, L. Gonzalez, C. Jaye, Roles of surface chemistry and structural defects of activated carbons in the oxidative desulfurization of benzothiophenes. Fuel 163 (2016) 223.
6. M. Campos-Martin, M.C. Capel-Sanchez, J.L.G. Fierro, Highly efficient deep desulfurization of fuels by chemical oxidation. Green Chem. 6 (2004) 557.
7. Guidelines for Flue Gas Desulfurization (FGD) water sampling and analysis: Trace Metals EPRI, Palo Alto, CA ;2009. 1018223.
8. Y. Kuang, X. Zhang, S. Zhou, Adsorption of methylene blue in water onto activated carbon by surfactant modification. Water 12 (2020) 587.

9. R. Saravanan, S. Joicy, V.K. Gupta, V. Narayanane, A. Stephen, Visible light induced degradation of methylene blue using CeO_2/V_2O_5 and CeO_2/CuO catalysts. Mater. Sci. Eng. C 33 (2013) 4725.
10. P.C. Vandevivere, R. Bianchi, W. Verstraete, Review: Treatment and reuse of wastewater from the textile wet-processing industry: Review of emerging technologies. J. Chem. Technol. Biotechnol. 72 (1998) 337
11. I.A.W. Tan, A.L. Ahmad, B.H. Hameed, Adsorption of basic dye on high-surface area activated carbon prepared from coconut husk: Equilibrium, kinetic and thermodynamic studies. J. Hazard. Mater. 154 (2008) 337.
12. B. Lellis, C. Z. Fávaro-Polonio, J. Alencar, P. Julio, C. Polonio, Effects of textile dyes on health and the environment and bioremediation potential of living organisms. Biotechnol. Res. Int. 3 (2019) 275.
13. S.A. Kraemer, A. Ramachandran, G.G. Perron, Antibiotic pollution in the environment: from microbial ecology to public policy. Microorganisms 7 (2019) 180.
14. F. Su, P. Li, J. Huang, M. Gu, Z. Liu, Y. Xu, Photocatalytic degradation of organic dye and tetracycline by ternary Ag_2O/AgBr-CeO_2 photocatalyst under visible-light irradiation. Sci. Rep. 11 (2021) 85.
15. A.V. Augugliaro, A. Paola, E. Garcıa-Lopez, V. Loddo, G. Marcı, L. Palmisano, Removal of drugs in aqueous systems by photoassisted degradation. J. Appl. Electrochem. 35 (2005) 765.
16. S.J. Harris, M. Cormican, E. Cummins, Antimicrobial residues and antimicrobial-resistant bacteria: impact on the microbial environment

and risk to human health-A Review. Hum. Ecol. Risk Assess. 18 (2012) 767.

17. M. Yu, C. Sun, L. Wang, K. Zang, M. L. Zhou, Y. Zheng, Semi-coke activated persulfate promotes simultaneous degradation of sulfadiazine and tetracycline in a binary mixture. Chem. Eng. J. 416 (2021) 129122
18. N. Milić, M. Milanović, N.G. Letić, M.T. Sekulić, J. Radonić, I. Mihajlović, M.V. Miloradov, Occurrence of antibiotics as emerging contaminant substances in aquatic environment. Int. J. Environ. Health Res. 23 (2013) 296.
19. A. Anas, J. Sobhanan, K.M. Sulfiya, C. Jasmin, P.K. Sreelakshmi, V. Biju, Advances in photodynamic antimicrobial chemotherapy. J. Photochem. Photobiol. C (2021) 100452.
20. G. Claessens, U. Hahn, T. Torres, Phthalocyanines: From outstanding electronic properties to emerging applications. Chem. 8 (2008) 75.
21. J. Mack, M. J. Stillman, Photochemical Formation of the Anion Radical of Zinc Phthalocyanine and Analysis of the Absorption and Magnetic Circular Dichroism Spectral Data. Assignment of the Optical Spectrum of ZnPc(-3)]. J. Am Chem. Soc. 116 (1994) 1292.
22. A.M. Schaffer, M. Gouterman. E. R. Davidson, Extended Hückel calculations on metal phthalocyanines and tetrazaporphins. Theor. Chim. Acta 30 (1973) 9.
23. A.J. McHugh, M. Gouterman. J.C. Weiss, Porphyrins XXIV. Energy, oscillator strength, and Zeeman splitting calculations (SCMO-CI) for phthalocyanine, porphyrins, and related ring systems. Theor. Chim. Acta 24 (1972) 346.

24. H.N. Ravala, D.S .Sutarb, V.R Rao, Copper (II) phthalocyanine based organic electronic devices for ionizing radiation dosimetry applications. Org. Electron 14 (2013) 1281.

25. Z. Deng, Z. Lü, Y.Chen, Y. Yina, Y. Zou, J. Xiao, Y. Wang, Aluminum phthalocyanine chloride as a hole injection enhancer in organic light-emitting diodes. Solid State Electron 89 (2013) 22.

26. J. Aimi, P.Wang, C-C. Shih, C-F. Huang, T. Nakanishi, M. Takeuchi, H-Y. Hsueh, W-C. Chen, A star polymer with a metallo-phthalocyanine core as a tunable charge storage material for nonvolatile transistor memory devices. J. Mater. Chem. C 6 (2018) 2724.

27. L. Martín-Gomis, F. Fernández-Lázaro, Á. Sastre-Santos, Advances in phthalocyanine-sensitized solar cells (PcSSCs). Mater. Chem. A 2 (2014) 15672.

28. X. Zhao, X-Q Yan, Qiang Ma, Jun Yao, X-L. Zhang, Z-B Liu, J-G Tian, Nonlinear optical and optical limiting properties of graphene hybrids covalently functionalized by phthalocyanine. Chem. Phys. Lett. 577 (2013) 62.

29. A.A. Atta-Eyisona, G.D Anukwah, R. Zugle, Photocatalysis using zinc oxide-zinc phthalocyanine composite for effective mineralization of organic pollutants. Catal. Commun. 160 (2021) 106357.

30. A. Erdogmus, M. Arıcı, Novel soluble octa-substituted phthalocyanines bear-ing chloro and long alkyl chain containing fluorine: Synthesis, characterization and photophysical and photochemical properties. Fluor. Chem. 166 (2014) 127.

31. M.S. Rodriguez-Morgade, G. de la Torre, T. Torres, in The Porphyrin Handbook, eds. K. M. Kadish, K. M. Smith, R. Guilard, Academic Press, San Diego vol. 15 (2003) pp 125.

32. C.V. van Nostrum, R.J.M. Nolte, Functional supramolecular materials: self-assembly of phthalocyanines and porphyrazines. Chem. Comm. 21 (1996) 2385.

33. V.N. Nemykin, S.V. Dudkin, F. Dumoulin, C. Hirel, A.G. Gürek, V. Ahsen, Synthetic approaches to asymmetric phthalocyanines and their analogues. Arkivoc (2014) 142.

34. N. Kobayashi, R. Kondo, S.I. Nakajima, T. Osa, New route to unsymmetrical phthalocyanine analogs by the use of structurally distorted subphthalocyanines. J. Am. Soc. 112 (1990) 9640.

35. T. Yonekura, T. Ohsaka, F. Kitamura, K. Tokuda, Synthesis and electrochemical properties of bis(octacyanophthalocyaninato)neodymium(III) complex. J. Porphyr. Phthalocy. 9 (2005) 54.

36. A. Jablonski, Über den mechanismus der photolumineszenz von farbstoffphosphoren. Z. Phys. 94 (1935) 38.

37. P. W. Atkins, in Physical Chemistry, P.W. Atkins (Ed.), Oxford University Press, Oxford, 6th Edition, (1998) Chapter 17.

38. K. Ishii, N. Kobayashi, in The Porphyrin Handbook, K.M. Kadish, K.M. Smith, R. Guilard, (Eds.), Elsevier Science, New York, vol. 16 (2003) Chapter 102.

39. J.P. Celli, B.Q. Spring, I. Rizvi, C.L. Evans, K.S. Samkoe, S. Verma, B.W. Pogue, T. Hasan, Imaging and Photodynamic Therapy:

Mechanisms, Monitoring, and Optimization. Chem. Rev. 110 (2010) 2795.

40. D. Phillips, A lifetime in photochemistry; some ultrafast measurements on singlet states. Proc. Math. Phys. Eng. Sci. 472 (2016) 20160102.
41. C.-M. Yang, C. -H. Wu, H. -H. Liao, K. -Y. Lai, H.-P. Cheng, S. -F. Horng, Enhanced photovoltaic response of organic solar cell by singlet-to-triplet exciton conversion. Appl. Phys. Lett. 90 (2007) 133509.
42. W. Sun, G. Wang, Y. Li, M. J. F. Calvete, D. Dini, M. Hanack, Axial halogen ligand effect on photophysics and optical power limiting of some indium naphthalocyanines. J. Phys. Chem. A 111 (2007) 3263.
43. S. Fery-Forgues, D. Lavabre, Are fluorescence quantum yields so tricky to measure? A demonstration using familiar stationery products. Chem. Educ. 76 (1999) 1260.
44. A. Ogunsipe, J. Chen, T. Nyokong, Photophysical and photochemical studies of zinc (II) phthalocyanine derivatives-effects of substituents and solvents. New J. Chem. 28 (2004) 822.
45. A.M. Brouwer, A.M. Standards for photoluminescence quantum yield measurements in solution. Pure App. Chem. 83 (2011) 2213.
46. A.G. Ryder, S. Power, T.J. Glynn, J.J. Morrison, Proc, Box C/D RNA guides for the ribose methylation of archaeal tRNAs. The tRNATrp intron guides the formation of two ribose-methylated nucleosides in the mature tRNATrp. Nucleic Acids Res. 9 (2001) 4518.
47. A.H. Clayton, K. Nectarios, H.C. Stephen, C.N. Edouard, Dual-channel photobleaching FRET microscopy for improved resolution of protein association states in living cells. Eur. Biophy. J. 34 (2005) 82.

48. H. Du, R.C.A Fuh, J. Li, L.A. Corkan, J.S. Lindsey, Photochem CAD: A computer-aided design and research tool in photochemistry and photobiology. Photochem. Photobiol. 68 (1998)141.
49. J.S. Hsioao, B.P. Krueger, R.W Wagner, T.E. Johnson, J.K. Delaney, D.C. Mauzerall, G.R. Fleming, J.S. Lindsey, D. F. Bocian, R.J. Donohoe, Soluble synthetic multiporphyrin arrays: Modular design and synthesis. J. Am. Chem. Soc. 118 (1996) 11181.
50. T.H. Tran-Thi, C. Desforge, C. Thiec, S. Gaspard, Singlet-singlet and triplet-triplet intramolecular transfer processes in a covalently linked porphyrin-phthalocyanine heterodimer. J. Phys. Chem. 93 (1989) 1226.
51. T. Nyokong, E. Antunes, In Eds. K.M. Kadish, K.M Smith, R. Guilard, The Handbook of Porphyrin Science. Chapter title: Photochemical and photophysical properties of metallophthalocyanine, Singapore: World Scientific vol. 7 (2010) pp. 247.
52. S.L. Murov, Carmichael, G.L. Hug, Handbook of photochemistry (2nd edn) M. Decker, New York (1993)
53. N.A Kuznetsova, N.S Gretsova, V.M Derkacheva, O.L Kaliya, E.A Lukyanets, Sulfonated phthalocyanines: aggregation and singlet oxygen quantum yield in aqueous solutions. J. Porphyr. Phthalocyanines 7 (2003) 147.
54. S. Mapukata, N. Kobayashi, M. Kimura, T. Nyokong, Asymmetrical and symmetrical zinc phthalocyanine-cobalt ferrite conjugates embedded in electrospun fibers for dual photocatalytic degradation of azo dyes: Methyl Orange and Orange G. J. Photobiol. A Chem. 379 (2019) 112.

55. S. Mapukata, N. Nwahara, T. Nyokong, The photodynamic antimicrobial chemotherapy of Stapphylococcus aureus using an asymmetrical zinc phthalocyanine conjugated to silver and iron oxide based nanoparticles. J. Photobiol. A Chem. 402 (2020) 112813.
56. A. Luna-Flores, M. A. Valenzuela, J. A. Luna-López, A. D. Hernández de la Luz, L. C. Muñoz-Arenas, M. Méndez-Hernández, J. L. Sosa-Sánchez, Synergetic enhancement of the photocatalytic activity of TiO_2 with visible light by sensitization using a novel push-pull zinc phthalocyanine. Int. J. Photoenergy 2017 (2017) 9.
57. Z. Gao, X. Tao, Y. Cui, T. Satoh, T. Kakuchi, Q. Duan, Synthesis of end-functionalized poly(N-isopropylacrylamide) with group of asymmetrical phthalocyaninevia atom transfer radical polymerization and its photocatalytic oxidation of Rhodamine B. Polym. Chem. 2 (2011) 2590.
58. G.G. Matlou, T. Nyokong, Photophysico-chemical properties and photoinactivation of Staphylococcus Aureus using zinc phthalocyanines linked silver nanoparticles conjugates. Dyes Pigm.176 (2020) 108237.
59. S. Temizel, T. Çakır, Ç. Altuğ, M. Sevim, Novel polymers with cobalt(II)phthalocyanine moieties as effective heterogeneous photocatalysts for visible-light-driven photodegradation of organic dyes in aqueous solution. J. Photobiol. A Chem. 401 (2020) 1127412.
60. N.M. lele, K.Z. Tshentu, G. Priniotakis, P. Westbroek, T. Nyokong, Photodynamic inactivation of Staphylococcus aureus using low

symmetrically substituted phthalocyanines supported on a polystyrene polymer fiber. Dyes Pigm. 96 (2013) 500.

61. R.M. Abdelhameed, M.El-Shahat, M. A.A. El-Ghaffar, Boosting the photocatalytic activity of Ti-MOF via emerging with metal phthalocyanine to degrade hazard textile pigments. Alloys Compd. 896 (2022) 162992.
62. O.L. Osifeko, T. Nyokong, Effects of symmetry and the number of positive charges on the photocatalytic activity of indium phthalocyanines when embedded in electrospun fibers. Inorg. Chim. Acta 458 (2017) 50.
63. O.L. Osifeko, M. Durmus, T. Nyokong, Physicochemical and photodynamic antimicrobial chemotherapy studies of mono-and tetra-pyridyloxy substituted indium (III) Phthalocyanines. J. Photochem. Photobiol. A Chem. 301 (2015) 47.
64. O.L. Osifeko, I. Uddin, P.N. Mashazi, T. Nyokong, Physicochemical and antimicrobial photodynamic chemotherapy of unsymmetrical indium phthalocyanines alone or in the presence of magnetic nanoparticles. New J. Chem. 40 (2016) 271.
65. B. Cabir, M. Yurderi, N. Caner, M.S. Agirtas, M. Zahmakiran, M. Kaya, Methylene blue photocatalytic degradation under visible light irradiation on copper phthalocyanine-sensitized TiO2 nanopowder. Mater. Sci. Eng. B 224 (2017) 9.
66. S. Gümrükçü, M. Özçeşmeci, E. Sezer, B. Ustamehmetoğlu, E.Hamuryudan, In-situ synthesis of phthalocyanines on electrospun

TiO_2 nanofiber by solvothermal process for photocatalytic degradation of methylene blue. Turk. J. Chem. 45 (2021) 2034.

67. A. Hısır, G.K. Karaoglan, O. Avcıata, Synthesis of tetracarboxy phthalocyanines modified TiO_2 nanocomposite photocatalysts and investigation of photocatalytic decomposition of organic pollutant methylene blue under visible light. J. Mol. Struct. 1266 (2022) 133498.
68. Chen Chen, Zhanhu Ma, Shiying Zhou, Tianqi Li, Xiaoling Sun, Cobalt-Tetracarboxyl-Phthalocyanine Linked with Fe_3O_4/Chitosan Microsphereas—Efficient Catalyst for Dye Degradation. Catal. Lett. 147 (2017) 2399.
69. W. Vallejo, C. Diaz-Uribe, Á. Cantillo, Methylene blue photocatalytic degradation under visible irradiation on TiO_2 thin films sensitized with Cu and Zn tetracarboxy-phthalocyanines. J. Photobiol. A Chem. 299 (2015) 80.
70. X. Tang, Y. Liu, Heterogeneous photo-Fenton degradation of methylene blue under visible irradiation by iron tetrasulphophthalocyanine immobilized layered double hydroxide at circumneutral pH. Dyes Pigm. 134 (2016) 397.
71. R. Liu, J. Zhang, Z. Xu, D. Zhao, S. Sun, Visible light photocatalytic oxidative desulfurization using Ti-MCM-41-loaded iron phthalocyanine combined with ionic liquid extraction. J. Mater. Sci. 53 (2018) 4927.
72. G. Zhang, B. Liu, H. Zhou, Y. Yang, W. Chen, J. Zhao, Graphene wrapped phthalocyanine: Enhanced oxidative desulfurization for dibenzothiophene in fuel. Appl. Organometal. Chem. 32 (2018) 4477.

73. S-W. Li, Y-Y.L. Yang, Z. Liu, R.-M. Gao, J-she Zhao, Photocatalytic oxidation desulfurization of model diesel over phthalocyanine/La0.8Ce0.2NiO3. Colloid Interface Sci. 460 (2015) 8.
74. S. Chen, W. Lu, Y. Yao, H. Chen, W. Chen, Oxidative desulfurization of dibenzothiophene with molecular oxygen catalyzed by carbon fiber-supported iron phthalocyanine. React. Kinet. Mech. Catal. 111 (2014) 525.
75. K. Wang, L. Yu, S. Yin, H. Li, H. Li, Photocatalytic degradation of methylene blue on magnetically separable FePc/Fe_3O4 nanocomposite under visible irradiation. Pure Appl. Chem. 81 (2009) 2327.
76. A. Samokhvalov, Desulfurization of real and model liquid fuels using light: photocatalysis and photochemistry. Catal. Rev. Sci. Eng. 54 (2012) 281.
77. Y. Sun, W. Zheng, Sh. Fu, R.P. Singh, Immobilization of iron phthalocyanine on 4-aminopyridine grafted polystyrene resin as a catalyst for peroxymonosulfate activation in eliminating tetracycline hydrochloride. J. Chem. Eng. 391 (2020) 123611.
78. Z. Huang, Bi. Zheng, S. Zhu, Y. Yao, Y.Ye, W. Lu, W. Chen, Photocatalytic activity of phthalocyanine-sensitized TiO2–SiO2 microparticles irradiated by visible light. Mater. Sci. Semicond. Process 25 (2014) 148.
79. G. Zhang, J. Ren, W. Zhao, M. Tian, W. Chen, Photocatalytic desulfurization of thiophene base on molecular oxygen and zinc phthalocyanine/g-C3N4. Res. Chem. Intermed. 44 (2018) 5547.

80. K. Li, Y. Pang, Q. Lu, In situ growth of copper(II) phthalocyanine sensitized electrospun CeO2/Bi2MoO6 nanofibers: a highly efficient photoelectrocatalyst towards degradation of tetracycline. Inorg. Chem. Front. 6 (2019) 3215.

81. M.L. Maya-Treviño, J.L. Guzmán-Mar, L. Hinojosa-Reyes, A. Hernández-Ramírez, Synthesis and photocatalytic activity of ZnO-CuPc for methylene blue and potassium cyanide degradation. Mater. Sci. Semicond. Process 77 (2018) 74.

82. Y. Heab, Z. Huanga, Z. Mac, B. Yaoa, H. Liud, L. Hua, Q. Zhaoa, Q. Yanga, D. Liua, D. Du, Highly efficient photocatalytic performance and mechanism of α-ZnTcPc/g-C3N4 composites for methylene blue and tetracycline degradation under visible light irradiation. Appl. Surf. Sci. 498 (2019) 143834.

83. W. Vallejo, C. Diaz-Uribe, Á. Cantillo, Methylene blue photocatalytic degradation under visible irradiation on TiO_2 thin films sensitized with Cu and Zn tetracarboxy-phthalocyanines. J. Photobiol. A Chem. 299 (2015) 80.

84. M. Tian, Y.He, G. Zhang, Carbon nanotubes wrapped phthalocyanine: enhanced oxidative desulfurization for dibenzothiophene in fuel. J. Nanopart. Res. 23 (2021) 223.

85. M. Gao, G. Zhang, M. Tian, B. Liu, W. Chen, Oxidative desulfurization of dibenzothiophene by central metal ions of chlorophthalocyanines-tetracarboxyl complexes. Inorg. Chim. Acta 485 (2019) 58.

86. V. Saez, I. D. L. Souza, C. R. E. Mansur, Lipid nanoparticles (SLN & NLC) for delivery of vitamin E: a comprehensive review. Int. J. Cosmet. Sci. 40 (2018) 103.

87. M. Jena, S. Patil, Overview on Iron oxide magnetic nanoparticles and polyol method of synthesis. J. Biomed. Sci. 11 (2022) 6.

88. I. Khana, K. Saeed, I. Khan, Nanoparticles: Properties, applications and toxicities. Arab. J. Chem. 12 (2019) 209.

89. R. Daghrir, P. Drogui, D. Robert, Modified TiO_2 for environmental photocatalytic applications: A Review. Ind. Eng. Chem. Res. 52 (2013) 3581.

90. X. Hu, X. Liu, J. Tian, Y. Li, H. Cui, Towards full-spectrum (UV, visible, and near-infrared) photocatalysis: achieving an all-solid-state Z-scheme between Ag_2O and TiO_2 using reduced graphene oxide as the electron mediator. Catal. Sci. Technol. 7 (2017) 4193.

91. M. Mousavi, A. Habibi-Yangjeh, Metal tungstate semiconducting nanoparticles have gained much interest due to their wide range applications including: in photodegradation. Mater. Res. Bull. 105 (2018) 159.

92. F. Ahmadi, M. Rahimi-Nasrabadi, A. Fosooni, M. Daneshmand, Synthesis and application of $CoWO_4$ nanoparticles for degradation of methyl orange. J. Mater. Sci.: Mater. Electron. 27 (2016) 9514.

93. S. Kumar, A., Tarun, J. Saxena, C. Bansal, P. Kumari, Visible light-assisted photodegradation by silver tungstate-modified magnetite nanocomposite material for enhanced mineralization of organic water contaminants. Appl. Nanosci. 10 (2020) 1555.

94. M. Rahimi-Nasrabadi, S. M. Pourmortazavi, M. Aghazadeh, M. R. Ganjali, M. S. Karimi, P. Novrouzi, Optimizing the procedure for the synthesis of nanoscale gadolinium(III) tungstate as efficient photocatalyst. J. Mater. Sci.: Mater. Electron. 28 (2017) 3780.

95. R. Karthiga, B. Kavitha, M. Rajarajan, A. Suganthi, Photocatalytic and antimicrobial activity of $NiWO_4$ nanoparticles stabilized by the plant extract. Mater. Sci. Semicond. Process 40 (2015) 123.

96. H-W. Shim, I-S. Cho, K.S. Hong, A-H. Lim, D-W. Kim, Wolframite-type $ZnWO_4$ nanorods as new anodes for li-ion batteries. J. Phys. Chem. C 115 (2011) 16228.

97. E. Antolini, E. R. Gonzalez, Tungsten-based materials for fuel cell applications. Appl. Catal. B 96 (2010) 245.

98. S.F. Anis, B. S. Lalia, A. O. Mostafa, R. Hashaikeh, Electrospun nickel–tungsten oxide composite fibers as active electrocatalysts for hydrogen evolution reaction. J. Mater. Sci. 52 (2017) 7269.

99. S.F. Anis, B.S. Lalia, G. Palmisano, R.Hashaikeh, Photoelectrochemical activity of electrospun $WO_3/NiWO_3$ nanofibers under visible light irradiation. J. Mater. Sci. 53 (2018) 2208.

100. Y. Bi, S. Zeng, H. Nie, M. Li, Q. Yang, G. Xia, D. Li, Self-complexation: the nature for high hydrodesulfurization activity of NiW_{O4} nanoparticles, Catal. Commun. 57 (2014) 5.

101. Y. Bi, H. Nie, D. Li, S. Zeng, Q. Yang, M. Li, $NiWO_4$ nanoparticles: a promising catalyst for hydrodesulfurization, Chem. Commun. 46 (2010) 7430.

102. N. Sozer, J.L. Kokini, Use of quantum nanodot crystals as imaging probes for cereal proteins. Food Res. Int. 57 (2014) 142.

103. P. Juzenas, W. Chen, Y.P. Sun, M.A.N. Coelho , R. Generalov, N. Generalova, I.L. Christensen, Quantum dots and nanoparticles for photodynamic and radiation therapies of cancer. Adv. Drug Delivery Rev. 60 (2008) 1600.

104. H. He, X. Sun, X. Wang, H. Xu, Synthesis of highly luminescent and biocompatible CdTe/CdS/ZnS quantum dots using microwave irradiation: a comparative study of different ligands. J. Lumin. 29 (2014) 837.

105. J. Britton, A.G. Martynov, D.O Oluwole, Y.G. Gorbunova, A. Y. Tsivadze, T. Nyokong, Improvement of nonlinear optical properties of phthalocyanine bearing diethyleneglycole chains: Influence of symmetry lowering vs. heavy atom effect. J. Porphyr. Phthalocy. 20(2016) 1296.

106. H. Chen, Y. Gong, R. Han, Cadmium Telluride Quantum Dots (CdTe-QDs) and Enhanced Ultraviolet-B (UV-B) radiation trigger antioxidant enzyme metabolism and programmed cell. PloS One 9 (2014) 110400.

107. Z.Y. Gu, L. Zou, Z. Fang, W.H. Zhu, X.H. Zhong, One-pot synthesis of highly luminescent CdTe/CdS core/shell nanocrystals in aqueous phase. Nanotech. 19 (2008) 135604.

108. A.M. Omer, Green energies and the environment. Renew. Sustain. Energy Rev. 12 (2008) 1789.

109. K.A. Shams, N.S. Abdel-Azim, I.A. Saleh, Mohamed-Elamir, F. Hegazy, M.M. El-Missiry, F.M. Hammouda Green technology:

Economically and environmentally innovative methods for extraction of medicinal & aromatic plants (MAP) in Egypt. J. Chem. Pharm. Res. 7 (2015) 1050.

110. M. T. Amin, A. A. Alazba, U. Manzoor1A Review of Removal of Pollutants from Water/Wastewater Using Different Types of Nanomaterials. Adv. Mater. Sci. Eng. 24 (2014) 825910.

111. Y. He, Z. Huang, Z. Ma, B. Yao, H. Liu, L. Hu, Q. Zhao, Q. Yang, D. Liu, D. Du, Highly efficient photocatalytic performance and mechanism of α-ZnTcPc/g-C_3N_4 composites for methylene blue and tetracycline degradation under visible light irradiation. Appl. Surf. Sci. 498 (2019) 14383.

112. N. Ahmad, E. S. Fitri, A. Wijaya, Amri, Mardiyanto, I. Royani, A. Lesbani, Catalytic oxidative desulfurization of dibenzothiophene utilizing composite based Zn/Al layered double hydroxide. Bull. Chem. React. Eng 17 (2022) 733.

113. F. Ahmad, D. Zhu, J. Sun, Environmental fate of tetracycline antibiotics: degradation pathway mechanisms, challenges, and perspectives. Environ. Sci. Eur. 33 (2021) 64.

114. P. Yang, Y. Ye, Z. Yan, Q. Li, K. Zhang, Y. Yang, Q. Zhang, H. Yin, D. Xi, F. Pan, Efficient removal of tetracycline in water by a novel chemical and biological coupled system with non-woven cotton fabric as carrier. Chin. Chem. Lett. 32 (2021) 2823.

115. R.A. Palominos, M.A. Mondaca, A. Giraldo, G. Peñuela, M. Pérez-Moya, D. Mansilla, Photocatalytic oxidation of the antibiotic tetracycline on TiO_2 and ZnO suspensions. Catal. Today 144 (2009) 100.

116. C. Thamaraiselvan, M. Noel, Membrane processes for dye wastewater treatment: Recent progress in fouling control. Crit. Rev. Environ. Sci. Technol. 45 (2015) 1007.

117. I.M. Bulai, Ezio Venturino, Biodegradation of organic pollutants in a water body. J. Math. Chem. 54 (2016) 1387

118. X. Luo, L. Zhang, J. Hazard. High effective adsorption of organic dyes on magnetic cellulose beads entrapping activated carbon. Mater. 171 (2009) 340.

119. F. Su, P. Li, J. Huang, M. Gu, Z. Liu, Y. Xu, Photocatalytic degradation of organic dye and tetracycline by ternary Ag_2O/AgBr-CeO_2 photocatalyst under visible-light irradiation. Sci. Rep. 11 (2021) 85.

120. A. Ahmad, A. Hayat, M. Ur Rahman, J. Khan. Am. J. Clin, Phthalocyanines derivatives as control approach for antimicrobial photodynamic therapy. Microbiol. Antimicrob. 2 (2019) 1041.

121. M. Wainwright, T. Maisch, S. Nonell, K. Plaetzer, A. Almeida, G.P. Tegos, M.R. Hamblin. Photoantimicrobials-are we afraid of the light? Lancet Infect. Dis. 17 (2017) 49.

122. B. Mai, Y. Gao, M. Li, X. Wang, K. Zhang, Q. Liu, Photodynamic antimicrobial chemotherapy for *Staphylococcus aureus* and multidrug-resistant bacterial burn infection in vitro and in vivo . Int. J. Nanomed. 12 (2017) 5915.

123. E.L.M Coitiño, A. Mella, G.I. Cárdenas-Jirón, Theoretical assessment of the photosensitization mechanisms of porphyrin-ruthenium(II) complexes for the formation of reactive oxygen species. J. Photochem. Photobiol. A 294 (2014) 68.

124. J. Wilson, C.A. Golab, Photodynamic therapy of cancer: An update. Cancer J. Clin. 61 (2011) 250.

125. S.S. Lucky, K.C. Soo, Y. Zhang. Nanoparticles in photodynamic therapy. Chem. Rev. 115, (2015) 1990.

126. W. Fan, P. Huang, X. Chen, Overcoming the Achilles' heel of photodynamic therapy. Chem. Soc. Rev. 45 (2016) 6488.

127. N. Nwaji, S. Dingiswayo, J. Mack, T. Nyokong, Photophysical and enhanced nonlinear optical response in asymmetric benzothiazole substituted phthalocyanine covalently linked to semiconductor quantum dots. Spectrochim. Acta A Mol Biomol. Spectrosc. 204 (2018) 629.

128. S. Mgidlana, D. O. Oluwole, T. Nyokong, Fabrication of efficient nonlinear optical absorber using Zn phthalocyanine-semiconductor quantum dots conjugates. Polyhedron 159 (2019) 102.

129. D.O. Oluwole, A.V. Yagodin, J. Britton, A.G. Martynov, Y. G. Gorbunova, A.Y. Tsivadze, T. Nyokong, Optical limiters with improved performance based on nanoconjugates of thiol substituted phthalocyanine with CdSe quantum dots and Ag nanoparticles. Dalton Trans. 46 (2017) 16190.

130. O. Adegoke, T. Nyokong, Probing the sensitive and selective luminescent detection of peroxynitrite using thiol-capped CdTe and CdTe@ZnS quantum dots. J. Lumin. 134 (2013) 448.

131. O. Osifeko, T. Nyokong, Synthesis and physicochemical properties of zinc and indium phthalocyanines conjugated to quantum dots, gold and magnetic nanoparticles. Dyes Pigm. 131 (2016) 186.

132. N. Nwaji, D.O. Oluwole, J. Mack, M. Louzada, S. Khene, J. Britton, T. Nyokong, Improved nonlinear optical behaviour of ball type indium(III) phthalocyanine linked to glutathione capped nanoparticles. Dyes Pigm. 140 (2017) 417.

133. K. Sanusi, S. Khene, T. Nyokong. Enhanced optical limiting performance in phthalocyanine-quantum dot nanocomposites by free-carrier absorption mechanism, Opt. Mater. 37 (2014) 572.

134. N. Nwaji, J. Mack, T. Nyokong, An optical limiting study in aminophenoxy substituted phthalocyanine in the presence of semiconductor quantum dots, J. Lumin. 203 (2018) 247.

135. J. Britton, M. Durmus, V. Chauke, T. Nyokong, Poly methyl methacrylate films containing metallophthalocyanines in the presence of CdTe quantum dots: Non-linear optical behaviour and triplet state lifetimes. J. Mol. Stru. 209 (2013) 1054.

136. P. Matlaba, T. Nyokong, Synthesis, electrochemical and photochemical properties of unsymmetrically substituted zinc phthalocyanine complexes. Polyhedron 21 (2002) 2463.

137. M.S. Agırtas, C. Karatas, S. Ozdemir, Synthesis of some metallophthalocyanines with dimethyl 5-(phenoxy)-isophthalate substituents and evaluation of their antioxidant-antibacterial activities. Spectrochim. Acta Mol. Biomol. Spectrosc. 135 (2015) 20.

138. E. Dube, N. Nwaji, D.O. Oluwole, J. Mack, T. Nyokong, Investigation of photophysicochemical properties of zinc phthalocyanines conjugated to metallic nanoparticles. J. Photochem. Photobiol. A: Chem. 349 (2017) 148.

139. Z. Chen, S. Dong, C. Zhong, Z. Zhang, L. Niu, Z. Li, F. Zhang, Photoswitching of the third-order nonlinear optical properties of azobenzene-containing phthalocyanines based on reversible host–guest interactions. J. Photochem. Photobiol. A: Chem. 206 (2009) 213.

140. S. D'Souza, E. Antunes, T. Nyokong, Synthesis and photophysical studies of CdTe quantum dot-monosubstituted zinc phthalocyanine conjugate. Inorg. Chim. Acta 367 (2011) 173.

141. C. Huang, M. Ke, Synthesis of peripheral and non-peripheral substituted metallophthalocyanines. Chinese Patent Application No. 200710200223, 2007.

142. D.O. Oluwole, E. Prinsloo, T. Nyokong, Photophysicochemical properties of nanoconjugates of zinc(II) 2(3)–mono–2–(4–oxy)-phenoxy)acetic acid phthalocyanine with cysteamine capped silver and silver–gold nanoparticles. Polyhedron 119 (2016) 434.

143. Y.I. Openda, P. Sen, M. Managa, T. Nyokong, Acetophenone substituted phthalocyanines and their graphene quantumdots conjugates as photosensitizers for photodynamic antimicrobialchemotherapy against *Staphylococcus aureus*. Photodiagnosis Photodyn. Ther. 29 (2020) 1016072.

144. G.G. Matlou N. Kobayashi M. Kimura T. Nyokong Synthesis and photophysical studies of asymmetrical zinc phthalocyanine-magnetic nanoparticles conjugates. New J. Chem 41 (2017) 123009.

145. Y.Köysal, S. Isik, N. Akdemir, E. Agar, C. Kantar, 4-(3,5-Dimethoxyphenoxy) phthalonitrile. Acta Crystallogr. 60 (2004) 930.

146. D.O. Oluwole, T. Nyokong, Comparative photophysicochemical behaviour of nanoconjugates of indium tetracarboxyphenoxy-phthalocyanines covalently linked to GSHCdTe/ZnSe/ZnO. J. Photochem. Photobiol. 312 (2015) 34.

147. O.M. Bankole, T. Nyokong, Comparative studies on photophysical and optical limiting characterizations of low symmetry phthalocyanine linked to Fe_3O_4–Ag core–shell or hybrid nanoparticles. New J. Chem. 59 (2016) 10016.

148. A. Fashina, E. Antunes, T. Nyokong, Characterization and photophysical behavior of phthalocyanines when grafted onto silica nanoparticles. Polyhedron 53 (2013) 278.

149. K.E. Sekhosana, E.Antunes, S. Khene, S. D'Souza, T. Nyokong, Fluorescence behavior of glutathione capped CdTe@ZnS quantum dots chemically coordinated to zinc octacarboxy phthalocyanines. J. Lumin. 136 (2013) 255.

150. K. Sanusi, E. Antunes, T. Nyokong, Optical nonlinearities in nonperipherally substituted pyridyloxyphthalocyanines: a combined effect of symmetry, ring-strain and demetalation, Dalt. Trans. 43 (2014) 999.

151. P. Sen, A. Sindelo, D. M. Mafukidze, T. Nyokong Synthesis and photophysicochemical properties of novel axially disubstituted silicon (IV) phthalocyanines and their photodynamic antimicrobial chemotherapy (PACT) activity against Staphylococcus aureus. Synth. Met. 258 (2019) 11620.

152. M.J. Stillman, T. Nyokong, in: C.C. Leznoff, A.B.P. Lever (Eds.), Phthalocyanines. Principles and Properties New York, vol. 1, (2003).

153. I. Özcesmici, Synthesis and fluorescence properties of phthalocyanines with dibromo- and tribromo-phenoxy functionalities. Synth. Met. 176 (2013) 128.

154. T. Nyokong, in: J. Jiang Series, D.M.P. Mingos (Eds.), Electronic Spectral and Electrochemical Behaviour of Near Infrared Absorbing Metallophthalocyanines, Structure and Bonding: Functional Phthalocyanine Molecular Materials, vol. 135, Springer, (2010) 45.

155. H.P. Karaoglu, A.K. Burat, α- and β-substituted metal-free phthalocyanines: synthesis, photophysical and electrochemical properties. Molecules 25 (2020) 1914

156. M. Jeyakanthan, U. Subramanian, R.B. Tangsali, Enhanced photoluminescence of $CoWO_4$ in $CoWO_4$ /$PbWO_4$ nanocomposites, J. Mater. Sci Mater. Electron. 29 (2018) 1914.

157. X. Dang, X. Dong, H. Wang, X. Zhang, H. Ma, M. Xue, Controllable Fabrication of Ordered Mesoporous Bi_2WO_6 and Its High Photocatalytic Activity under Visible Light. Int. j. photoenergy Volume 2014, Article ID 146892, 7 pages http://dx.doi.org/10.1155/2014/146892

158. L. Li, J.-F. Zhao, N. Won, H.o. Jin, S. Kim, J.-Y. Chen, Quantum dot-aluminum phthalocyanine conjugates perform photodynamic reactions to kill cancer cells via fluorescence resonance energy transfer. Nanoscale Res. Lett. 7 (2012) 386.

159. B.D. Viezbicke, S. Patel, B.E. Davis, D.P. Birnie, Evaluation of the Tauc method for optical absorption edge determination: ZnO thin films as a model system. Phys. Status Solidi B 252 (8) (2015) 1700.

160. F.A. Alharthi, M. Shashank, J. Shashikanth, R. Viswantha, A.A. Abdulaziz, A. JariS, A.A. Mabkhoot, S.J. Mohammed, G. Nagaraju Hydrothermal synthesis of α-$SnWO_4$: Application to lithium-ion battery and photocatalytic activity. Ceram Int. 47 (2021) 10242.

161. University of California at Davis, Chemistry, 10.5: Semiconductors - Band Gaps, Colors, Conductivity and Doping at Davis, Libre Text (2021).

162. Y.P. Bhoi, D.P. Rout, B.G. Mishra, Photocatalytic Chemoselective Aerobic Oxidation of Thiols to Disulfides Catalyzed by Combustion Synthesized Bismuth Tungstate Nanoparticles in Aqueous Media. J. Clust. Sci. 27 (2016) 267.

163. S.M. El-Sheikh, M.M. Rashad, Novel Synthesis of Cobalt Nickel Tungstate Nanopowders and its Photocatalytic Application. J. Clust. Sci. 26 (2015) 743.

164. T. Ejima, T. Banse, H. Takatsuka, Y. Kondo, M. Ishino, N. Kimura, M. Watanabe, I. Matsubara, Microscopic optical and photoelectron measurements of MWO_4 (M= Mn, Fe, and Ni). J. Lumin. 59 (2006) 119.

165. S. Murni, M. Zawawi, R. Yahya, A. Hassan, H.N.M Ekramul Mahmud, M.N. Daud, Structural and optical characterization of metal tungstates (MWO_4; M=Ni, Ba, Bi) synthesized by a sucrose-templated method. Chem. Cent. J. (2013). 80http://journal.chemistrycentral.com/content/7/1/80

166. H.Q. Li, Y.M. Cui, W.S. Hong, High photocatalytic performance of BiOI/Bi_2WO_6 toward toluene and reactive brilliant red. Appl. Surf. Sci. 264 (2013) 581.

167. J.L. Rico, M. Albiter, J. Espino, J.S.J. Hargreaves, M. Ostroumov, L.I. Salcedo, K. Wilson Synthesis and ammonolysis of nickel and cobalt tungstates and their characterisation. J. Saudi Chem. Soc. 20 (2016) 405.

168. A.W. Snow, J.R. Griffith, N.P. Marullo, Syntheses and characterization of heteroatom-bridged metal-free phthalocyanine network polymers and model compounds. Macromolecules 17 (1984) 1614.

169. R. Jenkins R.L Synder in: Introduction to X-ray diffractometry, New York: Wiley & Sons; 1996.

170. S.O. Alfaro, A. Martínez-de la Cruz, Synthesis, characterization and visible-light photocatalytic properties of Bi_2WO_6 and $Bi_2W_2O_9$ obtained by co-precipitation method. Appl. Catal. A 383 (2010) 128.

171. A. Kaur, S.K. Kansal, Bi_2WO_6 nanocuboids: An efficient visible light active photocatalyst for the degradation of levofloxacin drug in aqueous phase. Chem. Eng. J. 302 (2016) 194.

172. A.L.M. de Oliveira, J.M. Ferreira, M.R.S. Silva, S.C. de Souza, F.T.G. Vieira, E. Longo, A.G. Souza, I.M.G. Santos, Influence of the thermal treatment in the crystallization of $NiWO_4$ and $ZnWO_4$. J Therm. Anal. Calorim. 97 (2009) 167.

173. J. Robertson, T.J. Bandosz, Photooxidation of dibenzothiophene on TiO_2/hectorite thin films layered catalyst. J. Colloid Interface Sci. 299 (2006) 125.

174. J. Mack, N. Kobayashi, Low Symmetry Phthalocyanines and Their Analogues. Chem. Rev. 111 (2011) 281.

175. J. A. Kloepfer, S. E. Bradforth, J. L. Nadeau, Photophysical properties of biologically compatible CdSe quantum dot structures. J. Phys. Chem. B 109 (2005) 9996.

176. A.K. Pal, S. Varghese, D.B. Cordes, A.M.Z. Slawin, I.D.W. Samuel, E. Zysman- Colman, Near-infrared fluorescence of silicon phthalocyanine carboxylate esters. Sci. Rep. 7 (2017) 12282 doi: 10.1038/s41598- 017-12374.

177. B. Keskin , O. Okuyucu , A. Altındal , A. Erdogmus, Novel indium (III) phthalocya- nines; synthesis, photophysical and humidity sensing properties. New J. Chem. 40 (2016) 5537.

178. M. G. Debacker, O. Deleplanque, B. van Vlierberge, F. X. Sauvage, A Laser Photolysis Study of Triplet Lifetimes and of Triplet-Triplet Annihilation Reactions of Phthalocyanins DMSO Solutions. Laser Chem. 8 (1988) 1-11.

179. R. Darwent, P. Douglas, A. Harriman, G. Porter, M.C. Richoux, Metal phthalocyanines and porphyrins as photosensitizers for reduction of water to hydrogen. Coord. Chem. Rev. 44 (1982) 83.

180. M.A. Idowu, S. Xego, Y. Arslanoglu, J. Mark, E. Antunes, T. Nyokong, Photophysicochemical behaviour and antimicrobial properties of

monocarboxy Mg (II) and Al (III) phthalocyanine-magnetite conjugates, Spectrochim. Acta Part A. 193 (2018) 407.

181. P.M. Sivakumar, G. Sheshayan, M. Doble, Experimental and QSAR of acetophenones as antibacterial agents. Chem. Biol. Drug Des. 72 (2008) 303.

182. F.D. Halstead, M. Rauf, N.S. Moiemen, A. Bamford, C.M. Wearn, A.P. Fraise, P.A. Lund, B.A. Oppenheim, M.A. Webber, The antibacterial activity of acetic acid against biofilm-producing pathogens of relevance to burns patients. PLoS One 10 (2015) 0136190.

183. I. Malık, J. Csollei, J. Jampılek, L. Stanzel, I. Zadrazilova, J. Hosek, S. Pospısilova, A. Cızek, A.Coffey, J. O'Mahony The Structure–Antimicrobial Activity Relationships of a Promising Class of the Compounds Containing the N-Arylpiperazine Scaffold. Molecules 21 (2016) 1274.

184. C. Marambio-Jones, E. M. V. Hoek A review of the antibacterial effects of silver nanomaterials and potential implications for human health and the environment J. Nanopart Res. 12 (2010) 1531.

185. S. J. Olusegun, G. Larrea, M. Osial, K. Jackowska, P. Krysinsk, Photocatalytic Degradation of Antibiotics by Superparamagnetic Iron Oxide Nanoparticles. Tetracycline Case. Catalysts 11 (2021) 124.

186. A .H. Zyoud, A . Zubi, S.H. Zyoud, M.H. Hilal, S. Zyoud, N. Qamhieh, A.R. Hajamohideen, H.S. Hilal, Kaolin-supported ZnO nanoparticle catalysts in self-sensi- tized tetracycline photodegradation: zero-point charge and pH effects.Appl. Clay Sci. 182 (2019) 105294.

187. J. Wu, H. Zhang, N. Oturan, Y. Wang, L. Chen, M.A. Oturan, Application of response surface methodology to the removal of the antibiotic tetracycline by electrochemical process using carbon-felt cathode and DSA (Ti/RuO 2-IrO_2) anode. Chemosphere 87 (2012) 614.

188. Y. Shi , Z. Yang , B. Wang , H. An , Z. Chen , H. Cui , Adsorption and photocat- alytic degradation of tetracycline hydrochloride using a palygorskite-supported Cu_2O-TiO_2 composite. Appl. Clay Sci. 119 (2016) 311.

189. I. Dalmázio, M.O. Almeida, R. Augusti, T.M.A. Alves, Monitoring the degradation of tetracycline by ozone in aqueous medium via atmospheric pressure ioniza- tion mass spectrometry. J. Am. Soc. Mass Spectrom. 18 (2007) 679.

190. M.S. Jang K.S. Doh J.S. Kang Y.S. Jeon K.S. Suh S.T. Kim A comparative split-face study of photodynamic therapy with indocyanine green and indole-3-acetic acid for the treatment of acne vulgaris. Br. J. Dermatol. 165 (2011) 1095.

191. S.L. Chen, X.J. Huang, Z.K. Xu, Functionalization of cellulose nanofiber mats with phthalocyanine for decoloration of reactive dye wastewater. Cellulose 18 (2011) 1295.

192. D. Melgoza, A. Hern´andez-Ramírez, J.M. Peralta-Hern´andez, Comparative efficiencies of the decolourisation of Methylene Blue using Fenton's and photo- Fenton's reactions. Photochem. Photobiol. Sci. 8 (2009) 596, https://doi.org/ 10.1039/b817287k.

193. P. Qu, J. Zhao, T. Shen, H. Hidaka, TiO2-assisted photodegradation of dyes: A study of two competitive primary processes in the degradation

of RB in an aqueous TiO2 colloidal solution. J. Mol. Catal. A: 129 (1998) 257.

194. C. Randorn, S. Wongnawab, P. Boonsinb, Bleaching of Methylene Blue by hydrated titanium dioxide. ScienceAsia 30 (2004) 149.

195. S. Gorduk, O. Avciata, U. Avciata, Photocatalytic degradation of methylene blue under visible light irradiation by non-peripherally tetra substituted phthalocyanine-TiO_2 nanocomposites. Inorg. Chim. Acta 471 (2018) 137.

196. S. Balasurya, S. Alfarra, L.L. Raju, A.Chinnathambi, S.A. Alharbi, A.M. Thomas, S.S. Khan, Novel CoWO4-Ag2MoO4 NCs: Synthesis, enhanced photocatalytic activity under visible-light irradiation and its antimicrobial activity. Surf. Interfaces 25 (2021) 101237.

197. J.R. Zugle, T. Nyokong, Zinc(II) 2,9,16,23-tetrakis4-(N-methylpyridyloxy)] phthalocyanine anchored on an electrospun polysulfone polymer fiber: application for photosensitized conversion of methyl orange. J. Mol. Cat. A: Chem. 366 (2013) 247.

198. K.V. Kumar, K. Porkodi, F. Rocha, Langmuir-Hinshelwood kinetics – a theoretical study. Catal. Commun. 9 (2008) 82.

199. M. Sheik-bahae, A.A. Said, E.W. Van Stryland, High-sensitivity, single-beam n2 measurements. Opt. Lett. 14 (1989) 955.

200. Y. Chen, M. Hanack, Y. Araki, O. Ito, Axially modified gallium phthalocyanines and naphthalocyanines for optical limiting. Chem. Soc. Rev 34 (2005) 517.

201. Y. Liu, Y. Chen, L. Cai, J. Wang, Y. Lin, J.J. Doyle, W.J. Blau, Optical limiting properties of axially substituted indium phthalocyanines in the solid PMMA composite films. Mater. Chem. Phys. 107 (2008) 189-192.

202. T. Pritchett, Models for Saturable and Reverse Saturable Absorption in Materials for Optical Limiting. ARL (2002) 1.

203. T.H. Wei, D.J. Hagan, M.J. Sence, E.W. Van Stryland, J.W. Perry, D.R. Coulter, Direct measurements of nonlinear absorption and refraction in solutions of Phthalocyanines. Appl. Phys. B 54 (1992) 46.

204. Y. Chen, L.R. Subramanian, M. Fujitsuka, O. Ito, S. O'Flaherty, W.J. Blau, T. Schneider, D. Dini, M. Hanack, Synthesis and Optical Limiting Properties of Axially Bridged Phthalocyanines: (tBu4PcGa)2O] and (tBu4PcIn)2O]. Chem. Eur. 8 (2002) 4248.

205. J. Lakowiecz Principles of fluorescence spectroscopy, 2nd edn. Kluwer Academic/Plenum Publishers, New York (1999).

206. G. de la Torre, P. Vazquez, F. Agullj-Ljpez, T. Torres, Role of structural factors in the nonlinear optical properties of phthalocyanines and related compounds. Chem. Rev 104 (2004) 3723.

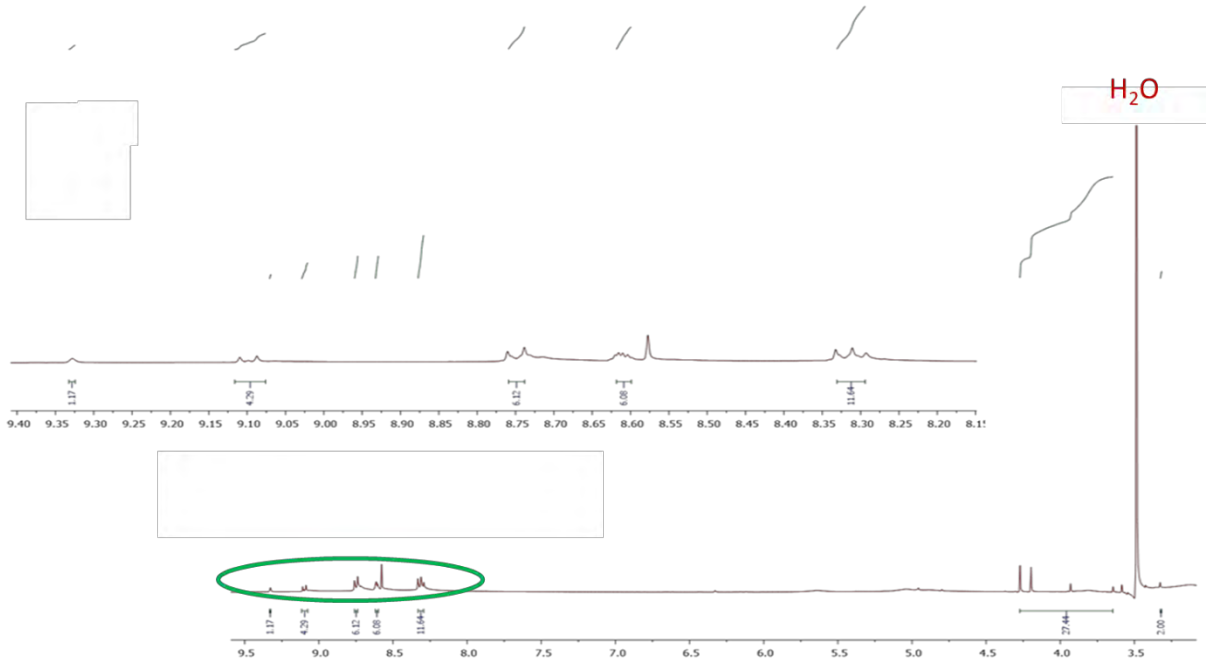

Figure A1: Proton NMR for complex **1**-ethanoic in DMSO.

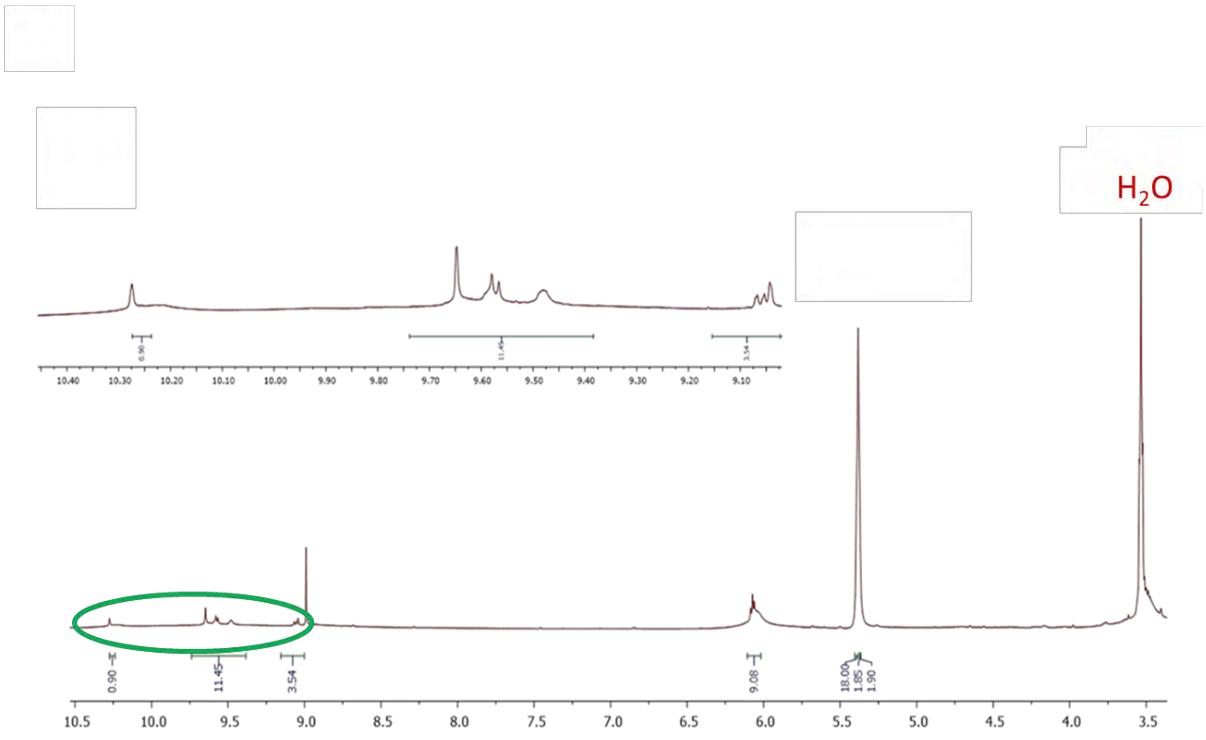

***Figure A2**: Proton NMR for complex **2**-propionic* in DMSO.

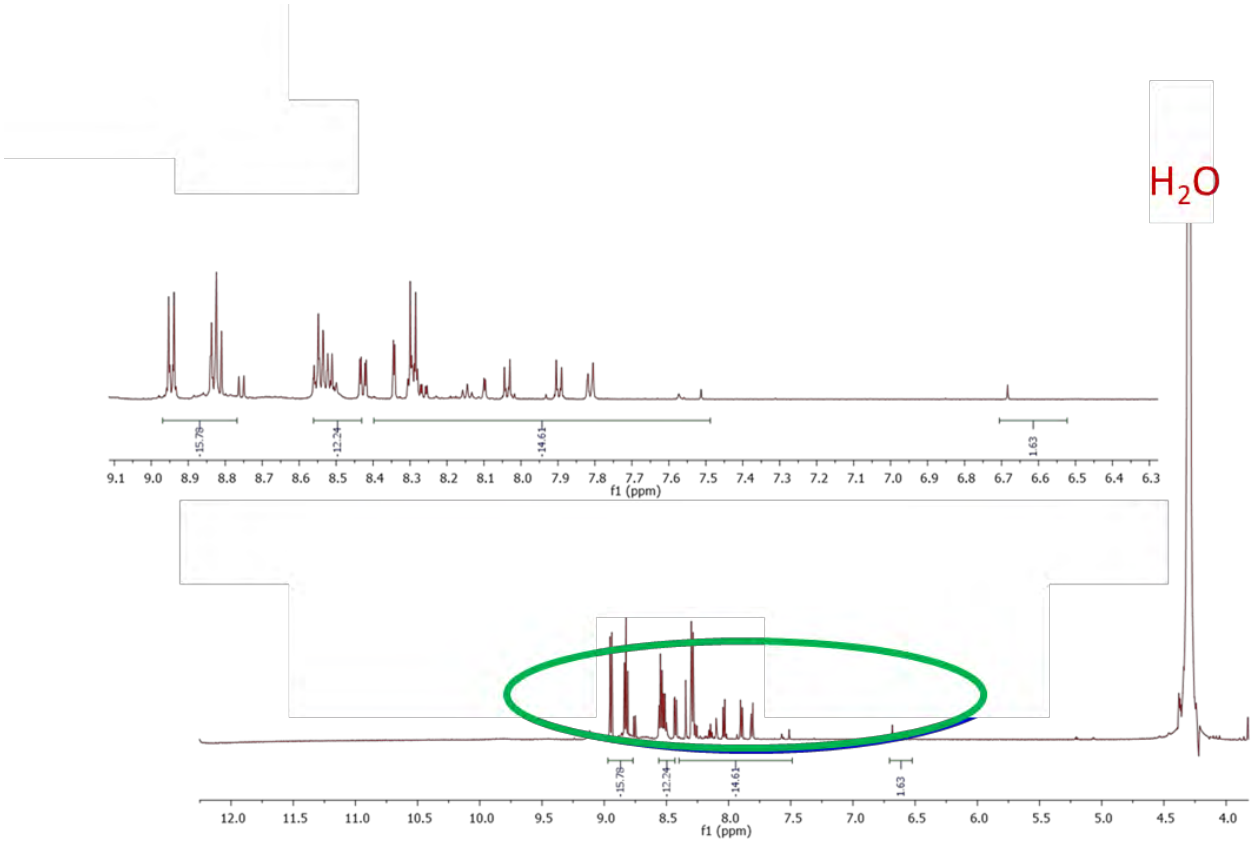

Figure A3: Proton NMR for complex **3**-NH_2 in DMSO.

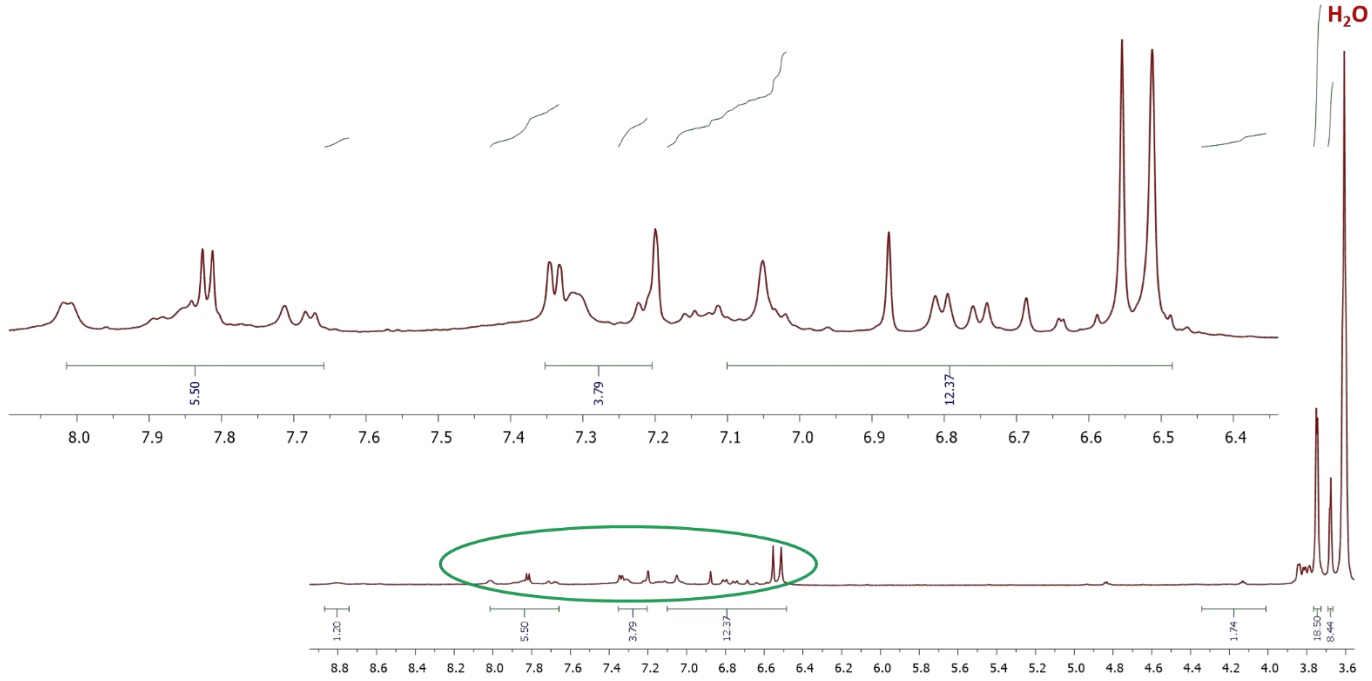

Figure A4: Proton NMR for complex **4**-acetic in DMSO.

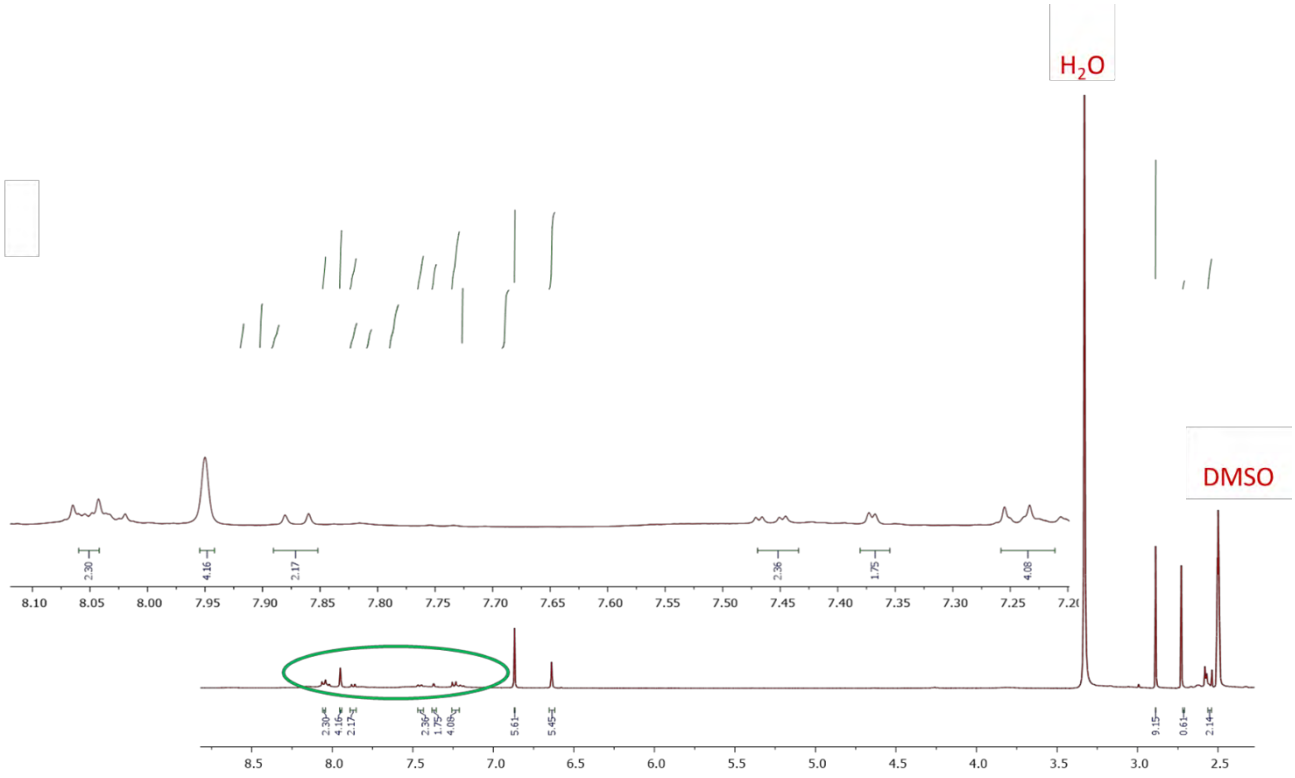

Figure A5: Proton NMR for complex **5**-acetic in DMSO.

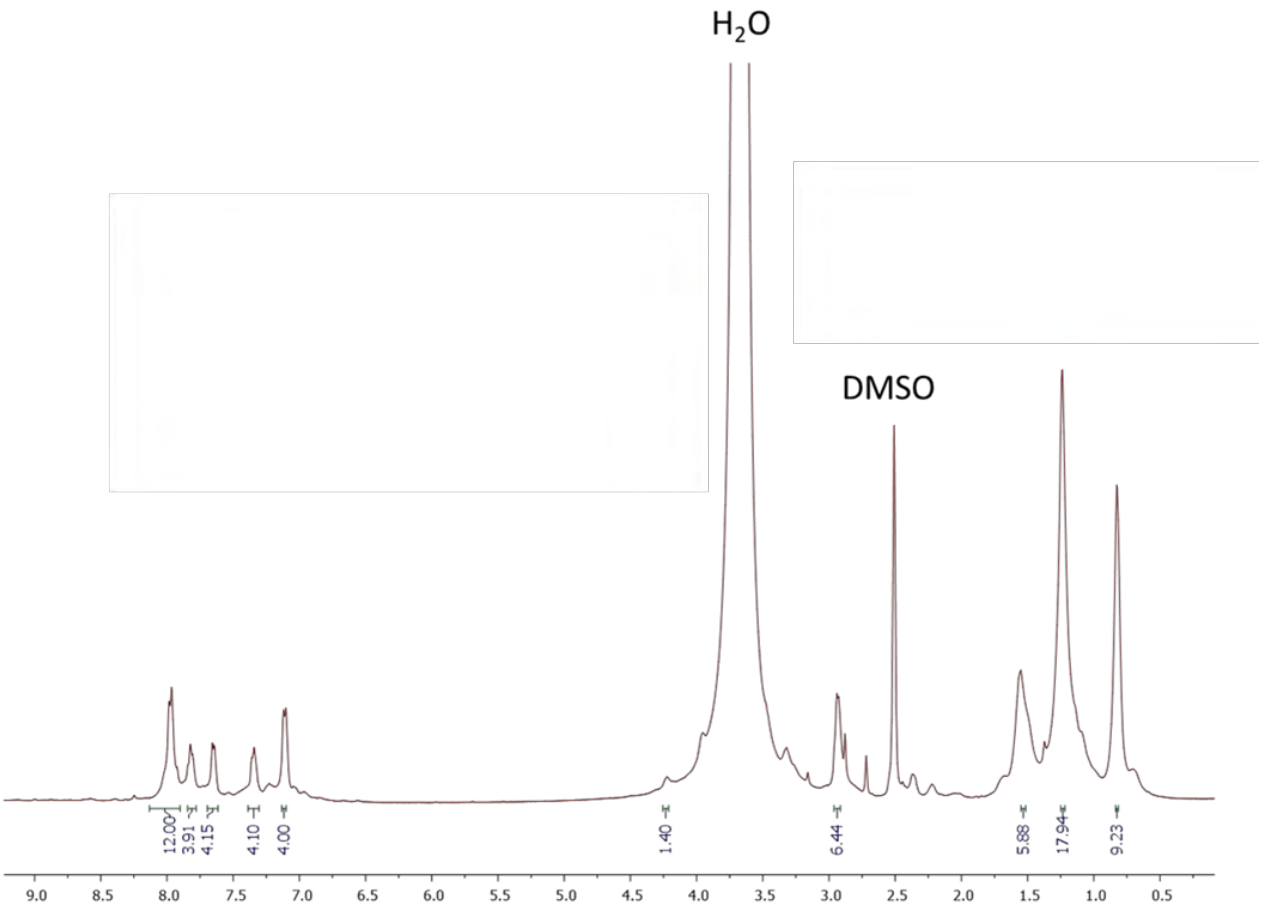

Figure A6: Proton NMR for complex **6**-COOH in DMSO.

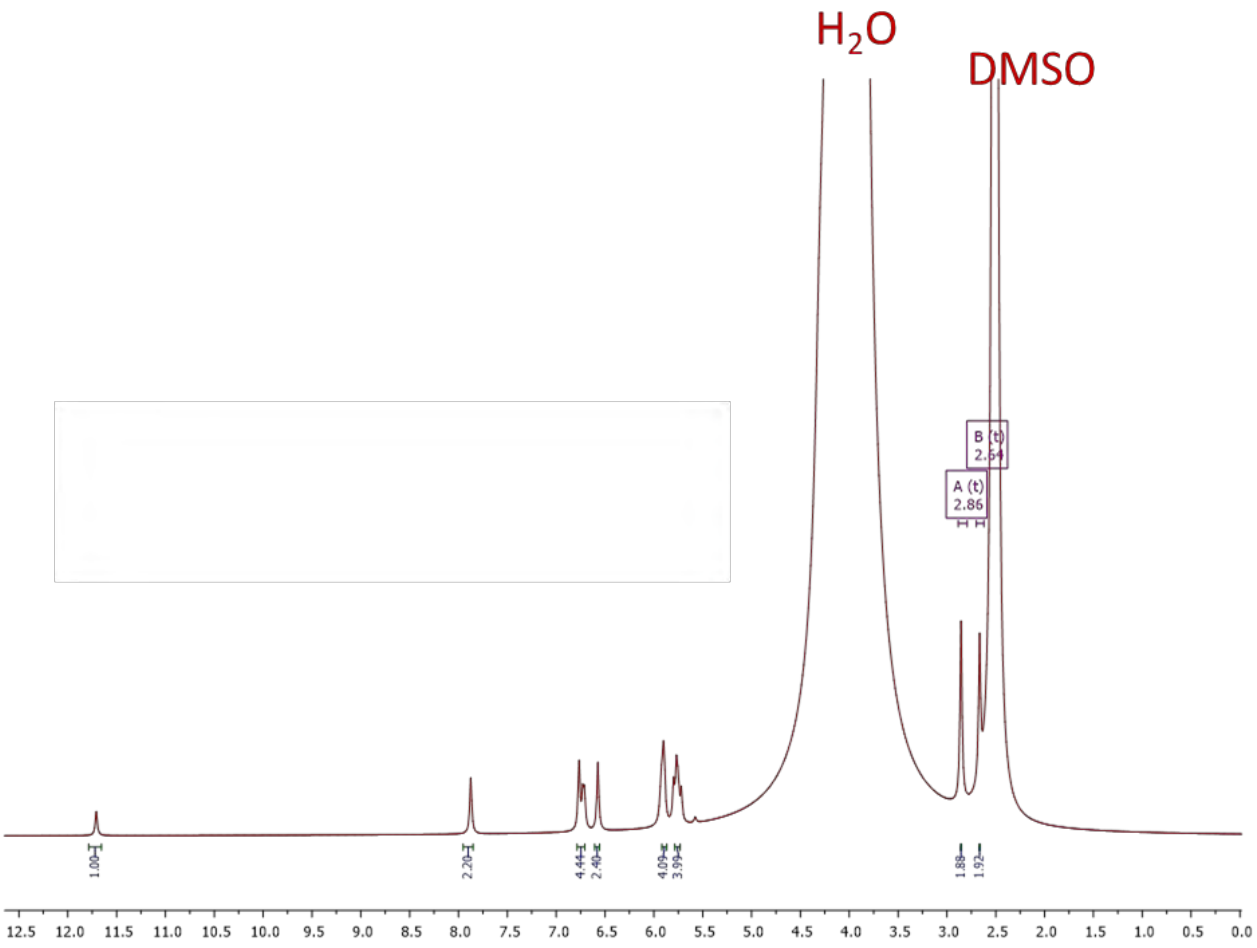

***Figure A7**: Proton NMR for complex **7**-propionic* in DMSO.

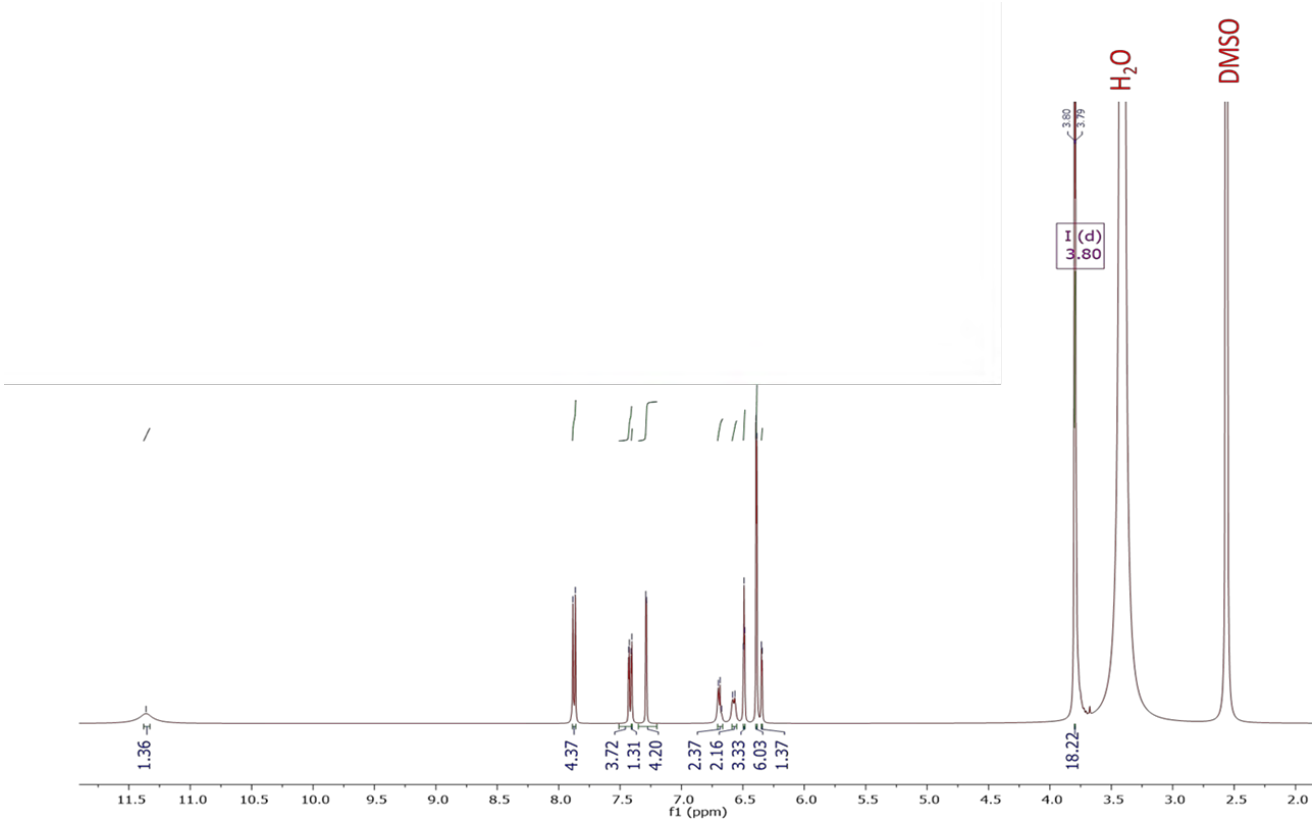

***Figure A8**: Proton NMR for complex **8**-acrylic* in DMSO.

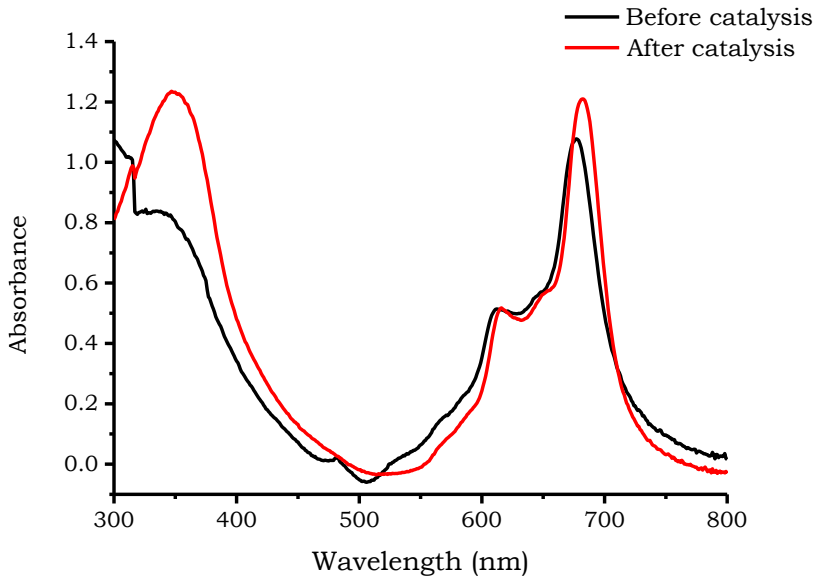

***Figure A9**: Solid state Absorption spectra of photocatalysts (**4**-COOH-$NiWO_4$ used as an example) before and after use.*

Table A1: Initial rates, rate constants (k_{obs}) and half-lives ($\tau_{1/2}$) of various initial concentrations for degradation of TC using Pc complexes and conjugates in water.

TC] (10^{-5} M)	k_{obs} ($\times 10^{-3}$ min^{-1})					Initial rates ($\times 10^{-8}$ mol $L^{-1}min^{-1}$)					$\tau_{1/2}$($\times 10^{1}$ min)				
	5-acetic	**5**-acetic-Ag_2WO_4	**5**-acetic-Ag-Fe_3O_4	**5**-acetic-$NiWO_4$	**5**-acetic-$CoWO_4$	**5**-acetic	**5**-acetic-Ag_2WO_4	**5**-acetic-Ag-Fe_3O_4	**5**-acetic-$NiWO_4$	**5**-acetic-$CoWO_4$	**5**-acetic	**5**-acetic-Ag_2WO_4	**5**-acetic-Ag-Fe_3O_4	**5**-acetic-$NiWO_4$	**5**-acetic-$CoWO_4$
1.45	2.74	3.03	2.85	2.77	3.35	3.98	4.39	4.13	4.02	4.86	25	22	24	20	20
2.70	1.36	1.55	1.45	1.24	1.47	3.68	4.18	3.91	3.35	3.97	50	44	47	55	47
3.80	0.74	1.03	0.86	0.78	0.88	2.83	3.9	3.26	2.96	3.34	93	67	80	88	78
4.45	0.54	0.83	0.64	0.61	0.71	2.38	3.69	2.85	2.71	3.15	128	83	108	113	97
6.62	0.29	0.48	0.31	0.31	0.36	1.56	3.17	2.05	2.05	2.38	239	144	223	223	198

Table A2: Initial rates, rate constants (k_{obs}) and half-lives ($\tau_{1/2}$) of various initial concentrations for degradation of MB using Pc and conjugates in water.

[MB] ($\times 10^{-5}$ *M)*	k_{obs} ($\times 10^{-3}$ min^{-1})					Initial rates ($\times 10^{-7}$ mol $L^{-1}min^{-1}$)					$\tau_{1/2}$($\times 10^{2}$min)				
	5-acetic	**5**-acetic- Ag_2WO_4	**5**-acetic- Ag-Fe_3O_4	**5**-acetic $NiWO_4$	**5**-acetic- $CoWO_4$	**5**-acetic	**5**-acetic Ag_2WO_4	**5**-acetic-Ag-Fe_3O_4	**5**-acetic $NiWO_4$	**5**-acetic $CoWO_4$	**5**-acetic	**5**-acetic- Ag_2WO_4	**5**-acetic- Ag-Fe_3O_4	**5**-acetic $NiWO_4$	**5**-acetic $CoWO_4$
2.63	6.76	8.58	9.79	6.70	8.73	1.74	2.25	2.57	1.76	2.29	1.04	0.16	0.8	0.20	0.79
3.32	4.74	6.76	7.66	4.48	6.83	1.45	2.24	2.54	1.55	2.26	1.46	0.20	0.10	0.30	1.01
4.23	3.65	5.26	5.69	3.68	4.85	1.43	2.22	2.4	1.48	2.05	1.9	0.26	0.14	0.37	1.43
5.51	2.52	4.02	3.50	2.48	3.65	1.37	2.21	1.93	1.36	2.01	2.75	0.34	0.23	0.55	1.90
5.68	1.71	3.84	3.06	2.28	2.65	0.78	2.18	1.74	1.29	1.50	4.05	0.36	0.27	0.60	2.62

Table A3: Initial rates, rate constants (k_{obs}) and half-lives ($\tau_{1/2}$) of various initial concentrations for degradation of TC using Pcs and conjugates in *n*-Octane.

[DBT] *(× 10^{-5} M)*	k_{obs} (× 10^{-3} min^{-1})					Initial rates (× 10^{-8} mol $L^{-1}min^{-1}$)					$\tau_{1/2}$(× 10^{1}min)				
	5-acetic	**5**-acetic Ag_2WO_4	**5**-acetic Ag-Fe_3O_4	**5**-acetic $NiWO_4$	**5**-acetic $CoWO_4$	**5**-acetic	**5**-acetic-Ag_2WO_4	**5**-acetic-Ag-Fe_3O_4	**5**-acetic-$NiWO_4$	**5**-acetic-$CoWO_4$	**5**-acetic	**5**-acetic Ag_2WO_4	**5**-acetic Ag-Fe_3O_4	**5**-acetic $NiWO_4$	**5**-acetic $CoWO_4$
1.43	3.52	4.22	4.65	3.87	4.58	5.04	6.04	6.65	5.54	6.55	19	*16*	*14*	*17*	
2.85	1.34	1.61	1.77	1.47	1.74	3.83	4.59	5.05	4.213	4.97	51	*42*	*39*	*46*	*39*
3.16	0.99	1.19	1.31	1.09	1.29	3.14	3.768	4.14	3.45	4.08	69	*58*	*52*	*63*	*53*
5.71	0.45	0.53	0.58	0.49	0.58	2.55	3.06	3.37	2.80	3.31	155	*129*	*117*	*141*	*119*
6.41	0.24	0.29	0.32	0.27	0.32	1.59	1.90	2.09	1.74	2.06	279	*232*	*211*	*254*	*214*